Lattice Models in Materials Science

Diffusion, Trabecular Bone Remodelling and Linear Elastic Networks

DISSERTATION

zur Erlangung des akademischen Grades
doctor rerum naturalium
(Dr. rer. nat.)
im Fach Physik

eingereicht an der
Mathematisch-Naturwissenschaftlichen Fakultät I
Humboldt-Universität zu Berlin

von
Herr Mag. Markus Hartmann
geboren am 15.02.1977 in Wien

Präsident der Humboldt-Universität zu Berlin:
in Vertretung: Prof. Dr. Hans Jürgen Prömel

Dekan der Mathematisch-Naturwissenschaftlichen Fakultät I:
Prof. Thomas Buckhout, PhD

Gutachter:

1. Prof. Dr. Peter Fratzl
2. Prof. Dr. Lutz Schimansky-Geier
3. Prof. Dr. Franz-Dieter Fischer

eingereicht am: 8. September 2005
Tag der mündlichen Prüfung: 10. Januar 2006

Abstract

This thesis presents the results of investigations on three independent research topics of modern biophysical and materials science research: substitutional diffusion in binary alloys, the remodelling process in trabecular bone and the prediction of mechanical properties of self assembling, amphiphilic bilayers. The basic description of all three projects is based on lattice models, a highly successful class of models that are used in several fields of modern physics to describe physical processes. For the diffusional process in alloys, which on a microscopic scale manifests itself in a discrete site exchange between one atom and a neighbouring vacancy, it was investigated how this microscopic description can be reconciled with a macroscopic continuum model. In a computer simulation exact microscopic averages were used to determine macroscopic properties, like Onsager's coefficients. These were then compared to theoretical predictions of different accuracy. Following the same strategy – comparing averaged results from microscopical simulations with purely continuum mechanical calculations – interdiffusion problems were investigated. It was shown that for obtaining an appropriate macroscopic description it is essential to fully include the behaviour of the vacancy in the description, which is – due its complexity – often omitted.

For the investigations on remodelling of trabecular bone, bone's architecture was mapped onto a lattice and the local mechanical state of each element was determined by a simplified mechanical model. A local remodelling law was then used to translate this mechanical information into a signal that determined the rate of change of the architecture at that special point. This rate of change was given by a stochastic description, i.e. the remodelling law gave the probabilities for bone formation and resorption, respectively. The development of the model was guided by the aim to give a good balance in the accuracy of the description of the mechanical and biological part. The simple, but fast, algorithm to assess the mechanical properties of the structure gave the possibility to test a variety of biological hypotheses, concerning the special form of the remodelling law. It was shown that a stochastic description of the remodelling process demands the formulation of both, a formation and a resorption probability, since – in contrast to conventional simulations with deterministic rate equations – a pure net effect does not suffice to describe the process. Furthermore it was shown that a non-linear remodelling law is a better candidate to describe the remodelling process in real bone than a linear one. Finally the model was used to describe osteoporosis, a wide spread disease affecting trabecular architecture. It was concluded that in the features attributed to osteoporosis one has to distinguish between normal ageing of bone's architecture and additional changes that stem from pathological alterations in the regulatory system.

A simple concept was introduced to model the mechanical properties of self-assembled membranes. The (amphiphilic) molecules forming the membrane are assumed to occupy a regular lattice, nearest neighbours are connected by linear, elastic springs. Different spring constants are assumed for different atomic pairs. The full elastic matrix of a given structure was solved and the elastic modulus, the Poisson ratio and the bending rigidity of the system determined. It was shown that the bending rigidity exhibits a pronounced concentration dependence, varying over orders of magnitude in a small concentration regime, giving very flexible membranes at one end (bending rigidities of the order of kT), very stiff ones at the other (bending rigidities up to three orders of magnitude larger than kT).

Keywords:
Diffusion, Onsager Coefficients, Interdiffusion, Bone Remodelling,
Osteoporosis, Amphiphilic Membranes, Computer Simulation

Zusammenfassung

In der vorliegenden Arbeit wurden drei unabhängige Problemfelder moderner biophysikalischer und materialwissenschaftlicher Forschung untersucht: substitutionelle Diffusion in binären Legierungen, der Umbauprozess in trabekulärem Knochen und die Voraussage mechanischer Eigenschaften, insbesondere der Biegesteifigkeit, selbstorganisierender amphiphiler Membrane. Für alle drei Problemfelder wurden Gittermodelle gewählt, um ausgesuchte Fragestellungen zu untersuchen. Für den Fall der Diffusion in Legierungen war dies inwieweit sich der Diffusionprozess, der sich auf atomarer Ebene als diskrete Platztäusche von einzelnen Atomen und Leerstellen manifestiert, auf einer größeren, makroskopischen, Ebene mit Hilfe einer kontinuumstheoretischen Theorie beschreiben lässt. Zu diesem Zwecke wurden exakte mikroskopische Mittelwerte herangezogen, um makroskopische Größen, insbesondere die Onsager Koeffizienten, zu bestimmen. Die so erhaltenen Koeffizienten wurden dann mit theoretischen Voraussagen unterschiedlicher Genauigkeit verglichen. Zusätzlich wurde das technologisch wichtige Problem der Interdiffusion untersucht, wobei auch hier die exakte atomistische Diffusion einer makroskopischen kontinuumsmechanischen Berechnung gegenübergestellt wurde. Es zeigt sich, dass die sorgfältige thermodynamische Berücksichtigung der Leerstellen für eine genaue Beschreibung des Problems auf einer makroskopischen Ebene essentiell, aber auch sehr schwierig ist.

Im Fall der Beschreibung des Umbauprozesses in trabekulärem Knochen wurde die spongiöse Architektur des Knochens auf ein Gitter abgebildet und mittels einer vereinfachten mechanischen Beschreibung die lokale Belastung in jedem Knochenelement bestimmt. Mittels einem ebenfalls lokalem Umbaugesetz wurde diese mechanische Information in ein Signal umgesetzt, das den Umbau der Struktur an jedem ihrer Punkte bestimmte. Der Umbau der Struktur wurde durch eine stochastische Beschreibung vorgegeben, das Umbaugesetz gab eine lokale Wahrscheinlichkeit für den An- bzw. Abbau eines Knochenelements in jedem Punkt. Bei der Entwicklung dieses Modells wurde besonderer Wert auf eine ausgewogene Bilanz zwischen mechanischer und biologischer Beschreibung des Prozesses gelegt. Der schnelle, wenn auch vereinfachende, Algorithmus zur mechanischen Beschreibung der Struktur gab die Möglichkeit mehrere biologische Hypothesen bezüglich der genauen Form des Umbaugesetzes zu prüfen und auf deren Plausibilität zu prüfen. Es wurde gezeigt, dass die stochastische Beschreibung des Umbauprozesses die genaue Formulierung einer An- und Abbauwahrscheinlichkeit verlangt, da eine reine Netto-Anbaurate das Problem nicht ausreichend beschreiben kann. Weiters ergaben die Untersuchungen, dass ein nicht-lineares Umbaugesetz bessere Übereinstimmung mit experimentellen Ergebnissen als ein rein lineares liefert. Weiters wurde das Krankheitsbild der Osteoporose untersucht und es konnte eine Unterscheidung zwischen einem normalen Alterungsprozess der Knochenstruktur und einer krankhaften Veränderung gezogen werden.

Um die mechanischen Eigenschaften selbstorganisierender Membrane zu bestimmen, wurden linear elastische Federkräfte zwischen benachbarten Molekülen angenommen. Die Moleküle selbst waren auf einem regulären Gitter angeordnet. Die elastischen Gleichungen wurden für unterschiedliche Anordnungen der Moleküle und unterschiedliche Konzentrationen gelöst. Die volle elastische Matrix und daraus die gewünschten Eigenschaften wurden bestimmt. Es wurde gezeigt, dass die Biegesteifigkeit solcher Membrane in einem begrenzten Konzentrationsbereich um mehrere Größenordnungen variieren kann – von extrem weich mit einer Biegesteifigkeit unter kT bis sehr steif mit einer Biegesteifigkeit von mehreren hundert kT.

Schlagwörter:
Diffusion, Onsager Koeffizienten, Interdiffusion, Knochenumbau, Osteoporose, amphiphile Membrane, Computersimulation

Da verlor ich den leichten Mut,
zu wissen begehrt' es den Gott
Die Walküre, 2. Aufzug

Doch niemals Launen, immer ein Müssen!
Immer ein neues beklommenes Staunen.
Ariadne auf Naxos, Oper

Tutto nel mondo è burla.
L'uom è nato burlone,
La fede in cor gli ciurla,
Gli ciurla la ragione.
Falstaff, Atto Terzo

Contents

1 Introduction 1

I Diffusion in multicomponent alloys 7

2 Basics of Diffusion 11
- 2.1 Macroscopic diffusion laws 12
  - 2.1.1 The diffusion couple 13
  - 2.1.2 Onsager's Coefficients 16
- 2.2 Microscopic diffusion laws 16
  - 2.2.1 The random alloy model 18
- 2.3 Closing the gap between microscopic and macroscopic theories 20
  - 2.3.1 Darken's concept 20
  - 2.3.2 Manning's concept 21
  - 2.3.3 Moleko's concept 22
  - 2.3.4 Svoboda's concept 22
  - 2.3.5 Allnatt's concept 23

3 Determination of Onsager's Coefficients 25
- 3.1 The Model 25
- 3.2 Measuring Onsager's Coefficients 26

4 Interdiffusion 35
- 4.1 Calculation of Concentration Profiles 36
- 4.2 Results and discussion 36

5 Conclusion and Outlook - Diffusion 43

II Trabecular Bone remodelling 47

6 Concepts of Bone Remodelling 53

6.1 The Wolff-Roux Law 58
6.2 The Mechanostat 59
6.3 Adaptive Elasticity 60
6.4 Computational remodelling 61
6.5 Stochastic Remodelling without mechanical feedback 63

7 The Model – Stochastic Remodelling with mechanical feedback 65
7.1 Mechanics – Two way painting algorithm 66
7.2 Biology – The feedback loop 71
7.3 Simulations and data evaluation 74

8 Simulation Results 79
8.1 Simulations on 2-dimensional lattices 79
8.1.1 Test runs 80
8.1.2 Bone remodelling 85
8.2 Simulations on 3-dimensional lattices 90
8.2.1 Simulations with one and the same net remodelling law 90
8.2.2 Simulations with different types of remodelling laws . . 95

9 Interpretation 97
9.1 (Indirect) coupling of formation and resorption rates—BMUs . 98
9.2 Stochastic remodelling with the same net remodelling law . . . 98
9.3 Stochastic remodelling with different types of remodelling laws 100
9.4 The reaction of the system to perturbations 103
9.5 Speculations on the remodelling law of real bone 105
9.6 Bone diseases—Osteoporosis 105

10 Conclusion and Outlook - Bone Remodelling 111

Simulation Parameters 115

III Linear Elastic Networks 117

11 Linear Elastic Networks 121
11.1 Mechanical equilibrium 121
11.2 The stiffness matrix of a homogenous crystal 123
11.3 Elastic properties of membranes 128
11.3.1 Stiff A-A bonds 128
11.3.2 Stiff A-B bonds 132

12 Final Remarks – Elastic Properties of Membranes **135**

Bibliography **137**

Publications **147**

Acknowledgements **197**

List of Figures

1.1 The triangle of dynamical reactions, structure and mechanical properties . . . 3
1.2 Comparison of a phase separating alloy and trabecular bone . 5

2.1 Diffusion Couple . . . 13
2.2 Tracer Diffusion Coefficients . . . 19

3.1 Emergence and time development of concentration gradients . 28
3.2 Two ways of measuring tracer diffusion coefficients . . . 30
3.3 Onsager's coefficients . . . 31
3.4 Can the sum rules be fulfilled? . . . 33

4.1 Time development of concentration profiles . . . 37
4.2 Concentration profiles for several values of ω_B . . . 38
4.3 Scaled profiles . . . 39
4.4 The interdiffusion coefficient for different values of the atomic exchange frequencies . . . 40
4.5 Comparison of the atomistic MC simulation and a continuum mechanical calculation . . . 41
4.6 The vacancy distribution for early times . . . 42

5.1 The hierarchical structure of bone . . . 50

6.1 Development of a human vertebra . . . 53
6.2 Bone's remodel cycle . . . 55
6.3 The feedback loop . . . 57
6.4 The direction of trabeculae according to Wolff and the stress trajectories in a human build crane . . . 58
6.5 Frost's Remodelling Law . . . 60

7.1 Schematic representation of the used remodelling program . . 66
7.2 Schematic representation of the painting algorithm . . . 68

7.3 The coupling of deformations parallel and perpendicular to the loading direction 69
7.4 Remodelling Law after Beaupre 73
7.5 A collection of different Remodelling Laws (I) 77
7.6 A collection of different Remodelling Laws (II) 78

8.1 Regular Grids as starting configuration 81
8.2 Time Development of the bone mass for different initial configurations 82
8.3 Time evolution of originally thick and tilted struts 83
8.4 Time evolution of originally thin and tilted struts 84
8.5 Time Development of Architecture—2D 86
8.6 Time Development of Histomorphometric Parameters—2D . . 87
8.7 Effect of different values of the critical volume change 88
8.8 2-Dimensional age map of bone elements 89
8.9 The 3-dimensional structure of bone for different remodelling laws 91
8.10 Histomorphometric data corresponding to different remodelling laws 92
8.11 Slightly modified remodelling law 93
8.12 Architectural snapshots for three different types of remodelling laws 95
8.13 Histomorphometric Parameters for different types of remodelling laws 96
8.14 Trabecular thickness distribution 96

9.1 The indirect coupling of resorption and deposition rates 99
9.2 The set point concept 101
9.3 Strain distribution 102
9.4 Steady state bone mass for different turnover rates 104
9.5 Osteoporotic Bone 107
9.6 Age map for different turnovers 108

11.1 The unit cell of a triangular lattice 122
11.2 The unit cell of a homogenous crystal 124
11.3 Three different strain states 125
11.4 Schematic side-view of a bilayer membrane 128
11.5 Snapshots of the configuration for stiff A-A bonds 129
11.6 Bending rigidity and Poisson ratio as a function of composition for stiff A-A bonds 132
11.7 Snapshots of the configuration for stiff A-B bonds 133

11.8 Bending rigidity and Poisson ratio as a function of composition for stiff A-B bonds 134

Chapter 1

Introduction

Until the beginning of the second half of the twentieth century the large building of physics was usually subdivided into two different disciplines: theoretical and experimental physics. While the first tries to develop mathematical models to explain the world surrounding us and to make predictions on the outcome of physical experiments, the latter one tries to conduct experiments to, first, verify or falsify a theoretical model and, second, to discover new effects that still need a physical theory to be explained. This interconnexion of both disciplines has proved to be very successful and has resulted in a number of epoch-making discoveries that, first, significantly improved our understanding of the world around us and, second, shaped our daily life tremendously. Newton's mechanics, Maxwell's electrodynamics, Einstein's theory of relativity or quantum mechanics are only some examples. But with the rise of computational technology around 1950 a third discipline arose, placed somewhat in between the traditional areas of experimental and theoretical physics: computational physics. On the one hand computers give possibilities to perform calculations that are too lengthy and complicated to be done manually. On the other hand computers make it possible to implement theoretical model systems and then to perform experiments on them that would not be possible in reality. For example a theoretical model might be a simplification – a "pure" system – not to be found in nature. Or some experimental conditions might not be easily achieved in reality, i.e. the computer gives the possibility to go "beyond Nature": it is no problem to perform an experiment at infinite or zero temperature in a computer experiment, while both can not be achieved in a classical experiment. Another big advantage in a computer experiment is that the system is known in every detail, each desired quantity can be determined easily. Furthermore a computer experiment lacks the noise and experimental uncertainties inherent in each real experiment. But of course there are also drawbacks in the use of computers. A significant disadvantage is the limited size of systems that can be investigated (a macroscopic system consists of $\approx 10^{23}$ atoms, system sizes in computational calculations are typically limited by an order of 10^6), which may blur the final results (e.g. smearing out of discontinuities that occur in the thermodynamic limit).

Nowadays computational physics has established as the third discipline and is widely used in almost every field of physics giving complementary results to theoretical calculations and experimental observations. Several models and concepts have been developed, one of the most prominent is the class of lattice models. In these kind of models space is discretized and the elements of the investigated system, be it atoms, molecules, molecular motors or any other physical entity, can not move continuously in space, but on discrete lattice points. This discretization process is motivated by one of the following two reasons: first, the lattice structure may be inherent in the physical problem, e.g. there are lots of materials that crystallize in a regular lattice structure (metals and alloys are the most prominent examples). The atoms forming this structure are mostly occupying the given lattice sites, on a much shorter time scale than the residence time of an atom on a special site the exchange of an atom with a neighbouring vacancy may occur (a process called diffusion). If one is not interested in the jump process itself, but only in the resulting structure, it is feasible to model the jump as an instantaneous event, the atom hopping from lattice site 1 to 2. Second, discretizing space and time is a necessity in a computer program. Storing and processing of infinitely many coordinates – as a continuous space or time variable would give – is simply not possible. That's why the surface of a membrane is discretized (triangulated), before its thermal fluctuations can be modelled in a computer simulation. The first part of this thesis deals with problems of the first kind: the diffusion process in binary, crystalline alloys is investigated. In the second part the remodelling process in human trabecular bone is investigated. Trabecular bone is a sponge like structure (material scientists call it a *cellular structure*) consisting of roughly 20% bone material, the rest is marrow and fat. On the scale investigated bone material is seen to be a continuous material, but according to the difficulties described before, in the approach presented in this thesis bone's architecture is mapped onto a cubic lattice, occupied sites corresponding to bone, empty ones to marrow. This characterisation results in an approximated bone architecture, but enables to use a fast algorithm to assess the mechanical state of the system and to study a variety of different biological hypotheses.

Lattice models are used to study changes in global properties of a system due to local dynamical reactions. The physical origin of these reactions may be very different, as they are in the problems studied in this thesis: (a) diffusional jumps in the case of alloys, (b) the action of bone cells adding and removing bone material in the case of bone remodelling and adaptation and (c) chemical modification of head-groups in a membrane as a result of a change in pH or salt concentration (see also Figure 1.1).

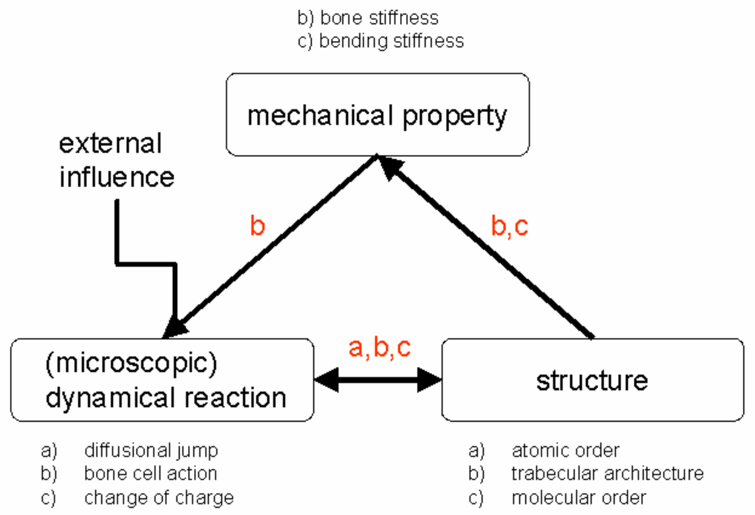

Figure 1.1: The inter-relation of (microscopic) dynamical reactions, structure and mechanical properties of the system, respectively, is the matter of interested for all topics discussed in this thesis. The full triangle is valid for all three topics, indicated in red are the inter-relations that were investigated in this thesis (the full triangle was analysed for the case of bone remodelling only).

Diffusion in alloys is a classical topic of material physics and materials science as it is of great interest for both, the basic as well as the applied sciences. Trabecular bone remodelling is an issue one would on the first hand attribute to biology or medicine. It was the advance of biological sciences, the rise of molecular and cell biology and the large amount of experimental data collected by biologists that led to the blurring of strict border lines between formerly separated sciences. First, between biology and chemistry, later on physicists and even mathematicians discovered the wide range of interesting biological problems that could be investigated by their methods. Biological systems are many body systems that can quite naturally be dealt with the methods of statistical physics. Furthermore biological systems are systems out of equilibrium. Very often concentration gradients have to be built up or have to be maintained to guarantee biological functionality. Since the second law of thermodynamics can not be overcome, these – active – processes need the input of energy, i.e. they would not occur spontaneously. Nature has invented several concepts to fulfil these tasks: molecular motors that transport cargo from one point in the cell to another, ion pumps that can actively pump selected ions in or out the cell to create concentration gradients and many more. A quantitative understanding of these processes can only be achieved by developing and analysing simplified models that grasp the main aspects of the underlying process. That is, where physics comes into a play. Most successes of physics were built on simple models that are still general enough to account for the observed effects – “make it as simple as possible, but not simpler”. But it is not only that existing physical models may be applied to describe biological systems, also new ones have to be developed to meet the challenges posed by biological systems. As already stated the complexity of biological systems, the number of components and also the structure of its components, exceeds by far the complexity of systems classical physics deals with.

From a material scientist’s point of view biological systems under mechanical load exhibit very interesting properties. First, structures like bone or wood show extraordinary mechanical properties that mostly stem from the geometrical arrangement of the building material and by the combination of materials with opposing properties. Understanding these structures and predicting their mechanical properties is an exciting problem for the physicist as well as the engineer, since mimicking these structures might open the possibility for innovative applications. Second, biological systems very often possess the ability to react to external stimuli to adapt to changing environmental conditions. E.g. a tree placed on a slipping hill, will once again turn towards the sun or bone will change its shape and strength according to the load patterns it experiences in daily life. To fulfil these tasks bone has to have the possibility, first, to measure mechanical loading and, second, to react to this input by changing the structure, i.e. by deposition or resorption of bone material. This fascinating process, mediated by mechanotransduction, i.e. the transformation of mechanical loading into chemical signals, is essential to understand bone’s evolution, but due to its high complexity is still poorly understood. An interdisciplinary approach, combining physicists, engineers, biologists and physicians, is necessary to reveal the hidden secrets of the transduction process.

A more detailed description of the inter-relation of dynamical reaction, structure and mechanical property (see Figure 1.1) can be seen in Figure 1.2 for the case of diffusion and bone remodelling. Metallic alloys consist of several types of atoms and vacancies distributed on a lattice. Precipitation and ordering can lead to a quite complex microstructure of the material (different phases of various geometric shape and atomic composition distributed in the sample) that significantly influence its physical properties (mechanical, electrical, etc.). Bone is a hierarchical organized material, the basic building

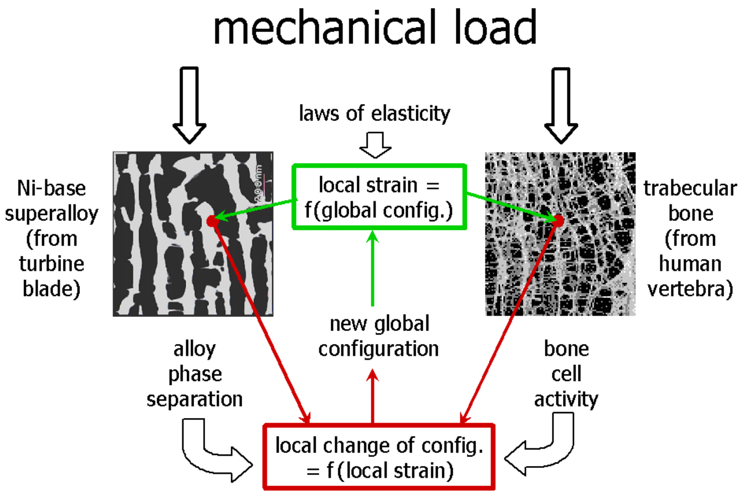

Figure 1.2: The similarities in the structure and time evolution of a phase separating alloy (left) and human trabecular bone (right) is shown. More information is found in the text.

elements are a nano composite of organic collagen – a protein arranged in a triple helix – and inorganic hydroxylapatite – a calciumphosphate. Despite these differences on the material level, a comparison of the structure of precipitates in alloys and the architecture of bone shows obvious similarities (see Figure 1.2). Also the time evolution of both systems can be explained by analogous laws. The atomistic diffusion process leading to phase separation in metallic alloys is determined by the local environment of the diffusing atom only. The local environment consists of, first, the kind of neighbouring atoms and, second, the local mechanical stresses and strains. The local diffusion process changes the local environment, which in turn affects the global configuration and consequently the local stresses and strains. This feedback process leads to the pronounced pattern formation during phase separation and rafting (directional coarsening). The process of trabecular bone remodelling is quite similar. Here the resorption/deposition of new bone material (done by specialized cells) is influenced by the local stresses and strains. The change of the local bone architecture also leads to a global change. Consequently these global changes affect local stresses and strains that affect cells' activity. This closes a similar feedback loop, also present in the phase separation problem (see Figure 1.2).

In the third part of this thesis the mechanical properties of membranes self-assembled from amphiphilic molecules are investigated. As simple model systems for biological compartments, like cell membranes or virus coatings, these structure are of great scientific interest. A better understanding of the basic principles and mechanisms leading to the special properties of these structures is a necessity to shed further light on still unsolved biological problems.

By applying methods of computational physics and making use of the advantages of a computer experiment all three problems – diffusion in binary alloys, trabecular bone remodelling and modelling the mechanical properties of membranes – are investigated and the obtained results are presented in this thesis. Performing the computer experiments it was paid much attention to keep them as close to real physical experiments as possible. Computer experiments can never be a substitution for real experiments, but they may help to improve our understanding of complex situations and be a guide to conduct further experiments.

Part I

Diffusion in multicomponent alloys

Diffusional processes manifest themselves in numerous situations in daily life. The mixing of two liquids (e.g. water and syrup) or two gases (e.g. the spread of a pleasant scent in a room) are only two out of many examples. But not only materials liquid or gaseous are affected by diffusional processes, also materials usually considered as hard and immobile, like metallic alloys, can exhibit quite remarkable diffusional properties, although the diffusional processes in hard matter are usually much slower and need more elevated temperatures than the ones in soft matter. In this thesis diffusional processes, i.e. the stochastic motion of single atoms, in crystalline alloys are investigated Glicksmann [2000]. These are of great interest for basic as well as for applied sciences. Diffusion in metallic alloys may lead to rearrangement of atoms, forming or dissolution of precipitates as well as coarsening Lifshitz and Slyozov [1961], Wagner [1961], Cahn [1962]. These effects are of tremendous importance for engineering sciences since they may affect material properties a great deal, changing them over order of magnitudes. On the other hand the basic atomistic mechanisms leading to these changes are of interest for the basic sciences like material physics and material science. Scientific progress has helped to begin to understand these processes in several systems, like in ordering or demixing alloys, and to predict the form and coarsening behaviour of precipitates in alloys under external load Fratzl and Penrose [1995, 1996], Weinkamer et al. [2000], Weinkamer and Fratzl [2003], Weinkamer et al. [2004a]. But despite these successes exact solutions for even the simplest model systems are still not available. All of the approaches mentioned above rely on simplifying assumptions, that may well or not apply to one situation or the other. Another complification arises from different theoretical approaches that can be used to describe these processes. For the modelling of phase separation these approaches include the sharp interface model, the diffuse interface model and the atomic lattice model, respectively Fratzl et al. [1999]. On a large scale it is convenient to use a continuum mechanics approach, which discards the atomistic nature of matter. This approach is based on the concept of macroscopic atomic fluxes that are caused by thermodynamic forces, i.e. gradients of the chemical potential. A linear relation between flux and thermodynamic force is assumed and the constituting equations are solved. Further complicating these approaches is the fact that the coefficients relating flux and force - the Onsager coefficients - are mostly not known and have to be estimated.

While on the large scale matter seems to be a continuum, and continuum models are the appropriate description for diffusion on this scale, it is known for almost 100 years that on a scale of several Å (10^{-10} m) matter is discrete and build up of atoms that - in the case of metallic alloys - form a regular lattice. The elementary diffusion process on this scale is the exchange of one atom with a neighbouring vacancy. A process that is regulated by atomic binding energies and in the general case dependent on the local environment of the participating vacancy and atom.

Bridging the gap between macroscopic continuum mechanics and microscopic atomistic jump processes is a challenging task and done by calculating Onsager's coefficients - the input for the macroscopic theory - from the microscopic details of the diffusion process. This calculation is not trivial and exact solutions exist only for very special systems, like self diffusion in pure metals or tracer diffusion of an infinitely diluted species in an otherwise homogenous material.

It is the aim of this thesis to investigate the diffusional process in a very simple model alloy, the random alloy. In an atomistic computer simulation tracer diffusivities and Onsager coefficients are determined. In collaboration with Jiří Svoboda, Czech Academy of Sciences, and F. D. Fischer, University of Leoben, the acquired data are then used as an input for a macroscopic theory and results are compared. Furthermore the obtained Onsager coefficients are compared to the prediction of different theories of different level of approximation to test their reliability.

Chapter 2

Basics of Diffusion

When in 1827 the british biologist Robert Brown observed the random motion of pollen particles, he was not aware that the process he had discovered and that now bears his name, is one of the most common phenomena present in nature. It should take almost another 100 years until Albert Einstein revealed and explained the underlying mechanisms leading to that phenomenon Einstein [1905]: the movement of suspended particles in a liquid is due to statistical collisions of the particle and the liquid's molecules (although the first mathematical modelling of Brownian motion has to be contributed to Louis Bachelier, who presented his PhD thesis "théorie de la spéculation" in 1900. There he developed the mathematical concepts of Brownian motion and applied it to describe stock exchange Courtault et al. [2000]). Einstein succeeded in relating thermodynamic, macroscopic quantities, like diffusion coefficients, viscosity and temperature, to atomic ones, like jump frequencies. In a time when the atomistic nature of matter was still under heavy discussion, Einstein's work was a milestone in establishing the new theory. Einstein's theory is a perfect example for the wide field of statistical mechanics, which aims to draw macroscopic conclusions by applying methods of mathematical statistics on systems containing many particles. It was Ludwig Boltzmann who established the theory and calculated the basic, empirical thermodynamic laws, like the ideal gas law, by assuming a gas consisting of many, non-interacting particles. Nowadays the atomistic nature of matter is out of question, but it still remains a challenging task to calculate macroscopic, measurable quantities out of the atomic details of any process. The same is true for the concept of diffusion, the random motion of particles or atoms. While on the macroscopic scale diffusion manifests itself in the smearing out of concentration profiles, on the atomistic scale the elementary diffusion process is the displacement of single atoms. In the present thesis the special case of substitutional diffusion in solid, crystalline samples is to be discussed. In this case the elementary diffusion process is the site exchange of one atom with a neighbouring vacancy. In the following sections the basic concepts of diffusion as well on the macroscopic as on the microscopic scale will be presented. The challenging task is then to find the connexion from one description to another.

2.1 Macroscopic diffusion laws

With little knowledge on the underlying atomistic and molecular processes Adolf Fick was the first to give a quantitative law to describe diffusional processes. His observation was that diffusional processes tend to smear out concentration profiles, therefore he proposed the simple linear ansatz (also known as Fick's first law)

$$\mathbf{j} = -D\nabla c \tag{2.1}$$

where $\mathbf{j}$ denotes the material flux, c stands for the concentration and D is the diffusion coefficient. Fick's law is valid for different diffusional processes, whereas the diffusion coefficient may be different to account for the different situations. E.g. the diffusion of an atom in a chemical homogenous environment without any chemical, i.e. composition, gradients, is called tracer diffusion and described by the *tracer diffusion coefficient* D_i, where i stands for the different atomic species. The principle of mass conservation in a diffusional process (the change of concentration in a given volume has to be compensated by a corresponding flux in or out the volume) leads to the following continuity equation

$$\nabla \cdot \mathbf{j} + \frac{\partial c}{\partial t} = 0. \tag{2.2}$$

Insertion of (2.2) into (2.1) leads to

$$\frac{\partial c}{\partial t} = \nabla(D\nabla c). \tag{2.3}$$

Assuming the diffusion coefficient constant – especially independent of the concentration c – leads to Fick's second law, the well known diffusion equation

$$\frac{\partial c}{\partial t} = D\triangle c \tag{2.4}$$

with $\triangle = \frac{\partial^2}{\partial x^2} + \frac{\partial^2}{\partial y^2} + \frac{\partial^2}{\partial z^2}$ the Laplace operator. Equation (2.4) is a linear, second order partial differential equation and has the fundamental solution, i.e. the solution for a point source at the origin as initial condition,

$$G(\mathbf{x}, t) = (4\pi Dt)^{-3/2}\exp\left(-\frac{\mathbf{x}^2}{4Dt}\right) \tag{2.5}$$

which gives decaying concentration profiles in time. The mean square displacement, i.e. the second moment of equation (2.5) is then given by

$$\left\langle \mathbf{x}^2 \right\rangle = 6Dt. \tag{2.6}$$

Because the mean square displacement is an experimentally easily measurable quantity, measuring the MSD is a standard technique to determine tracer diffusion coefficients in an experiment.

Since in this thesis only linear flows, i.e. quasi one-dimensional, problems are going to be considered (e.g. a thick diffusion couple), in the following we will restrict ourselves to the one-dimensional version of Fick's law

$$\begin{array}{rcll} \frac{\partial c}{\partial t} & = & D\frac{\partial^2 c}{\partial x^2} & D = const. \\ \frac{\partial c}{\partial t} & = & \frac{\partial}{\partial x}\left(D\frac{\partial c}{\partial x}\right) & D = D(c). \end{array} \tag{2.7}$$

2.1.1 The diffusion couple

Diffusive motion in the presence of chemical, i.e. composition, gradients, is called *chemical diffusion*. Chemical diffusion in binary substitutional alloys is also known as *interdiffusion*, which is characterized by an interdiffusion coefficient $\tilde{D}$ that in general is different from the tracer diffusion coefficient D. The most prominent example for interdiffusion is the classical diffusion couple (see Figure 2.1), which is also easily realized in physical experiments. Two uniform semi-infinite bars with different compositions are brought into contact and concentration profiles are measured. The initial condition for a diffusion couple is that one of the bars lacks solute, e.g. $c(x, 0) = 0$ for $x > 0$, and the other bar has got a uniform composition, i.e. $c(x, 0) = c_L$ for $x < 0$. By assuming the diffusion coefficient of the solute independent of composition

Figure 2.1: In a diffusion couple two different materials (A and B) are brought into contact (left) and the time evolution of the concentration profile is measured (right).

Fick's second law (2.4) is valid. Due to the linearity of Fick's second law new solutions may be found by superposition of existing solutions. By thinking the diffusion couple made of infinitely many point sources, whose solution is given by (2.5), the solution of the diffusion couple may be found to give (see e.g. chapter 4 in Glicksmann [2000])

$$c(x,t) = \frac{c_L}{2}\operatorname{erfc}\left(\frac{x}{2\sqrt{Dt}}\right) \tag{2.8}$$

with $\operatorname{erfc}(x) = 1 - \operatorname{erf}(x)$, $\operatorname{erf}(x)$ the error-function.

If the assumption of a constant diffusion coefficient does not hold, i.e. $D = D(c)$, equation (2.3) has to be applied to describe the diffusional process. Applying a so called Boltzmann-Matano transformation (see e.g. Chapter 11 in Glicksmann [2000]) the partial differential equation (2.3) can be transformed into an ordinary differential equation. Setting $\xi = \frac{x - X_M}{2\sqrt{t}}$ and doing the appropriate transformations in equation (2.3) leads to

$$-2\xi\frac{dc}{d\xi} = \frac{d}{d\xi}\left(\tilde{D}(c)\frac{dC}{d\xi}\right). \tag{2.9}$$

This equation is now an ordinary differential equation with variable ξ. The constant X_M – the Matano interface – corresponds to a special reference plane, i.e. the position where an equal amount of material has been flowing to the left and to the right. The formulation of Fick's second law as an ordinary differential equation gives a comfortable way to calculate the concentration dependent diffusion coefficient. According to the method of Sauer, Freise and denBroeder the diffusion coefficient for a diffusion couple can be found to give

$$\tilde{D}(c) = \frac{1}{2t\,(dc/dx)_{x'}}\left[(1-\Psi)\int_{x'}^{\infty}(c - c_R)dx + \Psi\int_{-\infty}^{x'}(c_L - c)dx\right]. \tag{2.10}$$

Ψ is given by

$$\Psi = \frac{c - c_R}{c_L - c_R}, \tag{2.11}$$

c_L and c_R are the concentrations on the left and right end of the diffusion couple, respectively. The method of Sauer, Freise and denBroeder gives the possibility to calculate concentration dependent diffusion coefficients by measuring concentration profiles and applying equation (2.10) to the obtained data. A way that was also followed in this thesis. A computer experiment analogous to a real interdiffusion experiments was performed and the obtained concentration profiles were analyzed according to equation (2.10).

Note that the interdiffusion process does only give rise to one concentration profile, the other giving no new information. It can therefore be described with only one single diffusion coefficient, the so called *interdiffusion coefficient* $\tilde{D}$. In the most general case $\tilde{D}$ is a combination of the tracer diffusion coefficients D_A and D_B of the alloy's constituents. Applying the method of Sauer, Freise and denBroeder to a given concentration profile measures the interdiffusion coefficient $\tilde{D}$.

Kirkendall Effect

If the two constituents of a diffusion couple differ in their diffusivities various physical effects may arise, the most prominent one the Kirkendall effect. Different diffusive speeds and therefore different atomic fluxes have to be compensated by a corresponding vacancy flux. This leads to generation of vacancies in one part of the sample and annihilation of vacancies in the other part and therefore to a macroscopic swelling and shrinking of the sample, respectively. This can be observed by macroscopic markers, e.g. scratches, that are placed on the sample's surface and start to move. In a standard Kirkendall experiment this marker motion is measured and the interdiffusion coefficient is determined. The standard theory for the Kirkendall effect (which is due to Darken) assumes dense sources and sinks for vacancies, i.e. the vacancy concentration is in thermodynamic equilibrium in each part of the sample (see e.g. chapter 17 in Glicksmann [2000]). Darken's result for the interdiffusion coefficient reads

$$\tilde{D} = y_B D_A^I + y_A D_B^I \tag{2.12}$$

where D_i^I are the *intrinsic diffusion coefficients* for A and B atoms, respectively. Intrinsic diffusion coefficients are measured in a co-moving frame of reference (the lattice fixed frame) and are given by (see e.g. Murch [2001])

$$D_A^I = D_A \left[1 + \frac{\partial \ln \gamma_A}{\partial \ln c_A} \right] \frac{f_{AA} - f_{AB} \frac{c_A}{c_B}}{f_A} \tag{2.13}$$

where $1 + \frac{\partial \ln \gamma_A}{\partial \ln c_A}$ is the thermodynamic factor, which is equal to 1 for an ideal solution. f_{ik} are collective correlation factors and f_A is the tracer correlation factor, respectively. The correlation factors are formally introduced in section 2.2. In Darken's analysis of the Kirkendall effect correlation effects are not taken into account, i.e. the Onsager matrix (see section 2.1.2) is assumed diagonal, that is why in his treatment the third term in equation (2.13) containing correlation factors cancels out. This third term is often referred to as the *vacancy-wind term* and describes the effect of the resulting vacancy flux that compensates the unbalanced atomic fluxes.

2.1.2 Onsager's Coefficients

The most accurate description of diffusional processes in multicomponent systems is to calculate the atomic fluxes of each species at all points in the sample. For systems close to equilibrium Lars Onsager proposed a linear relationship between the atomic fluxes and the thermodynamic driving forces. The driving forces for diffusional motion are the gradients of the chemical potentials μ_i. In an alloy containing n atomic species the fluxes j_i are then given by

$$j_i = \sum_{k=0}^{n} L_{ik} \nabla \mu_k \tag{2.14}$$

where the index 0 is denotes the vacancies. The coefficients L_{ik} are called Onsager's or kinetic coefficients. In his famous work from 1931 Lars Onsager showed that the Onsager matrix is symmetric Onsager [1931], i.e.

$$L_{ik} = L_{ki}. \tag{2.15}$$

Depending on the problem investigated there may exist even more relations between Onsager's coefficients. In a system where time evolution is described according to the vacancy mechanism the fluxes are constrained via

$$\sum_{i=0}^{n} j_i \equiv 0. \tag{2.16}$$

Inserting this constraint into equation (2.14) leads directly to

$$\sum_{i=0}^{n} L_{ik} = 0 \qquad \forall k. \tag{2.17}$$

The diffusional equations (2.14) can now be written as

$$j_i = \sum_{k=1}^{n} L_{ik} \nabla (\mu_k - \mu_0) \qquad 1 \leq i \leq n \tag{2.18}$$

where the sum runs only over the atomic components. The vacancy flux can be derived from equation (2.16).

2.2 Microscopic diffusion laws

On the atomistic scale the diffusion process consists of a site exchange between an atom and a neighbouring vacancy, i.e. atom and vacancy perform a so called *random walk*. The total displacement $\mathbf{R}$ of an atom is the sum of its respective jump vectors

$$\mathbf{R} = \sum_{i=1}^{n} \mathbf{r}_i \tag{2.19}$$

where $\mathbf{r}_i$ are the n successive jump vectors. Since in a random walk positive and negative displacements have the same probability, the mean value of $\mathbf{R}$ is equal to zero. But the mean square displacement, which is a measure of the width of the distribution curve, is different from zero and given by

$$\left\langle \mathbf{R}^2 \right\rangle = \sum_{i=1}^{n} \left\langle \mathbf{r}_i^2 \right\rangle + 2 \sum_{i=1}^{n-1} \sum_{j=1}^{n-i} \left\langle \mathbf{r}_i \cdot \mathbf{r}_{i+j} \right\rangle . \tag{2.20}$$

The second term in the sum in equation (2.20) contains average values of the product of jump vectors at different times. A perfect random walk is defined such that each atomic jump is completely independent from the previous ones, i.e. no correlations are present, therefore the correlational term in equation (2.20) cancels out. Since the vacancy breaks the symmetry of the diffusion process, the situation of completely uncorrelated walks is rarely found. Examples would be the diffusion of a single atom on an empty lattice or the diffusion of a single vacancy in a pure material. But in general correlation effects can not be neglected. They arise because if atom and vacancy exchange places, the vacancy still remains in the vicinity of the atom and a jump of the atom back to its original position, cancelling the previous diffusion jump, is more likely than it would be in an uncorrelated process. The *tracer correlation factor* f is defined as the “deviation” from a perfect Random Walk

$$f = \lim_{n \to \infty} \left(1 + \frac{2 \sum_{i=1}^{n-1} \sum_{j=1}^{n-i} \left\langle \mathbf{r}_i \cdot \mathbf{r}_{i+j} \right\rangle}{\sum_{i=1}^{n} \left\langle \mathbf{r}_i^2 \right\rangle} \right) . \tag{2.21}$$

For a perfect random walk the correlation factor is equal to 1. In the general diffusion process, when correlations are present, the tracer correlation factor takes a value $0 \leq f \leq 1$. Keeping in mind, that in the case of diffusion on a (cubic) lattice all vectors $\mathbf{r}_i^2$ are the same and equal to r^2, the equation for the mean square displacement (2.20) can now be written as

$$\left\langle \mathbf{R}^2 \right\rangle = n r^2 f \tag{2.22}$$

with n the number of jumps.

Equation (2.22) gives the mean square displacement, which is a macroscopic quantity already determined in equation (2.6), by purely microscopic considerations. Combining the two equations one obtains Einstein's famous result Einstein [1905]

$$D = \frac{1}{6}\frac{n}{t}r^2 f. \tag{2.23}$$

The macroscopic tracer diffusion coefficient D is now determined by microscopic quantities, where n/t is the jump frequency of the diffusant, i.e. the number of jumps per time unit. The underlying lattice structure of matter – very important on microscale but not to be seen on macroscale – is transmitted by the correlation factor f.

2.2.1 The random alloy model

The random alloy model is the simplest model possible to study non trivial effects in diffusional processes. It was first introduced by Manning Manning [1971] and despite its simplicity exact analytical results for the Onsager coefficients and diffusion coefficients have not been found yet. In the random alloy model $i = 1 \ldots n$ atomic components occupy a given lattice, the index 0 is reserved for vacancies. Modelling the diffusional process via the vacancy mechanism each atomic component i is assigned an exchange frequency ω_i for exchanges with a vacancy. Only nearest neighbour jumps are allowed.

In the investigations presented in this thesis the random alloy model was used to describe the diffusion in a system of only two atomic components A and B and vacancies V on a face centred cubic (fcc) lattice. The atomic components were assigned exchange frequencies ω_A and ω_B, respectively. The complex behaviour of even such a simple model system is best visualized by the behaviour of the tracer diffusion coefficients of the two atomic components as a function of composition (see Figure 2.2). The tracer diffusion coefficients were obtained measuring the mean square displacement $\langle \mathbf{R}_i^2 \rangle$ of each species as a function of time and making use of equation (2.6). The exchange frequency $\omega_A = 1$ of species A was held fix, whereas $\omega_B = 0,\ 0.01,\ 0.1,\ 0.2,\ 0.5$ and 1, respectively. Although the curves exhibit a complicated behaviour some general aspects can be observed: Firstly, in the limit ($y_A \rightarrow 1$) D_A approaches 0.065125 for all values of ω_B. Secondly the curves are monotone increasing with y_A. Both aspects can be understood qualitatively. In the limit of high concentrations of A the self diffusion limit of A in A is reached. In this case the tracer diffusion coefficient is given by (see equation (2.23))

$$D_A = \frac{r^2 y_0 \omega_A f_0}{6} \tag{2.24}$$

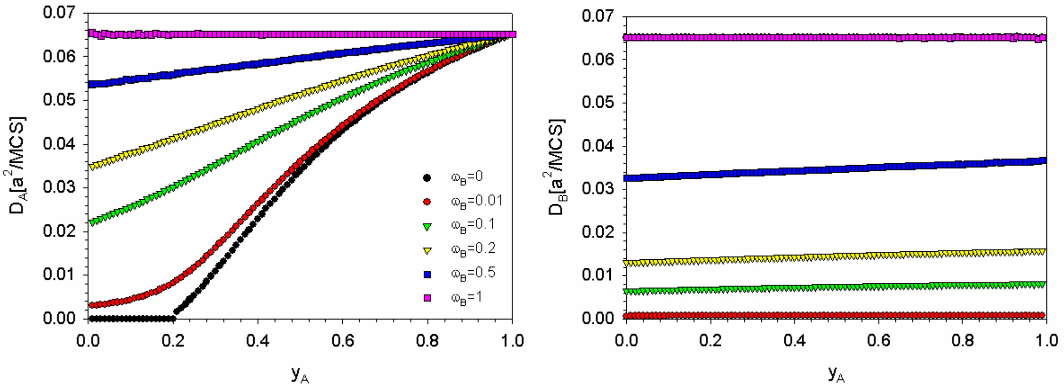

Figure 2.2: The tracer diffusion coefficients of A and B as a function of composition. y_A denotes the site fraction of species A. The exchange frequency of A $\omega_A = 1$ was held fix, whereas ω_B was varied. The diffusion coefficients show a complex behaviour. In the case of immobile B atoms the diffusion coefficients of the faster species A can even drop to zero, when y_A falls below the percolation threshold.

where r is the distance of an elementary diffusion jump ($r = \sqrt{2}a/2$ for the fcc lattice) and f_0 is the geometric correlation factor, which depends on diffusion mechanism and lattice only. For the vacancy mechanism and fcc lattice $f_0 \approx 0.7815$. The jump frequency is given by the product of the vacancy concentration and the exchange frequency. The increase in diffusivity with higher concentrations of the fast component A is due to the fact, that the mobility of the vacancy is decreased, when the number of slow atoms is increased. In this case there will be more attempts of the vacancy to exchange with the slower B atoms, which are less probable successful than exchanges with A atoms. So it gets less probable for an A atom to find a vacancy to perform an exchange, which in turn reduces the mobility of the fast component. In the extreme case of immobile B atoms ($\omega_B = 0$) the mobility of A even drops to zero, when the concentration falls below the percolation threshold. This property was used to estimate the percolation threshold in several lattices via MC simulations Murch and Rothman [1981]. The described effects are due to correlations in successive atomic jumps, i.e. the atoms do not perform a perfect random walk, which was described in the previous section (see also Murch [2001], Glicksmann [2000]).

Since in the random alloy model no interaction energies between the atomic components themselves or the atoms and the vacancies are assumed, each configuration has the same energy. The free energy of mixing is therefore completely determined by the entropy and the system follows the rules of an ideal solution, which gives the chemical potential μ_i of each species i

as a function of composition according to Pelton [2001]

$$\mu_i = RT \ln y_i + \mu_0 \tag{2.25}$$

with R the universal gas constant, T the temperature and y_i the site fraction of species i. μ_0 is a constant. In this special case the thermodynamic factor is equal to 1.

2.3 Closing the gap between microscopic and macroscopic theories

Due to correlation effects, the direct calculation of Onsager's coefficients for a given system is a challenging task and even for a system as simple as the random alloy no exact solution has been found until now. But nevertheless there exist a number of approximate solutions, the most important ones shall be mentioned below. The approach of Darken, Svoboda and Allnatt do not refer to a special microscopic model, they express Onsager's coefficients in terms of the tracer diffusion coefficients independent of the microscopic details. The approach of Moleko is valid for the random alloy model only. Manning's concept gives the kinetic coefficients as well in terms of tracer diffusion coefficients (independent of the microscopic details) as well as in jump frequencies (dedicated to the random alloy). For matter of convenience the correlated part of the kinetic coefficients is often separated in the collective correlation factor f_{ik}. It is defined analogous to the tracer correlation factor introduced in equation (2.22) according to

$$\begin{aligned} L_{ik} &= L_{ik}^{(0)} f_{ik} \\ L_{ik}^{(0)} &= \frac{r^2 y_0 \omega_i y_i}{6RT\Omega}, \end{aligned} \tag{2.26}$$

Ω denoting the mean atomic volume. Therefore determining Onsager's coefficients essentially means to determine the collective correlation factors. As a matter of convenience in the following sections, which describe the different theoretical approaches in determining Onsager's coefficients, both concepts of L_{ik} and f_{ik}, respectively, will be used interchangeably.

2.3.1 Darken's concept

Darken's theory is designed for systems, where no gradient of μ_V exists, i.e. ideal sources and sinks for vacancies Darken [1948], Glicksmann [2000]. It is assumed that Fick's first law holds for each atomic component, i.e. there are no cross terms and no coupling of the diffusive motion of the involved particles

$$\mathbf{j}_i = -D_i \nabla c_i = -\frac{D_i}{\Omega} \nabla y_i \qquad i = A, B. \tag{2.27}$$

$c_i = y_i/\Omega$ is the concentration of species i, i.e. number of atoms per volume, Ω is the mean atomic volume. Comparing equations (2.27) with (2.14) one finds

$$L_{AA} = \frac{D_A y_A}{\Omega RT} \qquad L_{BB} = \frac{D_B y_B}{\Omega RT} \qquad L_{AB} = 0. \tag{2.28}$$

Darken's concept is not restricted to the random alloy. Therefore, given the – experimental measurable – tracer diffusion coefficients the kinetic coefficients can be determined for each system. Darken's drawback is to neglect cross terms in the Onsager matrix, i.e. the coupling of diffusive fluxes of different species. But this coupling exists even in the random alloy and vanishes only in the case of tracer diffusion of dilute A in solvent B (or dilute B in solvent A, respectively) (see Figure 3.1).

2.3.2 Manning's concept

Manning calculated the kinetic coefficients for the random alloy Manning [1971]. His results give two expressions for Onsager's coefficients. Firstly, as a function of the tracer diffusion coefficients:

$$L_{ik} = \frac{y_i D_i}{\Omega RT} \left(\delta_{ik} + \frac{1 - f_0}{f_0} \frac{y_k D_k}{y_A D_A + y_B D_B} \right) \qquad i, k = A, B \tag{2.29}$$

and

$$L_{iV} = -\frac{y_i D_i}{\Omega RT f_0} \qquad i = A, B \qquad\qquad L_{VV} = \frac{y_A D_A + y_B D_B}{\Omega RT f_0}.$$

Secondly, as a function of exchange frequencies

$$\begin{array}{ll} f_{AA} = 1 - \frac{2\omega_A y_B}{\Gamma} & f_{AB} = \frac{2\omega_B y_B}{\Gamma} \\ f_{BA} = \frac{2\omega_A y_A}{\Gamma} & f_{BB} = 1 - \frac{2\omega_B y_A}{\Gamma} \end{array} \tag{2.30}$$

with

$$\begin{aligned} \Gamma \;=\; & \frac{1}{2}(M_0 + 2)(y_A \omega_A + y_B \omega_B) - \omega_A - \omega_B + 2(y_A \omega_B + y_B \omega_A) + \\ & + \sqrt{\left[\frac{1}{2}(M_0 + 2)(y_A \omega_A + y_B \omega_B) - \omega_A - \omega_B \right]^2 + 2 M_0 \omega_A \omega_B} \end{aligned}$$

where

$$M_0 = \frac{2f_0}{1-f_0}.$$

Manning derived his expressions by assuming the same escape frequency for the detachment of a vacancy from an A or B atom, i.e. one single time constant for the loss of correlations. In contrast to Darken's concept the Onsager matrix is no longer assumed diagonal, $L_{AB} \neq 0$ which gives a much better description of diffusion in the random alloy. Despite the fact that Manning achieved his equations by considering the special diffusion mechanism of the random alloy, his results are valid beyond the random alloy. Lidiard [1986] showed that the equations (2.29) do not only hold for the random alloy but for any material, when two macroscopic assumptions are valid: First, the average velocity of an isotope in a self-diffusion experiment equals the corresponding average velocity in a chemical diffusion experiment. Second, the mobility of the atoms in a chemical diffusion experiment is related to the corresponding tracer diffusion coefficient in the same way as for a pure material having the same type of defects and lattice structure. Lidiard's results prove that Manning's equations can even be applied to materials, where the atomistic laws of diffusion are not that well characterised as they are in the Random Alloy.

2.3.3 Moleko's concept

By generalising Manning's approach Moleko and co-workers found expressions for the kinetic coefficients that proved to be more accurate over a wide range of exchange frequencies than Manning's results Moleko et al. [1989], Belova and Murch [2000a,b]. The main difference to Manning's theory is the definition of different escape frequencies for the vacancy for each atomic species and not only to use one single escape frequency. But nevertheless in Belova and Murch [2000a] the surprising result is presented that for the binary random alloy Moleko's formalism gives exactly the same solution as Manning in equation (2.30). But one has to be aware, that although equation (2.30) gives a very accurate description for the binary random alloy, that this is not the case for equation (2.29).

2.3.4 Svoboda's concept

Svoboda and co-workers used Onsager's principal of maximum entropy production to calculate Onsager's coefficients Onsager [1931], Svoboda et al. [2002], Hartmann et al. [2005]. This approach is completely macroscopic, no details of the atomistic diffusion mechanisms enters the derivation (except for the tracer correlation factor, which is the link connecting microscopic and macroscopic "world"). Starting point of the calculations is the symmetric and positive definite dissipation matrix B_{ij}. The total Gibbs energy dissipation rate Q is then given as a quadratic form of the fluxes via

$$Q = \int_V \left(\sum_{i,k=0}^{n} B_{ik} j_i j_k \right) dV \tag{2.31}$$

which has to take a maximum with respect to the fluxes. Since the details of the calculation can be found in Hartmann et al. [2005], here only the main results shall be presented: The Onsager coefficients take the following form

$$L_{ik} = C_{ik}^{-1} \tag{2.32}$$

with $C_{ik} \equiv B_{ik} - B_{0k} - B_{i0} + B_{00}$. The matrix C_{ik} results from the dissipation matrix by elimination of the vacancy flux which is given by equation (2.16). Note first that the matrix C_{ik} is symmetric and second that the entries $C_{i0} = C_{0i} \equiv 0$. Furthermore, assuming a diagonal dissipation matrix one can show that

$$L_{ik} = A_i \left(\delta_{ik} - \frac{A_k}{\sum_{l=0}^{n} A_l} \right) \qquad i, k = 0, \cdots n \tag{2.33}$$

where the coefficients A_i reflect the atomic mobilities and are the inverse eigenvalues of the matrix B_{ik}. In a last step the coefficients A_i have to be determined. By applying Lidiard's two macroscopic assumptions (see section 2.3.2) it is found that

$$\begin{array}{ll} A_i = \frac{y_i D_i}{\Omega R T} & i = 1, \cdots n \\ A_0 = -\frac{1}{1-f_0} \sum_{i=1}^{n} A_i . & \end{array} \tag{2.34}$$

Comparison of these results with equation (2.29) (Manning's result) shows that these two approaches are equivalent: assuming a diagonal dissipation matrix and taking into account Lidiard's macroscopic assumptions leads directly to Manning's formalism.

2.3.5 Allnatt's concept

Allnatt and Allnatt [1984], Allnatt [1982] describe a method to determine Onsager's coefficients that is closely related to the method of determining tracer diffusion coefficients via Einstein's equation (2.6). It is found that

$$L_{ik} = \frac{\langle \Delta \mathbf{R}_i(t) \cdot \Delta \mathbf{R}_k(t) \rangle}{6 n \Omega R T t} \qquad i, j = A, B \tag{2.35}$$

where

$$\Delta\mathbf{R}_i(t) = \sum_{m=1}^{N_i} \Delta\mathbf{r}_i(m,t) \tag{2.36}$$

is the sum over all displacements of atoms of species i at time t. n denotes the number of moles of all species and T the temperature. Due to the analogy of equation (2.35) with equation (2.6) this approach is often called *generalised Einstein's equations*. The Einstein equation links the displacement of one single atom to its tracer diffusion coefficient, the generalised Einstein equations link the displacement of the entire system of A or B atoms to the Onsager coefficients. While the displacement of single atoms suffices to determine tracer correlation factors and tracer diffusion coefficients, respectively, the determination of collective correlation factors and Onsager coefficients, respectively, requires the determination of collective displacements of the system. Since in a computer experiment the displacement of all atoms of all species are known in every detail, Allnatt's concept is a perfect tool to measure Onsager's coefficients in a computer experiment. In contrast to a real measurement this simulations are done in thermodynamical equilibrium, without any composition gradients.

Chapter 3

Determination of Onsager's Coefficients in a MC experiment

As described in the previous sections lots of different theoretical approaches exist, determining Onsager's coefficient for a general material (equations (2.28), (2.29) and (2.33), respectively) or for the special case of the random alloy (equations (2.30) and Moleko's concept). A computer experiment provides the possibility to test this different approaches and to detect its ranges of validity. Since the binary random alloy model is, first, an often described model system and, second, easy to translate into a computer code, it was chosen to test the presented theories. A computer simulation gives the opportunity to determine the tracer diffusion coefficients via equation (2.6) and in a second independent simulation run to determine Onsager's coefficients (either via the generalised Einstein's equation (2.35) or via the method of imposing fluxes to the system as described in the next section). The measured diffusion coefficients can then be plugged into the presented equations to calculate the kinetic coefficients and these can then be compared to the measured ones.

3.1 The Model

The simulations have been performed on a fcc lattice with cubic lattice constant a. The geometry was chosen such, that in x-direction 16 units cell and in y- and z-direction, respectively, 64 units cells were placed. This corresponds to $N = 262144$ lattice sites. This asymmetric configuration was chosen, because in the simulations a flux is going to be imposed on the system along the x-direction. To ensure linear concentration profiles along this axis, it was kept as short as possible. Each lattice site could either be occupied by an A atom, a B atom or a vacancy, respectively. The lattice was first randomly filled with A and B atoms corresponding to a special site fraction, later on a definite number of vacancies was introduced in the system. The time evolution was modelled according to the rules of vacancy dynamics: a vacancy could exchange with one of its neighbouring atoms. The A atoms were assigned a jump probability of 1, the jump probability for B atoms was chosen $\omega_B = 0.1$. In each simulation step one of the vacancies and one of its neighbours were chosen at random. When the neighbouring site was occupied by an A atom the exchange was done. If the neighbouring site was occupied by a B atom, a random number p was drawn. If $p \leq \omega_B$ then the atom and the vacancy changed places, otherwise the configuration was kept. The time scale in our simulations was 1 Monte Carlo Step (1 MCS), which means one jump trial per lattice site. The outcome of a simulation run is a de facto one-dimensional concentration profile, which was obtained by averaging the atoms in planes with $x = const.$, i.e. planes with equal symmetry, resulting in profiles $y_A(x)$, $y_B(x)$ and $y_V(x)$, respectively.

3.2 Measuring Onsager's Coefficients

Equation (2.14) shows that a gradient in the chemical potential will lead to an atomic flux. For systems with small gradients in the chemical potential, i.e. concentration gradients, Onsager assumed a linear relationship between gradients and fluxes. The relation between them is mediated via the symmetric and positive definite Onsager matrix. Knowing gradients and the resulting fluxes gives the opportunity to calculate the kinetic coefficients according to equation (2.14). Since in computer simulations the system is known in "every detail" gradients and fluxes can be easily determined and therefore the calculation of Onsager coefficients is possible for simple model systems. In Murch and Thorn [1979a], Murch [1980] the determination of the kinetic coefficients was done by imposing a gradient of the chemical potential on the system and measuring the resulting fluxes. Another possibility is the in-field method, where the particles are assumed charged and move in an external electrical field Murch and Thorn [1977, 1979b], Murch [1982]. This approach makes use of the fact that equation (2.14) and the kinetic coefficients remain unchanged no matter of the nature of the driving force - be it a gradient in the chemical potential or an electric field. Our approach was not to impose a concentration gradient on the system, but constant atomic fluxes j_A, j_B and j_V, respectively. This leads to the emergence of a concentration gradient which was measured and used to calculate Onsager's coefficients Hartmann et al. [2005].

Imposing the fluxes on the system was done the following way: each time step Δt one atom of species i on the right border of the sample (x-coordinate $x = 7$) was exchanged with an atom of species j on the left border of the sample (x-coordinate $x = -8$). This leads to a positive flux j_i, which is balanced by a negative flux j_j

$$j_i = -j_j = \left(\Delta t \cdot d^2\right)^{-1} . \tag{3.1}$$

In the simulations presented in this thesis $d = 64$, which is the dimension in y- and z-direction, respectively. But the flux of species i can not only be balanced by one species j, but by both other species. E.g. let every n-th time step Δt an atom A be exchanged with a vacancy, all other times with a B atom. Then it is found

$$\begin{aligned} j_A &= \left(\Delta t \cdot d^2\right)^{-1} \\ j_B &= -\left(\tfrac{n}{n-1}\Delta t \cdot d^2\right)^{-1} \\ j_V &= -\left(n\Delta t \cdot d^2\right)^{-1} . \end{aligned} \tag{3.2}$$

The conservation of fluxes (2.16) is evidently fulfilled. These (constant) atomic fluxes lead to gradients in atomic and vacancy concentrations, which can be measured. Figure 3.1 shows the typical time evolution of a concentration gradient generated by an imposed flux. Starting from a random distribution of atoms a gradient starts to build up, which reaches a steady state after approximately 10000 MCS. After becoming stationary the gradient can be determined by a linear regression. The emergence of a vacancy gradient shows, that the Onsager matrix is not symmetric, since the vacancy flux is exactly zero.

Together with equations (2.18) the kinetic coefficients can then be determined. For the binary alloy they read

$$\begin{aligned} j_A &= -RTL_{AA}\left[\frac{\nabla y_A}{y_A} - \frac{\nabla y_V}{y_V}\right] - RTL_{AB}\left[\frac{\nabla y_B}{y_B} - \frac{\nabla y_V}{y_V}\right] \\ j_B &= -RTL_{BA}\left[\frac{\nabla y_A}{y_A} - \frac{\nabla y_V}{y_V}\right] - RTL_{BB}\left[\frac{\nabla y_B}{y_B} - \frac{\nabla y_V}{y_V}\right] \end{aligned} \tag{3.3}$$

where equation (2.25) was used to replace the gradients in the chemical potentials μ_k by concentration gradients. Together with a set of imposed fluxes j_A and j_B and the measured concentration gradients ∇y_A, ∇y_B and ∇y_V equation (3.3) forms a set of 2 linear equations in 4 (taking into account the symmetry of the Onsager matrix only 3) unknowns L_{AA}, L_{AB}, L_{BA} and L_{BB}. Therefore at least two independent simulation runs with a different choice of fluxes had to be performed to get enough equations to solve equation (3.3) unambiguously. To improve statistics even 6 different runs with different sets

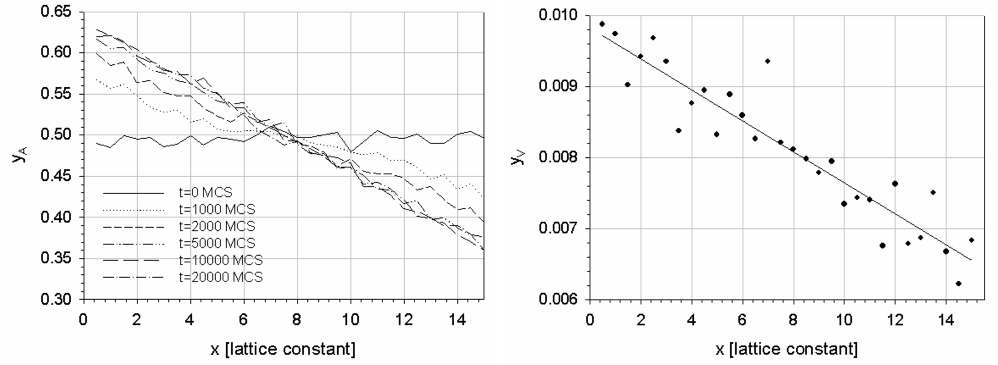

Figure 3.1: Time development of the concentration gradients for an imposed flux of $j_A = -j_B = 0.001$, $j_V = 0$. The emergence of both, an atomic concentration gradient (left) as well as a vacancy concentration gradient (right), can be seen. Since the vacancy flux is zero the vacancy concentration gradient shows that the Onsager matrix is not diagonal. After latest 10000 MCS the gradients have reached a steady state and they are then determined by a linear regression.

of fluxes were used. Choosing the fluxes two requirements had to be met: first, the fluxes had to be chosen big enough to ensure measurable concentration gradients. Second, the gradients had to be small enough to avoid accumulation of one species on one side and to avoid non-linear gradients. Table 3.1 lists the used fluxes. Since it gets very difficult to obtain continuous, measurable concentration gradients, if the composition of the atoms get too small, the results presented are restricted to concentration ranges $0.1 \leq y_A \leq 0.9$. These runs together with equation (3.3) now form a set of

	j_A	j_B	j_V
1	4.8	-4.8	0.0
2	8.0	0.0	-8.0
3	0.0	4.8	-4.8
4	8.0	-4.0	-4.0
5	-1.2	2.4	-1.2
6	-2.4	-2.4	4.8

Table 3.1: The used fluxes in our simulations. All fluxes are presented in units of $10^{-4}/\left(a^2 \cdot \mathrm{MCS}\right)$

12 equations in 4 unknowns which is overdetermined. The solution of such an overdetermined set of equations is done by a linear least-square approach, where a set of reduced equations has to be solved Press et al. [1992]

$$\left(\mathbf{A}^T \cdot \mathbf{A}\right) \cdot \mathbf{x} = \mathbf{A}^T \cdot \mathbf{b} \tag{3.4}$$

where the original (overdetermined) set of equations is $\mathbf{A} \cdot \mathbf{x} = \mathbf{b}$. Equations (3.4) represent now a set of linear equations in as many unknowns as equations, which is easy to solve.

A classical tracer experiment was the first test to examine the method of imposing fluxes and measuring concentration gradients. In a tracer experiment no chemical gradients exist, the only existing gradient is a gradient between one species of atoms, e.g. the A-atoms, and one of its isotopes, the so called *tracer* A'. Since A and A' are chemically equivalent these gradients will neither lead to a flux nor to a gradient in B or the vacancies and for this simple situation Fick's first law applies

$$j_{A'} = -\frac{D_A}{\Omega} \nabla y_{A'} \tag{3.5}$$

where D_A is the tracer diffusion coefficient of species A for the concentration $y_A + y_{A'}$. In the simulations the tracer experiment was realised by dividing the A-atoms into A and A' and the flux was now imposed by exchanging A with A' as described before. The developing gradients were measured and via equation (3.5) the tracer diffusion coefficient of A was calculated. This was then compared to the tracer diffusion coefficient obtained by measuring the mean square displacement of species A as described in chapter 2.2.1 and Figure 2.2. The comparison is shown in Figure 3.2. As can be see the two lines coincide, so it can be concluded that imposing fluxes and measuring gradients is a suitable method to calculate Onsager's coefficients in a computer experiment. In a next step the kinetic coefficients L_{AA}, L_{BB}, L_{AB} and L_{BA}, respectively, were determined. The fluxes seen in table 3.1 were imposed on the system, resulting concentration gradients were measured and Onsager's coefficients were obtained by making use of the equations (3.3) and (3.4). In Figure 3.3 the results of this calculations are shown. The measured kinetic coefficients as well as the predictions from the four described concepts are shown – Darken - short dashed (equation (2.28)), Manning/Svoboda - long dashed (equations (2.29) and (2.33)) and Moleko/Manning - solid lines (equation (2.30)). The small blue dots show the results obtained by making use of the generalised Einstein's equations (2.35).

Comparing the predictions of the different theoretical approaches with the simulations results, the different degree of accuracy of the different approaches is obvious. Darken's concept provides the roughest description, only in the case of the diffusion of an infinitely solution in an otherwise pure solvent Darken gives the right solution. The approach of Manning/Svoboda gives a better description of the situation, giving the correct result in both extreme cases ($y_A \to 0, 1$), but still deviating from the right solution for concentration values in between. The best description is given by the theory of

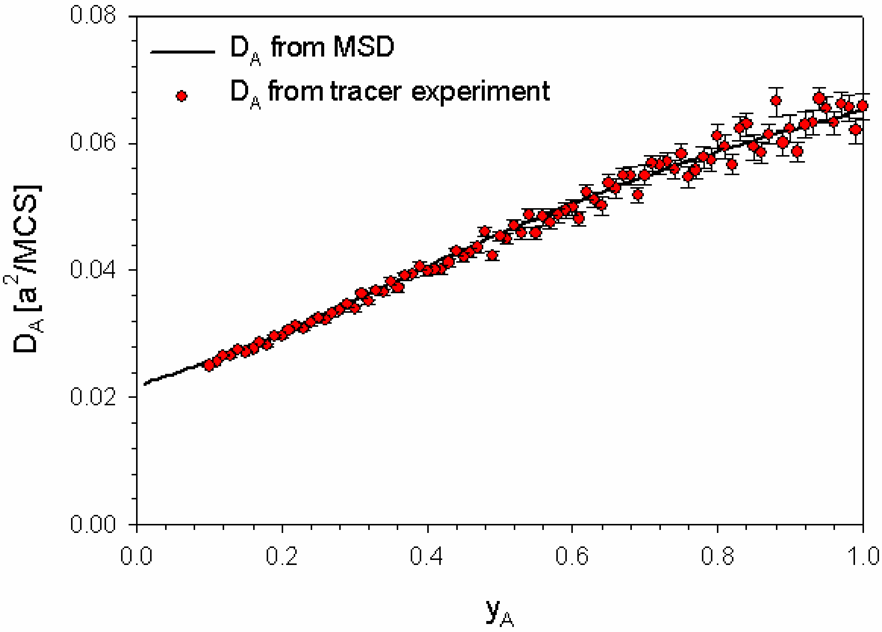

Figure 3.2: A comparison of the measured tracer diffusion coefficient for species A. Red circles: measured by imposing a constant flux ($j_{A'} = 0.0006$ $1/(a^2\text{MCS})$ on the system. Solid, black line: measured by determining the mean square displacement of the atoms.

Moleko.

The two simulation procedures to determine the kinetic coefficients also show some differences. The method of Allnatt gives less noisy, statistically better results, than the method of imposing fluxes and measuring concentration gradients. Allnatt's method is based on the calculation of the kinetic coefficients in chemical equilibrium, whereas the flux-concentration measurements are performed out of chemical equilibrium. Since Onsager's Ansatz (2.14) is only valid for systems near to thermodynamic equilibrium it might be possible that non-linear effects are responsible for the deviation of the measured kinetic coefficients from the results of Moleko and Allnatt for concentrations y_A near 1.

Furthermore it was investigated whether Svoboda's theory that uses the principle of maximum entropy production can be further generalised to give more precise results. Starting from a diagonal dissipation matrix the equations (2.33) were deduced. Applying Lidiard's two macroscopic assumptions the coefficients A_i were determined in terms of the tracer diffusion coefficients of the two diffusing species. Lidiard's first assumption leads to the determination of the atomic mobilities A_i with $i > 0$, the second one to the

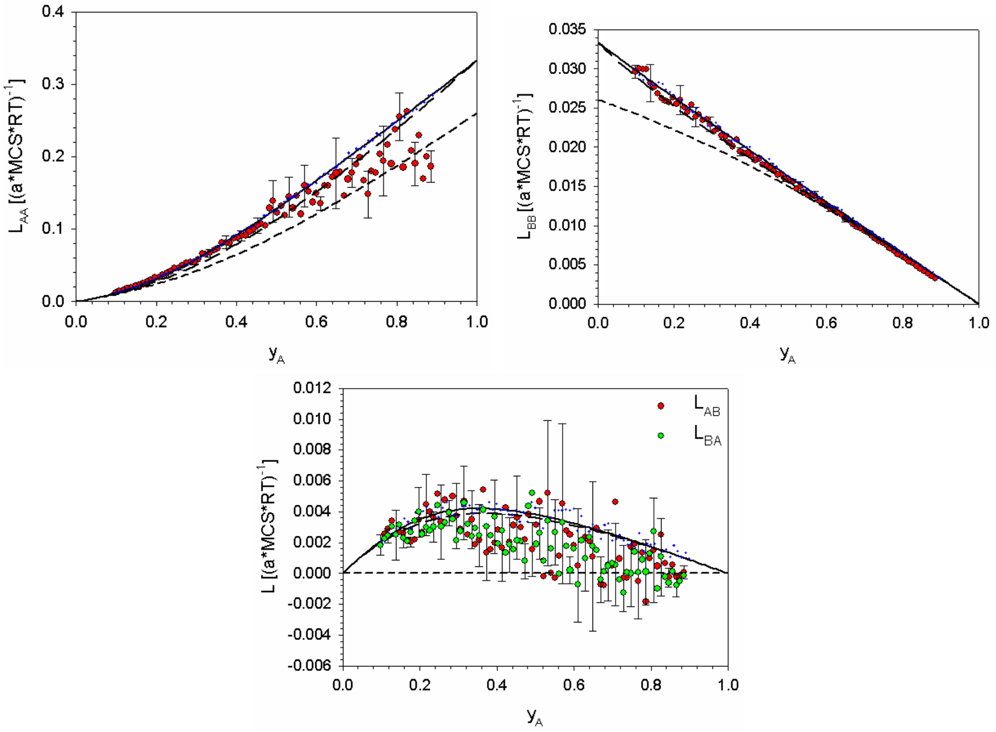

Figure 3.3: The results for the determination of Onsager's coefficients are shown

mobility A_0 of the vacancy. Let's examine the two assumptions a bit closer. Onsager's approach describes all diffusional processes (the kinetic coefficients are assumed independent of the force), especially it is valid for a tracer diffusion experiment. Assume a n-component alloy prepared in that way that the only existing composition gradient is a gradient between A and its isotope A'. Therefore all other gradients and fluxes – especially the vacancy flux – are exactly zero. By simple calculations it is possible to express the flux of the tracer as a function of vacancy flux (which is zero) and gradient in A' only (see Lidiard [1986])

$$j_{A'} = \left[L_{A'A'} - \frac{L_{A'A} \sum_{i=1}^{n} L_{iA'}}{\sum_{i=1}^{n} L_{iA}} \right] \nabla(\mu_{A'} - \mu_0) - \frac{L_{A'A}}{\sum_{i=1}^{n} L_{iA}} j_0. \tag{3.6}$$

The argument is now that the kinetic coefficients have to describe every diffusional situation, quite so the case of tracer diffusion. But in this case it is known that Fick's first law applies, which puts the atomic flux in relation to the tracer diffusion coefficient and the tracer gradient $\nabla y_{A'}$. Combining these two equations gives a relation between the kinetic coefficients and the tracer diffusivities for the atomic species. This is Lidiard's first assumption.

The same argument was followed in Hartmann et al. [2005] to connect the atomic mobilities A_i to the tracer diffusivities.

Lidiard's second assumption is that the mobility of species i is related to the tracer diffusivity D_i in the same way as for a pure material having the same type of defects and the same lattice structure. The mobility is defined as the average drift velocity per unit force and is calculated by applying the same force to all atomic species. This second assumption essentially means that the ratio of atomic and vacancy correlation factor is independent of composition and leads to the calculation of A_V by equating atomic and vacancy jumps and taking into account the correlation factor. While Lidiard's first assumption is very fundamental and discarding it would essentially mean to discard Onsager's approach, the same is not true for the second assumption. So it is a legitimate question to ask, whether it is possible by discarding assumption 2, i.e. some other choice of A_V, to correctly describe the Random Alloy? To investigate this question, one should refer to the sum rules that exactly apply to the Random Alloy Moleko and Allnatt [1988]. They read

$$\frac{1-f_{AA}}{\omega_A y_B} = \frac{1-f_{BB}}{\omega_B y_A} = \frac{f_{AB}}{\omega_B y_B} = \frac{f_{BA}}{\omega_A y_A}. \tag{3.7}$$

Moleko's equations fulfil the sum rules trivially, but is it also possible to make Svoboda's equations (2.33) fulfil the sum rules by some other choice of the constant A_V? Rewritten in terms of correlation factors Svoboda's equations read

$$f_{ik} = f_i \delta_{ik} - \frac{f_i f_k y_k \omega_k}{y_A \omega_A f_A + y_B \omega_B f_B + a_V} \tag{3.8}$$

with $a_V = (6\Omega RT/r^2)A_V$. Insertion into the sum rules leads to 2 equations in only one unknown a_V

$$\begin{aligned} (1-f_A)\left(y_A\omega_A f_A + y_B\omega_B f_B + a_V\right) + f_A^2\omega_A y_A &= -f_A f_B \omega_A y_B \quad (3.9)\\ (1-f_B)\left(y_A\omega_A f_A + y_B\omega_B f_B + a_V\right) + f_B^2\omega_B y_B &= -f_A f_B \omega_B y_A. \quad (3.10) \end{aligned}$$

These two equations are therefore only soluble if

$$\frac{f_A\omega_A}{1-f_A} = \frac{f_B\omega_B}{1-f_B}. \tag{3.11}$$

In Figure 3.4 the right hand side of this equation is plotted against the left hand side. If the condition was fulfilled the points would lie on the straight $y = x$, which is not the case.

To summarise: Starting from a diagonal dissipation rate and two macroscopic assumptions Svoboda derived general expressions for the kinetic coefficients describing diffusion in a general alloy system. The first of the two

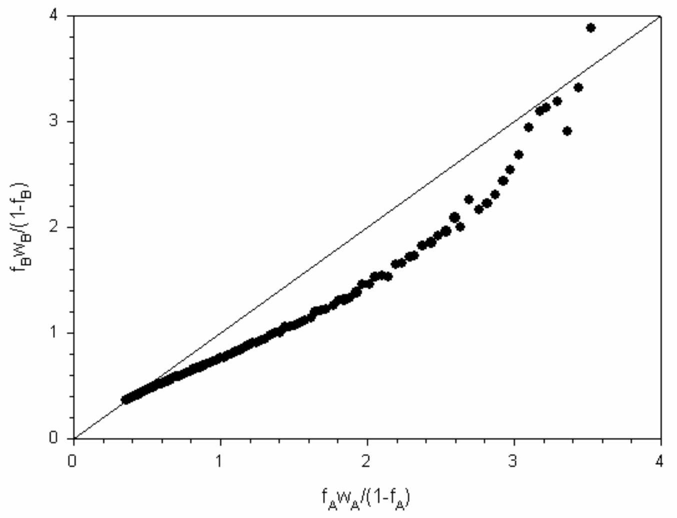

Figure 3.4: The Figure shows the right hand side of equation (3.11) plotted against the left hand side. Since the data points do not lie on the straight $y = x$ it is not possible to fully describe the random alloy in the framework of Svoboda's theory starting with a diagonal dissipation rate.

assumptions states, that the kinetic coefficients are only dependent on the local concentrations and apply to all possible configurations, especially for the case of tracer diffusion. While this assumption – though not proven – is the basis of Onsager's description, the second one states that the ratio of atomic correlation factor and vacancy correlation factor is independent of composition. This second assumption leads to the evaluation of the mobility A_0 of the vacancy. This assumption needs not to hold exactly, therefore it was investigated, if the random alloy could be exactly described by some other choice of A_0. Figure 3.4 shows that this is not the case. Since it does not seem feasible to discard the first assumption, it is necessary to include off-diagonal terms in the dissipation matrix (see equation (2.31)), to fully describe the random alloy.

Chapter 4

Interdiffusion

As previously described (see section 2.1.1) the experimental realisation of a diffusion couple (see Figure 2.1) together with non-reciprocal diffusivities, i.e. different values of the diffusion coefficient for A and B atoms, gives rise to a remarkable effect: the Kirkendall effect. Since a diffusion couple is a widely used model system to measure diffusion coefficients in a physical experiment, computer simulation methods were used to perform a classical interdiffusion experiment in the computer and to compare the results of this atomistic simulations to outcomes of a continuum mechanical, i.e. macroscopic, approach. But there is a drawback in performing an interdiffusion Monte Carlo computer experiment. A necessary condition for the Kirkendall effect is the generation and annihilation of vacancies. For a theoretical treatment the vacancy concentration is assumed to be in thermodynamical equilibrium everywhere in the sample. On the other hand almost all Monte Carlo simulations are based on the principle of a constant number of lattice sites, which makes the generation and annihilation of vacancies, if not impossible, extremely difficult. That is why in the simulations presented in this thesis the other extreme is chosen, no sources and sinks of vacancies. The same condition was also chosen in the continuum mechanical calculations the Monte Carlo results have been compared with. Beginning with a distribution of A and B atoms as depicted in Figure 2.1 (left) the concentration profile is monitored with respect to time and doing a standard Sauer-Freise-denBroeder evaluation equation (2.10) the interdiffusion coefficient $\tilde{D}$ is determined. This interdiffusion coefficient can then be compared to an expression that follows from Svoboda et al. [2002].

4.1 Calculation of Concentration Profiles

The concentration profiles were obtained, by starting the simulation from a special initial configuration, namely all A atoms (B atoms, respectively) were placed on lattice sites with negative (positive, respectively) x-coordinates (see Figure 2.1) – the macroscopic dimensions of the samples were two cubes with $64 \times 64 \times 64$ unit cells each (one unit cell consisted of 4 atoms) that were connected at the plane $x = 0$. The vacancy was placed randomly. The simulations were done for times 0 to 100000 MCS. Every 500 MCS the concentration profile was written out. These simulations were done with a single vacancy. To obtain vacancy concentration profiles for this special case, the vacancy concentration $y_V(x)$ was not evaluated by spatial averaging, but by a temporal average. For a given time interval it was counted how often the vacancy passed a plane $x = const.$, which also results in a spatial varying vacancy concentration $y_V(x)$. Knowing both – the atomic and the vacancy concentration profiles – it is possible to specify a vacancy concentration depending on y_A, more exactly

$$y_V(y_A) = y_V(x(y_A)) \tag{4.1}$$

with $x\,(y_A)$ the inverse function of $y_A\,(x)$. Figure 4.1 shows two typical curves to illustrate the behaviour of the A-concentration and vacancy concentration profiles. The vacancy concentration was normalised to the equilibrium vacancy concentration, which was simply 1/256, as there were $2 \cdot 128$ lattice planes with $128 \cdot 64$ sites over which the vacancy was equally distributed in equilibrium. This homogenous distribution is due to the fact that in the Random Alloy there are no chemical interactions between the alloy's constituents and therefore no reason for the vacancy to prefer any lattice site.

4.2 Results and discussion

For several values of ω_B, namely 0.01, 0.1, 0.5 and 1, concentration profiles were obtained. A comparison of these profiles at the same time shows that with increasing ratio of ω_A/ω_B interdiffusion is significantly slowed down (see Figure 4.2). This can be understood easily, since the mixing of the two atomic species requires both the faster component A to advance in the former B-regime, but also the slower component B in the A-regime. This process is hindered the smaller ω_B is chosen. The Boltzmann transformation which transformed Fick's second law in an ordinary differential equation (see equation (2.9)), shows that the profiles should depend only on one reduced

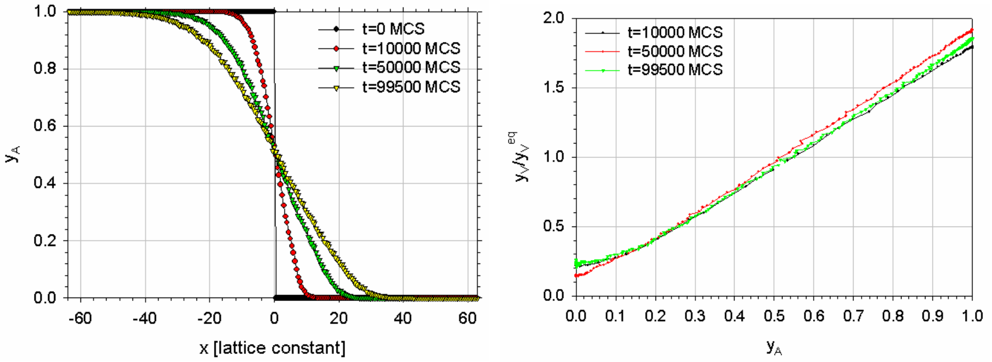

Figure 4.1: left: The concentration profiles for $t = 0$, 10000, 50000 and 99500 MCS, respectively ($\omega_B = 0.01$).
right: the vacancy concentration y_V normalised by the vacancy concentration in equilibrium y_V^{eq}.

variable, i.e. the profiles should scale. Plotting the curves vs. the reduced parameter $\lambda = \frac{x}{\sqrt{t}}$ makes them to collapse onto one single curve - a behaviour that is only changed for early times (the rectangular starting profile does obviously not scale) or when finite size effects come into play. Figure 4.3 visualizes the scaling behaviour for $\omega_B = 0.01$, 0.1, 0.5 and 1, respectively. According to this analysis a single parameter – the interdiffusion coefficient $\tilde{D}$ – suffices to describe the obtained profiles. This interdiffusion coefficient can be calculated by the method of Sauer, Freise and denBroeder which was introduced earlier. Figure 4.4 shows the resulting Interdiffusion coefficient $\tilde{D}$ as a function of composition and for different ratios of the atomic exchange frequencies. In Svoboda et al. [2002] the authors presented a derivation of Onsager's coefficients by means of tracer diffusion coefficients. Although in this derivation vacancy correlation effects were neglected, it gives a prediction of the interdiffusion coefficient for the case of no sources and sinks for vacancies. This interdiffusion coefficient is given by

$$\tilde{D} = \frac{y_V}{y_V^{eq}} \frac{D_A D_B}{y_A D_A + y_B D_B} \tag{4.2}$$

which easily can be compared with our results. In Figure 4.4 the black curves show the interdiffusion coefficient obtained by a Sauer-Freise-denBroeder analysis of the resulting concentration profiles. The red curves correspond to the interdiffusion calculated by equation (4.2). For this calculation the vacancy concentration $y_V(y_A)$ and the tracer diffusivities $D_A(y_A)$ ($D_B(y_A)$, respectively) have to be known for the same values of y_A. Since the vacancy concentration was not exactly known at the values $y_A = 0, 0.01, \ldots, 0.99, 1$

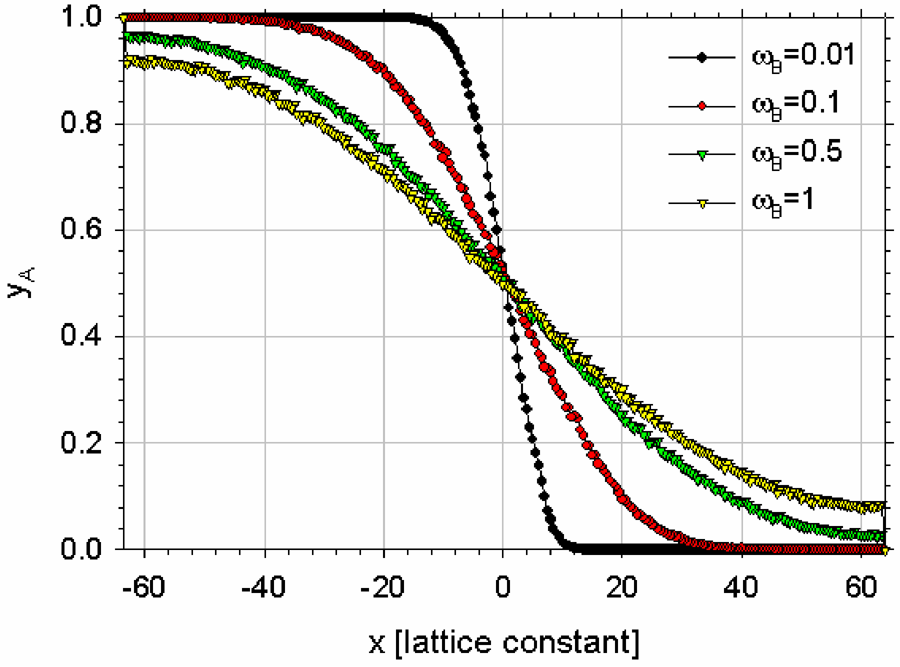

Figure 4.2: The concentration profiles for different values of ω_B at 10000 MCS. The effect of slowing down of mixing with decreasing ω_B is clearly visible.

a linear interpolation was done to determine the vacancy concentration at the desired positions. Figure 4.4 shows that equation (4.2) – although derived by neglecting vacancy correlation effects – fits the data remarkable well. The agreement of the data is the better the more the ratio of the exchange frequencies approaches 1, i.e. the atoms get indistinguishable. For indistinguishable atoms the interdiffusion coefficient can be calculated analytically. It is $\tilde{D} = D_A = D_B$, where one has to consider that in this special case the vacancy concentration is at its equilibrium value at all points in the sample. For large ratios, i.e. 0.01, the deviations of the two curves get more pronounced, which is also to be expected.

Equation (4.2) was evaluated by the rough approximation $A_V = A_A + A_B$. To find a formula analogous to equation (4.2) by the use of equation (2.34) is still missing and should further help to improve the results shown in Figure 4.4.

To further compare the results obtained by the continuum-theory and our atomistic simulations, the tracer diffusion coefficients obtained by the random alloy model were taken as input for calculations according to Svoboda et al. [2002] for the case of no sources and sinks for vacancies (i.e. constant

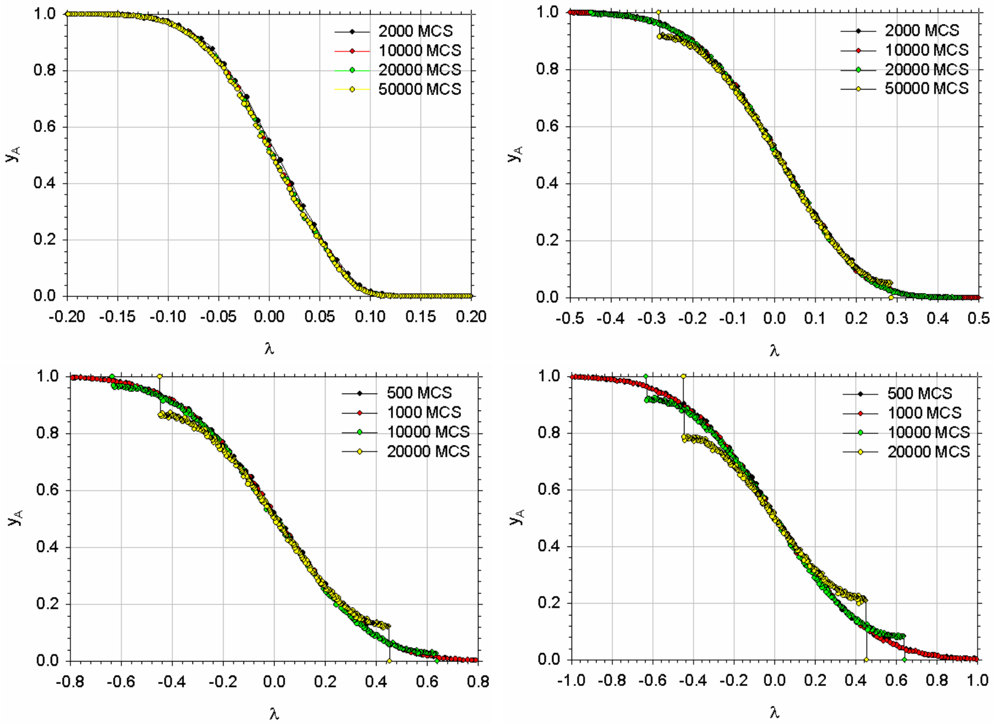

Figure 4.3: The scaling behaviour for $\omega_B = 0.01$ (top-left), $\omega_B = 0.1$ (top-right), $\omega_B = 0.5$ (bottom-left) and $\omega_B = 1$ (bottom-right), respectively. The concentration y_A is plotted against the reduced parameter $\lambda = \frac{x}{\sqrt{t}}$. With increasing ω_B, i.e. speeding up of the mixing process, pronounced finite size effects occur even at a rather early stage of time.

number of vacancies). This continuum theory enables to calculate the time evolution of concentration profiles of all species including vacancies. The reduced concentration profiles and the dependence of the vacancy concentration on the concentration of A atoms could be compared. The results are shown in Figure 4.5. The agreement between the data is good, although deviations in the reduced profiles and the vacancy concentration profiles can be observed. Two reasons account for this fact: first, the continuum mechanical theory used to calculate the profiles is Svoboda's model with a diagonal dissipation matrix. As was shown in the previous chapter this can not account for an exact description of the random alloy. Second, there is a "time" effect in the vacancy-concentration. As could already be seen in Figure 4.1 the vacancy-concentration is not fully independent of time, but varies a little. This is due to the fact, that the vacancy concentration, does not only depend on the concentration y_A, but also on the volume fraction of material with composition y_A and since this changes with time, so does the vacancy-

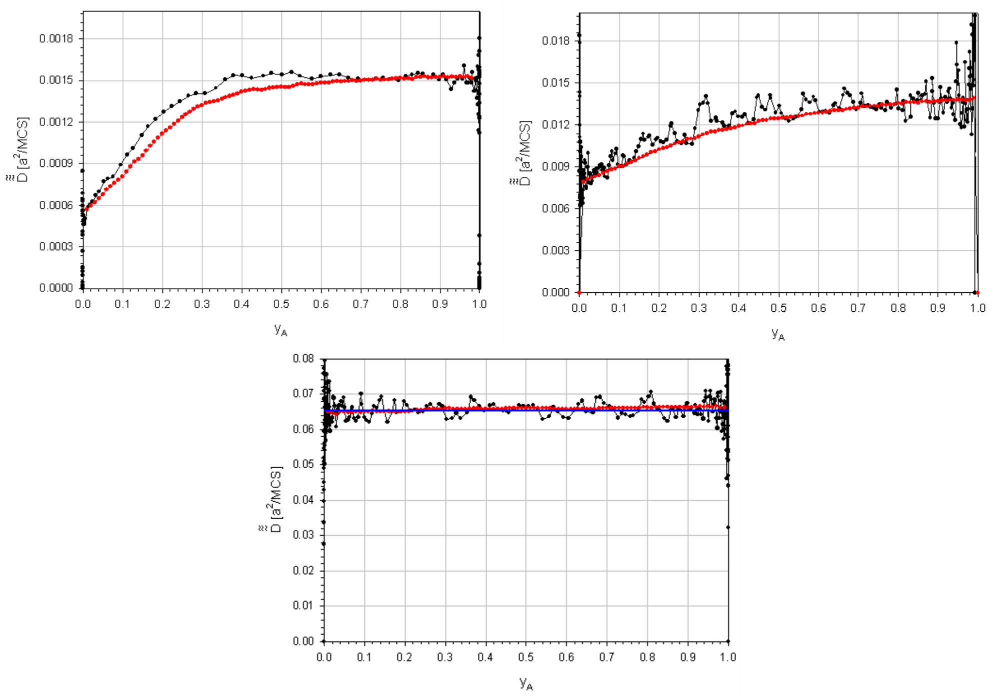

Figure 4.4: The interdiffusion coefficient for different values of the atomic exchange frequencies. Top left $\omega_B = 0.01$, top right $\omega_B = 0.1$, bottom $\omega_B = 1$. Black symbols denote values obtained by a Sauer-Freise-denBroeder analysis, red symbols the evaluation according to equation (4.2). The blue line in the graph for $\omega_B = 1$ shows the theoretical value of the interdiffusion coefficient of $\tilde{D} = 0.06513$.

concentration. But despite these small discrepancies, which could be further minimised by the use of a more general continuum mechanical model, e.g. Svoboda's approach with a non-diagonal dissipation matrix, the atomistic and macroscopic results prove to be nearly identical for a wide concentration range.

Finally it was also tried if dynamic effects could be predicted by Monte Carlo simulations. It was predicted by continuum mechanical calculations that for early times starting from a spatially constant vacancy concentration a vacancy poor region should emerge in the part of the slower diffuser close to the initial interface. This is because the vacancies near the interface are easily drawn in by the fast diffuser, where they are easily distributed. On the other hand the flow in from vacancies from the outer part of the slow diffuser region is too slow to compensate. To investigate these transient effects the simulations were not done with a single vacancy, but with 2000 vacancies. Therefore the vacancy distribution presented are not obtained by a temporal

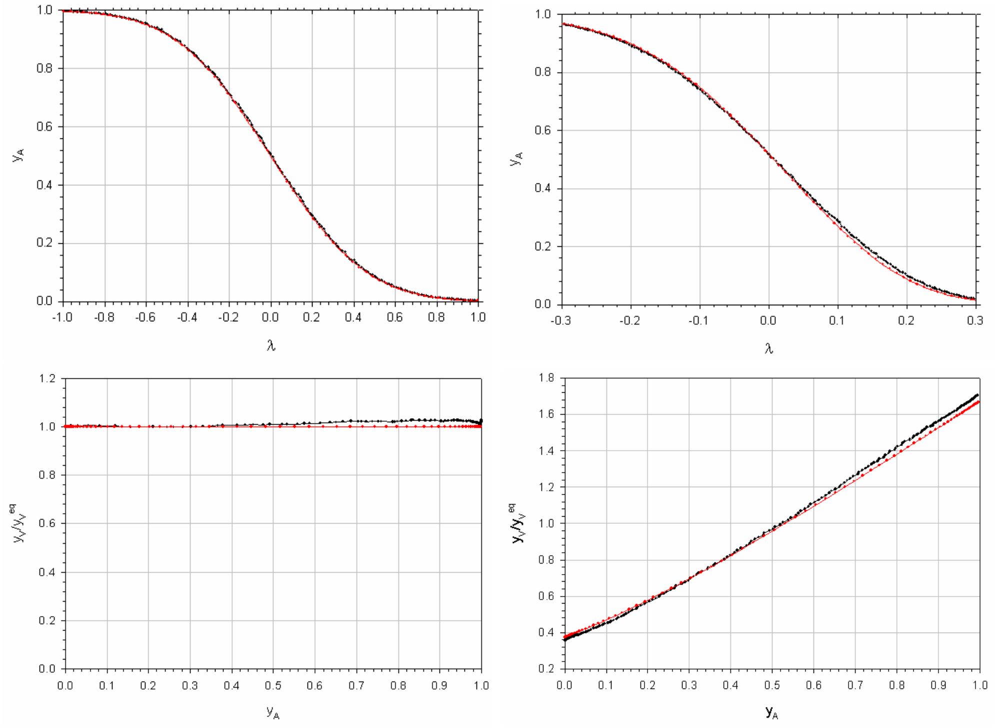

Figure 4.5: A comparison of the results obtained by an atomistic Monte Carlo simulation (black) and a continuum mechanical calculation (red) is shown. The reduced profiles for the A-concentration (top) and vacancy concentration profiles (bottom) are plotted for two different values of the atomic exchange frequency: $\omega_B = 1$ (left) and $\omega_B = 0.1$ (right), respectively.

average, but are concentration profiles in the normal sense. Figure 4.6 shows these transient effects in the vacancy distribution. Three different continuum mechanical models were used to evaluate the vacancy profiles for early times. First the theory of Darken, which gives the green line. Second the theory of Svoboda, that was presented in Svoboda et al. [2002]. In these calculations crude assumptions were made in order to evaluate A_V. Most significantly the presented value A_V was always positive. These assumptions lead to a poor description of the actual profiles (red line). A better estimate of A_V as presented in Hartmann et al. [2005] (see also equation (2.34)) – A_V is now given a negative value – gives a reasonable well description of the profiles. The still existing deviations are not surprising since it was shown in chapter 3.2 that describing the diffusional process with a diagonal dissipation rate – as it was done to calculate the presented values of the mobilities A – is not sufficient to fully describe diffusion in an alloy.

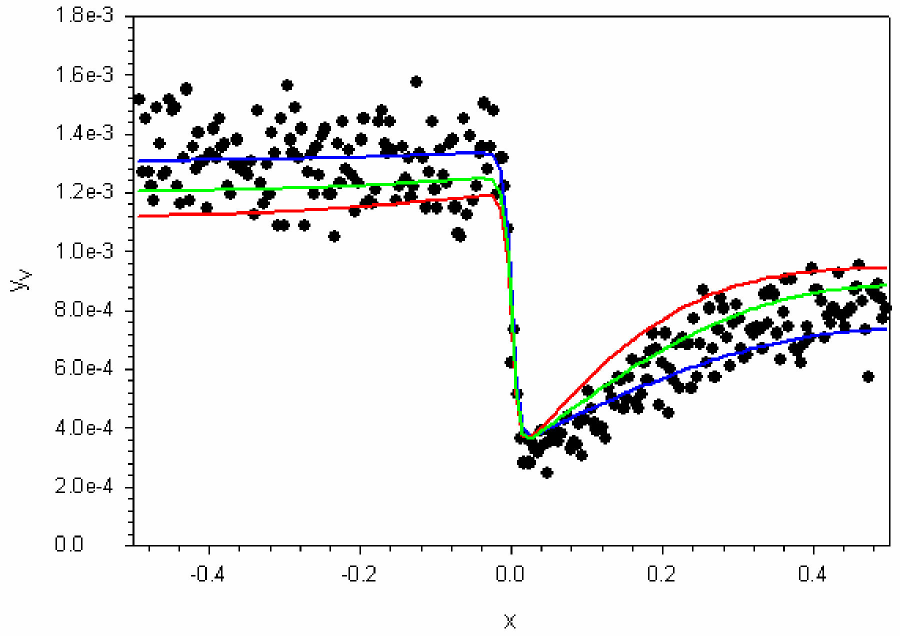

Figure 4.6: The vacancy distribution for early times. The graph shows the result of a Monte Carlo simulation (black dots) and continuum mechanical calculations, where the theories of Darken (green line), Svoboda as given in Svoboda et al. [2002] (red line) and Svoboda as given in Hartmann et al. [2005] (blue line) were used.

Chapter 5

Conclusion and Outlook - Diffusion

In this thesis Monte Carlo techniques were applied to diffusional problems in material physics. The field of interest was substitutional diffusion in binary alloys. Diffusion is a process covering several time and length scales. On the microscopic scale of several Ångström and several femto-seconds the fundamental diffusion event is described by atomic site exchanges. Whereas on the macroscopic level (sample sizes of cm and diffusion times of days or even weeks) diffusion manifests itself in the smearing of continuous concentration profiles. Due to the difference in the involved scales different concepts have been developed to give an appropriate description of the diffusional process on the scale investigated. Bridging the gap between macroscopic and microscopic description, i.e. calculation of the macroscopic quantities describing diffusion out of the atomic details of the elementary jump processes, is the field of statistical mechanics. But because of the complexity of the involved systems exact solutions are possible only for few, simple systems. To gain results for models closer to physical reality the use of approximations in the calculations is inevitable. Since the impacts of these approximations is not always well understood it was the aim of this thesis, to compare the predictions of different macroscopic theories to the results of atomistic Monte Carlo simulations for a simple model alloy. Starting from an atomistic computer experiment – where all atomic details of the diffusional process were known – continuum mechanical averages were calculated and compared to the predictions of the theoretical approaches by Darken, Manning, Svoboda and Moleko, which show different levels of approximation. It was shown that Manning's and Svoboda's concept, although derived on different paths, are equivalent. Determining the tracer diffusion coefficients and Onsager's coefficients in two independent simulation runs provided the basis for a comparison of the different models. It was shown that Darken's concept gives only a poor description of the diffusional processes, whereas Manning's/Svoboda's model describes the situation better. The most accurate description is given by the model of Moleko, with the drawback that Moleko's model is especially designed for the random alloy and can not readily be applied to more general systems. Although Manning's model was originally also developed for the random alloy, it was shown by Lidiard that Manning's results are valid beyond the random alloy. On the other hand Svoboda's concept is entirely based on a macroscopic description, the only input are diffusion coefficients, and is therefore applicable to all model systems (if diffusion coefficients can be defined). But the version of Svoboda's model described in this paper has another big drawback. In this thesis it was shown that it is not possible to describe the random alloy exactly by Svoboda's description. This is due to the fact that the dissipation matrix was assumed diagonal. Our results show that an exact description of diffusional problems demands to include off-diagonal terms in the dissipation matrix. Therefore the drawback of Svoboda's theory – the incomplete description of diffusional processes with a diagonal dissipation matrix – is at the same time its big advantage: it is possible to generalise Svoboda's concept beyond the concept of Manning to account for all diffusional effects.

Additionally to the determination of Onsager's coefficients interdiffusion problems were studied. The starting configuration of a classical diffusion couple was prepared and the resulting concentration profiles were monitored. The obtained profiles, which showed excellent scaling behaviour, were analysed with a Sauer, Freise, den Broeder analysis which gave the interdiffusion coefficient as a function of composition. This was then compared to the expressions given by Darken and Svoboda. Furthermore using the tracer diffusion coefficients obtained from a Monte Carlo experiment concentration profiles were also obtained by continuum mechanical calculations. Both, the atomic and vacancy concentration profiles, were compared to the Monte Carlo results. The reduced profiles show very similar behaviour. Small deviations are most probably due to the approximation of a diagonal dissipation matrix in Svoboda's approach.

Several experiments can be thought of to continue this work. One extension is the generalisation to alloys not forming an ideal solution, most striking ordering solids. These alloys can be most effectively studied by implementing atomic interactions in the model, e.g. denoting each configuration pair $\langle ij \rangle)$ an interaction energy ϵ_{ij}. Describing the configuration of the lattice with spin variables results in an Ising-like interaction Hamiltonian that now governs the thermodynamic behaviour – especially the jump frequencies – of the system. This is the natural extension of the random alloy model, the exchange frequencies of the atomic species not being constant any more but dependent on the local environment of atom and vacancy. Within this model the attraction or repulsion of atoms and vacancies, respectively, is easily tuneable. Apart from effects arising from ordering tendencies of the alloy, interesting new features can also be expected by introducing some attraction by the vacancy and one atomic species.

Another route to extend the presented work is the investigation of multicomponent alloys beyond the binary alloy. For more than two atomic components the results of Manning (relating jump frequencies and Onsager's coefficients) and Moleko are not equivalent any more. An interesting question to answer is, if the presented descriptions stay accurate for a ternary or higher alloy or if they fail with the increasing complexity of the system.

Part II

Trabecular Bone remodelling

Bone can be classified in two major groups: compact and trabecular bone Currey [2002]. While compact bone, which is found e.g. in the shaft of long bones or in the outer shell of the skull, is a solid structure with a porosity of less than 10 %, trabecular bone, found at the end of long bones or inside the vertebrae, is a spongy structure with a porosity of more than 80 %. Both classes of bone are built up from the same material – a nano-composite of collagen and hydroxylapatite. From a material scientists point of view bone is a hierarchical structured material, which is demonstrated in Figure 5.1 for the example of a vertebra. The highest level is considered the whole vertebra as found in the human body. Zooming inside the vertebra trabecular bone is formed of a spongy structure with a porosity of more than 80 %. On this scale bone forms an open-pored cellular structure, similar to a foam. The single struts forming the structure are called *trabeculae*. Further increasing the magnification the structure of one trabeculae can be seen. It is built up in a lamellar manner, different sheets of material laid above one another. At the molecular level, bone is a composite of two different materials with opposing properties. A soft, but tough protein, the collagen, formed by three collagen chains arranged in a triple helix. The other component is a stiff, but brittle mineral, the hydroxylapatite, a calciumphospate. Stiffness and toughness are two very different properties. Stiffness is a measure how much force is needed to extend a material, i.e. the slope of the stress-strain curve. Toughness measures how much energy is needed to break a material, i.e. the area under the stress-strain curve. In most materials stiffness and toughness are two opposing properties. Materials that are very stiff, e.g. ceramics, are breaking easily. On the other hand, materials that are soft, e.g. rubber, can be deformed easily but it is very hard to break them. It is obvious, that the material bone needs to meet both requirements. In daily life it has to be stiff enough to wear loads without considerable deformations, but it also has to be tough enough to withstand impacts and unusual loadings (so called error loads) without breaking. The special design and arrangement of organic and inorganic material in bone reconciles both aspects and gives a structure almost as stiff as pure mineral and almost as tough as pure collagen Jäger and Fratzl [2000], Gao et al. [2003].

The mechanical properties of the living structure bone are influenced by all its hierarchical levels. It is known that a failure on one of the hierarchies also affects all other levels and may lead to a severe distortion of the bone as a whole. Severe bone diseases like osteoporosis or osteogenesis imperfecta (OI), the brittle bone disease, are prominent examples. OI stems from a point defect in the genetic code (i.e. a defect at the lowest hierarchical level), which gives a slightly different assembly of collagen building up bone. Normally the collagen triple helix is formed by two $\alpha 1$ and one $\alpha 2$ collagen chains. In the

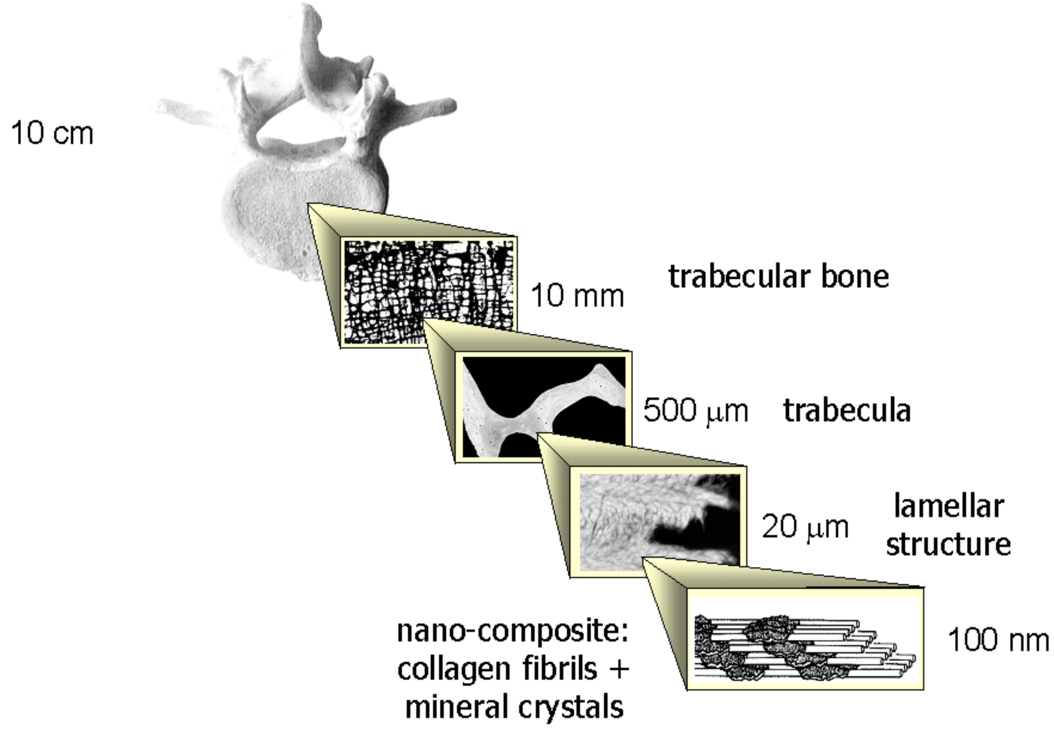

Figure 5.1: The hierarchical structure of bone shown for the human vertebra. Different levels of hierarchy can be seen. On the scale of several centimetres the whole vertebra can be recognised. But zooming in the structure shows, that on the scale of millimetres trabecular bone exhibits a spongy structure with a porosity of 80 or more percent. On the scale of several 100 μm single trabeculae can be found, that form the spongy structure one level above. Further increasing magnification the lamellar structure of the material gets visible. Finally, on the molecular level bone is a composite material formed by a soft, but tough protein – the collagen – and a stiff, but brittle mineral – the hydroxylapatite.

case of OI this helix is solely consisting of three $\alpha 1$ collagen chains. This defect does not only affect the collagen assembly, but leads to severe failures, like mal-mineralization and architectural deficiencies on the trabecular level, resulting in extreme brittleness of the bone as a whole Misof et al. [1997], Camacho et al. [1999], Grabner et al. [2001], Rauch and Glorieux [2005]. Thus, understanding each of the existing levels and their interrelation is of great importance.

In this thesis the remodelling process in trabecular bone is the field of interest. This remodelling process takes place on the hierarchical level of trabeculae and manifests itself in the change of bone mass and/or trabecular architecture. It is believed that this process is mechanically influenced, which poses many questions: Which mechanical signal does bone sense? How does bone sense it? How is the mechanical signal transformed into a chemical signal that cells are sensitive to (mechanotransduction)? How do the cells react to the signal? Several theoretical models exist that focus on the mechanical description of bone and impose phenomenological rules on the architectural development of bone that depend on the local value of a (mechanical) stimulus. Since the nature of this stimulus and the reaction of the body to this stimulus has not yet been unambiguously identified the focus of the investigations in this thesis is shifted from a precise mechanical description of bone to a more detailed investigation of the influence of different biological hypotheses on the remodelling process. The idea is to implement different assumptions on the underlying control processes in a computer code and to analyse their effects on bone's architecture and time evolution. The computer time gained by the simplified mechanical description allows to test a large variety of different hypotheses concerning the biological feedback loop and to perform intensive parameter studies. The aim of the present work is to draw (indirect) conclusions on the remodelling process. Although the mechanical parameters are assessed by a simplified model, the results presented should be qualitatively valid and allow to draw conclusions on the basic principles of the regulatory process governing bone's evolution, since one and the same mechanical model has been used for each of the simulations done. Accurate mechanical predictions, needed e.g. for the design of prostheses, are not the aim of the presented work. A more precise mechanical description is inevitably for investigations of this kind.

This second part of the thesis is organised as follows: In the next chapter the process of bone remodelling is explained and several theoretical concepts trying to give a theoretical framework for this phenomenon are introduced. In chapter 7 the model developed and used in this thesis is presented. In chapter 8 the simulations results are presented. First the results on a 2-dimensional lattice are shown and the measured parameters are explained. Then more realistic 3-dimensional results are presented. The next chapter 9 is dedicated to the interpretation of the results, the potential benefit for a better understanding of bone diseases and medication, and indirect conclusions on the feedback loop governing real bone remodelling are drawn. Finally the presented results are summarised and an outlook for further investigations is given.

Chapter 6

Concepts of Bone Remodelling

Beside its hierarchical structure, bone shows additional remarkable properties. Bone is not simply once built and then remains unchanged, but it undergoes a permanent change. In this sense bone is not static, but a living and evolving organ. On the one hand bone can change its shape and geometrical arrangement in order to meet mechanical loading events experienced in daily life, a process that is called *modelling*. On the other hand bone is also able to just maintain its structure, e.g. repair microdamage or remove dead bone, a process that is called *remodelling*. In Figure 6.1 the evolution of a human vertebra from the embryonic to the adult age is shown. In the prenatal phase, when the embryo is swimming in the amniotic sac the body does not feel any gravitation and the arrangement of trabeculae is almost radial. After birth the loading pattern of the bone changes, the body starts to feel the effect of gravitation. This in turn leads to a rearrangement of trabeculae in the principal loading directions. In the adult age the reorientation process is completed and the trabeculae are arranged preferentially in horizontal and vertical directions. Although Figure 6.1 seems very appealing to prove the re-

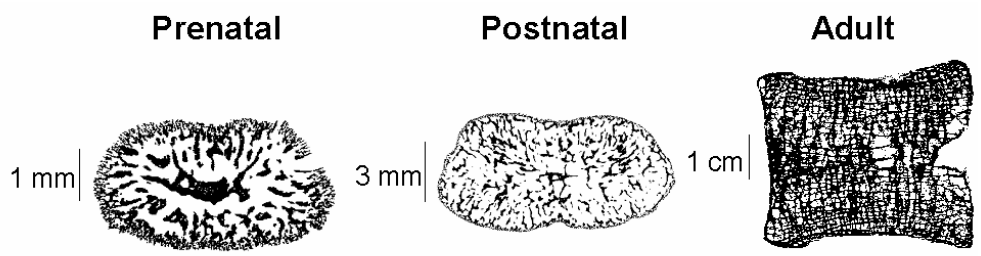

Figure 6.1: The development of the human vertebra from the embryonic phase (left) to the adult stage (right) is shown (Figure taken from Roschger et al. [2001]).

orientation of trabeculae due to loading conditions, this re-orientation is not unquestioned. The main point of criticism is that although it is true that the body does not feel any gravitational forces in the embryonic state, the same is not true for muscle forces that act from the very beginning of life. Since several studies revealed that muscle loading is the most important factor on bone Özkaya and Nordin [1999], Rittweger et al. [2005] maintenance, Figure 6.1 does not confirm a re-alignment of trabeculae due to external forces, all the more since the vertebra grows during this time.

For compact bone the influence of mechanical forces on its architecture is well established by a number of experiments (which are very hard, if not impossible to do on trabecular bone). To mention only one, Johnson et al. [2000] investigated the effect of asymmetric loading on the bones of racing greyhounds. The races are always performed in counter-clockwise direction on circular tracks, which gives rise to an asymmetric loading pattern. This asymmetry was also found in the bone mineral density when comparing right and left central tarsal bones of active greyhounds. In retired greyhounds no asymmetry was found, the effect had vanished.

In order to fulfil the described tasks of modelling and remodelling the body has the ability to remove bone elements as well as to deposit new bone. This is done by two specialised body cells, the *osteoblasts*, which form new bone, and the *osteoclasts* which resorb bone. In Figure 6.2 it is shown, how these cells work together to make new bone. In the resting phase the surface of bone is covered with lining cells (flat elongated cells, which in the activation process become osteoblasts) and therefore protect bone from the attack of osteoclasts. When the remodelling process is activated, these lining cells withdraw and leave the surface open for the osteoclasts to start doing their work. Osteoclasts, which are big, multinuclear cells, can now approach the surface. There they build up a resorption cavity, by creating an acidic environment and dissolving the mineral out of the bone matrix. Once the mineral is gone the collagen is taken out and fragmented. After the withdrawal of osteoclasts the osteoblasts can now assess the bone surface and create new bone by depositing collagen molecules, which then self assemble to the bone matrix. After the collagen was laid down, the mineralization process starts, which reinforces the bone matrix. In this process of forming new bone, it may happen that osteoblasts are left behind and buried alive in the bone matrix. These cells do not die, but differentiate to *osteocytes*; cells that live in the bone matrix and are interconnected by a network of canaliculi (i.e. long appendices of the cells that are interconnected via gap-junctions). Therefore it is probable that the osteocytes are able to communicate with each other and that they are also able to send signals to the bone surface. This makes the osteocytes network a perfect candidate to be the mechanical

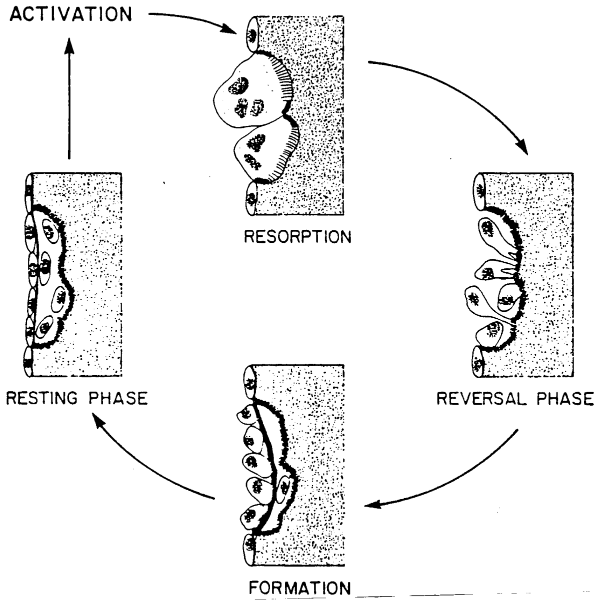

Figure 6.2: The (re)model cycle in bone. First (left) in the resting phase, bone's surface is covered by lining cells (which later on will become osteoblasts) and the system is resting. Then, after the activation, the lining cells withdraw from the bone surface and the osteoclasts (big, multinuclear cells) can reach the bone surface and form a resorption cavity (top). After the osteoclast's work is done, they withdraw and leave place for the osteoblasts to approach the bone surface (right). The osteoblasts now start to fill the cavity left by the osteoclasts (bottom, formation phase). During this formation process it may happen that some of the osteoblasts are left behind and buried alive in the bone matrix (Figure taken from Favus and Christakos [1999]).

sensors in bone, that regulate bone's development Mullender and Huiskes [1997], Klein-Nulend et al. [1995], Burger and Klein-Nulend [1999], Burger et al. [2003]. But despite these appealing properties of the osteocyte network, it has not been clarified until today, if the osteocytes really act as mechanical sensors, not to mention which the stimulus is, they react to and how the signalling pathway to regulate osteoblasts and -clasts action works.

The last paragraph described bone as a hierarchical and living structure, but even this is not sufficient to fully describe bone. Bone is also intelligent in the sense that the deposition and resorption of bone material does not occur randomly. Rather it seems that the cells obey to well defined mechanical rules, where to put new bone and where to remove it. But although the existence of such rules is (quite) obvious, their exact formulation is still out of reach and under high debate. This is mostly due to two reasons: first, until today no direct measurement could be performed that relates the rate of bone resorption or deposition, respectively, to a given mechanical stimulus. Not even the nature of the stimulus has been unambiguously identified until today. The difficulty of such experiments is obvious. On the one hand in vivo measurements suffer from an ill defined mechanical environment – the loading patterns in bone are highly complex – and the difficulty to extract precise measured quantities Juncosa et al. [2003], Fritton and Rubin [2001]. On the other hand mechanically well defined in vitro experiments suffer from the fact, that cells behave completely different in an artificial environment than they do in vivo Brown [2000], Basso and Heersche [2002], Brown [2001]. Second, it is well established knowledge that bones do not only serve as mechanical entities in the body. Bone's purpose is not only to hold up the body and to allow for movement, but to serve as the main calcium reservoir in the body. This aspect is of special importance in the period of pregnancy and short after, because calcium is needed to build up the bones of the foetus and is one of the main components of mother milk. Since bone cells are very sensitive to sexual hormones, e.g. oestrogen, drastic hormonal changes, i.e. during the period of pregnancy or during the menopause, have a tremendous effect on bone's evolution. Keeping these facts in mind one has to be aware that although mechanical influences are of outstanding importance for bone's evolution this is not the entire truth. This coupling of mechanical and non-mechanical influences poses a further complication in understanding bone's development.

A way to understand the remodelling process in bone is that of a (biological) feedback loop. Mechanical sensors (most likely the osteocytes) sense the local mechanical state of bone and signal this information to the surface. According to this information bone cells resorb or deposit bone, which in turn leads to a change in the structure of bone, which is again sensed by the osteocytes and send back to the surface. More exact, the mechanical properties of a given bone structure influence bone remodelling, i.e. the change of bone structure; this remodelling again changes bone's mechanical properties and influences therefore the remodelling process. This closes the feedback loop. In Figure 6.3 this process is visualised.

In numerous experimental investigations the role of several potential mechanical stimuli on bone evolution were investigated. These experiments focus either on the effect that a given stimulus has on the mechanical properties of bone Goodship et al. [1998], Murray et al. [2001] or – more basic – that it has on the expression of messenger agents and chemical signalling by bone cells. While the first mentioned experiments include the investigation of the effects of cycling loading, as well as the influence of different amplitudes and frequencies Mosley et al. [1997], Mosley and Lanyon [1998], Oxlund et al. [2003], the latter ones showed that bone cells react most sensitively to

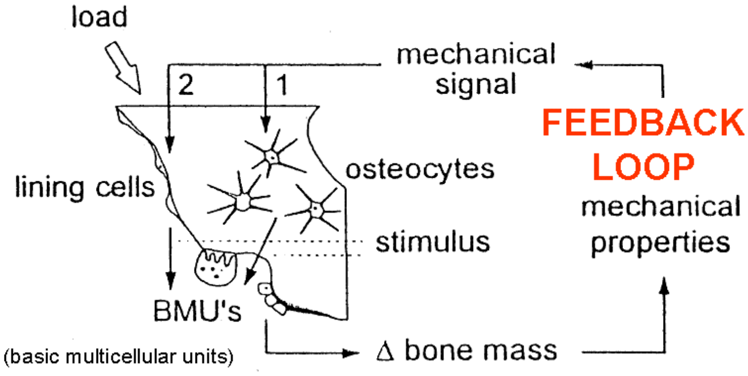

Figure 6.3: The biological feedback loop: the resorption of bone by osteoclasts leads to changed mechanical properties, which is sensed by the osteocytes, which send a signal to the osteoblasts to activate bone formation (remodelling, i.e. bone maintenance). But also a change in the external load, would lead to a changed mechanical environment that osteocytes would sense and therefore activate osteoblasts and - clasts, respectively. This in turn would lead to bone adaptation, i.e. modelling (Figure taken from Favus and Christakos [1999]).

shear stresses Neidlinger-Wilke et al. [1995], Bakker et al. [2001], Ehrlich and Lanyon [2002]. A mathematical concept modelling the interactions between osteoblast and osteoclast activities was developed in Lemaire et al. [2004].

Computer simulations are a perfect tool to investigate such a feedback process, but several difficulties have to be overcome. First, one has to find an appropriate description of the mechanics of the trabecular bone structure. Usually this is done with Finite Element (FE) methods, but since these are computationally costly this thesis follows another route. Second, it has to be specified in which way bone cells react to a given stimulus. Due to the lack of experimental data several different mathematical laws have been proposed to describe bone's reaction to a special loading configuration. In the following these mathematical laws giving the response of the bone cells as a function of the stimulus (stress, strain, strain-energy density, ...) are going to be called *remodelling laws* (RL). Since up to now none of these laws could be verified by experimental observations, the following strategy is followed in this thesis: Several different RLs are implemented in a computer code and their effect on the morphology and evolution of bone are investigated. By comparison of these results to experimental data from real bone, indirect conclusions on the RL governing the evolution of real bone are drawn. In the next section different approaches relating bone's evolution and loading configuration are presented with the emphasis put on computational models.

6.1 The Wolff-Roux Law

More than 100 years ago, the german anatomist Julius Wolff discovered a strong resemblance of the trabeculae in the human femoral head and the trajectories of principal stresses in a human build crane of similar shape (see Figure 6.4). This led Wolff to the postulation of the law, which states that the trabeculae in human bone follow the directions of principal stresses Wolff [1892] and that the adaptational processes in bone are guided by a maximal strength/minimal weight principle. As we know today, in its original formulation Wolff's law is not able to describe bone properly. A review about the "false premise of Wolff's law" can be found in Cowin [1997], where the author points out several flaws in Wolff's law, e.g. the human build crane is made out of a homogenous, isotropic material, trabecular bone – on the tissue level – is a spongy structure with a porosity of more than 80 %. Therefore Wolff's law should state, *trabeculae follow the directions of principal stresses, if bone would be made of a homogenous, isotropic material.* Furthermore there are infinitely many trajectories of principal stresses, i.e. they lie dense in a mathematical sense (for clarity only a finite number is depicted in the left part of Figure 6.4). If trabeculae would really follow the trajectories of principal stresses, bone should be completely filled with material, which is obviously not the case. But despite these apparent flaws in

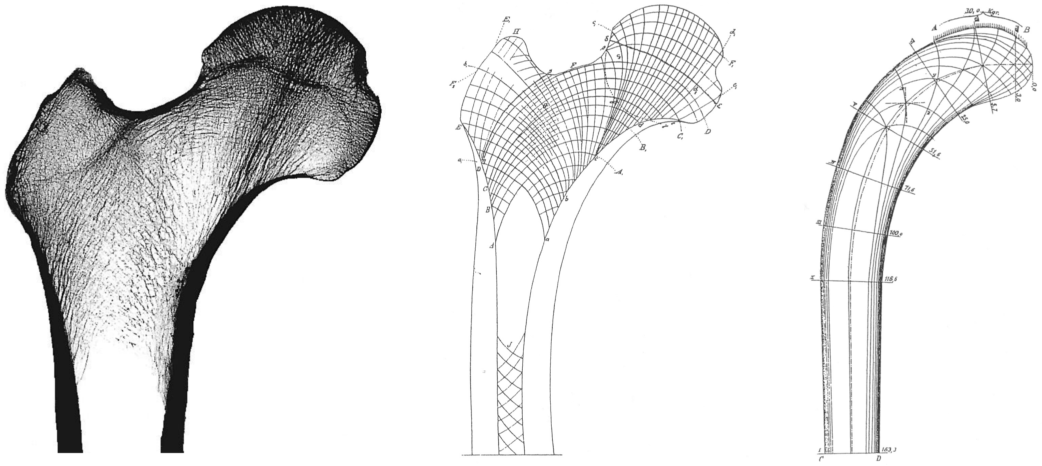

Figure 6.4: Left: the human femoral head. Middle: the direction of trabeculae as described by Wolff. Right: The stress trajectories of a human build crane of similar shape as the femoral head. The similarities in the trabecular pattern in bone and the direction of the principal stresses in the crane led to the postulation of Wolff's law (Figure taken from Wolff [1892]).

Wolff's law, the merit of Wolff was to recognise that the deposition of bone is not random, but obeys to some rules and seems to be mechanically controlled. As shown recently, e.g. Huiskes [2000], the original version of Wolff's law relating the orientation of trabeculae with stress trajectories and relying on a maximal strength/minimal weight concept is misleading. Huiskes points out that the similarity between trabecular orientation and stress trajectories is circumstantial, not causal, and that a reformulation of Wolff's law, which is influenced by ideas of Wilhelm Roux Roux [1881] and may therefore be called *Wolff-Roux law*, is a more realistic proposition Huiskes [2000]. The Wolff-Roux law states that bone is deposited where mechanically needed and resorbed where not needed. This is a local reformulation of Wolff's law and this idea of local adaptation is used as basis for all bone remodelling concepts presented in this thesis.

6.2 The Mechanostat

Based on numerous experimental observations Harold Frost proposed a remodelling concept which he named *mechanostat* Frost [1987, 1998, 2001, 2003, 2004]. The name stems from the analogy with a thermostat, a device to control the temperature. A simple thermostat is a device that switches on heating once a definite threshold temperature is reached. Frost's idea was that bone physiology might work the same way. He assumed the experienced strain as the control variable (the analogue to the temperature in a thermostat) and proposed that there is a *lazy* region, i.e. the region of normal activity (AW – adapted window), where the system is resting. But once the activity falls below a certain threshold value of the strain (DW – disuse window) – Frost suggests a strain value of 50 to 100 microstrain – bone is going to lose mass, strength and stiffness. On the other hand, if another threshold value of the strain is exceeded (MOW – mild overload window) – Frost's suggestion is a value of 1000 to 1500 microstrain – bone is going to gain mass, strength and stiffness (see Figure 6.5). In this sense Frost's mechanostat is a somewhat sophisticated thermostat, namely a thermostat that is able to cool if the temperature is too high and that is able to heat if the temperature is too low. Although the mechanostat can explain some of the experimentally observed facts in bone remodelling, see e.g. Frost [2003] for a list of 32 features of bone remodelling that are explained by the mechanostat, it certainly has its flaws as pointed out by e.g. Turner [1999]. The most prominent failure of the mechanostat is that it predicts that the bone mass should rapidly drop to zero, when there is no mechanical load (disuse). But the experimental observation is that bone loss due to disuse

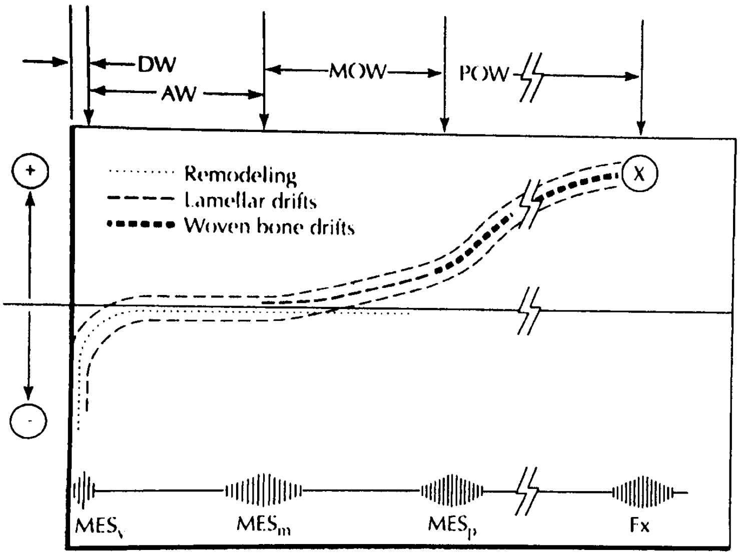

Figure 6.5: This figure summarizes the idea of the mechanostat. In the disuse window (DW) bone loses mass and strength, while in the adapted window (AW) bone strength and mass is maintained (this window corresponds to the lazy zone). In the mild overload window (MOW) bone mass and strength is increased, while in the pathological overload window (POW) microdamage is accumulated until bone fails. (Figure taken from Frost [2001])

slows down with time.

Nevertheless Frost's ideas have often been used to describe and investigate bone remodelling. As an example for the implementation of a RL according to Frost, i.e. a RL with a lazy zone, see van der Linden et al. [2004]. In this paper the authors calculated the surface strain distribution of selected bone samples and implemented the remodelling procedure the following way: elements with strains located in the lazy zone are unaffected, elements with strains below the lazy zone are resorbed and new material is added next to elements with strains above the lazy zone. This procedure was repeated until almost all elements ($>$ 99.8 %) were in the lazy zone.

6.3 Adaptive Elasticity

Stephen Cowin and co-workers were the first to propose a mathematical model to describe bone remodelling. They developed a phenomenological theoretical framework to describe adaptation processes in compact as well as in trabecular bone, which they called *adaptive elasticity* Cowin and Hegedus [1976], Cowin [1986, 1993]. Adaptive elasticity is a concept based on linear elasticity together with additional constitutive equations to describe, first, the change in material properties due to alterations of material density (especially its stiffness) and, second, the change in shape (compact bone) or in geometry (trabecular bone). The basic concept is to define a (local) remodelling equilibrium strain state ϵ_0. The driving force for changes in bone density or shape is assumed to be the difference between the actual strain state and ϵ_0. For compact bone the constitutive equations then read

$$S(x) = \mathbf{B}\,(\epsilon - \epsilon_0) \tag{6.1}$$

$$\frac{\partial \rho}{\partial t} = a(\rho) + \mathrm{tr}\,(A(\rho)\mathbf{E}) \tag{6.2}$$

with $S(x)$ the speed of the external bone surface at location x in direction normal to the surface, $\mathbf{B}$ a row vector of remodelling parameters, ϵ the strain vector and $\mathbf{E}$ the strain tensor. $\partial\rho/\partial t$ is the change of bone density, a is a function of the current density and $A(\rho)$ is a remodelling rate parameter.

For the studies of trabecular bone the change of the external shape, i.e. the speed of the surface, is exchanged with a change of the fabric tensor $\mathbf{H}$. The fabric tensor is a second rank tensor, which describes the geometrical arrangement of bone, i.e. the alignment of trabeculae. In this description trabecular bone is seen as continuous structure, characterized by its density and its fabric. The foam like nature of bone is averaged out. Once again constitutive equations have to be given, now for the change of fabric

$$\frac{\partial \mathbf{H}}{\partial t} = f\,(\mathbf{H}, \mathbf{E}, \rho) \tag{6.3}$$

and of the bone density

$$\frac{\partial \rho}{\partial t} = g\,(\mathbf{H}, \mathbf{E}, \rho)\,. \tag{6.4}$$

In the most general case the rate of change for $\mathbf{H}$ and ρ are functions of all three involved quantities: the fabric, the strain state and the bone density. By using Taylor expansions and neglecting higher order terms Cowin and co-workers obtained explicit expressions for equations (6.3) and (6.4). They can be found in Cowin et al. [1992], Hart [2001].

6.4 Computational remodelling

Using FE methods Rik Huiskes and co-workers formulated a theoretical framework to simulate bone remodelling. Starting with calculations for compact bone the equations for elasticity were solved and the strain-energy density was chosen as the stimulus for remodelling. These calculations were successfully used to describe the changes in bone architecture due to stress shielding effects induced by prostheses. Such computational results helped to significantly improve the design of such prostheses to prevent these effects, which can lead to loosening or breaking of the implants, which in turn leads to the need of a new operation Huiskes et al. [1987, 1989], van Rietbergen and Huiskes [2001]. Later on this concept was generalised and also applied to the remodelling process in trabecular bone Mullender and Huiskes [1995], Huiskes et al. [2000], Ruimerman et al. [2003, 2005a,b]. In their model the authors assume that the stimulus (in this case the local strain energy density) is sensed by the osteocytes which are embedded in the bone matrix. These osteocytes now give a signal to the bone surface which decays exponentially with the distance from the osteocyte. This exponential decay of the signal is called spatial influence function. On each point on the surface the signals from all osteocytes are summed up to give the resulting stimulus for bone formation, where a piecewise linear RL was chosen

$$\frac{\partial \rho}{\partial t} = \begin{cases} \tau(P(x,t) - P_0), & \text{for } P(x,t) > P_0 \\ 0, & \text{else} \end{cases} \tag{6.5}$$

with $P(x,t)$ the stimulus at location x and time t, P_0 a threshold value of the stimulus that has to be exceeded to start bone formation and τ a rate constant. $\partial\rho/\partial t$ is the change of bone density per time step. Bone resorption is executed with constant probability at random locations. The local elastic properties of the material bone are assumed to obey a power law with respect to the density, i.e. $E(x,y,z) \propto \rho^{\alpha}$. Such a power law dependence is typical for a foam-like material, where E is the effective elastic modulus of the foam and ρ is the volume fraction of the dense material Gibson and Ashby [1997]. So the mechanical assessment of the structure is done on a larger scale (averaging out the foam like structure) than the actual remodelling process that is carried out on the scale of single trabeculae that build up the foam. Another unsolved problem in the presented description arises from the inherent non-linearity of the basic equations: the stability of solutions is not guaranteed ("checker board" patterns) Mullender et al. [1994], even the existence and uniqueness of solutions has not been proven yet Cowin [1993].

In the framework of their model the authors successfully demonstrated that a trabecular structure emerged, was maintained and adapted to varying external loads.

6.5 Stochastic Remodelling without mechanical feedback

Representative for a variety of different remodelling schemes not using mechanical feedback, the model of Harrie Weinans and co-workers shall be presented van der Linden et al. [2001]. In their model the authors aim to describe the effect of bone loss due to remodelling by creating cavities and subsequent filling of the holes. Posing the restriction that the holes are not filled completely, but defining a resorption deficit, the authors model the formation deficit measured in real bone. Perforated trabeculae are not repaired, but removed. The input data like resorption depth, resorption deficit and remodelling space are based on biological data. The resorption cavities were formed at random locations (especially without any mechanical feedback) in the sample and the change in histomorphometric data, like bone mass, connectivity and stiffness are monitored. One of their main results is that the loss of stiffness is best prevented by reducing the resorption depth, rather than by a reduction of resorption deficit.

Other stochastic remodelling concepts without mechanical feedback can be found in e.g. Thomsen et al. [1994], Tabor and Rokita [2002], Tayyar et al. [1999].

Chapter 7

The Model – Stochastic Remodelling with mechanical feedback

In this chapter the simulation scheme developed by Weinkamer, Hartmann, Brechet and Fratzl, which is the basis for the results presented in this thesis, is described. The model comprises a stochastic description of the remodelling process that is controlled by mechanical feedback (see Figure 7.1 for a schematic representation of the program). The development of the model was guided by the aim to obtain a model with a good balance in the accuracy of the description of the mechanical as well as the biological part. Describing the remodelling process in a stochastic way, rather than with deterministic rate equations, is motivated by the following considerations: first, the elementary simulation step in our model is the action of one single osteoblast or osteoclast, i.e. the deposition or removal of one single bone packet. That is in contrast to other simulations, where only averaged values of net bone deposition or removal were investigated (i.e. an averaging procedure is carried out over many deposition and resorption events) and thus described by a rate equation. As is well known from experiments, there is a natural diversity in biological systems, i.e. the same kind of cells exposed to the same environment do not necessarily display the same behaviour, but can vary significantly in their responses. Second, it is possible that the remodelling process is not only an active process, but also passive processes like diffusion may play a crucial role, and diffusion itself is a stochastic process. Putting the pieces together – describing the action of single cells, the large number of cells involved, the natural diversity of these cells and the stochastic nature of underlying, basic processes – encourages to use a stochastic description of bone remodelling.

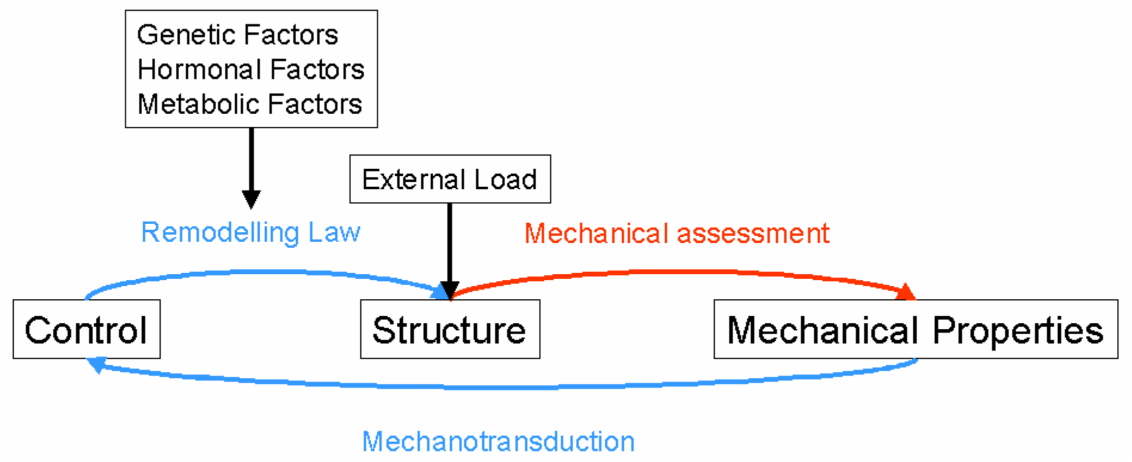

Figure 7.1: Starting from a given bone structure and known external loads, the mechanical properties of the structure and its local mechanical state (stress, strain) has to be evaluated. This is the *mechanical* part of the problem (shown in red). Then this mechanical information has to be transduced in chemical signals (*mechanotransduction*) which result in a special response of the cells. The response of the cells manifests itself in a change of the structure that changes the mechanical properties and local states, which closes the feedback loop. This second part – the mechanotransduction and response of the cells – may be called the *biological* part and – in our model – is described with an effective remodelling law (shown in blue). Furthermore it is known that biological factors can crucially influence the RL.

In the following the mechanical assessment of the structure is discussed. Since there are lots of unknowns in the biological part, the possibility to describe the mechanics by a time consuming FE approach was waived. The gained computational time was used to test a variety of different biological assumptions and to perform extensive parameter studies of the model. Then, in the second section, the feedback loop is closed by determining how the bone cells react on a given stimulus – that is extracted from the mechanical analysis from the first section – to change the structure.

7.1 Mechanics – Two way painting algorithm

In our model the structure of trabecular bone is mapped onto a quadratic (2D) or simple cubic (3D) lattice, respectively (lattice constant a and S_x, S_y and S_z, respectively, lattice sites in the specified direction). Each lattice site can be occupied, i.e. filled with bone matrix, or empty, i.e. filled with marrow. Since a vertebra consists of a shell of compact bone enclosing the core of trabecular bone, in the model fixed boundary conditions were chosen such that

$$\sigma_{xyz} \equiv 1 \qquad \forall (x,y,z) \in \partial V \tag{7.1}$$

with σ_{xyz} the spin variable at location (x, y, z) that takes the value 1 if the element is occupied and 0 if it is empty. ∂V denotes the boundary of the sample volume V. The architecture of bone is then characterized by the value of the spin variable $\sigma_{xyz} \in \{0, 1\}$ for each lattice site.

Given a special structure and an external load the local stresses and strains have to be calculated for each bone element. It is assumed that a constant force acts on the vertebra in z-direction. In a first step the load bearing elements of the structure have to be determined in each direction. It is assumed that the force “flows” like wet paint through the occupied elements Parkinson et al. [1997]. Starting in the plane $z = 0$ all occupied elements are labelled *connected*. Then the plane $z = 1$ is chosen. In a first step all occupied elements directly above a connected one are labelled connected. Then occupied elements to the left and to the right of connected elements are also labelled connected. This procedure is repeated for each layer until the last z-layer is reached. After that the procedure is repeated, now bottom-up, and exchanging the properties connected with *active* and occupied with connected. After the active elements have been determined in z-direction they are also determined in x- and (in the case of 3D) y-direction. The result of these calculations is a *loaded skeleton*, which consists of all elements that are active in a special direction and therefore also experience load and contribute to the load bearing in that direction. Consequently all other elements (empty and non-active) are unloaded. We have

$$\text{active} \Rightarrow \text{connected} \Rightarrow \text{occupied} \tag{7.2}$$

That basic version of the painting algorithm leads to an angle of the force flow of 45° ($\tan\alpha = 1$), which is an arbitrary input into the mechanical description. First simulation results suggested that this value is too large to give realistic bone architectures, so the angle of force flow was restricted to smaller values by posing one additional condition: an element to the left or to the right of one connected (active) element was only then labelled connected (active), when the element two layers above (below) the main element was first: connected (active) and second: has a connected (active) element directly above (below). This additional condition leads to an angle of the force flow of $\approx 18.43°$ ($\tan\alpha = 1/3$).

Once the active elements have been determined in each direction the local stresses and strains of each of the active elements have to be calculated. The elastic energy W associated with an external force F_z applied in z-direction

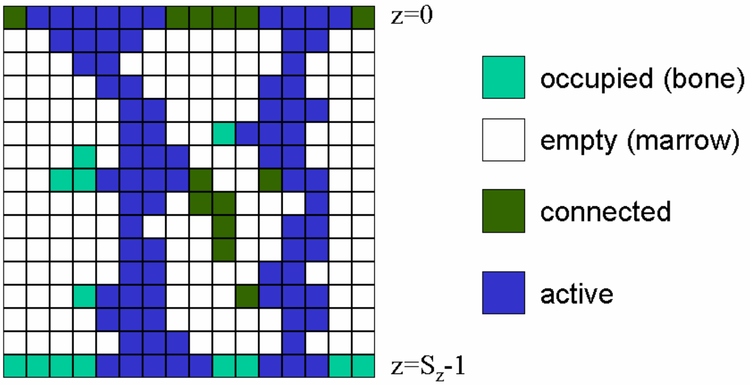

Figure 7.2: Schematic representation of the painting algorithm to determine the active (loaded) sites of a special bone architecture in z-direction. The algorithm starts in the top z-layer ($z = 0$) by labelling all occupied elements (cyan) as connected (green). In the subsequent layers all occupied elements directly beneath connected elements are also labelled connected, as are occupied neighbours directly to the left and right of connected ones. When the last layer ($z = S_z - 1$) is reached the procedure is repeated now from bottom to top to extinguish dead branches. Now the state variables change from occupied to connected and from connected to active (blue). The active skeleton (the set of all active elements) in z-direction are all elements experiencing load in that special direction.

on the sample can be written as follows

$$W = L_x L_y L_z \left[\frac{1}{2} E_x \left(\frac{\Delta L_x}{L_x} \right)^2 + \frac{1}{2} E_y \left(\frac{\Delta L_y}{L_y} \right)^2 + \frac{1}{2} E_z \left(\frac{\Delta L_z}{L_z} \right)^2 \right] - F_z \Delta L_z \tag{7.3}$$

with $L_i = aS_i$ the length of the sample in i-direction, ΔL_i the elongation in i-direction ($\Delta L_i / L_i = \epsilon_i$ the strain in i-direction) and E_i the global elastic (Young's) modulus in i-direction. The first term describes the energy stored in the sample (the energy density ρ of a material with Young's modulus E deformed by a strain ϵ is given by $\rho = \frac{1}{2} E \epsilon^2$), the second term is the work done by the external force F_z.

In the presented model it is assumed that F_z is acting on the vertebra solely in z-direction. But due to the inwaisting form of a vertebra such a force will result in effective forces, and consequently also in deformations, in directions perpendicular to the original loading direction (x- and y-direction, respectively). In the following the relation of deformations in the loading direction z and the other directions (x and y) is deduced. It is assumed that the macroscopic form of a vertebra may be described as an arc of a circle with constant length L. A deformation of this structure is realized by bringing together its ends by δz, which causes a maximum shift of the middle of the arc by δx (see Figure 7.3). Specifying the arc by its radius R and angle θ

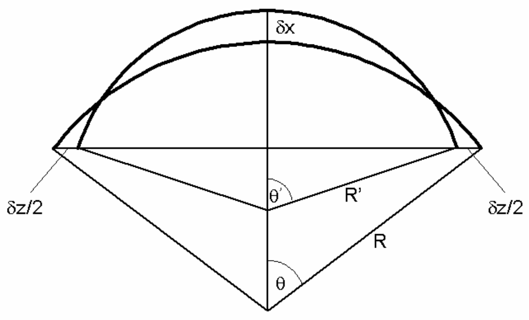

Figure 7.3: An arc of a circle with Radius R and angle 2θ is deformed by bringing its ends together by δz, which results in a perpendicular shift of δx. The deformed structure forms an arc of a circle with radius R' and angle $2\theta'$, such that the length of the arc is constant.

before bending and with R' and θ' after bending it is found that

$$\begin{aligned} R\theta &= R'\theta' && (7.4) \\ \delta x &= R'(1-\cos\theta') - R(1-\cos\theta) && (7.5) \\ \delta z &= 2R\sin\theta - 2R'\sin\theta'. && (7.6) \end{aligned}$$

With $\theta' = \theta + \delta\theta$ one obtains $R' = \frac{\theta}{\theta+\delta\theta}R$ and considering only small deformations, i.e. $\delta\theta \ll 1$, $\sin\theta' \approx \sin\theta + \delta\theta\cos\theta$ and $\cos\theta' \approx \cos\theta - \delta\theta\sin\theta$, where terms of higher than linear order were discarded. Insertion into the preceding equations yields

$$\delta x \approx \frac{1-\cos\theta-\theta\sin\theta}{2(\theta\cos\theta-\sin\theta)}\delta z \equiv k\delta z \qquad (7.7)$$

which gives a linear relationship between deformations in z- and x-direction with coupling constant k.

Due to the preceding calculations it is possible to connect the deformations in z-direction with deformations in x- and y-direction, respectively, which gives

$$\Delta L_x = \Delta L_y = k\Delta L_z \qquad (7.8)$$

Equation (7.3) can therefore be written

$$W = L_xL_yL_z\left[\frac{1}{2}E_x\left(\frac{k\Delta L_z}{L_x}\right)^2 + \frac{1}{2}E_y\left(\frac{k\Delta L_z}{L_y}\right)^2 + \frac{1}{2}E_z\left(\frac{\Delta L_z}{L_z}\right)^2\right] - F_z\Delta L_z \qquad (7.9)$$

Minimising this expression with respect to ΔL_z leads to

$$\Delta L_z = \frac{1}{k}\Delta L_x = \frac{1}{k}\Delta L_y = \frac{F_z}{k^2 E_x \frac{L_y L_z}{L_x} + k^2 E_y \frac{L_x L_z}{L_y} + E_z \frac{L_x L_y}{L_z}}. \tag{7.10}$$

Describing the loading situation with effective forces in all three directions gives

$$F_x^\star = L_y L_z E_x \frac{\Delta L_x}{L_x} \tag{7.11}$$

$$F_y^\star = L_z L_x E_y \frac{\Delta L_y}{L_y} \tag{7.12}$$

$$F_z^\star = L_x L_y E_z \frac{\Delta L_z}{L_z}. \tag{7.13}$$

Now the deformations ΔL_x, ΔL_y and ΔL_z caused by the external force F_z are determined. It is assumed that the material building up bone is isotropic and homogenous with elastic modulus E. Additionally it is assumed that the force in each layer is shared equally between the existing trabeculae. Let $M(z)$ be the number of trabeculae in a layer $z = const.$ and $N^j(z)a^2$ the area of the j-th trabecula ($j = 1, \cdots, M(z)$). The strain in the j-th trabecula at height z is therefore given by

$$\epsilon_z^j(z) = \frac{F_z^\star}{M(z)a^2 N^j(z) E}. \tag{7.14}$$

Now the strain is averaged first for the plane $z = const.$ and then for the whole vertebra

$$\bar{\epsilon} = \frac{\Delta L_z}{L_z} = \frac{1}{S_z}\sum_{z=0}^{S_z-1}\frac{1}{M(z)}\sum_{j=1}^{M(z)}\epsilon_z^j(z) = \frac{F_z^\star}{a^2 E}\frac{1}{S_z}\sum_{z=0}^{S_z-1}\frac{1}{M(z)^2}\sum_{j=1}^{M(z)}\frac{1}{N^j(z)} \equiv \frac{1}{S_z}\frac{F^\star}{a^2 E}A_z \tag{7.15}$$

with

$$A_z = \sum_{z=0}^{S_z-1}\frac{1}{M(z)^2}\sum_{j=1}^{M(z)}\frac{1}{N^j(z)} \tag{7.16}$$

Comparing equations (7.13) and (7.15) yields

$$E_z = \frac{S_z}{S_x S_y}\frac{E}{A_z}. \tag{7.17}$$

Similar calculations lead to

$$E_x = \frac{S_x}{S_y S_z}\frac{E}{A_x} \tag{7.18}$$

$$E_y = \frac{S_y}{S_x S_z}\frac{E}{A_y} \tag{7.19}$$

with

$$A_x = \sum_{x=0}^{S_x-1} \frac{1}{M(x)^2} \sum_{j'=1}^{M(x)} \frac{1}{N^{j'}(x)} \tag{7.20}$$

$$A_y = \sum_{y=0}^{S_y-1} \frac{1}{M(y)^2} \sum_{j''=1}^{M(y)} \frac{1}{N^{j''}(y)}. \tag{7.21}$$

The strains in one active element in all three directions are now given by

$$\epsilon_x(x,y,z) = \frac{F_x^\star}{Ea^2 M(x) N^{j'}(x)} \tag{7.22}$$

$$\epsilon_y(x,y,z) = \frac{F_y^\star}{Ea^2 M(y) N^{j''}(y)} \tag{7.23}$$

$$\epsilon_z(x,y,z) = \frac{F_z^\star}{Ea^2 M(z) N^{j}(z)}. \tag{7.24}$$

The (relative) volume change in one element (this is our choice for the stimulus) is evaluated according to

$$\Delta V(x,y,z)/V_0 = \epsilon_x(x,y,z) + \epsilon_y(x,y,z) + \epsilon_z(x,y,z). \tag{7.25}$$

Inserting equations (7.10), (7.17), (7.18) and (7.19) finally lead to

$$\Delta V(x,y,z)/V_0 = \Gamma \left(\frac{kA_yA_z}{M(x)N^{j'}(x)} + \frac{kA_xA_z}{M(y)N^{j''}(y)} + \frac{A_xA_y}{M(z)N^{j}(z)} \right) \tag{7.26}$$

with

$$\Gamma = \frac{1}{a^2 E} \frac{F_z}{k^2 \left(A_zA_y + A_xA_z\right) + A_xA_y}. \tag{7.27}$$

The analogous equation for a 2D-structure reads

$$\Delta V(x,z)/V_0 = \frac{1}{aE} \frac{F_z}{A_x + k^2 A_z} \left(\frac{kA_z}{M(x)N^{j'}(x)} + \frac{A_x}{M(z)N^{j}(z)} \right). \tag{7.28}$$

7.2 Biology – The feedback loop

In this thesis the remodelling process is described by an effective RL, as it is also used in the remodelling schemes presented in the last section with the basic difference that the rate of bone deposition and resorption, respectively, is not described by deterministic rate equations, but rather with stochastic formation and resorption probabilities. The underlying hypothesis is that bone cells are influenced by mechanical signals that trigger the location where new material is laid down or resorbed. This interaction – the mechanotransduction – is mediated via signalling pathways, including complex and not yet well understood biochemical processes like gene expression, receptor-ligand binding and so on. But in the end of the day all these processes result in a special behaviour of the bone cells, i.e. the probability to lay down new bone or to resorb already existing bone at a given point in the sample. Including all of these interactions in every detail in the model of bone remodelling is not feasible, hence the remodelling process is described by a phenomenological mathematical function. Its input is the stimulus at a certain point in the bone matrix and its output is a number that gives the probability for bone resorption and deposition at this point. All the biochemical processes – the way that leads from the mechanical stimulus to the cell's reaction – are sublimated in this functional dependence (see also Figure 7.1). Thus in our model all changes in the biochemical pathway, due to ageing, disease, hormonal changes and so on, will reflect in a change of this functional dependence of stimulus and cell reaction. Since the form of the RL governing bone's evolution has not yet been identified, in this thesis several very basic and simple functions will be implemented in a computer code and its influence on the emerging bone architecture will be discussed. By comparing these results to data from real bone it is possible to draw indirect conclusions on the RL governing the evolution of real bone.

Several proposals have been made to model the connexion of biology and mechanics. The most general one was proposed in Beaupre et al. [1990], which is motivated by Frost's idea of the mechanostat (see Figure 7.4). The authors assume a function consisting of 4 piecewise linear functions with slopes k_1, k_2, k_3 and k_4, respectively. k_1 and k_4 are of high magnitude and are responsible for bone loss due to disuse (k_1) and for high remodelling activity due to increased activity (k_4). The middle region of normal activity (a generalized lazy region) is divided in two parts with low changes in the remodelling activity. The first part is due to bone resorption (k_2) the second one to bone formation (k_3). Starting from this very general proposal it is possible to construct a variety of different RLs, some of them are summarized in Figures 7.5 and 7.6. The RLs are presented in two forms: First the net RL is given, i.e. the difference of osteoblastic and osteoclastic action, respectively, which is the only relevant function if describing the system by deterministic rate equations (the appropriate choice of the 4 slopes is written next to the net curves). Positive values of the net remodelling curve correspond to bone deposition, negative ones to bone resorption, respectively. In our stochastic model this net RL is the result of a combined action of osteoblasts and -clasts. On the right side of the table the net RL is split into the separate action of osteoblasts and -clasts. This splitting is of course not unambiguous, infinitely many different reactions of the cells may lead to the same net RL. In contrast to deterministic simulations it will be shown that this splitting has tremendous effects on the emerging structure, i.e. not only the net RL, but also its distinct parts are of importance for the remodelling process. Additionally some references are given to show which of the presented laws have been used in the past to describe the remodelling process of trabecular bone.

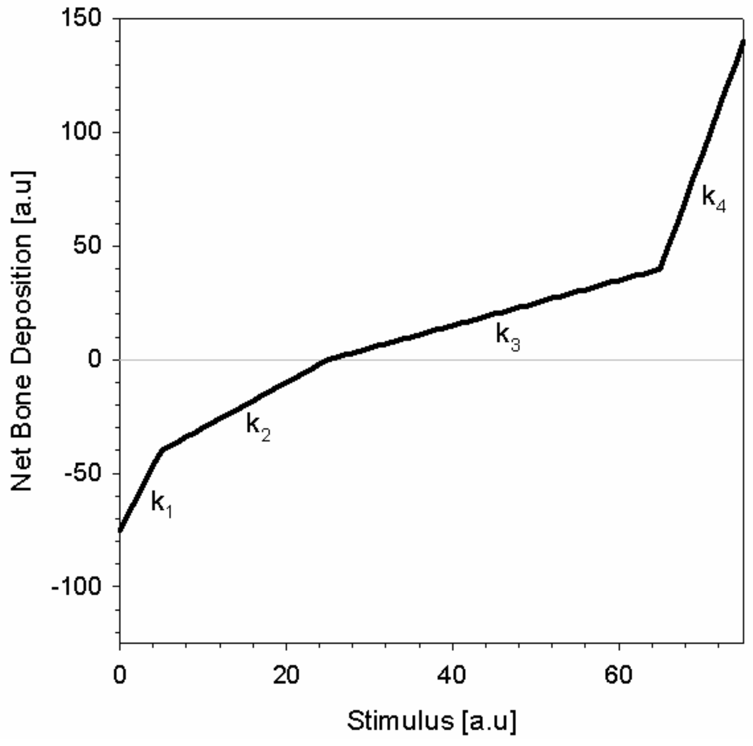

Figure 7.4: The general form of a RL proposed in Beaupre et al. [1990] consisting of 4 piecewise linear functions with slopes k_1, k_2, k_3 and k_4, respectively.

Roughly the RLs can be classified into three different classes: First, proposals 1, 2, 3 and 8 result in continuous functions, no abrupt changes in the cell's reaction to the stimulus are present. These will be called *linear* RLs in the following. Second, the functions, where the stimulus has to exceed one critical value after which the response of one of the cell's strongly changes, therefore the RL shows a discontinuity (a jump or a step) as can be seen in 4 and 5. These laws will be called *step* RLs. Third, the RLs that are influenced by H. Frost's concept of the mechanostat and therefore show a lazy zone that corresponds to the normal activity window, i.e. a region of no remodelling at all. These laws are described by 6 and 7 in the overview table and will be termed *Frost's* RLs.

7.3 Simulations and data evaluation

After choosing a certain RL, it has to be specified to which stimulus the cells should react. In the simulations presented in this work the strain values, more exact the (relative) volume change, in the local environment of the cells (i.e. the volume change of its nearest neighbours, see equation (7.26)) are assumed to play that special role.

Finally, after choosing stimulus and RL, it has to be defined, how a remodelling event can take place: A lattice site is chosen randomly. If the site is on bone's surface, i.e. if the element is occupied and at least one of its nearest neighbours is non-occupied or if the element is non-occupied and at least one of its nearest neighbours is occupied, it is kept, otherwise discarded. This rule takes account of the fact that bone forming and resorbing cells can not enter the bone matrix and can therefore only act at bone's surface. If the element is non-occupied the local stimulus for bone formation is calculated. According to equation (7.26) the volume change (i.e. the trace of the strain tensor) is evaluated. According to the chosen RL then the osteoblastic and -clastic responses are determined. Finally a random number (equally distributed between zero and one) is drawn. If the random number is smaller than the formation/resorption probability, the occupation state of the lattice site is changed (from zero to one for a formation trial or from one to zero for a resorption trial, respectively), otherwise it remains unchanged. This procedure is repeated and the resulting structures are written out and analysed according to standard histomorphometrical procedures. The most important histomorphometric parameters are Parfitt et al. [1987]:

- Bone Volume Fraction (BV/TV): the ratio of bone volume to tissue volume, i.e. the percentage of how much space of the trabecular bone is really occupied by bone in comparison to the macroscopic volume of the sample

  $$\frac{1}{S_x S_y S_z} \sum_{x,y,z} \sigma_{xyz} \tag{7.29}$$

  with σ_{xyz} the spin variable and S_i the sample dimensions in i-direction.

- Trabecular Number ($Tr.N$): the mean number of (active) trabeculae in a given direction. Accordingly

$$\frac{1}{S_i}\sum_{k=1}^{S_i} M(k) \tag{7.30}$$

gives the $Tr.N$ in i-direction, with $M(k)$ the number of trabeculae in layer k.

- Trabecular Area ($Tr.Ar$): the mean cross-sectional (active) area of one trabeculae in a given direction, given by

  $$\frac{1}{\sum_{k=1}^{S_i} M(k)} \sum_{k=1}^{S_i} \sum_{l=1}^{M(k)} Ar_k(l). \tag{7.31}$$

  $M(k)$ is the number of trabeculae in layer k and $Ar_k(l)$ is the (active) area of the l-th trabecula in layer k.

- Trabecular Thickness ($Tr.Th$): the mean thickness of one trabeculae. In 3-dimensional simulations the trabecular thickness is evaluated via the trabecular Area by calculation of the diameter of a circle with the same area as the trabeculae.

Non-geometrical quantities that are important for characterising trabecular bone are

- Bone Formation Rate, i.e. how much new bone is deposited per time unit (see e.g. Eriksen et al. [2002]).
- Bone Resorption Rate, i.e. how much bone is resorbed per time unit (see e.g. Eriksen et al. [2002]).
- Age distribution of bone packets, i.e. the probability to find a bone packet of a given age. By application of a mineralization law, which provides the degree of mineralization of bone as a function of age, the age distribution is easily convertible to a bone mineral density distribution (BMDD), which can be measured by quantitative backscattered electron imaging (qBEI) Roschger et al. [1998, 2003].
- Strain Distribution, i.e. the number of bone elements with a certain strain (in our simulations this corresponds to the distribution of the mechanical stimulus).
- Trabecular Thickness distribution, i.e. the distribution of trabeculae with a given thickness.

The exact RLs chosen to give formation and resorption probabilities, respectively, are listed at the end of this part of the thesis in the chapter *Simulation Parameters*. When other parameters were chosen, this is explicitly stated in the text. All the parameters and measured quantities are given in reduced units (i.e. the lattice constant a and the elastic modulus E of the bone material are both set to 1) and all derived quantities are given with respect to these fundamental units.

The time unit of the simulations was 1 Monte Carlo step (1 MCS), which means one resorption/deposition trial per lattice site. This artificial time unit can be converted to real time by using the fact, that the turnover of real bone, i.e. the time when bone is completely rebuilt, is approximately 4 years Eriksen [1986]. In a computer experiment it is easy to check when this condition is fulfilled.

Net Remodelling Law	Literature	Osteoclasts	Osteoblasts	
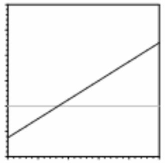 $k_1=k_2=k_3=k_4$	Mullender et.al, J. Biomech. **27**, 1389 (1994) Huiskes et.al., J. Biomech. **20**, 1135 (1987)		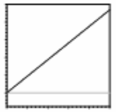	1
		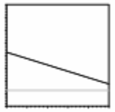	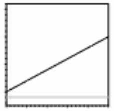	2
		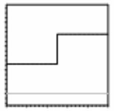	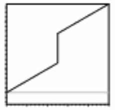	3
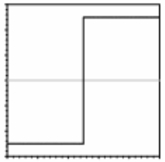 $k_1=k_4=0$ $k_2=k_3=\infty$			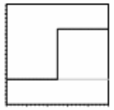	4
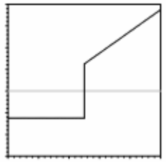 $k_1=0$ $k_2=k_3=\infty$ $k_4=k$	Weinkamer et. al., PRL **93**, 228102 (2004)		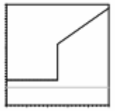	5

Figure 7.5: A collection of different RLs that either were proposed in the literature or that have been used in the simulations done in this thesis. All of the presented laws are special cases of the general RL given by Beaupre et al. [1990] which can be seen in Figure 7.4. Additionally to the net-RL it is also shown, how such a behaviour may be achieved by choosing the reaction of osteoblasts and osteoclasts accordingly.

Net Remodelling Law		Literature	Osteoclasts	Osteoblasts	
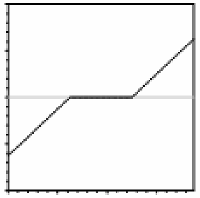	$k_1=k_4$ $k_2=k_3=0$	Frost, Anat. Rec. A **275A**, 1081 (2003) Huiskes et.al., J. Biomech. **20**, 1135 (1987) van der Linden et.al., J.Biomech. **37** , 367(2004)	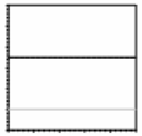	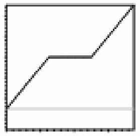	6
			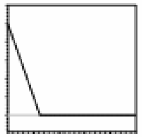	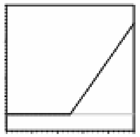	7
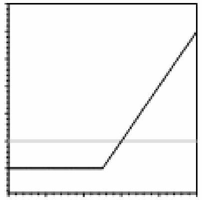	$k_1=k_2=k_3=0$ $k_4=k$	Huiskes et.al., Nature **405**, 704 (2000) Ruimerman et.al., Biorheology **40** , 315 (2003) Ruimerman et.al., Journal of Biomechanics **38** , 931 (2005)	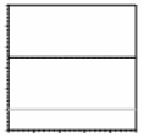	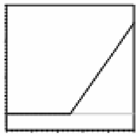	8

Figure 7.6: for figure caption see previous page

Chapter 8

Simulation Results

Several simulation runs with different RLs, different parameter values and starting from different initial conditions were performed. After selected time intervals the configuration was written out and analysed in terms of the histomorphometrical parameters, that are also measured in bone histomorphometry experiments working with real bone samples.

First the model was tested on a 2-dimensional lattice of size 1024×1024 ($= 1048576$). The RL chosen was Law 5 in Figure 7.5. First, to get an impression on the used model, some test runs were performed. Starting from regular grids the time evolution of the system was monitored. Furthermore the influence of different initial conditions was investigated. Then the sample was rotated to see if the struts would re-align according to the loading condition. Second, simulations related to the evolution of real bone were done. Starting from a homogenous bone mass distribution of high bone volume fraction the time evolution of the emerging architecture was monitored and analysed. Finally the influence of different remodelling parameters was analysed.

Then the simulations were extended to 3-dimensional samples of dimension $128 \times 128 \times 128$ ($= 2097152$) lattice points. It was investigated in which way the outcome of the simulations is changed, if one and the same net RL is composed of different responses of osteoblasts and osteoclasts. Then the effect of different types of RLs was analysed.

8.1 Simulations on 2-dimensional lattices

For the simulations done on 2-dimensional lattices RL 5 (see Figure 7.5) was used (see also Weinkamer et al. [2004b]). In this setting several parameters were freely adjustable. For the osteoblastic response these are

- the critical volume change ΔV_c, i.e. the location of the jump,

- the constant offset α, i.e. the (constant) probability of bone resorption below ΔV_c,
- the slope β, i.e. the slope of the linear increase in the osteoblastic response after ΔV_c which determines the height of the jump as well as the increase in bone formation probability after the jump and
- the (constant) bone resorption probability p_{OC}.

The choice of a constant resorption probability is based on two assumptions: first, that the osteoclasts react mainly to microdamage and, second, that the microdamage is randomly distributed in the system.

8.1.1 Test runs

Starting from different initial conditions (a random configuration, an empty frame, i.e. no elements except the boundaries are initially occupied, and a regular grid, respectively) it was shown, that nearly the same steady state bone mass was reached for each of these runs, on the other hand the architecture differed significantly. These results are summarized in Figures 8.1 and 8.2 where the architecture and the development of the bone mass are shown for the different starting configurations. By looking at the architectural snapshots it is possible to get information on the way in which the system evolves. Starting from a very fine mesh in the beginning (thin, but many rows and columns of material) lots of the trabeculae are lost by either merging or perforation – since they are thin few osteoclastic events suffice to perforate them. But the remaining ones are thickened until they overcome a critical size where perforation is not very probable anymore. In horizontal direction the trabeculae are eaten away too fast before they can reach the critical thickness and since trabeculae never come back they are lost forever. On the other hand starting from a coarser mesh (less, but thicker trabeculae), where the trabeculae exceeds the critical thickness from the beginning, proves to be a very stable configuration. Material is taken away, i.e. the trabeculae are thinned, until the appropriate bone volume fraction is reached, but none of the trabeculae is lost - neither in horizontal nor in vertical direction. These results show that the starting configuration has a massive impact on the final architecture, even if the bone mass is conserved (see Figure 8.2). Starting from a too fine mesh, osteoclastic resorption may lead to a rapid loss of horizontal trabeculae – in the worst case all are perforated and only vertical trabeculae remain, with the only exception of the boundary, that is accordingly thickened.

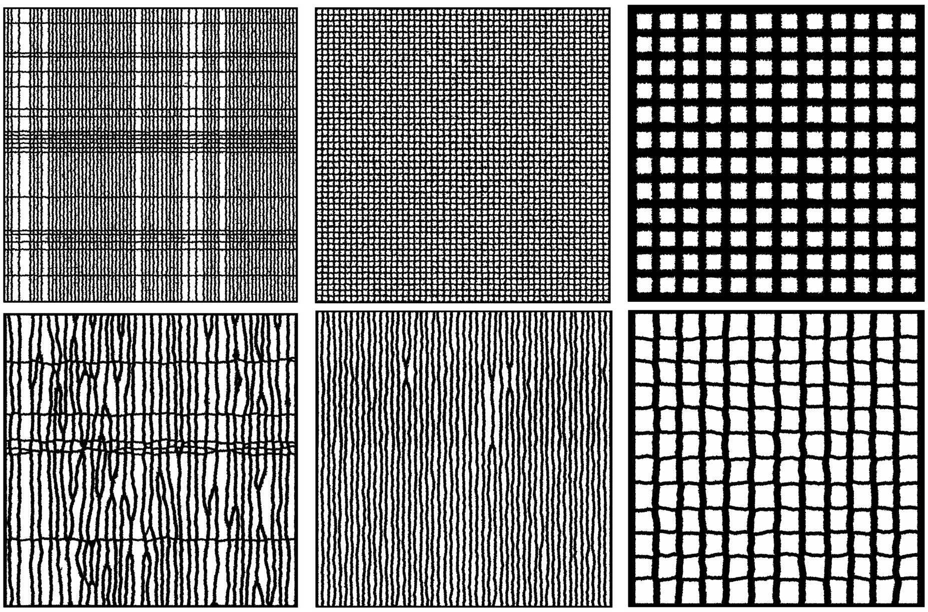

Figure 8.1: Starting from a regular grid of different sizes the final architecture can differ a lot, although the same bone volume fraction is reached. In the top row the almost unchanged grids are shown for early times (250 MCS), the bottom row shows the architecture at late times (9000 MCS). Three different starting grids are used: grid $3-10$ (left), grid $8-12$ (middle) and grid $32-48$ (right) (the first number gives the thickness of the columns, the second number gives the spacing of successive columns).

Furthermore the reaction of the system to different loading conditions was investigated. Since a different loading direction would require to adapt the mechanical assessment of the structure, i.e. a change in the painting algorithm, the mechanical assessment remained unaltered, but the sample was rotated. Starting from a regular grid with vertical bars tilted $\approx 14°$ ($\tan\alpha = 1/4$) to the vertical axis the time evolution of the system was monitored. Figure 8.3 shows the results. A structure starting from thick struts (original diameter 32 pixels) proves to be very stable. Since all elements in the tilted strut are active and the thickness of the strut exceeds the critical thickness of being highly stressed there is no driving force to straighten the trabeculae (since bending is not included in the mechanical description of the model, a tilted and a straight strut have the same energy). The only driving force that exists, is that deposition of bone on sides with acute and obtuse angle, respectively, does not pose a symmetric situation. While elements laid down on the acute side are automatically active, the same is not true for elements on the obtuse side (see Figure 8.3—right). This leads to a shift of the trabeculae, but the time scales are extremely large.

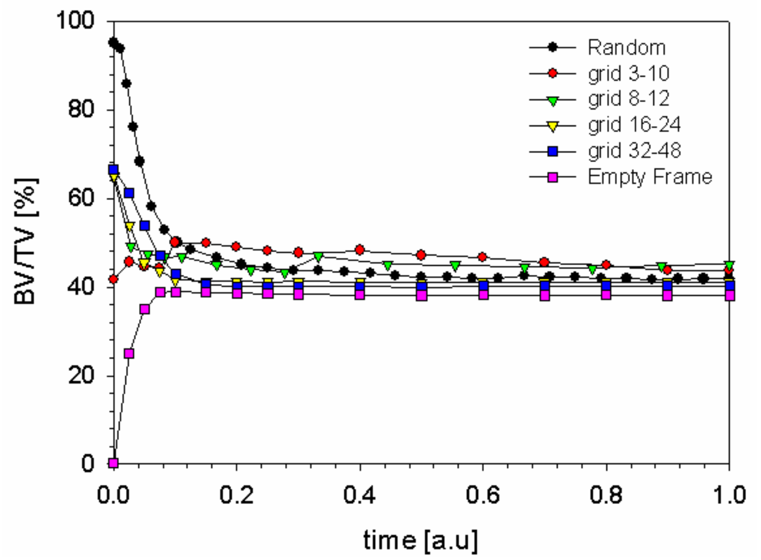

Figure 8.2: The time development of the bone mass for different starting configurations: a random filling of 95 % bone volume fraction, regular grids of size $x - y$, which means a thickness of x pixel of each column and a distance of y pixels between two successive columns, and a run starting from an empty frame.

Starting from thinner struts, the situation changes. Trabeculae that are so thin that they experience a stimulus larger than the threshold value (ΔV_c) are consequently thickened until they reach a thickness with a corresponding stimulus lower than ΔV_c. This leads to fast dynamics and changes in the system which also fasten the re-alignment of trabeculae. In Figure 8.4 the time evolution for this situation can be seen. In red the starting configuration is depicted (original thickness of vertical struts is 5 Pixel, the angle with respect to the vertical axis is $\approx\ 14°$), in black the configuration after 10000 MCS is shown. While the straightening of the vertical struts is clearly visible, the horizontal struts remain unaltered since they are already aligned with respect to the force flow. In the lower part of Figure 8.4 the corresponding angular correlation function is shown for the two depicted times. The angular correlation function $\tilde{G}(\alpha)$ is obtained from the standard correlation function $G(\mathbf{r}) = G(r, \alpha)$ by integration over the radius r.

$$\tilde{G}(\alpha) = \int G(r, \alpha) dr \tag{8.1}$$

Starting from an occupied lattice site the correlation function $G(\mathbf{r})$ gives the probability of finding another occupied site at (r), $\tilde{G}(\alpha)$ gives the probability of finding another occupied site in direction α. For the regular starting

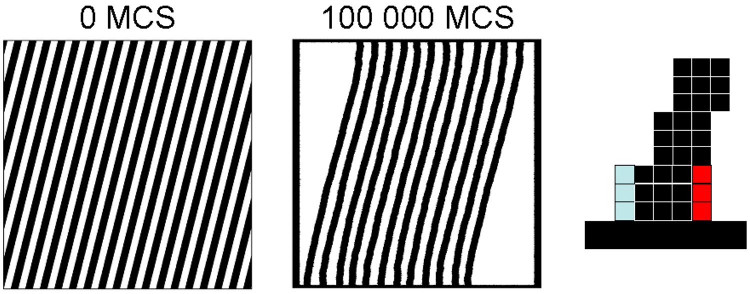

Figure 8.3: A regular structure with struts tilted ≈ 14° with respect to the vertical axis is used as starting configuration for the simulation. Since the struts exceed the critical thickness and bending is not included in the mechanical description of the model this configuration is very stable. Even at late times (right) a re-alignment of the struts in the vertical direction can only be seen at their tips close to the boundary. The small sketch on the right side of the figure shows the mechanism of straightening: The sketch shows a small section of a tilted strut. The special geometry of this situation breaks the symmetry of laying down new material on the acute side of the tilted strut (right, red elements) and on the obtuse side (left, blue elements), respectively. The red elements have some elements above, so it is probable that they are also active, i.e. experiencing load. The blue elements on the other hand have no elements above, so they are definitely not load bearing. This slight asymmetric situation leads to a drift of the trabeculae and consequently a straightening, but the time scale of this process can be very long.

grid two pronounced peaks are shown, one at zero degrees (representing the horizontal struts) and one at ≈ 76° (representing the vertical struts with a tilt angle of 14° with respect to the vertical axis). During time evolution the structure gets more irregular, both peaks broaden, but due to the realignment of trabeculae the peak corresponding to the vertical struts additionally shifts towards larger angles.

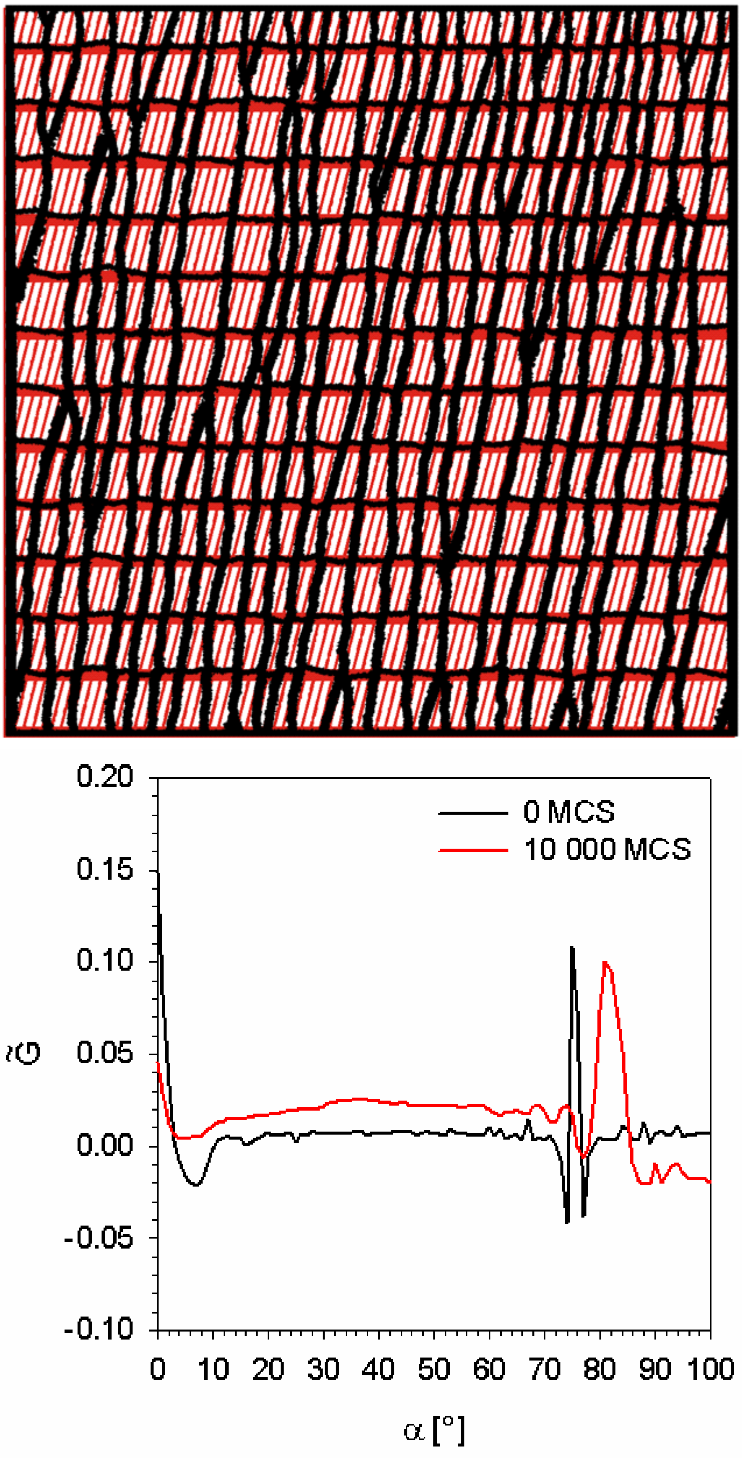

Figure 8.4: Top: Starting from thin, tilted vertical struts (thickness 5 Pixels, angle ≈ 14°) the re-alignment of trabeculae proceeds much faster. This is due to the pronounced remodelling activity to thicken the struts. In red the starting configuration can be seen, in black the evolving structure after 10000 MCS is shown.
Bottom: The angular correlation function $\tilde{G}(\alpha)$ of finding bone material in α-direction from a given occupied site (baseline corrected with the actual bone volume fraction). The shift of the peak corresponding to the vertical struts to values closer to 90° is visible, but this evolution slows down when the trabeculae exceed the critical thickness.

8.1.2 Bone remodelling

To avoid geometrical structures induced by the starting configuration, the simulation runs were started from a random configuration of bone with high bone volume fraction (95 %). Figure 8.5 shows the architectural evolution of bone for a given set of parameters ($\Delta V_c = 25$, for the other parameters see chapter *Simulation Parameters* at the end of this part), Figure 8.6 shows the corresponding histomorphometric parameters. The random starting configuration of bone material changes very fast to give a network like structure with struts (trabeculae) oriented preferentially in horizontal and vertical directions. This transformation is accompanied by a rapid loss in bone mass, the bone volume fraction decays from the originally 95 % to a value of approximately 40 % within the first simulation steps to take an almost constant value, while the emerging structures starts to coarsen, i.e. the number of trabeculae decreases, while the thickness of the remaining trabeculae increases Weinkamer et al. [2005]. Some authors claim to have found such a coarsening behaviour also experimentally, but these findings are still under high debate Frost [1999].

A parameter study of the problem showed that the system is most sensitive to a change in the critical strain ΔV_c. Figure 8.7 shows the architecture for six different values of the critical strain ($\Delta V_c = 15,\ 20,\ 25,\ 30,\ 35$ and 40). The snapshots were taken at different times and chosen to show the differences in emerging architecture, which is profoundly affected by the change in ΔV_c, as are the histomorphometric parameters. By making the osteoblasts more sensitive to the stimulus, i.e. for a low value of the critical volume change, there is considerable more bone material laid down and the structure is very coarse, showing no fine mesh of trabeculae, but rather very few, thick struts. By making the cells less sensitive, i.e. by raising the critical volume change by shifting the jump in the RL to higher values of the stimulus, one observes a loss in bone mass accompanied by a refinement of the structure – much more and thinner trabeculae are formed. Raising the critical volume change even more leads to a rapid loss of trabeculae – more pronounced in vertical than in horizontal direction – and a further decrease in bone mass. In this case there is also no forming of a fine and connected mesh of trabeculae. It seems that there is only a small window for the critical volume change in which a reasonable trabecular architecture forms.

Another simulation result is the age map of bone, which can easily be converted in an age distribution of bone elements. A computer simulation gives the possibility to monitor the time when each bone packet was laid down and together with a mineralization law, i.e. the degree of mineralization with respect to time, the age distribution reflects the local state of

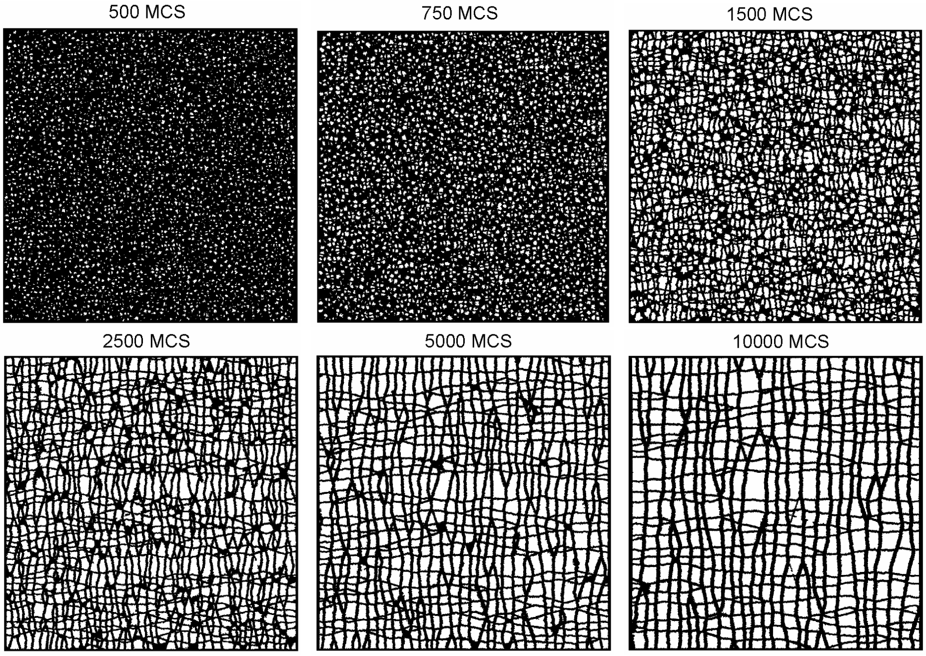

Figure 8.5: The architectural development of trabecular bone for several time. The initially random configuration of bone mass is quickly transformed into a network of trabeculae that are preferentially oriented in vertical and horizontal directions ($\approx$ 1500 MCS). This network then starts to coarsen, i.e. the number of trabeculae is decreasing, while the width of the remaining trabeculae is increasing at constant bone volume fraction.

mineralization of each bone element. Since osteoblasts deposit unmineralized collagen which afterwards starts to mineralise, young bone is less mineralised and accordingly softer than older bone. Figure 8.8 shows such an outcome for a standard simulation run. The age map shows different remarkable properties: first, it shows the points of pronounced activity. These are the locations in the sample, where two or more trabeculae meet and therefore form an imperfection in the structure. These spots are the locations of elevated turnover to eliminate these defects from the system. Second, this elevated turnover may result in trabeculae that completely consist of new material and therefore appear completely red (see the inset in Figure 8.8). But these trabeculae are definitely not newly formed, they are just drifting by deposition of new material on one side and subsequent resorption on the other side. Third, most trabeculae consist of an inner shell of older bone coated by a layer of young bone on their surface. A situation that is not too surprising, since bone deposition and resorption are only performed on the bone's surface, it is to be expected that the interfaces are the areas of pronounced activity.

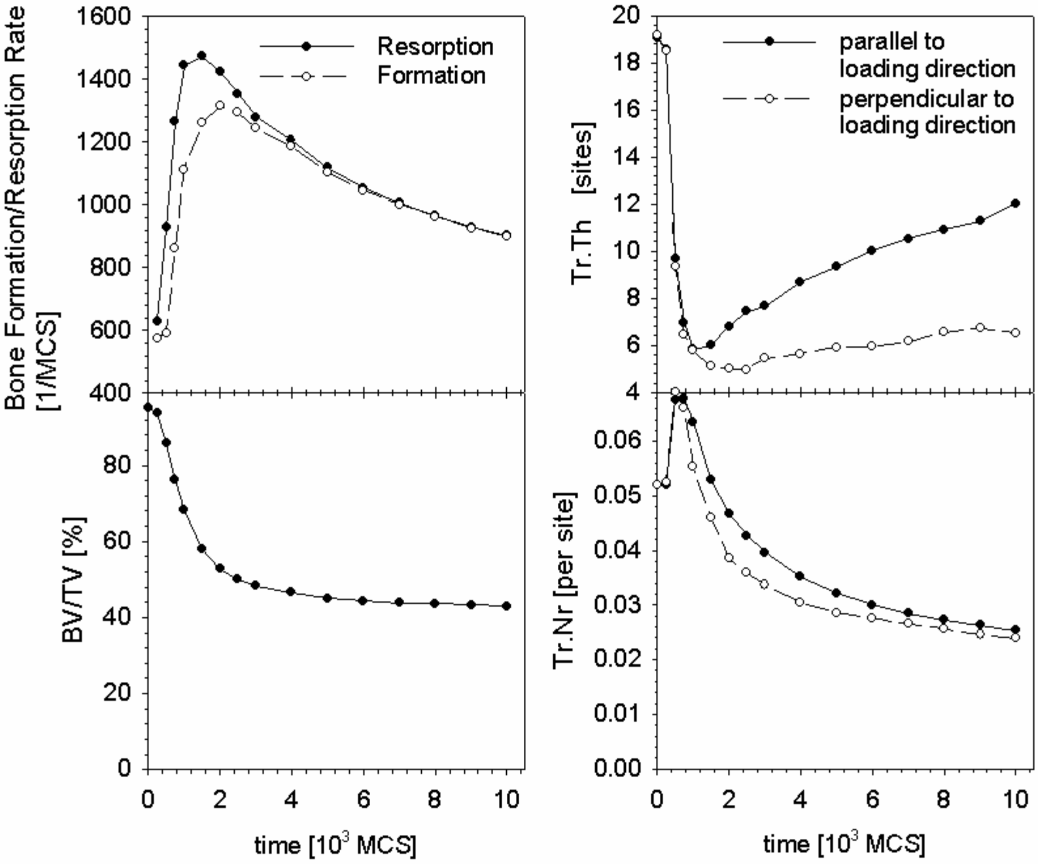

Figure 8.6: The time development of the most important histomorphometrical parameters (the corresponding architecture can be seen in Figure 8.5). Starting from bottom-left in clockwise order the bone volume fraction, resorption/deposition rates, the mean trabecular thickness and mean trabecular number, respectively, can be seen.

Further investigations of the 2-D model concerning e.g. the description of the coarsening process by a power law or the global effective mechanical properties of the whole vertebra can be found in the publications at the end of this thesis Weinkamer et al. [2004b, 2005].

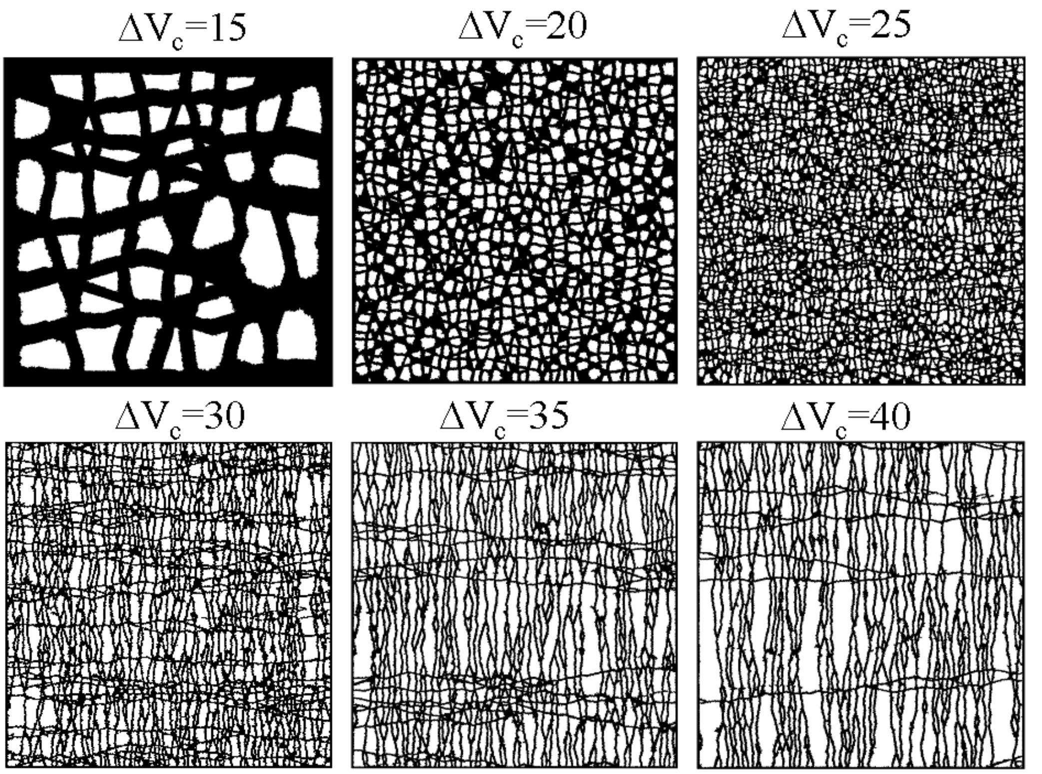

Figure 8.7: The evolving architectures for different values of the critical volume change ΔV_c. The increased bone mass with lower values of ΔV_c is visible, whereas a fine structured trabecular mesh can only be observed for values of the critical volume change close to 25. With exception of the snapshots for very low ΔV_c (15 and 20, respectively) all pictures were taken at a time of 1500 MCS. Since the increased deposition probability of new bone material for low values of ΔV_c increases the time constant to obtain a significant trabecular pattern the snapshot for $\Delta V_c = 15$ was taken at 10000 MCS and for $\Delta V_c = 20$ at 2500 MCS, respectively.

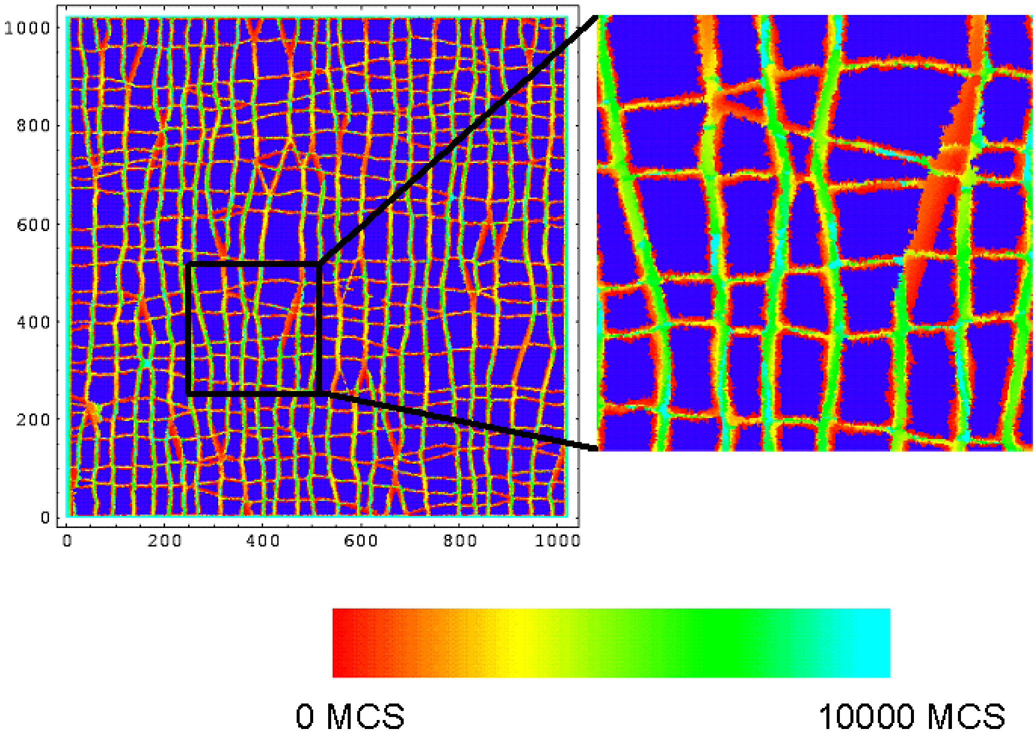

Figure 8.8: The age map of bone elements, where young bone corresponds to a red colour code, old bone is shown in cyan. The inset shows a magnification of the depicted area.

8.2 Simulations on 3-dimensional lattices

After testing the simulation program in 2-dimensional systems the algorithm was generalised to 3-dimensional geometries to perform more realistic simulations. By implementing different RLs and studying the effect on the architectural development of bone it was the aim to shed further light on the governing principles of the remodelling process in bone.

8.2.1 Simulations with one and the same net remodelling law

It was investigated in which way the outcome of a simulation may vary if one and the same net RL was composed by different choices in osteoblastic and osteoclastic response. This dependence on the single cell's responses and not only on their combined action is a feature that distinguishes the presented stochastic simulations from simulations with deterministic rate equations. As the simplest ansatz for a RL a linear law was chosen, that could be made of the entries 1, 2 and 3 from Figure 7.5. The three choices for osteoblastic and osteoclastic response were motivated by the following considerations. In RL 1 a linear response of the bone forming cells and a constant response of the bone resorbing cells are assumed. A linear response to the stimulus is the simplest possible ansatz one can think of to describe the cells' reaction to the stimulus. A constant bone resorption probability assumes that the osteoclasts are sensitive to microdamage which is homogenously distributed. In RL 2 both the osteoblasts and -clasts are sensitive to the stimulus: Bone is deposited where needed (linear increase in the deposition probability with higher stimulus) and resorbed where not needed (linear decrease in resorption probability with higher stimulus). RL 3 assumes that the turnover is strongly enhanced by the presence of microdamage in the sample. Different from RL 1 it is now assumed that microdamage is not distributed randomly in the sample, but that microdamage occurs at locations of high mechanical strain, i.e. at locations with high stimulus. To repeat, all three laws were chosen such that the difference in osteoblastic and osteoclastic response, i.e. the net RL, always resulted in exactly the same function (see Chapter *Simulation Parameters* at the end of this part for a detailed description of the used functions).

Figure 8.9 shows the architecture of the simulated structures using these three different RLs. The differences in architecture are visible at first sight, as well as the differences in histomorphometric parameters (see Figure 8.10).

Several aspects are striking: first, while RL 1 and RL 3 lead to almost

Figure 8.9: The evolving trabecular architecture for different RLs chosen. RL 1 (left), RL 2 (middle) and RL 3 (right) – all snapshots taken at 2000 MCS

the same steady state bone mass, the remodelling process using RL 2 gives a much higher bone volume fraction. Second, the remodelling process according to RL 2 is characterized by a very high turnover, which is a factor $2 - 3$ higher than in the other two simulations. Third, the trabecular architecture, described by trabecular number and trabecular area, is different for all three RLs. The trabecular area is lowest for RL 2 and highest for RL 3, while the opposite is true for the trabecular number. The architecture achieved by RL 1 gives intermediate values. The figures also show that the anisotropy between horizontal and vertical directions in one simulation run are much smaller than the differences due to different RLs.

How can one understand these differences? RL 2, where there is both a linear increase in bone deposition probability and a linear decrease in bone resorption probability with increasing stimulus, shows the most obvious differences. The large bone mass as well as the increased turnover show a remarkable difference to all other simulations. A closer look at the bone volume fraction shows another difference to the other simulations. While in the simulations done with RL 1 and 3, respectively, almost all of the occupied sites are also active, this is not the case for RL 2 – almost 15 % of the occupied sites are not active in this case and are therefore not contributing to the load transfer in the system. This is due to one property of the remodelling law that distinguishes it from all the other laws used. In RL 2 there is a finite probability for bone deposition even at zero values for the stimulus. This gives the possibility for growing trabeculae perpendicular to the main loading direction, which is not possible when the bone formation probability is zero at zero stimulus. This additional trabecular growth can be seen in Figure 8.9 (middle). By choosing the deposition probability zero at zero

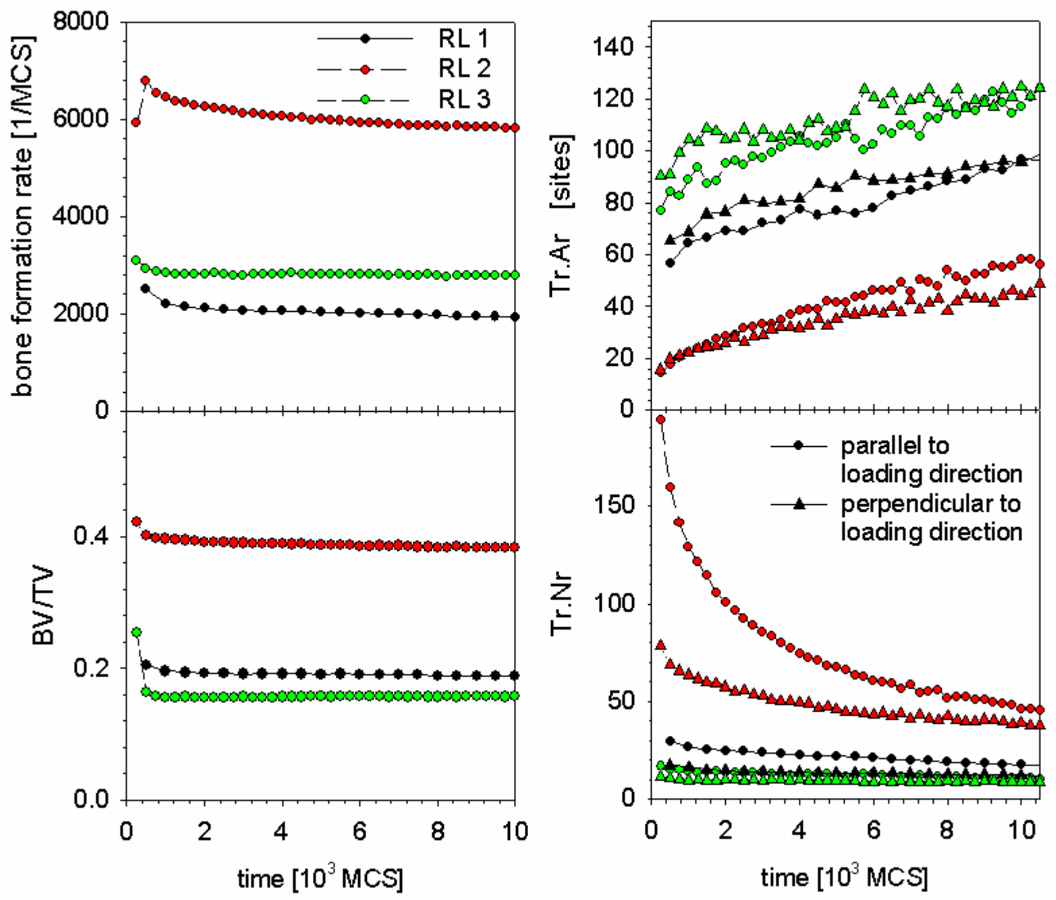

Figure 8.10: Histomorphometric data corresponding to the simulations with different remodelling laws. Colours indicate different RLs (black—RL 1, red—RL 2 and green—RL 3, respectively), symbols indicate the directional dependence of the data (circles—parallel to loading direction and triangles—perpendicular to loading direction).

stimulus the trabeculae are forced to exhibit smoother surfaces, the lying down of a new bone package is only possible if at least one of the nearest neighbours is active, i.e. load bearing. This prevents the unregulated growth of bone that is not load bearing.

To see if this explanation is correct, another simulation run was started, with a RL close to RL 2 but slightly changed in the vicinity of the origin. Once again the formation and resorption probabilities were chosen such that the same net RL was given. For values of the stimulus greater than 10 RL 2 was used to calculate the probabilities, but below a value of 10 for the stimulus the osteoblastic probability was set to zero. The resulting functions can be seen in Figure 8.11. The simulation runs according to this RL showed

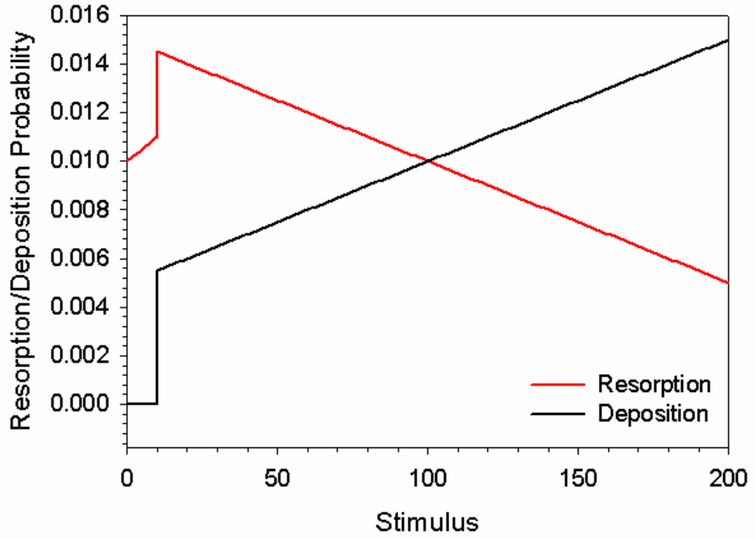

Figure 8.11: A slightly modified RL, to make the deposition probability start from zero.

that the amount of occupied but non-active elements as well as the total bone mass decreased significantly. The fraction of active elements to the occupied ones changes from about 65 % to 90 %, while the total bone mass still remains a bit higher than in the simulations using RL 1 and RL 3.

But there also differences between RL 1 and RL 3. These differences can not be seen in the steady state bone volume fraction, but the architecture is different. RL 1 exhibits a lower trabecular area and a higher trabecular number than remodelling RL 3. This effect is explained by the jump in formation/deposition probabilities in RL 3. The main part of this effect may be explained by the bone resorption probability. Only trabeculae that are very thin experience a stimulus that boost the remodelling activity. With the higher resorption probability the chance of perforating these thin trabeculae rises and since trabeculae never come back, i.e. once gone they are lost forever, the speeding up of the coarsening can be explained.

These experiments show clearly that slight deviations in the bone formation and resorption probabilities – even if they occur only at a very limited range of the stimulus as e.g. in the case of the modified Law 2 – can have pronounced effects on the resulting architecture of trabecular bone. One and the same net remodelling law may create trabecular patterns that differ significantly in architecture and bone mass.

After investigation of different realisations of linear RLs, two realisations of Frost's RL were implemented. The main feature of Frost's RL – the lazy zone, i.e. a region with no net remodelling –, may be realised by two fundamentally different choices of osteoblastic and osteoclastic response (see RL 6 and 7 in Figure 7.6). While in RL 6 there is a region in which bone deposition and resorption are equal, but different from zero, in RL 7 there is a region in which bone deposition and resorption probabilities are both set to zero. As in the investigations of the linear RL deposition and resorption probabilities were carefully chosen to make them result in exactly the same net RL. Also for the case of Frost's remodelling the consequences for the remodelling process are completely different. While in RL 6 the stochastic nature of the remodelling process as it was introduced in the presented simulation scheme is present at all values of the stimulus and leads to the already known phenomena from previous simulations, like coarsening of the structure, this stochastic element is eliminated in the simulations with RL 7. Trabeculae that experience a stimulus larger than the lazy zone, i.e. trabeculae that are too thin, are going to be thickened until the stimulus is decreased to the upper limit of the lazy zone. Then the remodelling process is going to stop, since bone deposition and resorption probabilities are exactly zero at this point. The same argument holds for trabeculae that are too thick, i.e. their stimulus is too low and lies below the lazy zone. These trabeculae are going to be thinned by successive resorption events until their stimulus reaches the lower limit of the lazy zone. Then resorption and deposition probability are once again both zero and the remodelling process comes to an end. Trabeculae with stimuli located in the lazy zone from beginning are not remodelled at all. Since the remodelling process comes to an end for all trabeculae also the coarsening process does not take place and the system reaches a state that is sometimes called homeostasis: the system reaches a stable equilibrium and the structure does not evolve anymore. This is confirmed by the measured formation/deposition rates in the system, both tend to zero (for late stages only 1.5 remodelling events are counted per MCS, whereas more than 1700 events are counted for RL 6). Such a state is the final state in simulations without stochastic event where bone loss and gain, respectively, are described by deterministic rate equations, e.g. Huiskes et al. [2000], or in Cowin's adaptive elasticity model Cowin [1993]. The inhibitation of coarsening is reflected in the trabecular number and area, respectively. For RL 7 the trabecular number is a factor 3 to 10 higher than for corresponding simulations with RL 6, while the trabecular area is correspondingly smaller.

8.2.2 Simulations with different types of remodelling laws

After comparing simulations that were done with one and the same net RL, investigations were done to compare different types of RLs, namely linear, step like and Frost RLs (RLs 1, 4 and 6 in Figures 7.5 and 7.6). A typical architectural snapshot for these three runs can be seen in Figure 8.12, the corresponding standard histomorphometric parameters can be seen in Figure 8.13. The used remodelling parameters can be found at the end of this part in the chapter *Simulation Parameters*. The snapshots show a different architecture for all three RLs. Most prominent the structure obtained by a step like RL, exhibits more sharp surfaces than in both the other calculations, the surface for the Frost RL is the roughest.

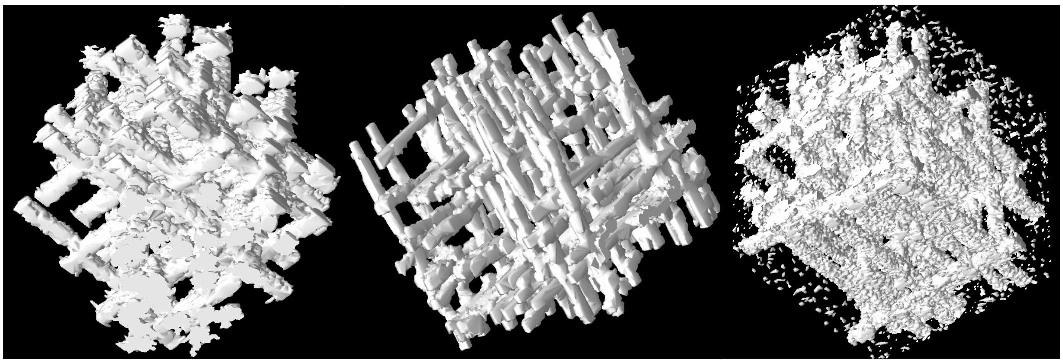

Figure 8.12: The figure shows typical architectural snapshots obtained by three different types of RLs: linear (left—2000 MCS), step like (middle—1000 MCS) and Frost (right—2000 MCS). The parameters of the used RLs may be found in the chapter *Simulation Parameters* at the end of this part.

Also the histomorphometric parameters show pronounced differences. Although the simulations parameters were chosen to result in a similar bone volume fraction and also the coarsening process is clearly visible for all three simulations, the base line of trabecular area and number differed significantly. As expected trabecular number and area are related indirectly: a low trabecular area, is accompanied by high trabecular numbers (RL 4), while the other is true for high trabecular areas (RL 1 and 6).

This different behaviour of the different RLs can also be seen in the trabecular thickness distribution (see Figure 8.14). The peak of the distribution is shifted to smaller values for the step RL, whereas both the linear and Frost remodelling show thicker trabeculae.

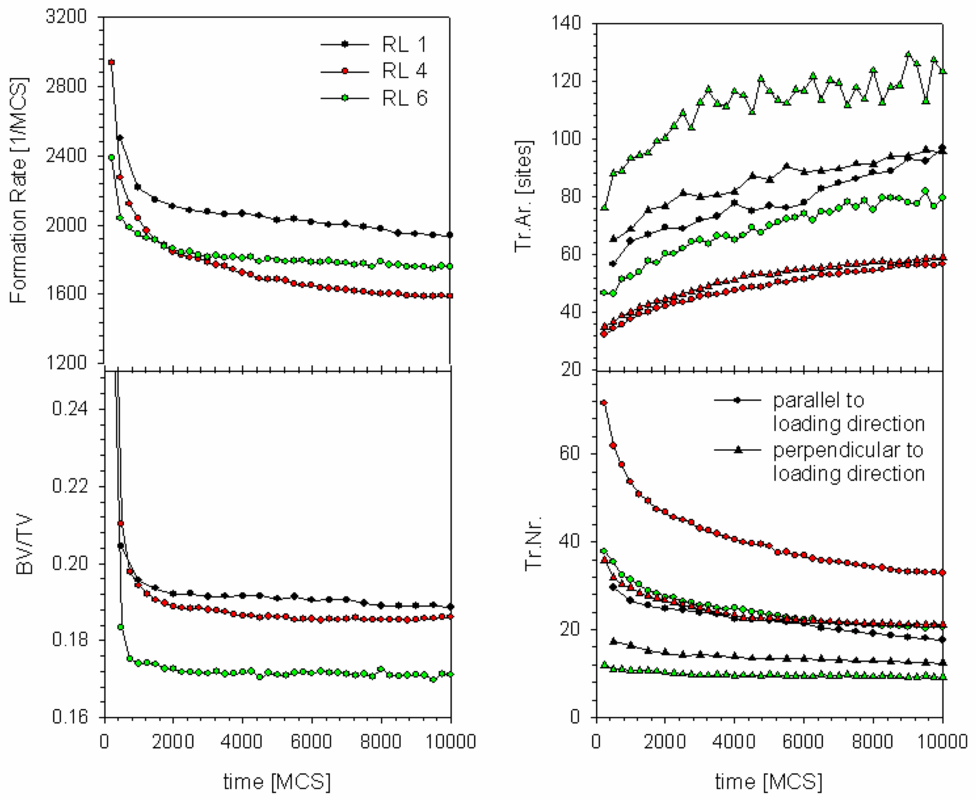

Figure 8.13: The figure shows the evolution of the standard histomorphometric parameters for the three investigated RLs.

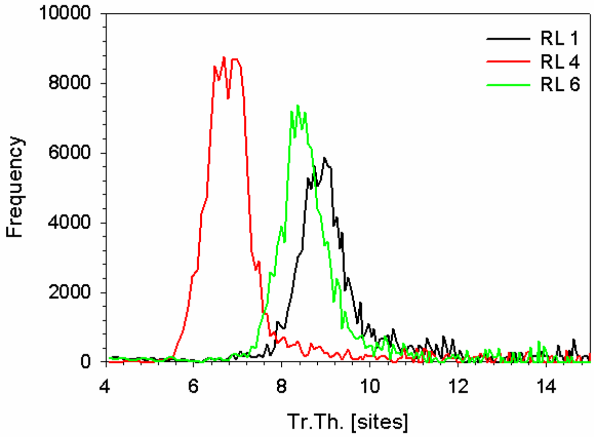

Figure 8.14: The trabecular thickness distribution for the three investigated RLs.

Chapter 9

Interpretation

The remodelling process in trabecular bone was studied by implementation of different (hypothetical) RLs, i.e. the response of bone resorbing and depositing cells to the value of a given local mechanical stimulus. One of the most striking features for all the simulations was the emergence of a favoured time direction. All the simulations showed a coarsening of the structure, i.e. a decrease in trabecular number and an increase in trabecular thickness with time. This stems from a special property of the simulation process: because of the stochastic nature of the remodelling process, the thickness of a given trabecula is fluctuating in time. If it gets too thick – no problem – it will decrease its width in the following iteration steps, but on the other hand if it gets so thin, that the trabecula is perforated the stimulus is lost and it will be resorbed. More exact, trabeculae can only be lost, but they can not be newly formed. This asymmetry naturally leads to a loss of trabeculae, which is compensated by a thickening of the remaining trabeculae since the bone volume fraction is constant.

Moreover, the coarsening process is a very slow process. Since it is known that a complete turnover in real bone takes around 4 years, it is possible to transform the computational time scale of MCS in a real time. For the 2-dimensional simulations 1000 MCS are equivalent to 10 years, for the 3-dimensional calculations 1000 MCS are equivalent to approximately 20 years. These numbers are valid for the standard simulation runs (parameters can be found in the *Simulation Parameters* chapter), changed parameters, especially a changed resorption probability, will of course alter this conversion factor. This estimation of the real time of the investigated process shows, first, that the presented simulation scheme is capable of determining the evolution of bone for a human life time and beyond and, second, that the time scales of the involved processes, like coarsening, correspond well to the time scales real bone experiences during a human life span.

9.1 (Indirect) coupling of formation and resorption rates—BMUs

Another feature of the model is the coupling of bone formation and resorption rate. A prominent model of bone remodelling is to divide osteoblasts and osteoclasts in so called basic multicellular units (BMUs), which are assumed to be strictly coupled, so that after a bone resorption event subsequent filling in of the cavities occurs Eriksen [1986]. On the contrary the simulations presented in this thesis as well as other computational approaches Huiskes et al. [2000] show that a purely mechanical coupling suffices to describe the observed effects. The emergence of a steady state bone mass clearly shows that bone formation and resorption rate have to compensate, furthermore if the resorption probability is suddenly raised the deposition rate almost instantaneous follows, which can be seen in Figure 9.1. In a simulation run the resorption probability was instantaneous raised from its standard value of 0.007 to 0.01. The deposition rate follows almost immediately, although no direct coupling between the cells was assumed. The increased resorption probability leads to a stronger thinning of the trabeculae, which then of course experience a higher load, i.e. a higher stimulus. This in turn leads to the elevated deposition rate.

9.2 Stochastic remodelling with the same net remodelling law

The investigations on the same net RL showed that the outcome of the simulations depended crucially on how this net law was composed. This is a remarkable difference to simulations with deterministic rate equations, where only the difference in bone deposition and resorption rates are of interest. Furthermore the description of the remodelling process with resorption and deposition probabilities leads in general to a continuous change in architecture, i.e. a coarsening process, that does not arise in deterministic calculations, where once the structure has reached its final configuration, i.e. the local stimulus takes the value of its set point in each point in the sample (or at least in each point of the bone surface if surface remodelling is assumed), no further change in architecture takes place: the system is in homeostasis. But in contrast to these simulations such a homeostatic state has not yet been reported in literature, on the contrary all performed experiments suggest a continuous change in bone's architectural parameters, some experiments even claim to have observed a coarsening process in real bone

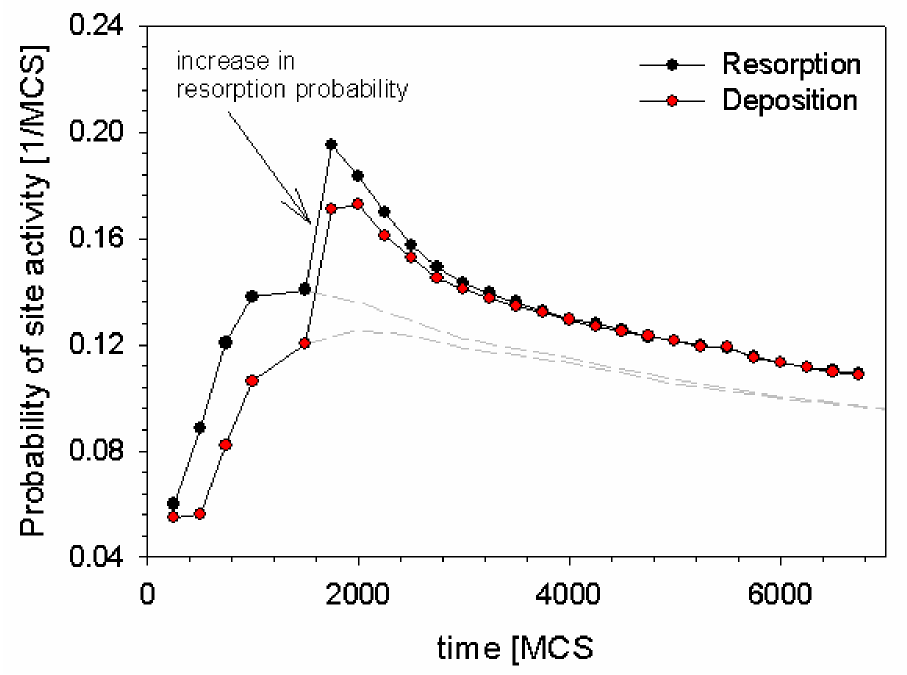

Figure 9.1: The instantaneous rise of the resorption probability (1500 MCS) leads to an almost simultaneous increase in the formation rate. The normal evolution of the resorption/deposition rates without the instantaneous increase in resorption probability is depicted by the grey-dashed lines.

Frost [1999].

The observation that the remodelling process does not only depend on the net RL, but also on the two functions it is composed of, poses the problem to formulate these two functions. As shown there are many different probabilities to compose one and the same net RL out of different responses for bone deposition and resorption. Instead of describing the problem with one linear function that is characterized by two parameters (its slope k and intercept d) several new parameters may enter the problem. In Figure 7.5 $1-3$ only some suggestions are listed of how such a combination may result in the same net RL. The variety ranges from a combination of linear and constant functions over two linear functions to functions that even are discontinuous. The architecture of the sample differs significantly on the type of RLs chosen. Some of the aspects can be understood easily, others prove to be more subtle. Although the RLs presented in this thesis are fundamental functions, the actual deposition/resorption probabilities prove to be much more complicated. The actual probability for a bone deposition/resorption event is the product of finding a proper place, i.e. a place on bone's surface, with the probability given by the RL evaluated at this special place. That is why not only the RL itself, but also the geometry it creates, has a tremendous effect on the remodelling process, e.g. the average number of active neighbours of a given surface site is of crucial importance (but of course the RL is the only determining parameter, since the geometry is itself determined in a non-trivial manner by the RL).

By choosing RL 1 from Figure 7.5 as reference the simulations showed that the simulations results achieved by RL 3 do not significantly differ in bone mass, but that the coarsening process, i.e. the loss of thin trabeculae and the simultaneous thickening of thicker trabeculae to account for the loss of bone material, proceeds much faster. This can be understood by the increase in remodelling activity for higher values of the stimulus: in regions with a higher stimulus, i.e. thin trabeculae, the turnover is significantly increased, which in turn increases the perforation probability for these highly stressed trabeculae. This is the reason for the speeding up of the coarsening process, which reflects itself in the decreased trabecular number and increased trabecular thickness in these simulations (see Figures 8.6 and 8.10).

Simulations with RL 2 show other remarkable differences: first the steady state bone mass exceeds by far the steady state bone mass from simulations done with RL 1. A closer look shows that a significant fraction of the occupied sites are not active, i.e. they are not load bearing, while in all other simulations almost all of the occupied elements are load bearing as well. This difference stems from the fact that in RL 2 there is a finite probability for bone deposition even at zero stimulus. Although the resorption probability is even higher this leaves a finite probability for the growth of trabeculae perpendicular to the loading direction which is not possible in RLs with zero deposition probability at zero values of the stimulus. This increased bone mass and non-targeted growth can clearly be seen in the architectural snapshot (see Figure 8.9), furthermore the histomorphometric parameters show that the number of trabeculae significantly increased (which is due to the unregulated growth of non-load bearing elements), while their average area decreased.

9.3 Stochastic remodelling with different types of remodelling laws

Furthermore three different types of RLs were investigated: linear RLs, step-like RLs and Frost's RLs (see Figure 7.5 and 7.6). One striking difference in these three types of RLs is their degree of control of the structure. The most rigid control is realised by step-like RLs, the most flexible control by RLs with a lazy zone, i.e. RLs motivated by the mechanostat concept introduced by H. Frost. The degree of control is best explained with the concept of the set point of the system (see Figure 9.2): in all RLs chosen there is an intersection point

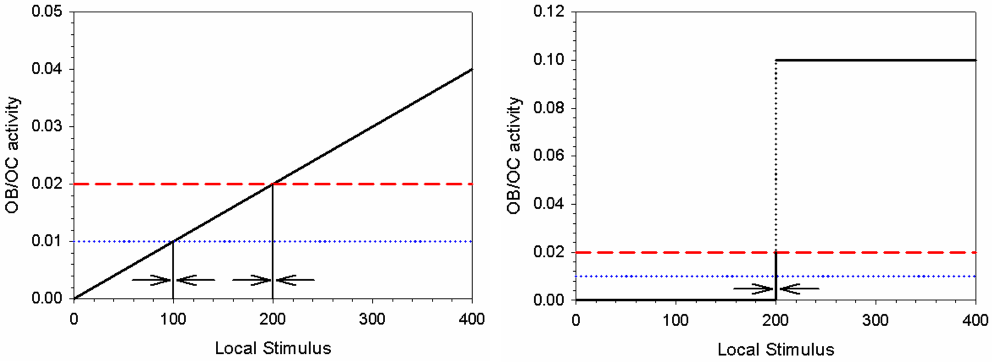

Figure 9.2: The figure shows that the set point, i.e. the intersection point of resorption (red dashed and blue dotted lines, respectively) and deposition (solid black line) probability with respect to the stimulus changes with a changed resorption probability in the case of a linear RL (left), but stays constant for a step-like RL (right).

of deposition and resorption probability with respect to the stimulus. Below this point there is more resorption than deposition, which tends to increase the stimulus, above this point there is more deposition than resorption and the stimulus is accordingly lowered. So the regulatory process tends to drive the system in a state where all elements experience this special value of the stimulus. This point is the *set point* of the control. In the case of a linear RL the difference in resorption and formation probabilities is very small in the vicinity of the set point, therefore pronounced fluctuations around this point are possible, i.e. the system is not very rigidly controlled. On contrary for step like remodelling the difference in resorption and deposition probabilities always takes a finite value (greater than zero), i.e. fluctuations are suppressed and the system is strongly controlled. For Frost's RL the singular set point is displaced by an extended region where the formation and deposition probabilities take the same value, i.e. in this entire region there is no control at all, thus the system is very loosely controlled. The degree of control is reflected by the steady state strain distribution for the three investigated cases (see Figure 9.3). The narrowing of the distribution for the step like RL shows the more rigid control in this case. Since the strain also serves as the mechanical stimulus, i.e. the control variable, the bone elements are forced in a narrower strain distribution than for the other two RLs. As expected the distribution is broadest for the Frost RL, where

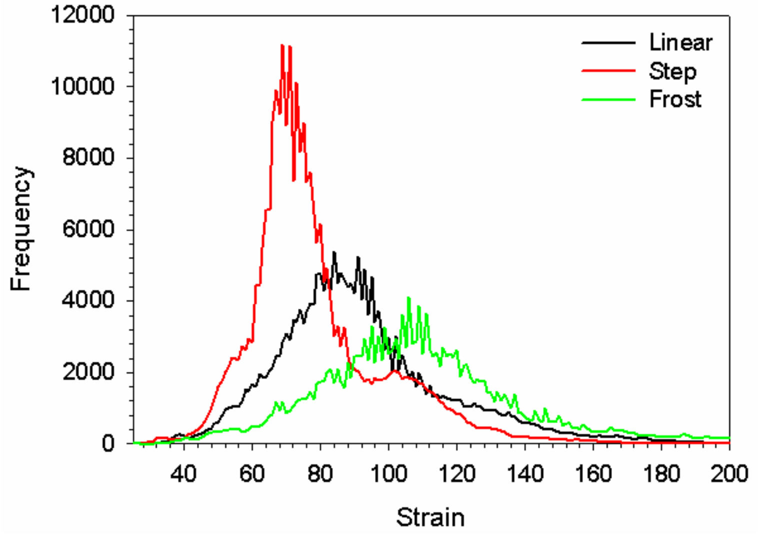

Figure 9.3: The steady state strain distribution for the three RLs investigated: linear (black) with a set point of 100, step (red) with a set point of 200 and Frost (green) with a lazy zone in a stimulus region from 100 to 150.

the lazy zone realises a region with absolutely no control at all.

Another feature of these distributions is the shift of the peak to higher strain values for linear and Frost RLs. This effect stems from a subtle effect of the regulatory system. The stimulus for bone resorption/deposition is the sum of the strains of the neighbouring lattice sites. The very rigid control of the step RL tends to produce very smooth trabecular surfaces, since the deposition probability for new bone is exactly zero, when the trabecular width exceeds a given value. This means that most of the elements at the surface – and that are therefore prone to the action of osteoblasts and osteoclasts, respectively – have got at least three active neighbours. The peak strains in the distribution show that on average three neighbours suffice to reach the set point of 200. In the case of the more flexible control for linear and Frost RLs the same does not hold. The bone surfaces tend to be much more rough than in the case of step remodelling, which means that very often the bone elements do only have one active neighbour, which has to give the set point of 100 in this case. The even greater shift to larger strain values for Frost remodelling is due to the fact that the lazy zone was chosen to be in the region between 100 and 150 units of the stimulus.

9.4 The reaction of the system to perturbations

An additional interesting feature is the reaction of the system to perturbations, e.g. a changed turnover rate due to a changed resorption probability. It was investigated in which way systems controlled by Law 1 and Law 4 (see Figure 7.5) differ in their response to a changed turnover, i.e. to different resorption probabilities. The motivation of these experiments is given by medicine since it is possible by special medication (anabolic or anti-resorptive treatment) to act exclusively on one cell type. An anti-resorptive treatment (bisphosphonates) focuses on the osteoclasts and inhibits bone resorption. This treatment is modelled in our system by varying the bone resorption probability and leaving all other parameters unchanged. The two RLs chosen were a step like deposition probability (Law 4) and a linear one (Law 1) – see Figure 7.5. The chosen deposition probabilities are the standard ones, which can be found in the final chapter of this part, while the bone resorption probability was varied over one order of magnitude from 0.01 to 0.001. The different response of the system can be seen in Figure 9.4, where the steady state bone mass is plotted against the inverse resorption probability. The steady state bone mass remains unaltered when a step like deposition probability is chosen (Law 4) and changes drastically when a linear one is chosen (Law 1). This effect can be explained with the behaviour of the set point of the regulatory mechanism for changed osteoclastic responses. For a linear RL the intersection point of formation and resorption probability changes with new values of the resorption probability, accordingly does the set point (see Figure 9.2). The same does not hold for a step-like formation probability, there the set point remains unchanged for every resorption probability (as long as the resorption probability is chosen smaller than the height of the step). Since the set point determines the strain distribution in the system and this distribution is strongly influenced by the bone mass, it is evident that a changed set point will have profound effects on the steady state bone mass, while a fixed set point will not result in these deviations.

Although the set point concept is able to explain the differences in behaviour of the systems to perturbations for different types of RLs (especially linear and step like RLs), one should be aware that due to the coupling of geometry and remodelling inherent in the model this is not the entire truth. As described previously simulations with one and the same net RL, thus also with the same set point, may develop completely different bone volume fractions. Furthermore, one and the same set point may not correspond to the same value of the bone volume fraction for different types of RLs. More exact, the set point for the simulations done with the linear RL 1 was 100, while it was 200 for simulations with the step like RL 4. Despite that difference in

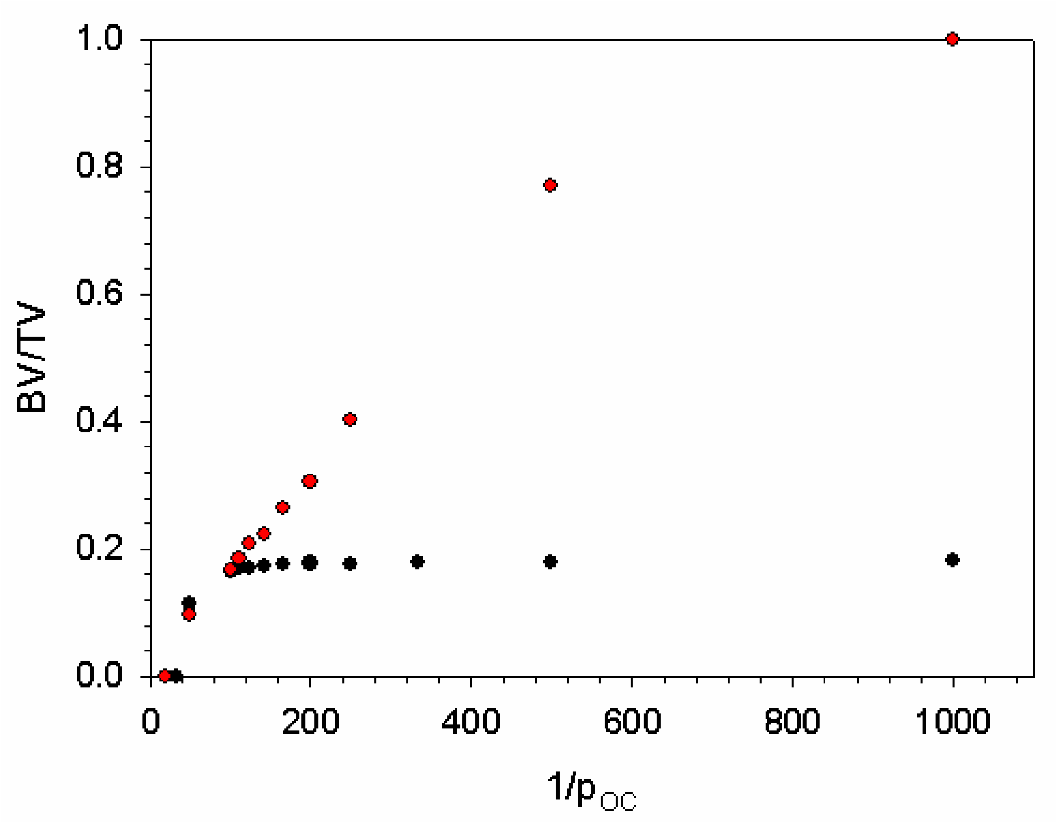

Figure 9.4: The figure shows the steady state bone mass as a function of the inverse resorption probability, i.e. the turnover rate. Two different deposition probabilities were chosen: step like (black dots) and linear (red dots). While the bone mass stays unaffected by the turnover rate for the step like remodelling law, it changes drastically in the linear case.

the set point the bone volume fraction is comparable for both simulation runs (as can be seen in Figure 8.13). As already mentioned this effect stems from geometrical influences: the effective probability for a remodelling event is not solely given by the RL, but by the product of the resorption/deposition probability and the probability of finding a proper place for resorption/deposition (i.e. the OC/OB surface). Another influence is given by the average number of active neighbours for any active element.

9.5 Speculations on the remodelling law governing the evolution of real bone

The presented observations give additional information on the regulatory system in real bone: since there are no experimental observations that trabeculae may grow perpendicular to the loading direction, it seems reasonable to assume that the bone deposition probability is zero at zero stimulus – or at least very small. Furthermore clinical studies showed that antiresorptive treatment of postmenopausal osteoporosis, i.e. the resorption of bone is prevented by hindering the osteoclasts from doing their job, resulted only in a slightly increased bone mass ($10-15$ %) Pérez-López [2004], Weinstein et al. [2003]. Comparing these experimental facts with the results from the presented simulations, it seems reasonable to assume that the RL governing real bone's evolution is neither a linear relation between stimulus and response of the cells nor a RL with a lazy zone (the repression of bone resorption would have an even stronger effect on the set point than for a linear RL, since an entire non-regulated region would collapse to a single point), but rather a step-like response. Even if a real step is most probably not realised in a biological system, it seems reasonable to assume that there is a small region in the stimulus where the response of the cells changes rapidly and shows strong non-linear behaviour, i.e. there exists some kind of activation threshold.

9.6 Bone diseases—Osteoporosis

Another aim of the presented simulation scheme is to come to a better understanding of diseases that may arise due to a failure in the regulation mechanism controlling bone remodelling. In the presented model such a failure in the regulation process would manifest itself in a change of the RL, i.e. in a change of the functional dependence of the cells response to the given stimuli. In life such a change my be caused by hormonal changes, as they occur e.g. during menopause. As stated before the regulatory mechanism of bone is strongly interconnected with sexual hormones so menopause has a tremendous effect on bone evolution. It is well reported that the onset of menopause is accompanied by a strong enhancement of bone turnover – most probable caused by a strong increase in bone resorption – which leads to a severe loss of bone mass accompanied by a strong alteration of bone's architecture. As a result the quality of bone may rapidly decrease, an effect that is called postmenopausal osteoporosis and that poses an ever rising risk to modern societies. Due to the rapid increase in life expectancy more and more people are facing severe problems corresponding to the decreased quality of their bones, e.g. increased fracture risk or even non-traumatical fractures (especially of the hip and the vertebras). Women are especially affected, but also men suffer from this disease. It is estimated that 30 % of postmenopausal white women in the US suffer from osteoporosis, which rises to 70 % for women over the age of 80. The corresponding costs for the health care system are $13.8 billion per year Ray et al. [1997]. In Germany each year $3.5 - 4$ million hospital days are accounted for by osteoporosis, the direct costs of this illness are estimated by DM 3.7 billion (≈ 1.9 billion Euro) Brecht and Schädlich [2000].

The ultimate reason for postmenopausal osteoporosis has not been found until now, but since several studies show that this disease is accompanied by a strong increase in turnover it seems reasonable to attribute (postmenopausal) osteoporosis to a failure in the regulation mechanism controlling bone remodelling Lanyon and Skerry [2001]. By an alteration of the RL in our simulations a situation comparable to the stage of menopause may be created in the computer and the effect on bone's architecture can be studied. These investigations will give more insights in the reasons for osteoporosis, e.g. if it is reasonable to attribute postmenopausal osteoporosis to a change in the feedback system and what might be the best strategy to treat this disease.

Since due the discussion of the last paragraph a RL with an activation threshold seems to be most probable candidate for the RL in real bone, the discussion of osteoporosis is based on the 2-dimensional simulations done with RL 5.

In terms of bone architecture postmenopausal osteoporosis is often described by, first, a reduced bone mass and, second, by a coarser structure and higher anisotropy in trabecular architecture. In Figure 9.5 the outcome of a simulation run compared with an inset from sections through a real vertebra can be seen: young-healthy (left) and old-osteoporotic (right). The top row of the architectural snapshots shows the normal ageing process of bone with no changes of the remodelling law with age ($\Delta V_c = 25$). As can be seen some architectural features attributed to osteoporosis can already be found by such a normal, i.e. non-pathological ageing process. Especially the coarsening of the structure is striking. The low row of the figure shows the architectural evolution for a system with a slightly changed remodelling law ($\Delta V_c = 30$). As can be seen such a slight change in the activation threshold can have severe effects on the architecture, by accelerating the coarsening of the structure. Even worse, the shift of the activation threshold also leads to a reduction of the bone mass, compared to a normal ageing process.

Another question arising in the treatment of osteoporosis are the long-term effects of a bisphosphonate treatment, i.e. the inhibitation of bone

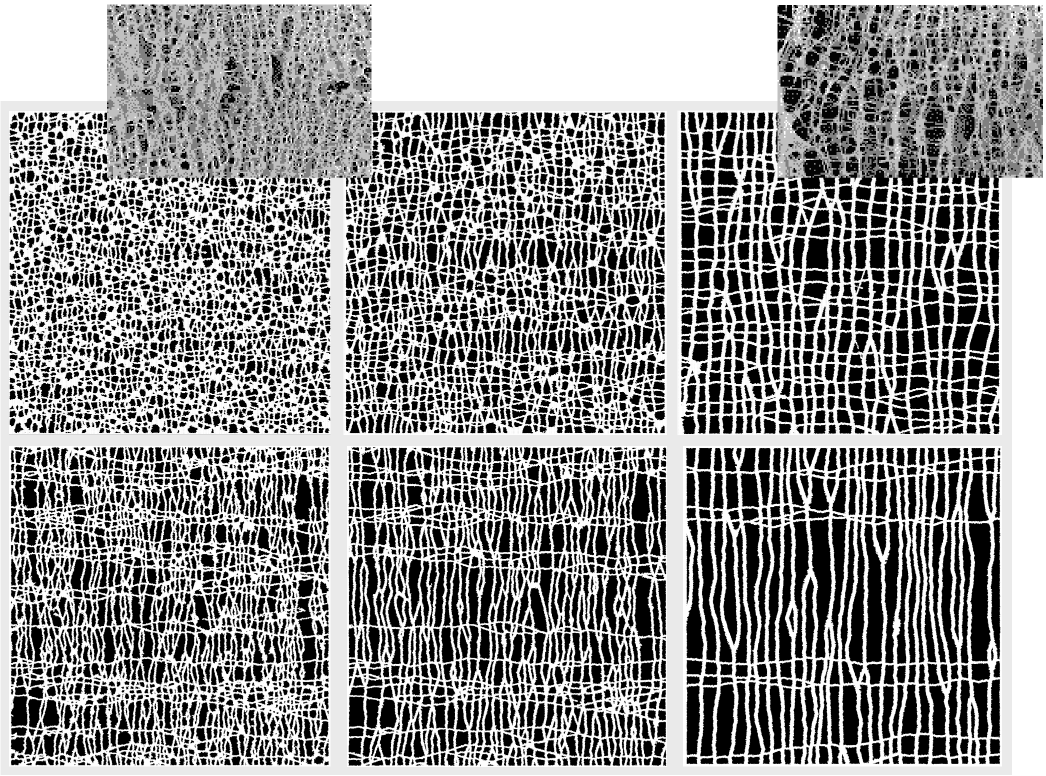

Figure 9.5: In the figure the outcome from simulations done with RL 5 are compared with slices from real bone. The left inset shows young and healthy bone, while the right inset shows old and osteoporotic bone (to give a better comparison to the insets, the simulated structures are shown inversed – white corresponds to bone, black to marrow). The upper row shows a normal ageing process of the structure with no changes in the remodelling law ($\Delta V_c = 25$), whereas the lower row shows the outcome for a remodelling law where the activation threshold was slightly shifted to higher values of the stimulus ($\Delta V_c = 30$). The figure shows that even a normal ageing process results in a coarser architecture, as can also be seen in the insets, by changes in the remodelling law this effect may be strongly enhanced and accelerated.

resorption. Even though this medication proves to be a versatile tool to prevent bone mass loss, the effects on accumulation of microdamage are widely unexplored Nyman et al. [2004]. One of the main reasons for bone remodelling is the removal of microdamage, i.e. small cracks, that develop in the bone matrix. An accumulation of microdamage in a special region of the material may strongly weaken it, thus the material is going to fail at relatively low loads that an undamaged material would easily bear. Since by an inhibitation of the remodelling process bone loses its ability of self-repair, the risk of material failure by fatigue increases with subsequent treatment. In the simulations done in this thesis material failure was not incorporated, but investigation of the age distributions of selected simulations runs, showed that with decreasing resorption probability this distribution shifted to later times, which means the average age of bone elements increased. Since microdamage accumulates with time, the shift to later times can also be seen as a shift to more elevated concentrations of microdamage that weaken the material. Figure 9.6 shows an age map of bone for two different values of the resorption probability ($p_{OC} = 0.007$ and 0.01, respectively). Both simulation runs were starting from the same configuration, i.e. the evolution of the structure is easily comparable. The figure clearly shows that the amount of older bone

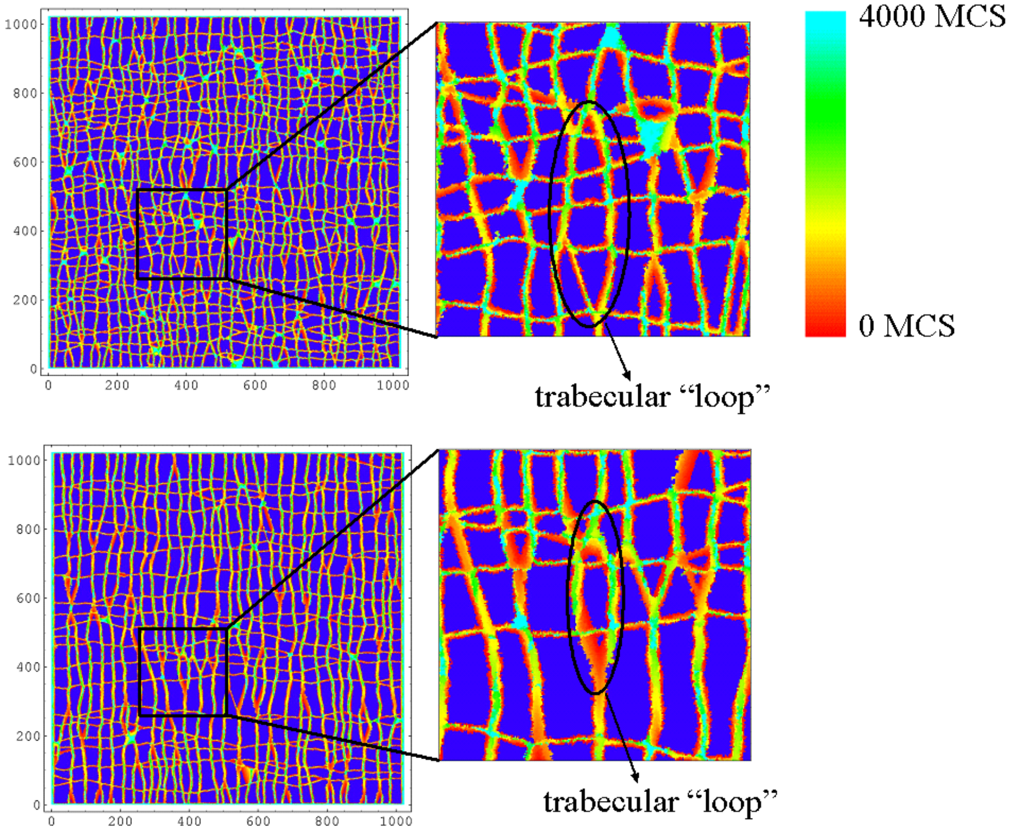

Figure 9.6: The figure shows the age map for two different values of the turnover. Starting from the same configuration the results are shown for a resorption probability of 0.007 (top) and 0.01 (bottom).

(cyan) decreases significantly with a higher turnover. On the other hand this is equivalent to an increased concentration of microdamage for lower turnovers. Furthermore the elevated coarsening velocity for higher turnover can be seen. First, the increased thickness of the trabeculae for the higher turnover is visible by comparing the two insets. Second, the trabecular "loop" which can be seen in the middle region of both insets is considerable smaller for the elevated turnover.

Clinically the symptoms of postmenopausal osteoporosis are most often explained by the higher turnover rate accompanying the hormonal changes in menopause. The simulations presented in this thesis suggest that at least two different processes are responsible for the structural changes in bone found in osteoporotic patients Weinkamer et al. [2004b]. First, there is a normal ageing phenomenon that drives the architecture into a coarser, more anisotropic structure. As already explained that favoured time direction is given by the fact that trabeculae can only be lost, but never newly formed. An increased turnover as observed in postmenopausal women is going to fasten this process, the coarsening will proceed faster, but the bone mass is not going to change. Second, a change in the bone mass can not be attributed to a change in resorption probability alone, but has to be attributed to a lower sensitivity of the bone forming osteoblasts. By shifting their activation threshold to higher values of the stimulus, bone mass is going to decrease and the trabeculae will be thinned, which in turn increases the probability of perforation and consequently the loss of trabeculae.

Chapter 10

Conclusion and Outlook - Bone Remodelling

A model to investigate the remodelling process in trabecular bone was presented. In contrast to other computational models the emphasis was not put on a strictly accurate description of the mechanical state of the sample, but rather on a balance in the accuracy of the mechanical and biological description of the problem. A fast, but simple, algorithm to assess the mechanical properties of the system gave the possibility to test and to judge a variety of different biological hypotheses. At the core of the mechanical model is the assumption that thin trabeculae are more stressed than thick trabeculae. A further approximation is neglecting bending forces and moments. The model presented varies in some important points from previous simulations: first, the structure of bone is regarded to be built of several discrete bone packets. There is no need to perform coarse graining procedures to describe trabecular bone as continuum with a given density. Second, osteoblasts and osteoclasts are treated as two distinct entities, both with their own response to a given stimulus. Bone formation and resorption is modelled as a stochastic process, the remodelling law gives the relation of the local stimulus and formation and resorption probabilities, respectively. Third, this stochastic nature of the remodelling process is a further distinction from previous simulations, where often deterministic rate equations – relating the stimulus with the rate of change in bone density – are used to describe the remodelling process.

The simulations showed that in contrast to simulations with deterministic rate equations the net remodelling law does not suffice to describe the remodelling process. One and the same net remodelling law results in a different bone mass and architecture depending on the choice of the responses of bone forming and resorbing cells on the stimulus. Furthermore – although some of the histomorphometric parameters like the bone mass may reach a steady state – an overall homeostatic state is never reached, the structure continuously changes. Most prominent a coarsening process is found, i.e. the trabecular number decreases while the average thickness increases at constant bone volume fraction. This feature can be observed for all used remodelling laws.

Investigating the effect of different types of remodelling laws, conclusions on the remodelling law in real bone were drawn: first, the bone deposition probability is zero – at least very small – for zero stimulus and, second, that a non linear functional dependence of the deposition probability from the stimulus is most likely, i.e. a threshold value of the stimulus has to be exceeded to strongly enhance the deposition of new bone.

Furthermore, common bone disease patterns that are attributed to a failure in the regulatory mechanism of bone development, like (postmenopausal) osteoporosis were mapped on the model. The characteristics of osteoporosis were shown to consist of three distinct parts: first, a natural ageing and coarsening phenomenon, which can not be contributed to a pathological malfunctioning of the regulatory system, second, an acceleration of this natural coarsening process by a highly increased turnover due to hormonal changes during menopause and, third, a loss of bone mass due to a decreased sensitivity of the bone forming osteoblasts by a shift of the activation threshold to higher values of the stimulus.

Future work that has still to be done includes, first, additional investigations on the mechanical model. In the assessment of the mechanical state of the sample the most important assumption is, that thin trabeculae are more stressed than thicker trabeculae. A check of this assumption by the accurate finite element methods is necessary. Furthermore a mechanical rating of the developing structures is still missing. Is the mechanical performance dependent on the chosen RL? If yes, which RL gives the most potent structures? How do the mechanical properties evolve with time? These investigations can either be done by theoretical calculations or by mechanical tests performed on samples that were built with rapid prototyping methods from a structure produced in the computer. Second, it seems feasible to use the model to investigate clinical related topics, like the effects of special treatment of osteoporosis: What are the effects of anabolic treatment and antiresorptive treatment, respectively? Should they be given simultaneously or one after another? In which order? One possible road that might be followed is to define a standard (healthy) simulation run. Starting from this configuration changed physiological conditions, i.e. changed RLs, due to ageing, disease or medical treatment might be imposed and the effects studied. First tests of this kind were already presented in this thesis, but more detailed and extensive studies are necessary to fully exhaust the capabilities of the presented simulation scheme. E.g. the simulations can be made more realistic by describing the loss of bone mass with age with a time dependent activation threshold in the RL.

The most important feature of the model is the description of the remodelling process as a stochastic event, which gives a rich variety of effects not to be found in deterministic calculations. Despite the simplicity of the model (especially in the mechanical description) the results achieved are comparable, since one and the same model was used for all of the simulations. If the remodelling process in bone is really triggered by a mechanical feedback loop – and there are lots of experimental evidence that this is the case – then for the investigations done in this thesis, it should not matter that much, if this stimulus is really the one chosen or if the RL is a function of any other mechanical quantity. The main results of the presented simulations are mostly due to the properties of the RL (linear or discontinuous) which would not change if, e.g. the volume change would be exchanged with the strain-energy density or any other potential stimulus as long as the form of the RL remains unaltered. Of special interest in these investigations were the overall properties of a special chosen remodelling law, not the details of the process. It will not be possible to use the described model to design prostheses or to predict in detail the mechanical and biological consequences of the implantation of such a prostheses or the effect of a special training. The aim was to shed further light on the underlying feedback loop and to distinguish between several possibilities of its realization.

Simulation Parameters

The table below gives the value of the parameters characterising the remodelling laws used for the simulations presented in this thesis:

In this table x denotes the value of the stimulus, i.e. the summed volume changes of the neighbouring elements, with the only exception of Law 5, where x is the volume change of one neighbouring site and the sum runs over nearest neighbours, ΔV_c is the critical volume change, which gives the location of the activation threshold, i.e. the location of the step. H denotes the Heaviside step function, which takes the value zero for negative arguments and one for positive arguments. Law 5 is the RL that was used in the 2-dimensional simulations. All other laws were used for the 3-dimensional simulations.

Other parameters chosen (the same for all simulations) were an external stress of 10 and a coupling constant of $k = 0.9$ and 0.8 for the 2-dimensional and 3-dimensional simulations, respectively.

RL	Formation	Resorption
1	$p_{OB} = 0.0001 \cdot x$	$p_{OC} = 0.01$
2	$p_{OB} = 0.005 + 0.00005 \cdot x$	$p_{OC} = 0.015 - 0.00005 \cdot x$
3	$p_{OB} = \begin{cases} 0.0001 \cdot x & \text{if } x < 125 \\ 0.01 + 0.0001 \cdot x & \text{else} \end{cases}$	$p_{OC} = \begin{cases} 0.01 & \text{if } x < 125 \\ 0.02 & \text{else} \end{cases}$
4	$p_{OB} = \begin{cases} 0.0 & \text{if } x < 200 \\ 0.02 & \text{else} \end{cases}$	$p_{OC} = 0.01$
5	$p_{OB} = 0.003 + 0.1 \sum_{NN} \frac{x}{\Delta V_c} H\left(1 - \frac{x}{\Delta V_c}\right)$	$p_{OC} = 0.007$
6	$p_{OB} = \begin{cases} 0.0001 \cdot x & \text{if } x < 100 \\ 0.01 & \text{if } 100 \leq x \leq 150 \\ 0.0001 \cdot x - 0.005 & \text{else} \end{cases}$	$p_{OC} = 0.01$
7	$p_{OB} = \begin{cases} 0 & \text{if } x < 150 \\ 0.0001 \cdot x - 0.015 & \text{else} \end{cases}$	$p_{OC} = \begin{cases} -0.0001 \cdot x + 0.01 & \text{if } x < 100 \\ 0 & \text{else} \end{cases}$

Table 10.1: The parameters characterising the used RLs. The number in the first column specifies the RL (as they were introduced in Figures 7.5 and 7.6), the second and third column gives the functional dependence of formation and resorption probability, respectively.

Part III

Linear Elastic Networks

Recently describing and understanding self assembly processes in nature has become something like a *hot* topic in basic sciences. Self assembly processes are of tremendous importance in biological system, e.g. the self-assembly of proteins to give their functionality (the self assembly of single collagen molecules to a triple helix as basic building blocks of bone is only one example) or the self-assembly of the bilayer membranes enclosing living cells. Cellular membranes composed of a variety of different lipids and proteins are extremely complicated structures, that is why for a basic understanding of the fundamental properties of these self assembled structures much more simple model structures composed of only few components are investigated.

The building of membranes can be reached by dissolving amphiphilic molecules in water. Amphiphilic molecules consist of two different parts, a hydrophilic (polar, charged) head and a hydrophobic (non-polar, uncharged, fatty) tail. This schizophrenic structure of the molecules leads to a variety of different morphologies, since the hydrophobic tails are shielded from water contact by the hydrophilic heads. The morphologies reach from micelles, vesicles, cylinders to flat membranes. The realised morphology may depend on several parameters like the kind of involved molecules, their composition, their concentration in solution, the temperature, pH-value and so on Israelachvili et al. [1976], Fukuda et al. [1990].

But not only the form of the evolving structures is of interest, also their mechanical properties is the focus of many studies. To describe one of the observed phenomena is the main goal of this part of this thesis. It was found by investigations of membranes composed of oppositely charged head groups that the bending rigidity, i.e. the ability of the membrane to undergo thermal fluctuations, may vary over several orders of magnitude depending on external parameters, like pH value Dubois et al. [2001]. In the next chapter of this thesis a model is given to explain these features and to give a unifying picture of the involved processes.

Chapter 11

The elastic properties of linear elastic networks

To understand the mechanical properties of flat membranes (sheets) composed of two different amphiphiles (A and B) with oppositely charged head groups we propose the following model. The molecules are assumed to occupy a regular, triangular lattice with the two vectors $\mathbf{a} = (1,0)a$ and $\mathbf{b} = (1/2, \sqrt{3}/2)a$ as a basis. Nearest neighbours are supposed to be connected by linear elastic springs characterised by a spring constant k.

11.1 Mechanical equilibrium

The mechanical equilibrium of a configuration is given by the set of the displacements of all atoms that makes the sum of external and internal forces vanish or – equivalently – makes the total energy of the system minimal. Since each atom has 6 neighbours, each atom experiences the force of 6 springs (see Figure 11.1). The force of one spring is given by

$$\mathbf{F} = k|\Delta\mathbf{r}|\mathbf{n} \tag{11.1}$$

where k is the corresponding spring constant, $|\Delta\mathbf{r}| = |\mathbf{r}_2 - \mathbf{r}_1| - |\mathbf{r}_2^0 - \mathbf{r}_1^0| = |\mathbf{r}_2 - \mathbf{r}_1| - a$ and $\mathbf{n}$ is the vector of unity pointing in the connexion line of the two atoms. $\mathbf{r}_1$ and $\mathbf{r}_2$ are the actual positions of the two atoms, $\mathbf{r}_1^0$ and $\mathbf{r}_2^0$ are the equilibrium positions of the two atoms without strain (stress), which give the equilibrium distance of the atoms, i.e. the lattice constant a. Denoting the force exerted on the i-th atom by its l-th neighbour (numbering of neighbours according to Figure 11.1) with $\mathbf{F}_i^l$ one finds

$$\mathbf{F}_i^1 = k_i^1 \left(|\mathbf{r}_i^1 - \mathbf{r}_i| - a\right) \frac{\mathbf{r}_i^1 - \mathbf{r}_i}{|\mathbf{r}_i^1 - \mathbf{r}_i|} = k_i^1 \left(1 - \frac{a}{|\mathbf{r}_i^1 - \mathbf{r}_i|}\right) \left(\mathbf{r}_i^1 - \mathbf{r}_i\right). \tag{11.2}$$

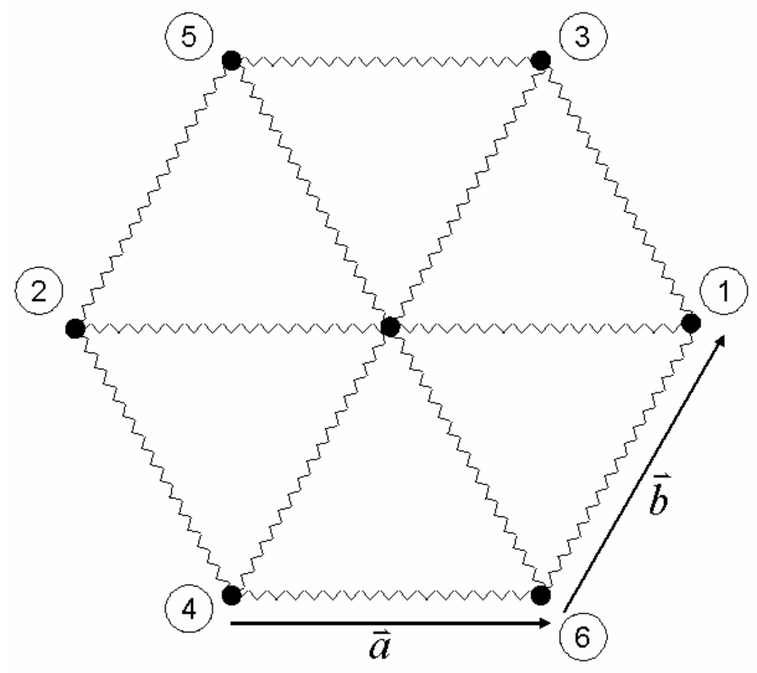

Figure 11.1: The unit cell of a triangular lattice is shown. An atom and its 6 nearest neighbours are depicted. The connecting springs are indicated by zigzag lines.

Being interested in small deformations, it is intuitive to set

$$\mathbf{r}_i^1 - \mathbf{r}_i = \begin{pmatrix} x_i^1 - x_i \\ y_i^1 - y_i \end{pmatrix} = \begin{pmatrix} a(1+\epsilon) \\ \eta \end{pmatrix} \tag{11.3}$$

with ϵ, $\eta \ll 1$. With this convention one finds

$$|\mathbf{r}_i^1 - \mathbf{r}_i| = a\sqrt{(1+\epsilon)^2 + \eta^2} \approx a(1+\epsilon) \tag{11.4}$$

where terms of higher than linear order in ϵ and η were neglected. Insertion into equation (11.2) yields

$$\mathbf{F}_i^1 \approx k_i^1 \begin{pmatrix} x_i^1 - x_i - a \\ 0 \end{pmatrix}. \tag{11.5}$$

Analogous calculations yield

$$\mathbf{F}_i^2 \approx k_i^2 \begin{pmatrix} x_i^2 - x_i + a \\ 0 \end{pmatrix}, \tag{11.6}$$

$$\mathbf{F}_i^3 \approx \frac{k_i^3}{2} \left[x_i^3 - x_i - 2a + \sqrt{3}(y_i^3 - y_i) \right] \begin{pmatrix} 1/2 \\ \sqrt{3}/2 \end{pmatrix}, \tag{11.7}$$

$$\mathbf{F}_i^4 \approx \frac{k_i^4}{2}\left[-x_i^4 + x_i - 2a + \sqrt{3}(-y_i^4 + y_i)\right]\begin{pmatrix} -1/2 \\ -\sqrt{3}/2 \end{pmatrix}, \tag{11.8}$$

$$\mathbf{F}_i^5 \approx \frac{k_i^5}{2}\left[-x_i^5 + x_i - 2a + \sqrt{3}(y_i^5 - y_i)\right]\begin{pmatrix} -1/2 \\ \sqrt{3}/2 \end{pmatrix}, \tag{11.9}$$

and

$$\mathbf{F}_i^6 \approx \frac{k_i^6}{2}\left[x_i^6 - x_i - 2a + \sqrt{3}(-y_i^6 + y_i)\right]\begin{pmatrix} 1/2 \\ -\sqrt{3}/2 \end{pmatrix}. \tag{11.10}$$

From the special form of the resulting equations the physical meaning of the used approximations can be deduced. Discarding higher than linear order terms in the evaluation is equivalent to the assumption that the force between connected lattice sites always acts along the connexion line of the originally, undeformed lattice points. Furthermore the elongation of the spring leading to a force is determined by a projection of the actual vector connecting the atoms on the equilibrium distance vector. Thus we have in general

$$\mathbf{F}_i^l \approx k_i^l\left[\left(\mathbf{r}_i^l - \mathbf{r}_i\right)\cdot\frac{\mathbf{r}_i^{l0} - \mathbf{r}_i^0}{a} - a\right]\frac{\mathbf{r}_i^{l0} - \mathbf{r}_i^0}{a}. \tag{11.11}$$

The condition for mechanical equilibrium now reads

$$\sum_{m=1}^{6}\mathbf{F}_i^m \equiv 0 \qquad \forall i. \tag{11.12}$$

For a lattice with N lattice sites, this means to solve a system of $2N$ linear equations in as many variables. Mathematically the approximation of small deformations results in a system of linear equations that have to be solved, which greatly simplifies the problem. In all the presented simulations $a = 1$ was chosen.

11.2 The stiffness matrix of a homogenous crystal

Linear elasticity assumes a linear relation between stress and strain

$$\sigma_{ik} = C_{iklm}\epsilon_{lm} \tag{11.13}$$

with i, k, l and $m = 1, 2$ in two dimensions. Symmetry demands that $\sigma_{ik} = \sigma_{ki}$ and $\epsilon_{lm} = \epsilon_{ml}$. Therefore the stiffness matrix has to fulfil $C_{iklm} = C_{kilm} = C_{ikml}$. Furthermore – since the energy functional is a quadratic form of the strains – the relation $C_{iklm} = C_{lmik}$ is valid. Taking into account these symmetries equation (11.13) may be rewritten in terms of a simpler matrix equation (Voigt notation)

$$\sigma_i = C_{ik}\epsilon_k \tag{11.14}$$

with i, $k = 1, 2, 3$ and the substitution $(11) \rightarrow 1$, $(22) \rightarrow 2$ and $(12) \rightarrow 3$. The matrix C_{ik} is symmetric, i.e. in the most general case there are 6 independent elastic constants for a 2-D material. The stiffness matrix C fully describes the elastic behaviour of any material, the well known elastic constants, like elastic (Young's) modulus Y or Poisson ratio μ, are given as combinations of the elements of C:

$$\begin{array}{ll} Y_1 = C_{11} - \frac{C_{12}^2}{C_{22}} & \mu_1 = \frac{C_{12}}{C_{11}} \\ Y_2 = C_{22} - \frac{C_{12}^2}{C_{11}} & \mu_2 = \frac{C_{12}}{C_{22}}. \end{array} \tag{11.15}$$

For a material showing cubical symmetry ($C_{11} = C_{22}$) there is only one elastic modulus and one Poisson ratio given by

$$Y = C_{11}\left(1 - \mu^2\right) \qquad \mu = \frac{C_{12}}{C_{11}}. \tag{11.16}$$

Here and in the following Y and μ denote the 2-dimensional elastic modulus and Poisson ratio, its corresponding 3-dimensinonal values are given by E and ν, respectively.

In the following the full elastic matrix of a crystal as shown in Figure 11.2 is determined. One out of three strain states (see Figure 11.3) is applied to the crystal. The resulting stresses are evaluated and according to equation (11.14) the stiffness matrix is evaluated.

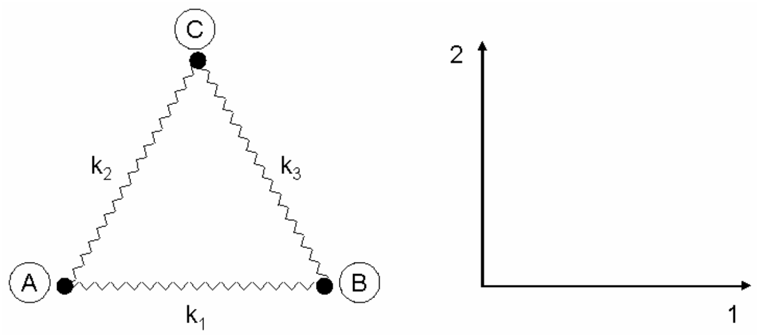

Figure 11.2: Left: the unit cell of a triangular lattice with three different spring constants. The crystal is thought to be built up by periodic repetition of this basis. Right: the Cartesian coordinate system that is used to determine stresses and strains.

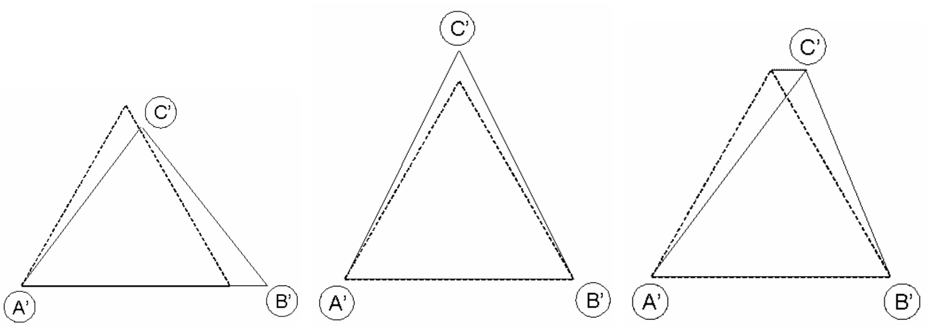

Figure 11.3: Three different strain states with 1. $\epsilon_1 = \epsilon$, $\sigma_2 = 0$ (left), 2. $\epsilon_{11} = 0$, $\epsilon_2 = \epsilon$, $\epsilon_3 = 0$ (middle) and 3. $\epsilon_1 = 0$, $\epsilon_2 = 0$, $\epsilon_3 = \epsilon$ (right).

1. The triangle is stretched along the line $\overline{AB}$, the points A and B are fixed, whereas C is free (see Figure 11.3 – left). The triangle is deformed until the springs k_2 and k_3, respectively, are unstretched, therefore feeling no force. For the height h' of the deformed triangle one finds

$$h' = \sqrt{1 - \left(\frac{1+\epsilon}{2}\right)^2} \approx \frac{\sqrt{3}}{2}\left(1 - \frac{1}{3}\epsilon\right) = h\left(1 - \frac{1}{3}\epsilon\right) \tag{11.17}$$

with $h = \sqrt{3}/2$ the height of the undeformed triangle. The forces applied to the three springs can be found by using equations (11.5), (11.7) and (11.9). It is found

$$\mathbf{F}_{BA} = k_1 \begin{pmatrix} \epsilon \\ 0 \end{pmatrix} \qquad \mathbf{F}_{CA} = k_2 \begin{pmatrix} 0 \\ 0 \end{pmatrix} \qquad \mathbf{F}_{CB} = k_3 \begin{pmatrix} 0 \\ 0 \end{pmatrix} \tag{11.18}$$

with $\mathbf{F}_{XY}$ is the force acting on Y by the spring connected to X. These forces have now to be transformed in the corresponding stresses. Therefore the forces are summed along the boundaries of the crystal and transformed according to

$$F_i = \sigma_{ik} df_k \tag{11.19}$$

where F_i is the i-th component of the Force $\mathbf{F}$ and df_k is the k-th component of the area normal vector. Denoting the total force acting on the bottom layer of the crystal $\mathbf{F}_B$ and the total force on the left layer $\mathbf{F}_L$ one finds

$$\mathbf{F}_B = \begin{pmatrix} -\sigma_{12} \\ -\sigma_{22} \end{pmatrix} L \qquad \mathbf{F}_L = \begin{pmatrix} -\frac{\sqrt{3}}{2}\sigma_{11} + \frac{1}{2}\sigma_{12} \\ -\frac{\sqrt{3}}{2}\sigma_{21} + \frac{1}{2}\sigma_{22} \end{pmatrix} L \tag{11.20}$$

with L the length of the crystal. Together with equation (11.18) it is found that

$$\mathbf{F}_B = \begin{pmatrix} 0 \\ 0 \end{pmatrix} \qquad \mathbf{F}_L = k_1 \begin{pmatrix} -\epsilon \\ 0 \end{pmatrix} L \tag{11.21}$$

and therefore

$$\sigma_1 = \frac{2k_1}{\sqrt{3}}\epsilon \qquad \sigma_2 = 0 \qquad \sigma_3 = 0. \tag{11.22}$$

The corresponding strains are given by

$$\epsilon_1 = \epsilon \qquad \epsilon_2 = -\frac{1}{3}\epsilon \qquad \epsilon_3 = 0. \tag{11.23}$$

Insertion into equation (11.14) gives

$$\begin{aligned} C_{11} &= \frac{1}{3}C_{12} + \frac{2}{\sqrt{3}}k_1 \\ C_{22} &= 3C_{12} \\ C_{23} &= 3C_{13}. \end{aligned} \tag{11.24}$$

2. According to the Figure 11.3 (middle) all three points of the triangle are fixed

$$A' = (0,0) \qquad B' = (1,0) \qquad C' = \left(\frac{1}{2}, \frac{\sqrt{3}}{2}(1+\epsilon)\right) \tag{11.25}$$

resulting in

$$\epsilon_1 = 0, \qquad \epsilon_2 = \epsilon \qquad \text{and} \qquad \epsilon_3 = 0. \tag{11.26}$$

The corresponding forces are given by

$$\mathbf{F}_{BA} = k_1 \begin{pmatrix} 0 \\ 0 \end{pmatrix}, \qquad \mathbf{F}_{CA} = \frac{3\epsilon}{8}k_2 \begin{pmatrix} 1 \\ \sqrt{3} \end{pmatrix} \qquad \text{and} \qquad \mathbf{F}_{CB} = \frac{3\epsilon}{8}k_3 \begin{pmatrix} -1 \\ \sqrt{3} \end{pmatrix}. \tag{11.27}$$

The total forces are then given by

$$\mathbf{F}_B = \frac{3\epsilon}{8} \begin{pmatrix} k_3 - k_2 \\ -\sqrt{3}k_2 - \sqrt{3}k_3 \end{pmatrix} L \qquad \mathbf{F}_L = \frac{3\epsilon}{8}k_3 \begin{pmatrix} -1 \\ \sqrt{3} \end{pmatrix} L, \tag{11.28}$$

the corresponding stresses are

$$\sigma_1 = \frac{\sqrt{3}}{8}\epsilon(k_2 + k_3) \qquad \sigma_2 = \frac{3\sqrt{3}}{8}\epsilon(k_2 + k_3) \qquad \sigma_3 = \frac{3}{8}\epsilon(k_2 - k_3). \tag{11.29}$$

Using equation (11.14) one finds

$$\begin{aligned} C_{12} &= \frac{\sqrt{3}}{8}(k_2 + k_3) \\ C_{22} &= \frac{3\sqrt{3}}{8}(k_2 + k_3) \\ C_{23} &= \frac{3}{8}(k_2 - k_3). \end{aligned} \tag{11.30}$$

3. To determine the still missing elements of the stiffness matrix a third deformation state – now including shear deformation – is investigated. According to Figure 11.3 (right) the points of the triangle are fixed to give

$$A' = (0,0), \qquad B' = (1,0) \qquad \text{and} \qquad C' = \left(\frac{1}{2} + \Delta x, \frac{\sqrt{3}}{2}\right) \tag{11.31}$$

which results in

$$\epsilon_1 = 0, \qquad \epsilon_2 = 0 \qquad \text{and} \qquad \epsilon_3 = \frac{\Delta x}{h} \equiv \epsilon. \tag{11.32}$$

Once again the forces have to be calculated

$$\mathbf{F}_{BA} = k_1 \begin{pmatrix} 0 \\ 0 \end{pmatrix}, \qquad \mathbf{F}_{CA} = \frac{\epsilon}{8} k_2 \begin{pmatrix} \sqrt{3} \\ 3 \end{pmatrix} \qquad \text{and} \qquad \mathbf{F}_{CB} = \frac{\epsilon}{8} k_3 \begin{pmatrix} \sqrt{3} \\ -3 \end{pmatrix}, \tag{11.33}$$

correspondingly the total forces are given by

$$\mathbf{F}_B = \frac{\epsilon}{8} \begin{pmatrix} -\sqrt{3}(k_2 + k_3) \\ 3(k_3 - k_2) \end{pmatrix} L \qquad \mathbf{F}_L = \frac{3\epsilon}{8} k_3 \begin{pmatrix} \sqrt{3} \\ -3 \end{pmatrix} L. \tag{11.34}$$

The stresses are found to give

$$\sigma_1 = \frac{\epsilon}{8}(k_2 - k_3), \qquad \sigma_2 = \frac{3\epsilon}{8}(k_2 - k_3) \qquad \text{and} \qquad \sigma_3 = \frac{\sqrt{3}\epsilon}{8}(k_2 + k_3). \tag{11.35}$$

Using once again equation (11.14) one finds

$$\begin{aligned} C_{13} &= \frac{1}{8}(k_2 - k_3) \\ C_{23} &= \frac{3}{8}(k_2 - k_3) \\ C_{33} &= \frac{\sqrt{3}}{8}(k_2 + k_3). \end{aligned} \tag{11.36}$$

Putting together the pieces the stiffness matrix now reads

$$C = \begin{pmatrix} \frac{\sqrt{3}}{24}(16k_1 + k_2 + k_3) & \frac{\sqrt{3}}{8}(k_2 + k_3) & \frac{1}{8}(k_2 - k_3) \\ \frac{\sqrt{3}}{8}(k_2 + k_3) & \frac{3\sqrt{3}}{8}(k_2 + k_3) & \frac{3}{8}(k_2 - k_3) \\ \frac{1}{8}(k_2 - k_3) & \frac{3}{8}(k_2 - k_3) & \frac{\sqrt{3}}{8}(k_2 + k_3) \end{pmatrix}. \tag{11.37}$$

For a system build up of identical springs, i.e. $k_1 = k_2 = k_3 \equiv k$ the matrix reduces to

$$C = \begin{pmatrix} \frac{3\sqrt{3}}{4}k & \frac{\sqrt{3}}{4}k & 0 \\ \frac{\sqrt{3}}{4}k & \frac{3\sqrt{3}}{4}k & 0 \\ 0 & 0 & \frac{\sqrt{3}}{4}k \end{pmatrix} \tag{11.38}$$

showing isotropic symmetry. Furthermore using equation (11.2) the elastic modulus and Poisson ratio of such a material is given by

$$Y = \frac{2\sqrt{3}}{3}k \qquad \mu = \frac{1}{3}. \tag{11.39}$$

11.3 Elastic properties of membranes

Bilayers that are composed of two amphiphiles with oppositely charged head groups show remarkable elastic properties. By variation of the pH value of the solution the composition of the membrane can be changed and these changes in composition lead to a decline in the elastic properties over several orders of magnitude. It is believed that additional hydrogen bonds occurring e.g. between carboxylic (anionic) head-groups in the absence of counter-ion different from H^+ are responsible for this effect Lynch et al. [1996]. This special situation was modelled as follows: it is assumed that the binding of the molecules without hydrogen bonds is very weak (spring constant k_2). The occurence of additional hydrogen bonds between one pair of atoms is described by assigning springs connecting A-A pairs a spring constant k_1 that is much stiffer than k_2, i.e. $k_2 \ll k_1$. In another study the stiff bonds k_1 were assigned the A-B pairs, all other pairs the soft bond k_2.

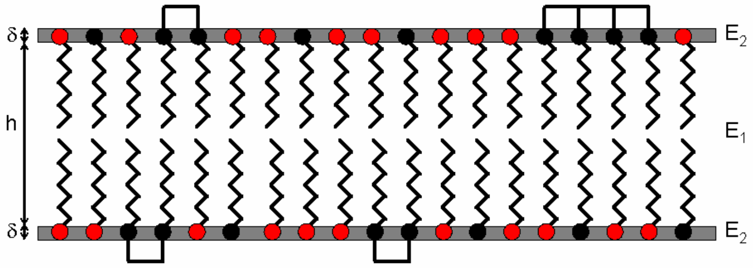

Figure 11.4: The figure shows a schematic sketch of a bilayer membrane. An amphiphilic molecule consists of a hydrophobic tail (zigzag line) and a hydrophilic head (black and red circles). The tail region of length h is completely shielded from water contact by the head region of width δ. The additional hydrogen bonds emerging by nearest neighbour contacts between the heads of one sort of molecules (black circles) are visualized by black bars.

11.3.1 Stiff A-A bonds

To determine the predictions of the model configurations of different molecular compositions were produced and these were analysed to give their elastic properties. Following standard Monte Carlo procedures the configurations were obtained by minimizing the total interaction energy given by Weinkamer et al. [1998], Glauber [1963], Kawasaki [1972]

$$U = J \sum_{\langle ij \rangle} \sigma_i \sigma_j . \tag{11.40}$$

The sum extends over nearest neighbour pairs, σ_i is a spin variable (not to be confused with the stress σ!) giving 1 (-1) if lattice site i is occupied by an A molecule (B molecule, respectively). The choice of the interaction parameter $J = 1 > 0$ led to the favouring of antiferromagnetic order.

Figure 11.5 shows snapshots of the configuration for some composition values. To make the pictures more clear only the strong bonds, connecting $A - A$ pairs are shown. The figure shows how a dense network of strong bonds for large concentrations of A molecules with only isolated islands of weak bonds, transforms into a hexagonal lattice (for concentrations of 0.66) and – with still decreasing concentration – the connexion of the existing bonds breaks down, leaving only isolated islands of strong bonds.

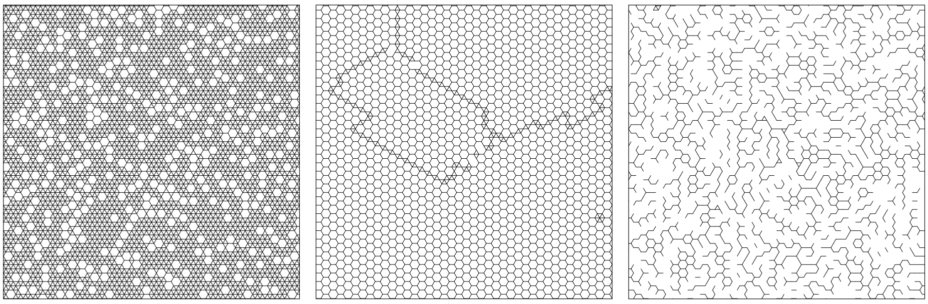

Figure 11.5: Three typical configurations for different concentrations of A molecules: 0.9 (left), 0.66 (middle) and 0.5 (right). Only the strong bonds between A-A pairs are shown.

To assess the elastic properties of each configuration three different deformation states were imposed on the sample.

$$\begin{pmatrix} \epsilon \\ 0 \\ 0 \end{pmatrix} \quad \begin{pmatrix} 0 \\ \epsilon \\ 0 \end{pmatrix} \quad \begin{pmatrix} 0 \\ 0 \\ \epsilon \end{pmatrix} . \tag{11.41}$$

The simulations were done with (pseudo)-periodical boundary conditions in all directions. In contrast to standard periodic boundaries where the positions of the atoms are mirrored, in the presented simulations periodic boundary conditions in the applied strain field were chosen. This means that the distance of one atom at the boundary and its mirrored counterpart is held fix. By an appropriate choice of these distance each desired strain state can be imposed on the system. Then the atoms were allowed to relax in their equilibrium position. The resulting forces on the bottom and left boundary were then evaluated and transformed into the appropriate stresses. Knowing stresses and strains the elastic constants could be easily calculated. The relaxation process of the molecules was done iteratively. One molecule was chosen randomly, its local equilibrium position was calculated with respect to its 6 neighbours and then the atom was moved into this new position. This process is now iterated until equilibrium was reached, i.e. until the energy of the system reached a minimum.

The bending rigidity of a membrane as sketched in Figure 11.4 is given by

$$\kappa = \int_{-h/2-\delta}^{h/2+\delta} \frac{E(z)}{1-\nu^2} z^2 dz = \frac{h^3}{12}\frac{E_1}{1-\nu^2} + \frac{(h+2\delta)^3 - h^3}{12}\frac{E_2}{1-\nu^2}, \qquad (11.42)$$

where E_1, E_2 and ν are the 3-dimensional elastic moduli of the tail- and head group region, respectively, and the 3-dimensional Poisson ratio. Therefore the change in bending rigidity $\Delta\kappa$ caused by the additional hydrogen bonds can be written

$$\Delta\kappa \approx \frac{h^2\delta}{2}\frac{\Delta E_2}{1-\nu^2} \qquad (11.43)$$

where $\delta \ll h$ was used. This expression scales with the square of the membrane thickness. So although the increase in bending rigidity stems from an increase in the elastic modulus of the head group region only, this effect is strongly enhanced by the length of the hydrophobic tails similar to a lever arm principle.

To define an order of magnitude for the spring constant k_1 we consider a Lennard-Jones potential with a binding energy of 40 meV (the strength of a typical hydrogen bond) and an equilibrium spacing of 0.8 nm (the typical spacing of two molecules). This sets

$$k_1 = 4.5 \text{ eV/nm}^2. \qquad (11.44)$$

Furthermore it is supposed that the other type of springs between $A - B$ and $B - B$ heads is much smaller – or that there is no binding at all. In the simulations presented in this thesis it was set $k_2 : k_1 = 0.0001$.

The simulations presented in this thesis are all done on a 2-dimensional membrane, accordingly the 2-dimensional stiffness matrix of the membrane is evaluated. The elements of the stiffness matrix of a corresponding 3-dimensional material can be found by multiplication with the membrane thickness. Also the elastic modulus and the Poisson ratio are defined differently in 2 than in 3 dimensions:

$$\nu = \frac{C_{12}}{C_{11} + C_{12}} \qquad C_{11} = \delta C_{11}^{3d} = \delta E \frac{1-\nu}{(1+\nu)(1-2\nu)}. \tag{11.45}$$

Insertion into equation (11.43) leads to the final result

$$\Delta\kappa = \frac{h^2}{2} Y. \tag{11.46}$$

Since the simulation results showed that the structure shows isotropic symmetry for all concentrations (i.e. $C_{11} - C_{12} - 2C_{66} \approx 0$), the use of only one elastic modulus and Poisson ratio to describe the membrane is justified. Furthermore it was shown that the Cauchy relation $C_{12} = C_{66}$ Born and Huang [1988] does not hold in general. This is not too surprising, since it was shown that the Cauchy relation is strictly only obeyed in a system with purely central forces and if each lattice point is center of symmetry. Due to the inhomogenities in the structure of the membrane, this symmetry condition is surely violated.

Figure 11.6 shows $\Delta\kappa$ and the Poisson ratio for various concentrations and for two different temperatures: $J/kT = 1$ and $J/kT = 0$, i.e. a random configuration of molecules. The length of the tail region was chosen 3 nm Zemb et al. [1999], leading to $\Delta\kappa \approx 22$ eV for a material consisting of only strong $A - A$ bonds.

The strong decay of the bending rigidity in a small concentration range is clearly visible. The bending rigidity falls over 4 orders of magnitude from a value of approximately 1000 kT (which gives extremely stiff, flat membranes) to 0.1 kT, a value which lies well below the room temperature limit, thus resulting in very soft and flexible structures. There is not much difference in the behaviour for both, the ordering case as well as the random structure. The only difference is that the ordering tendency leads to a more pronounced isolation of atoms than in the random case, which in turn leads to a bit faster decrease in bending rigidity for the ordered than for the random configuration.

In contrast to the bending rigidities, which show a very similar behaviour for the two simulation runs, the Poisson ratio exhibits remarkable differences. While the Poisson ratio shows only slight changes for the random configuration (an increase from 0.33 at the end points to approximately 0.4 for concentrations of 0.7), in the ordering case it exhibits a pronounced peak close to 1 for concentrations of 0.66. This behaviour is related to the superstructure of the ordered configuration, which forms a hexagonal super lattice

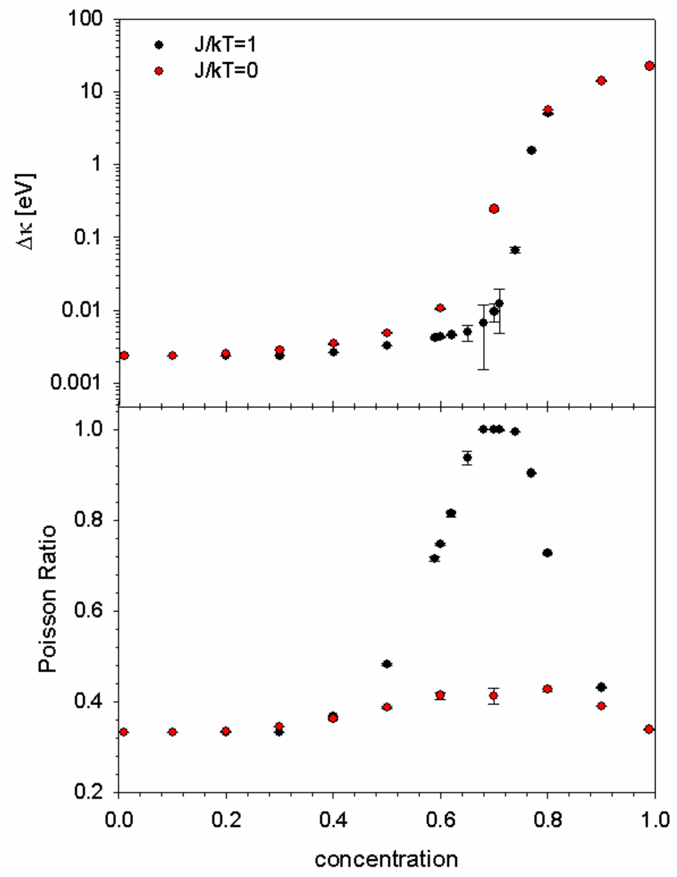

Figure 11.6: The bending rigidity $\Delta\kappa$ (top) and the Poisson ratio for various concentrations and two different temperatures.

for atomic compositions of 1 : 3 (which can be clearly seen in the middle of Figure 11.5). Since the elastic modulus of a hexagonal lattice is exactly zero (the bonds may follow the elongation by a simple re-alignment, they do not have to stretch), the corresponding Poisson ratio has to take the value of 1 (see equation (11.16)), which corresponds to a deformation without volume change (in 3-D the corresponding value of the Poisson ratio is 1/2).

11.3.2 Stiff A-B bonds

The same configurations that were analysed in the previous chapter are now investigated, but the stiff bonds k_1 are transferred from A-A to A-B pairs. Snapshots of these configurations may be see in Figure 11.7. In Figure 11.8 the results for the bending rigidity and the Poisson ratio are shown. As ex-

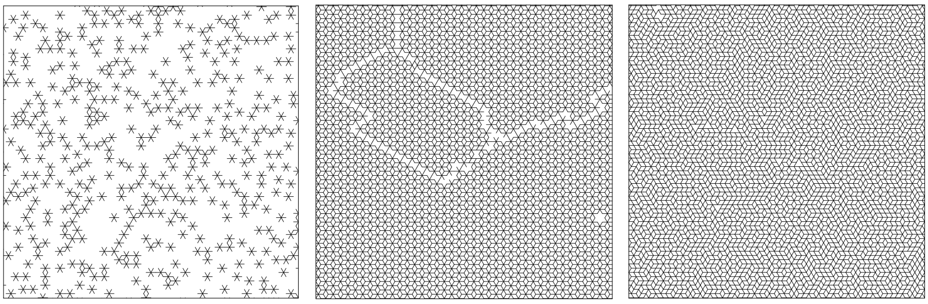

Figure 11.7: Three typical configurations for different concentrations of A molecules: 0.9 (left), 0.66 (middle) and 0.5 (right). Only the strong bonds between A-B pairs are shown.

pected the properties of the system are symmetric around the concentration value of 0.5, being less stiff at low and high concentrations (since only soft bonds are present) and much more stiff for concentrations around 0.5 (since most A-B bonds are present for this concentration). Additionally the figure shows that the bending rigidity does not vary in that large range as it did for the previous simulations. This is due to the fact that no concentration exists, where only stiff bonds are present, i.e. the system is always softened. In contrast to the previous simulations the obtained results show now that the bending rigidity takes higher values for the ordering case than for the random configuration. Furthermore, the highest value is taken for the superstructure of a hexagonal lattice. This can be understood since in this case really the maximum of possible bonds is achieved (all isolated atoms exhibit only stiff bonds).

Once again the most pronounced changes can be seen in the behaviour of the Poisson ratio, as in the previous simulations it stays almost constant for the random configuration and takes a pronounced maximum for the ordering case.

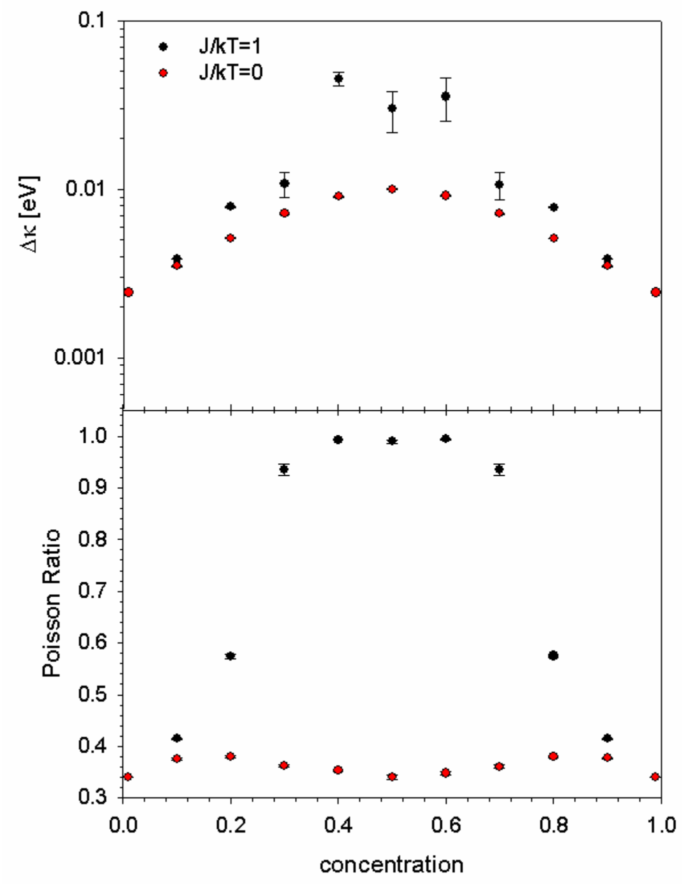

Figure 11.8: The bending rigidity $\Delta\kappa$ (top) and the Poisson ratio for various concentrations and two different temperatures.

Chapter 12

Final Remarks – Elastic Properties of Membranes

A simple model to account for the elastic behaviour of membranes in different external conditions was presented. The elastic interaction of the constituents of a membrane was modelled by linear elastic springs. Non-linear effects like buckling were neglected. The full elastic matrix of the material was calculated and all other mechanical properties deduced. In the framework of the presented model it was shown that mechanical properties like the bending rigidity or the Poisson ratio exhibit a pronounced concentration dependence and may vary over several orders of magnitude in a limited concentration range. By basic physical considerations an estimation for the value of the calculated rigidities could be given in real physical units. In the near future it is planned to compare the simulation results to measurements of the bending rigidity of the investigated membranes. These experiments will show, if the presented model is capable to explain the basic findings or if it has to be modified to give a more accurate description of the experiments. The assumption that each molecule may form up to 6 hydrogen bridges is very crude, for most molecules the number of hydrogen bonds they can simultaneously form is limited. So it may be necessary to include this in the description of the model, which would lower the value of the maximum bending rigidity.

Summarising: A model for predicting the mechanical properties of amphiphilic membranes was introduced. In first simulations its capability to qualitatively explain the behaviour of the bending rigidity of membranes was shown. By comparison to data from experiments a fine tuning of the model is planned, to give an even better – maybe quantitative – description of the investigated model systems.

Bibliography

M. E. Glicksmann. *Diffusion in Solids - Field Theory, Solid State Principles and Applications.* John Wiley & Sons, Inc., New York, 2000. ISBN 0 471 23972 0.

I. M. Lifshitz and V. V. Slyozov. The kinetics of precipitation from supersaturated solid solutions. *J. Phys. Chem. Solids*, 19:35, 1961.

C. Wagner. Theorie der Alterung von Niederschlägen durch Umlösen (Ostwald-Reifung). *Zeitschrift für Elektrochemie*, 65:581, 1961.

J. W. Cahn. On spinodal decomposition in cubic crystals. *Acta Metall.*, 10: 179, 1962.

P. Fratzl and O. Penrose. Ising-model for phase-separation in alloys with anisotropic elastic interaction.1. theory. *Acta Metallurgica Et Materialia*, 43:2921, 1995.

P. Fratzl and O. Penrose. Ising model for phase separation in alloys with anisotropic elastic interaction.2. a computer experiment. *Acta Mater.*, 44: 3227, 1996.

R. Weinkamer, H. Gupta, P. Fratzl, and J. L. Lebowitz. Dynamics of mesoscopic precipitate lattices in phase-separating alloys under external load. *Europhysics Letters*, 52:224, 2000.

R. Weinkamer and P. Fratzl. By which mechanism does coarsening in phase-separating alloys proceed? *Europhysics Letters*, 61:261, 2003.

R. Weinkamer, P. Fratzl, H. S. Gupta, O. Penrose, and J. L. Lebowitz. Using kinetic Monte Carlo simulations to study phase separation in alloys. *Phase Transit.*, 77:433, 2004a.

P. Fratzl, O. Penrose, and J. L. Lebowitz. Modeling of phase separation in alloys with coherent elastic misfit. *Journal of Statistical Physics*, 95:1429, 1999.

A. Einstein. Über die von der molekularkinetischen Theorie der Wärme geforderte Bewegung von in ruhenden Flüssigkeiten suspendierten Teilchen. *Annalen der Physik IV. Folge*, 17:549, 1905.

J. M. Courtault, Y. Kabanov, B. Bru, P. Crépel, I. Lebon, and A. Le Marchand. Louis Bachelier – on the centenary of *théorie de la spéculation. Mathematical Finance*, 10:341, 2000.

G. E. Murch. Diffusion in Crystalline Solids. In G. Kostorz, editor, *Phase Transformations in Materials*, D-69469 Weinheim, 2001. WILEY-VCH.

L. Onsager. Reciprocal relations in irreversible processes I. *Phys. Rev.*, 37: 405, 1931.

J. R. Manning. Correlation Factors for Diffusion in Nondilute Alloys. *Phys. Rev. B*, 4:1111, 1971.

G. E. Murch and S. J. Rothman. Diffusion, correlation and percolation in a random alloy. *Phil. Mag. A*, 43:229, 1981.

A. D. Pelton. Thermodynamics and Phase Diagrams of Materials. In G. Kostorz, editor, *Phase Transformations in Materials.* WILEY-VCH, 2001.

L. Darken. Diffusion, mobility and their interrelation through free energy in binary metallic systems. *Trans. Am. Inst. Min. Engrs.*, 175:184, 1948.

A. B. Lidiard. A note on Manning's relations for concentrated multicomponent alloys. *Acta. metall.*, 34:1487, 1986.

L. K. Moleko, A. R. Allnatt, and E. L. Allnatt. A self-consistent theory of matter transport in a random lattice gas and some simulation results. *Phil. Mag. A*, 59:141, 1989.

I. V. Belova and G. E. Murch. Collective diffusion in the binary random alloy. *Phil. Mag. A*, 80:599, 2000a.

I. V. Belova and G. E. Murch. Tracer correlation factors in the random alloy. *Phil. Mag. A*, 80:1469, 2000b.

J. Svoboda, F. D. Fischer, P. Fratzl, and A. Kroupa. Diffusion in multicomponent systems with no or dense sources and sinks for vacancies. *Acta Mater.*, 50:1369, 2002.

M. A. Hartmann, R. Weinkamer, P. Fratzl, J. Svoboda, and F. D. Fischer. Onsager's coefficients and diffusion laws - a monte carlo study. *Phil. Mag.*, 85:1243, 2005.

A. R. Allnatt and E. L. Allnatt. Computer simulation of phenomenological coefficients for atom transport in a random alloy. *Phil. Mag. A*, 49:625, 1984.

A. R. Allnatt. Einstein and linear response formulae for the phenomenological coefficients for isothermal matter transport in solids. *J. Phys. C: Solid State Phys.*, 15:5605, 1982.

G. E. Murch and R. J. Thorn. Calculation of the diffusion correlation factor by monte-carlo methods. *Phil. Mag. A*, 39:673, 1979a.

G. E. Murch. Chemical diffusion in highly defective solids. *Phil. Mag. A*, 41: 157, 1980.

G. E. Murch and R. J. Thorn. Computer simulation of ionic conductivity - application to β''-alumina. *Phil. Mag. A*, 36:529, 1977.

G. E. Murch and R. J. Thorn. Computer simulation of the drift mobility of an ionic impurity in an electric field. *Phil. Mag. A*, 39:259, 1979b.

G. E. Murch. An expression for the vacancy-wind effect in diffusion in a binary substitutional alloy. *Phil. Mag. A*, 46:151, 1982.

W. H. Press, S. A. Teukolsky, W. T. Vetterling, and B. P. Flannery. *Numerical Recipes in C.* Cambridge University Press, Cambridge CB2 2RU, UK, second edition, 1992.

L. K. Moleko and A. R. Allnatt. Exact linear relations between the phenomenological coefficients for matter transport in a random alloy. *Phil. Mag. A*, 58:677, 1988.

J. D. Currey. *Bones: structure and mechanics.* Princeton University Press, Princeton, New Jersey, 2002.

J. Jäger and P. Fratzl. Mineralized collagen fibrils: A mechanical model with staggered arrangement of mineral particles. *Biophysical Journal*, 79:1737, 2000.

H. Gao, B. Ji, I. Jäger, E. Arzt, and P. Fratzl. Materials become insensitive to flaws at nanoscale: lessons from nature. *PNAS*, 100:5597, 2003.

K. Misof, W. J. Landis, K. Klaushofer, and P. Fratzl. Collagen from the osteogenesis imperfecta mouse model (oim) shows reduced resistance against tensile stress. *Journal of Clinical Investigation*, 100:40, 1997.

N. P. Camacho, L. Hou, T. R. Toledano, W. A. Ilg, C. F. Brayton, C. L. Raggio, L. Root, and A. L. Boskey. The material basis for reduced mechanical properties in *oim* mice bones. *Journal of Bone and Mineral Research*, 14: 264, 1999.

B. Grabner, W. J. Landis, P. Roschger, S. Rinnerthaler, H. Peterlik, K. Klaushofer, and P. Fratzl. Age- and genotype-dependence of bone material properties in the osteogenesis imperfecta murine model (OIM). *Bone*, 29:453, 2001.

F. Rauch and F. H. Glorieux. Bisphosponate treatment in osteogenesis imperfecta: Which drug, for whom, for how long? *Annals of Medicine*, 37: 295, 2005.

P. Roschger, B. M. Grabner, S. Rinnerthaler, W. Tesch, M. Kneissel, A. Berzlanovich, K. Klaushofer, and P. Fratzl. Structural development of the mineralized tissue in the human l4 vertebral body. *J. Struc. Bio.*, 136:126, 2001.

N. Özkaya and M. Nordin. *Fundamentals of Biomechanics: equilibrium, motion, and deformation.* Springer, New York, 1999.

J. Rittweger, H. M. Frost, H. Schiessl, H. Ohshima, B. Alkner, P. Tesch, and D. Felsenberg. Muscle atrophy and bone loss after 90 days' bed rest and the effects of flywheel resistive exercise and pamidronate: Results from the LTBR study. *Bone*, 36:1019, 2005.

K. A. Johnson, P. Muir, R. G. Nicoll, and J. K. Roush. Asymmetric adaptive modeling of central tarsal bones in racing greyhounds. *Bone*, 27:257, 2000.

M. J. Favus and S. Christakos, editors. *Primer on the metabolic bone diseases and disorders of mineral metabolism.* Lippincott, Philadelphia, 1999.

M. G. Mullender and R. Huiskes. Osteocytes and lining cells: Which are the best canditates for mechano-sensors in cancellous bone? *Bone*, 20:527, 1997.

J. Klein-Nulend, A. van der Plas, C. M. Semeins, N. E. Ajubi, J. A. Frangos, P. J. Nijweide, and E. H. Burger. Sensitivity of osteocytes to biomechanical stress in vitro. *FASEB*, 9:441, 1995.

E. H. Burger and J. Klein-Nulend. Mechanotransduction in bone – role of the lacuno-canalicular network. *FASEB*, 13 (Suppl.):S101, 1999.

E. H. Burger, J. Klein-Nulend, and T. H. Smit. Strain-derived canalicular flow regulates osteoclast activity in a remodelling osteon – a proposal. *Journal of Biomechanics*, 36:1453, 2003.

N. Juncosa, J. R. West, M. T. Galloway, G. P. Boivin, and D. L. Butler. In vivo forces used to develop design parameters for tissue engineered implants for rabbit patellar tendon repair. *Journal of Biomechanics*, 36:483, 2003.

S. P. Fritton and C. T. Rubin. In vivo measurement of Bone Deformations using Strain Gauges. In S. C. Cowin, editor, *Bone mechanics handbook*, London, 2001. CRC.

T. D. Brown. Techniques for mechanical stimulation of cells in vitro: a review. *Journal of Biomechanics*, 33:3, 2000.

N. Basso and J. N. M. Heersche. Characteristics of In Vitro osteoblastic cell loading models. *Bone*, 30:347, 2002.

T. D. Brown. Devices and Techniques for in Vitro Mechanical Stimulation of Bone Cells. In S. C. Cowin, editor, *Bone mechanics handbook*, London, 2001. CRC.

A. E. Goodship, J. L. Cunningham, V. Oganov, J. Darling, A. W. Miles, and G. W. Owen. Bone loss during long term space flight is prevented by the application of a short term impulsive mechanical stimulus. *Acta Astronautica*, 43:65, 1998.

R. C. Murray, S. Vedi, H. L. Birch, K. H. Lakhani, and A. E. Goodship. Subchondral bone thickness, hardness and remodelling are influenced by short-term excercise in a site-specific manner. *Journal of Orthopaedic Research*, 19:1035, 2001.

J. R. Mosley, B. M. March, J. Lynch, and L. E. Lanyon. Strain magnitude related changes in whole bone architecture in growing rats. *Bone*, 20:191, 1997.

J. R. Mosley and L. E. Lanyon. Strain rate as a controlling influence on adaptive modeling in response to dynamic loading of the ulna in growing male rats. *Bone*, 23:313, 1998.

B. S. Oxlund, G. Ørtoft, T. T. Andreassen, and H. Oxlund. Low-intensity, high-frequency vibration appears to prevent the decrease in strength of the femur and tibia associated with ovariectomy of adult rats. *Bone*, 32:69, 2003.

C. Neidlinger-Wilke, I. Stalla, L. Claes, R. Brand, I. Hoellen, S. Rübenacker, M. Arand, and L. Kinzl. Human osteoblasts from younger normal and osteoporotic donors show differences in proliferation and $T_{GF\beta}$-release in response to cyclic strain. *Journal of Biomechanics*, 28:1411, 1995.

A. D. Bakker, K. Soejima, J. Klein-Nulend, and E. H. Burger. The production of nitric oxide and prostaglandin e_2 by primary bone cells is shear stress dependent. *Journal of Biomechanics*, 34:671, 2001.

P. J. Ehrlich and L. E. Lanyon. Mechanical strain and bone cell function: A review. *Osteoporosis International*, 13:688, 2002.

V. Lemaire, F. L. Tobin, L. D. Greller, C. R. Cho, and L. J. Suva. Modeling the interactions between osteoblast and osteoclast activities in bone remodeling. *Journal of Theoretical Biology*, 229:293, 2004.

J. Wolff. *Das Gesetz der Transformation der Knochen.* A. Hirschwald - Berlin, 1892.

S. Cowin. The false premise of Wolff's law. *Forma*, 12:247, 1997.

R. Huiskes. If bone is the answer, then what is the question? *J. Anat.*, 197: 145, 2000.

W. Roux. *Der Kampf der Theile im Organismus.* Engelmann - Leipzig, 1881.

H. M. Frost. Bone "mass" and the "mechanostat": a proposal. *Anatomical Record*, 219:1, 1987.

H. M. Frost. Changing concepts in skeletal physiology: Wolff's law, the mechanostat, and the "Utah paradigm". *American Journal of Human Biology*, 10:599, 1998.

H. M. Frost. From Wolff's law to the Utah paradigm: Insights about bone physiology and its clinical applications. *Anatomical Record*, 262:398, 2001.

H. M. Frost. Bone's mechanostat: a 2003 update. *Anatomical Record Part A*, 275A:1081, 2003.

H. M. Frost. A 2003 update of bone physiology and Wolff's law for clinicians. *Angle Orthodontist*, 74:3, 2004.

C. H. Turner. Toward a mathematical description of bone biology: the principle of cellular accommodation. *Calcified Tissue International*, 65:466, 1999.

J. C. van der Linden, J. S. Day, J. A. N. Verhaar, and H. Weinans. Altered tissue properties induce changes in cancellous bone architecture in aging and diseases. *Journal of Biomechanics*, 37:367, 2004.

S. C. Cowin and D. H. Hegedus. Bone remodeling 1: Theory of adaptive elasticity. *Journal of Elasticity*, 6:313, 1976.

S. C. Cowin. Wolff's law of trabecular architecture at remodeling equilibrium. *Journal of Biomechanical Engineering-Transactions of the Asme*, 108:83, 1986.

S. C. Cowin. Bone stress-adaption models. *Journal of Biomechanical Engineering-Transactions of the Asme*, 115:528, 1993.

S. C. Cowin, A. M. Sadegh, and G. M. Luo. An evolutionary wolff law for trabecular architecture. *Journal of Biomechanical Engineering-Transactions of the Asme*, 114:129, 1992.

R. T. Hart. Bone modeling and remodeling: Theories and computation. In S. C. Cowin, editor, *Bone mechanics handbook*, London, 2001. CRC.

R. Huiskes, H. Weinans, H. J. Grootenboer, M. Dalstra, B. Fudala, and T. J. Slooff. Adaptive bone-remodeling theory applied to prosthetic-design analysis. *Journal of Biomechanics*, 20:1135, 1987.

R. Huiskes, H. Weinans, and M. Dalstra. Adaptive bone remodeling and biomechanical design considerations for noncemented total hip arthroplasty. *Orthopedics*, 12:1255, 1989.

B. van Rietbergen and R. Huiskes. Load Transfer and Stress Shielding of the Hydroxyapatite-ABG Hip – a study of stem length and proximal fixation. *The Journal of Arthroplasty*, 16:55, 2001.

M. G. Mullender and R. Huiskes. Proposal for the regulatory mechanism of Wolff's law. *Journal of Orthopaedic Research*, 13:503, 1995.

R. Huiskes, R. Ruimerman, G. H. van Lenthe, and J. D. Janssen. Effects of mechanical forces on maintenance and adaptation of form in trabecular bone. *Nature*, 405:704, 2000.

R. Ruimerman, B. van Rietbergen, P. Hilbers, and R. Huiskes. A 3-dimensional computer model to simulate trabecular bone metabolism. *Biorheology*, 40:315, 2003.

R. Ruimerman, P. Hilbers, B. van Rietbergen, and R. Huiskes. A theoretical framework for strain-related trabecular bone maintenance and adaptation. *Journal of Biomechanics*, 38:931, 2005a.

R. Ruimerman, B. van Rietbergen, P. Hilbers, and R. Huiskes. The effects of trabecular-bone loading variables on the surface signaling potential for bone remodeling and adaptation. *Annals of Biomedical Engineering*, 33: 71, 2005b.

L. J. Gibson and M. F. Ashby. *Cellular Solids: structure and properties.* Cambridge University Press, Cambridge, New York, 1997.

M. G. Mullender, R. Huiskes, and H. Weinans. A physiological approach to the simulation of bone remodeling as a self-organizational control process. *Journal of Biomechanics*, 27:1389, 1994.

J. C. van der Linden, J. A. N. Verhaar, and H. Weinans. A three-dimensional simulation of age-related remodeling in trabecular bone. *Journal of Bone and Mineral Research*, 16:688, 2001.

J. S. Thomsen, Li. Mosekilde, R. W. Boyce, and E. Mosekilde. Stochastic simulation of vertebral trabecular bone remodeling. *Bone*, 15:655, 1994.

Z. Tabor and E. Rokita. Stochastic simulations of remodeling applied to a two-dimensional trabecular bone structure. *Bone*, 31:413, 2002.

S. Tayyar, P. S. Weinhold, R. A. Butler, J. C. Woodard, L. D. Zardiackas, K. R. St. John, J. M. Bledsoe, and J. A. Gilbert. Computer simulation of trabecular remodeling using a simplified structural model. *Bone*, 25:733, 1999.

J. Parkinson, A. Brass, G. Canova, and Y. Brechet. The mechanical properties of simulated collagen fibrils. *J. Biomechanics*, 30:549, 1997.

G. S. Beaupre, T. E. Orr, and D. R. Carter. An approach for the time-dependent bone modeling and remodeling – theoretical development. *Journal of Orthopaedic Research*, 8:651, 1990.

A. M. Parfitt, M. K. Drezner, F. H. Glorieux, J. A. Kanis, H. Malluche, P. J. Meunier, S. M. Ott, and R. R. Recker. Bone Histomorphometry: Standardization of Nomenclature, Symbols, and Units. *Journal of Bone and Mineral Research*, 2:595, 1987.

E. F. Eriksen, F. Melsen, E. Sod, I. Barton, and A. Chines. Effects of Long-term Risedronate on Bone Quality and Bone Turnover in Women with Postmenopausal Osteoporosis. *Bone*, 31:620, 2002.

P. Roschger, P. Fratzl, J. Eschberger, and K. Klaushofer. Validation of quantitative backscattered electron imaging for the measurement of mineral density distribution in human bone biopsies. *Bone*, 23:319, 1998.

P. Roschger, H. S. Gupta, A. Berzanovich, D. W. Dempster, P. Fratzl, F. Cosman, M. Parisien, R. Lindsay, J. W. Nieves, and K. Klaushofer. Constant mineralization density distribution in cancellous human bone. *Bone*, 32: 316, 2003.

E. F. Eriksen. Normal and pathological remodeling of human trabecular bone – 3-dimensional reconstruction of the remodeling sequence in normals and in metabolic bone-disease. *Endocrine Reviews*, 7:379, 1986.

R. Weinkamer, M. A. Hartmann, Y. Brechet, and P. Fratzl. Stochastic lattice model for bone remodeling and aging. *Phys. Rev. Lett.*, 93:228102, 2004b.

R. Weinkamer, M. A. Hartmann, Y. Brechet, and P. Fratzl. Architectural changes of trabecular bone caused by the remodeling process. *Mater. Res. Soc. Symp. Proc.*, 874:L1.9.1, 2005.

H. M. Frost. On the trabecular "thicknessŽŽ – Number problem. *Journal of Bone and Mineral Research*, 14:1816, 1999.

F. Pérez-López. Postmenopausal osteoporosis and alendronate. *Maturitas*, 48:179, 2004.

R. S. Weinstein, A. M. Parfitt, R. Marcus, M. Greenwald, G. Crans, and D. B. Muchmore. Effects of raloxifene, hormone replacement therapy, and placebo on bone turnover in postmenopausal women. *Osteoporosis International*, 14:814, 2003.

N. F. Ray, J. K. Chan, M. Thamer, and L. J. Melton. Medical expenditures for the treatment of osteoporotic fractures in the United States in 1995: Report from the national osteoporosis foundation. *Journal of Bone and Mineral Research*, 12:24, 1997.

J. G. Brecht and P. K. Schädlich. Burden of illness imposed by osteoporosis in Germany. *HEPAC Health Economics in Prevention and Care*, 1:26, 2000.

L. Lanyon and T. Skerry. Postmenopausal Osteoporosis as a Failure of Bone's Adaptation to Functional Loading: A Hypothesis. *Journal of Bone and Mineral Research*, 16:1937, 2001.

J. S. Nyman, O. C. Yeh, S. J. Hazelwood, and R. B. Martin. A theoretical analysis of long-term bisphosphonate effects on trabecular bone volume and microdamage. *Bone*, 35:296, 2004.

J. N. Israelachvili, D. J. Mitchell, and B. W. Ninham. Theory of self-assembly of hydrocarbon amphiphiles into micelles and bilayers. *Journal of the Chemical Society-Faraday Transactions II*, 72:1525, 1976.

H. Fukuda, K. Kawata, H. Okuda, and S. L. Regen. Bilayer-forming ion-pair amphiphiles from single-chain surfactants. *J. Am. Chem. Soc.*, 112:1635, 1990.

M. Dubois, B. Deme, T. Gulik-Krzywicki, J. C. Dedieu, C. Vautrin, S. Desert, E. Perez, and T. Zemb. Self-assembly of regular hollow icosahedra in salt-free catanionic solutions. *Nature*, 411:672, 2001.

M. L. Lynch, Y. Pan, and R. G. Laughlin. Spectroscopic and thermal characterization of 1 : 2 sodium soap fatty acid acid-soap crystals. *J. Phys. Chem.*, 100:357, 1996.

R. Weinkamer, P. Fratzl, B. Sepiol, and G. Vogl. Monte Carlo simulation of diffusion in a B2-ordered model alloy. *Phys. Rev. B*, 58:3082, 1998.

R. J. Glauber. Time-dependent statistics of ising model. *J. Math. Phys.*, 4: 294, 1963.

K. Kawasaki. In C. Domb and M. S. Green, editors, *Phase Transitions and Critical Phenomena*, New York, 1972. Academic Press.

M. Born and K. Huang. *Dynamical theory of crystal lattices.* Clarendon Press, Oxford, 1988.

T. Zemb, M. Dubois, B. Deme, and T. Gulik-Krzywicki. Self-assembly of flat nanodiscs in salt-free catanionic surfactant solutions. *Science*, 283: 816, 1999.

Publications

1. R. Weinkamer, M. A. Hartmann, Y. Brechet and P. Fratzl
   Stochastic lattice model for bone remodeling and aging
   Physical Review Letters **93**, 228102 (2004)

2. M. A. Hartmann, R. Weinkamer, P. Fratzl, J. Svoboda and F. D. Fischer
   Onsager's coefficients and diffusion laws – a Monte Carlo study
   Philosophical Magazine **85**, 1243 (2005)

3. R. Weinkamer, M. A. Hartmann, Y. Brechet and P. Fratzl
   Architectural changes of trabecular bone caused by the remodeling process
   Mater. Res. Soc. Symp. Proc. **874**, L.1.9.1 (2005)

4. M. A. Hartmann, R. Weinkamer, Th. Zemb, F.D. Fischer and P. Fratzl
   Switching mechanics with chemistry – a model for the bending rigidity of amphiphilic bilayers with oppositely charged head groups
   submitted

Reprinted with permission from:
R. Weinkamer, M. A. Hartmann, Y. Brechet and P. Fratzl
Stochastic lattice model for bone remodeling and aging
Physical Review Letters **93**, 228102 (2004)

(`http://link.aps.org/abstract/PRL/v93/e228102`)

PRL **93,** 228102 (2004) PHYSICAL REVIEW LETTERS week ending 26 NOVEMBER 2004

Stochastic Lattice Model for Bone Remodeling and Aging

Richard Weinkamer,[1,2] Markus A. Hartmann,[1,2] Yves Brechet,[3] and Peter Fratzl[1,2,4,*]
[1]*Max Planck Institute of Colloids and Interfaces, Department of Biomaterials, 14424 Potsdam, Germany*
[2]*Erich Schmid Institute of Materials Science, Austrian Academy of Sciences and University of Leoben, Austria*
[3]*ENSEEG, LTPCM, 38402 Domaine Universitaire de St. Martin d'Hères, Cedex, France*
[4]*Ludwig Boltzmann Institute of Osteology, Hanusch Hospital and UKH-Meidling, Vienna, Austria*

(Received 28 October 2003; published 23 November 2004)

We investigate the remodeling process of trabecular bone inside a human vertebral body using a stochastic lattice model, in which the ability of living bone to adapt to mechanical stimuli is incorporated. Our simulations show the emergence of a networklike structure similar to real trabecular bone. With time, the bone volume fraction reaches a steady state. The microstructure, however, coarsens with a typical length in the system following a power law. The simulation results suggest that a coarsening of the trabecular structure should occur as a natural aging phenomenon, not related to disease.

DOI: 10.1103/PhysRevLett.93.228102 PACS numbers: 87.19.Rr, 02.70.Uu, 05.70.Fh, 87.19.Xx

The internal spongious architecture of living trabecular bone (left inset of Fig. 1) is optimized to withstand the typical loads applied to it in daily life [1,2]. This optimization is due to the bone remodeling process by which specialized bone cells, the osteoclasts, remove mechanically disused or damaged bone, while osteoblasts deposit new bone matrix. The mechanical properties of bone are not only influenced by the trabecular architecture, but by all the different levels in the structural hierarchy [3–6]. Nevertheless, the total amount of trabecular bone as well as its architecture correlate strongly with the fracture incidence in aging or osteoporosis [7] and are the major quantities, which are clinically assessed. A number of attempts have been carried out to model the evolution of trabecular bone mass and architecture as a consequence of bone remodeling [8]. Essentially all these approaches are based on a paradigm which may be called Wolff-Roux law [9], stating that bone material is removed where the local mechanical stimulus is small and added where it is large. According to the mechanostat idea by Frost, bone deposition is activated once a threshold value for the mechanical stimulus is reached [10]. Because of the difficulties of in-vivo experiments, an identification of the stimulus and a precise formulation of the Wolff-Roux law is still missing. Based on this (still rather vague) biological description of the remodeling process, continuum models have been developed in which the bone geometry is described by a continuous density and where the actual propagation of stresses and strains throughout the bone structure are implemented by engineering approaches, mostly finite element modeling (FEM). In this way architectures could be predicted from the Wolff-Roux law, which strongly resembles natural trabecular structures [11–13]. All these descriptions of bone remodeling have in common that the mechanical properties are calculated with considerable accuracy, but with the drawbacks of a mean-field character of the model and of very extensive computer calculations. We propose a lattice model of bone remodeling where the rebuilding process occurs by deposition and removal of bone elements at the surface. Since such surface remodeling models [8] are beyond the FEM capabilities of modern computers, we are forced to simplify the mechanical assessment in our model. Being primarily interested in problems related to a medical context, we want to estimate the effect of external parameters (e.g., a medical treatment or the onset of menopause) on simple quantities, such as bone volume fraction, or average trabecular orientation. Recent simulations of bone remodeling performed in a medical context [14–16] have the serious defect, that the Wolff-Roux law is not considered and the removal and deposition of bone occurs randomly. In an effort to make it as simple as possible, but not simpler, we propose and study a model that is equally simple in handling the biology and the mechanics.

In our model, the spongious architecture of trabecular bone is mapped on a simple cubic lattice (lattice constant a) with occupied and nonoccupied lattice sites corresponding to sites filled with bone matrix and marrow, respectively. In the present Letter, we consider the two-dimensional version of the model, but the extension to three dimensions is straightforward. The whole system is a rectangular box with S_z lattice sites in the vertical z direction and S_x in the horizontal x direction. We model a human vertebral body, which consists of a thin outer shell of compact bone enclosing a core of trabecular bone. The structural boundary conditions are hence a fixed layer of occupied sites around the box. Although the loading situation in a vertebral body within the spine is known to be highly complex [17], a uniaxial loading along the vertical direction with a force F_z is assumed. In addition, we assume that, due to the inwaisting form of vertebral bodies, the deformation in z direction makes the lateral sides bulge inwards, creating a compressive load also in the x direction (Ref. [3], p. 162). The force F_z applied along the z direction leads to a reduction of the vertebral height by ΔL_z, in turn leading to a reduction in width of

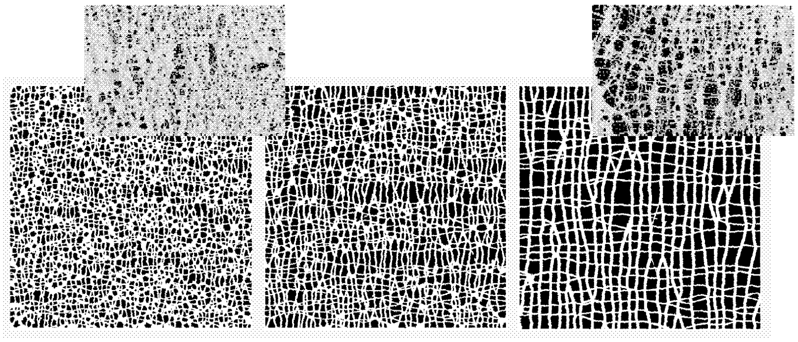

FIG. 1. Simulation snapshots at 3 times: 1.5 kMCS, 2.5 kMCS, and 10 kMCS, from left to right. Bone matrix is indicated white, marrow black. The starting configuration was a random arrangement of occupied sites of high volume fraction ($\rho_{\mathrm{init}} = 0.95$); $\hat{p}_c = 2.5$. The smaller, upper insets show for comparison micrographs of the trabecular bone inside a human vertebra: young and healthy on the left, old and osteoporotic on the right.

the vertebra by ΔL_x (effective negative Poisson ratio of the whole vertebral structure). For small deformations, this geometric coupling leads to a linear relationship $\Delta L_x = k\Delta L_z$. Measurements on human vertebrae suggest values of k in the order of 1. With E_x and E_z, the effective elastic moduli of the trabecular network in x and z direction, the total energy associated with the deformation of the vertebra is

$$W = L_x L_z \left[\frac{1}{2}E_x\left(\frac{\Delta L_x}{L_x}\right)^2 + \frac{1}{2}E_z\left(\frac{\Delta L_z}{L_z}\right)^2 + \frac{1}{2}(1 - \rho)K\left(\frac{\Delta L_x}{L_x} + \frac{\Delta L_z}{L_z}\right)^2\right] - F_z \Delta L_z, \tag{1}$$

the last term being the work of the force F_z, and $L_x = aS_x$, $L_z = aS_z$; K is the bulk modulus of bone marrow and ρ the bone volume fraction. For the purpose of this study we do not take into account the contribution from the marrow ($K = 0$) nor do we consider viscous effects due to viscoelasticity and fluid flow [18]. Minimizing (1) with respect to ΔL_z leads to the result that the system with an applied force F_z and geometrical constraints can be replaced by a system with two independent effective forces F_z^* and F_x^*:

$$F_z^* = \frac{F_z}{\frac{k^2 E_x L_z^2}{E_z L_x^2} + 1}, \qquad F_x^* = \frac{F_z}{\frac{E_z L_x^2}{k E_x L_z^2} + k}. \tag{2}$$

The transmission of the forces F_z^* and F_x^* through the network of bone trabeculae is described via contacts between neighboring occupied sites. In a first step, a two-way painting algorithm [19] is used to determine the loaded sites. Starting with a loaded top layer, the force is transmitted from a loaded site to a neighboring occupied site in the layer below, and additionally to its occupied nearest neighbors in the same layer. This algorithm is carried out layer by layer until the other end of the system is reached. Applying the painting algorithm also in the reverse direction, and keeping only the sites which have been painted twice, the network consisting of all loaded sites is obtained [19,20]. We assume that the applied force F_z^* is partitioned equally between the $M(z)$ loaded branches at level z. Hence, for the Jth branch of the loaded network, the local strain at a site at level z, $\epsilon_z^J(z)$, is given by:

$$aN^J(z)E\epsilon_z^J(z) = \frac{F_z^*}{M(z)}, \tag{3}$$

where $aN^J(z)$ is the thickness of branch J, and E the elastic modulus of the bone material (assumed isotropic). The average strain in z direction can be calculated for the whole vertebra:

$$\frac{\Delta L_z}{L_z} = \frac{1}{S_z}\frac{F_z^*}{Ea}\sum_{z=1}^{S_z}\frac{1}{[M(z)]^2}\sum_{J=1}^{M(z)}\frac{1}{N^J(z)} \equiv \frac{1}{S_z}\frac{F_z^*}{Ea}A_z. \tag{4}$$

All the architectural information about the loaded network is included in A_z, which is dimensionless. Equations analog to (3) and (4) also hold for the horizontal direction (by exchange of x and z). The maximal pressure p on a volume element at position (x, z), which is the mechanical stimulus the bone cells respond to in our model, is then given by:

$$\begin{aligned} p(x,z) &= \max\{|E\epsilon_x^{J'}(x)|, |E\epsilon_z^J(z)|\} \\ &= \frac{F_z}{A_x + k^2 A_z}\max\left\{\frac{kA_z}{M(x)aN^{J'}(x)}, \frac{A_x}{M(z)aN^J(z)}\right\}. \end{aligned} \tag{5}$$

Finally we have to specify the transition probability that a site at the interface changes its state. A fixed probability P^- that a bone site changes to marrow is chosen to describe the action of the osteoclasts [11]. The Wolff-Roux law [1,2] and the ideas of Frost [10] are reflected in the action of the osteoblasts, i.e., in the probability P^+ of forming new bone material. This probability increases with the number n of neighboring sites occupied, and with the pressure p_i acting on the neighboring sites. This latter term is activated only above a given threshold pressure, therefore:

$$P^+(x,z) = n\alpha + \beta\sum_{i=1}^{n} G_i, \qquad G_i = \begin{cases} 0, & \text{if } p_i < p_c \\ \frac{p_i}{p_c}, & \text{if } p_i \geq p_c \end{cases}, \tag{6}$$

where the maximal pressures at the neighboring sites p_i are obtained by Eq. (5). The parameter α denotes the probability of bone formation in absence of a high local pressure; β regulates the magnitude of the "mechanical activation." Note that only $\hat{p}_c \equiv p_c/(F_z/L_x)$ enters the final Eqs. (5) and (6) of our model and that changes in $\hat{p}_c$ can be due to either a different applied stress F_z/L_x or a different activation threshold p_c. Within our time unit—1 Monte Carlo step $= 1$ MCS—each site had, on average, the possibility to change once from bone to marrow or vice versa. Computation times for runs up to 10^4 MCS of less than 100 h on a standard PC (Pentium IV, 2.53 GHz) allowed us to perform an extensive parameter study of our model. Here, we report on the influence of $\hat{p}_c$ on the simulation outcome. Other parameters were assigned fixed values: $S_x = S_z = 1024$, $P^- = 0.007$, $\alpha = 0.003$, $\beta = 0.1$, and $k = 0.9$.

Figure 1 shows three snapshots of the time evolution of our model. The simulation was started with a random configuration of high bone volume fraction $\rho_{\text{init}} = 0.95$. With this homogeneous and isotropic starting configuration, the outcome should not be unintentionally predetermined. Already after short time (left) an intricate networklike structure emerged. While the bone volume fraction decreased, the architecture became coarser (middle) with the trabeculae aligned preferentially along the vertical z and the horizontal x direction. In comparison to the vertical trabeculae, the horizontal ones were thinner and fewer. At later times, ρ showed no further significant decrease (right, also Fig. 2), but the clearly anisotropic structure continued to coarsen. We performed simulations with different starting configurations, e.g., regular quadratic grids with different trabecular thickness and spacing, or a system without bone at all but the compact shell defined by the boundary conditions. For each simulation, the bone volume fraction reached a steady state around 5 kMCS at the latest (Fig. 2). Furthermore, for a given set of simulation parameters the steady state value for the loaded site fraction was independent of the starting configuration. Both of these statements, however, do not hold when looking at the resulting architecture itself. The model is such that trabeculae only disintegrate but are not reconstructed; consequently, the resulting architecture depends on the starting configurations. Despite the fact that the bone volume fraction stays constant, there was a permanent evolution of the trabecular architecture. Typical measures used in bone histomorphometry [21] varied with time: the thickness of the trabeculae increased, while their number decreased. Coarsening of structures with a constant volume fraction is a phenomenon generally encountered in the evolution of morphologies during phase transformations [22]. The coarsening process can then often be described by a single length scale R [23], e.g., the average thickness of trabeculae in our case, which follows a power law as a function of time, $R(t) \propto t^\gamma$, with an exponent γ. We calculate a typical length scale according to $R = \frac{2\rho(1-\rho)}{s}$, with ρ the bone volume fraction and s denoting the bone/marrow interface per unit volume. Figure 3 shows the time evolution of R for different values of $\hat{p}_c \equiv p_c/(F_z/L_x)$. A power law describes the data reasonably well. The coarsening exponent γ increased from about 1/5 to 1/3 with decreasing $\hat{p}_c$ (see inset of Fig. 3). The inset of Fig. 2 shows that when higher values of $\hat{p}_c$ were chosen, lower values for the steady state of the total volume fraction ρ were obtained with approximately a linear relationship between ρ (steady state) and $1/\hat{p}_c$. Parallel with the decrease of bone mass with increasing $\hat{p}_c$, the morphology changed from a networklike structure with vertical and horizontal trabeculae to structures where only a few isolated horizontal trabeculae remained. For high values of $\hat{p}_c$ we observed a columnar structure with only vertical trabeculae.

To establish a connection to the situation in real bone, we convert the lengths and time in the simulation into

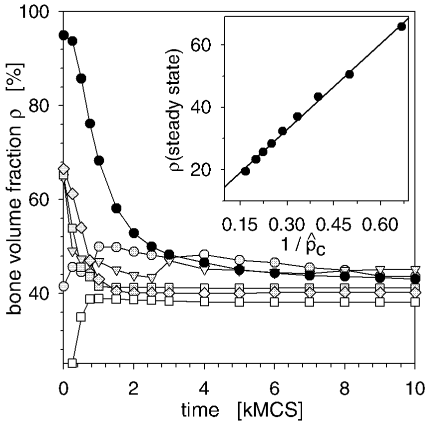

FIG. 2. The bone volume fraction ρ as a function of time for the same simulation parameters, but different starting configurations: random arrangement ($\rho_{\text{init}} = 0.95$) (full circle), empty system with only the frame of the boundary layer occupied (open square), and various regular grids (gray symbols), where grid l, m corresponds to a grid with trabecular thickness l and trabecular spacing n [grid 3,10 (circle), grid 8,12 (triangle), grid 16,24 (square), and grid 32,48 (diamond)]. The inset shows the steady state bone volume fraction as a function of $\hat{p}_c$, the straight line being a linear regression to the data.

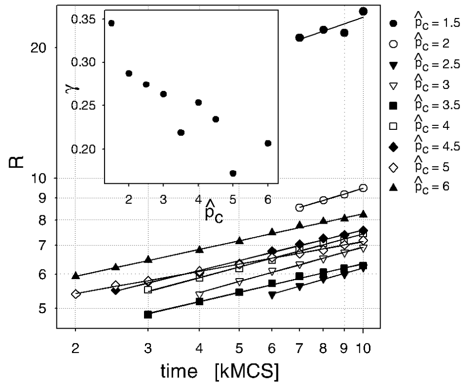

FIG. 3. Double logarithmic plot of the time dependence of a typical length R, as defined in the text, for different values of $\hat{p}_c$ [see Eq. (6)]. All simulations were started with a randomly, highly occupied ($\rho_{\mathrm{init}} = 0.95$) lattice. The number of data points varies since only times inside the coarsening regime with a constant bone volume fraction were included. Straight lines denote a linear regression. The inset shows the power law exponent γ versus $\hat{p}_c$.

physical quantities. Taking as benchmarks a mean trabecular thickness of about 170 μm and a time for a complete bone turnover of about four years for trabecular bone, we get for the model lattice constant $a \approx 30\ \mu$m and a conversion of 1 kMCS $\equiv$ 10 years for the representative simulation in Fig. 1. The time conversion implies that our simulations cover more than a human life. While in-vivo experiments have shown that not static loading, but the loading rate is probably the mechanical stimulus in bone [24,25], it was demonstrated in the appendix of [26] that results from statically loaded models can be transferred to study the effects of dynamical loading. Rik Huiskes and his coworkers also showed that a single local mechanical rule is sufficient to describe the process of bone remodeling (bone maintenance), but also the adaptation of bone to a changing environment (bone modeling), rendering this distinction almost artificial [11].

We follow this idea and present here a model where the Wolff-Roux law is implemented in the action of bone cells. However, bone deposition and resorption is described by adding or removing a discrete bone element, and not by continuously increasing or decreasing the local bone density. Moreover, we set aside a thorough description of the mechanics, e.g., the model does not account for bending moments and shear forces in the trabeculae. In return, we gain the possibility to study the development of a whole vertebra over times comparable to a human life and beyond. As a result, we obtain the time evolution of histomorphological parameters which are still underestimated in the clinical practice. Our model predicts that for a constant activation threshold for osteoblasts and a constant load pattern, the bone mass reaches a steady state value. Most interestingly, trabeculae thicken and their number decreases constantly with age [27] with a power law for the trabecular thickness R. The coarsening process is accompanied by an increasing anisotropy between vertical and horizontal trabeculae. These changes in architecture occur at constant volume fraction only as an age effect. A decrease in bone volume (eventually leading to osteoporosis), would correspond—within the framework of our model—to a change either in the load pattern (e.g., due to bed rest) or in the threshold value for osteoblast activation (e.g., due to modified hormone levels).

---

*Electronic address: fratzl@mpikg-golm.mpg.de

[1] J. Wolff, *Das Gesetz der Transformation der Knochen* (Hirschwald, Berlin, 1892).
[2] W. Roux, Arch. Anat. Physiol., Anat. Abt., 120 (1885).
[3] J. D. Currey, *Bones* (Princeton University Press, Princeton, NJ, 2002).
[4] S. Weiner and H. D. Wagner, Annu. Rev. Mater. Sci. **28**, 271 (1998).
[5] I. Jäger and P. Fratzl, Biophys. J. **79**, 1737 (2000).
[6] H. Gao *et al.*, Proc. Natl. Acad. Sci. U.S.A. **100**, 5597 (2003).
[7] C. H. Turner, Osteoporosis International **13**, 97 (2002).
[8] S. C. Cowin, J. Biomech. Eng. **115**, 528 (1993).
[9] Wolff [1] is often credited as being the first reporting a trabecular architecture optimized for the actual loading of the bone. Roux [2] has in fact formulated the concept of functional adaptation used in modern treatments of the subject [3,26,28]
[10] H. M. Frost, Anat. Rec. **219**, 1 (1987).
[11] R. Huiskes *et al.*, Nature (London) **405**, 704 (2000).
[12] R. Ruimerman *et al.*, Biorheology **40**, 315 (2003).
[13] K. Tsubota, T. Adachi, and Y. Tomita, Journal of Biomechanics **35**, 1541 (2002).
[14] J. C. van der Linden, J. A. N. Verhaar, and H. Weinans, J. Bone Miner. Res. **16**, 688 (2001).
[15] C. M. Langton *et al.*, Bone (N.Y.) **22**, 375 (1998).
[16] S. Tayyar *et al.*, Bone (N.Y.) **25**, 733 (1999).
[17] M. A. Adams and P. Dolan, Clinical Biomechanics **10**, 3 (1995).
[18] Y. P. Arramon and S. C. Cowin, Forma **12**, 209 (1997).
[19] J. Parkinson *et al.*, Journal of Biomechanics **30**, 549 (1997).
[20] G. H. Gunaratne *et al.*, Phys. Rev. Lett. **88**, 068101 (2002).
[21] A. M. Parfitt *et al.*, J. Bone Miner. Res. **2**, 595 (1987).
[22] K. Binder and P. Fratzl, in *Materials Science and Technology*, edited by G. Kostorz (Wiley-VCH, New York, 2001), Vol. 5, Chap. 6.
[23] P. Fratzl *et al.*, Phys. Rev. B **44**, 4794 (1991).
[24] C. Rubin *et al.*, Bone (N.Y.) **30**, 445 (2002).
[25] C. H. Turner, Bone (N.Y.) **23**, 399 (1998).
[26] R. Huiskes, J. Anat. **197**, 145 (2000).
[27] H. M. Frost, J. Bone Miner. Res. **14**, 1816 (1999).
[28] S. C. Cowin, Forma **12**, 247 (1997).

Reprinted with permission from:
M. A. Hartmann, R. Weinkamer, P. Fratzl, J. Svoboda and F. D. Fischer
Onsager's coefficients and diffusion laws – a Monte Carlo study
Philosophical Magazine **85**, 1243 (2005)

Philosophical Magazine,
Vol. 85, No. 12, 21 April 2005, 1243–1260

Onsager's coefficients and diffusion laws—a Monte Carlo study

MARKUS A. HARTMANN†‡, RICHARD WEINKAMER†‡,
PETER FRATZL*†‡, JIŘÍ SVOBODA§ and
FRANZ DIETER FISCHER‡¶||

†Max-Planck-Institute of Colloids and Interfaces, Am Mühlenberg 1,
D-14476 Golm, Germany
‡Erich-Schmid-Institute of Material Science, Austrian Academy of Sciences
and Institute of Metalphysics, University of Leoben, Jahnstrasse 12,
A-8700 Leoben, Austria
§Institute of Physics of Materials, Academy of Sciences of the Czech Republic,
Žižkova 22, CZ-61662 Brno,Czech Republic
¶Institute of Mechanics, Montanuniversität Leoben, Franz-Josef Straße 18,
A-8700 Leoben, Austria
||Materials Center Leoben GmbH, Leoben, Austria

(*Received 14 May 2004; in final form 16 November 2004*)

For a numerical description of multicomponent diffusion processes, the coefficients of the Onsager diffusion matrix are needed. We compare a number of models relating these parameters to experimentally accessible quantities, such as tracer diffusion coefficients. Since these models present different levels of approximation, we investigate the differences in Onsager parameters when they are determined from tracer diffusion. Moreover, we study an ideal solution alloy by Monte Carlo methods to determine the Onsager coefficients directly and using the model assumptions. Measuring atomic fluxes and site fraction gradients, our simulation method is more closely related to a real physical experiment than the usual simulation method of generalized Einstein equations. Onsager's variation principle for the calculation of the kinetic coefficients is extended and it is shown that a reasonable description, even of a simple alloy system, requires consideration of a non-diagonal dissipation matrix in the derivation of the diffusion equations.

1. Introduction

Several approaches have been used to obtain access to the kinetic (Onsager) coefficients that fully describe the diffusional process. The purpose of this paper is twofold. Firstly, it discusses the different theoretical approaches to calculate the Onsager coefficients from experimentally accessible parameters such as tracer

---

*Corresponding author. Email: peter.fratzl@mpikg.mpg.de

Philosophical Magazine
ISSN 1478–6435 print/ISSN 1478–6443 online
http://www.tandf.co.uk/journals
DOI: 10.1080/14786430412331333356

diffusion coefficients. These approaches are the Darken concept [1], Manning's Random Alloy model [2], Moleko's *et al.* self-consistent theory [3] and the approach of Svoboda *et al.*, which uses Onsager's extremal principle as a starting point to determine the kinetic coefficients [4]. A generalized version of this last approach is given, including non-diagonal terms in the dissipation matrix. To test the predictions of the different approaches we secondly present a new simulation method based on Monte Carlo techniques, creating a stationary non-equilibrium situation, which gives us the opportunity to determine Onsager's coefficients in a straightforward manner by measuring site fraction gradients for given fluxes in a computer experiment. A somewhat similar approach was employed by Murch [5, 6], who imposed a gradient in the chemical potential on the system and measured the resulting fluxes to determine the intrinsic diffusion coefficients, but did not calculate the kinetic coefficients L_{ik}. This was done in the work of Kehr *et al.* [7], where an external force was applied to one species by altering the jump probabilities in one direction. Another possibility to study diffusion in a computer experiment is the in-field method, where particles are assumed to be charged and an external electrical field is applied to the system [8–11]. We propose a method were constant fluxes are imposed on the system—although without the introduction of charges by the simultaneous removal and feeding in of atoms (vacancies, respectively) on two opposing sides of the system—and we measure the resulting site fraction gradients. From the fluxes and the site fraction gradients the full Onsager matrix is obtained. Since, in the binary case, the Onsager matrix consists of nine coefficients, we have to first use the symmetry of the coefficients L_{ik} and secondly the constraint $\sum_i L_{ik} = 0$, which follows from the conservation of fluxes, to gain access to all of the coefficients. This is an alternative to the method of Allnatt *et al.* [12], who determined the kinetic coefficients by making use of the generalized Einstein formulae. Our method is applied to the Random Alloy model and the results are compared with the predictions of Darken, Manning, Moleko *et al.* and Svoboda *et al.*

2. Macroscopic theory

Substitutional diffusion in crystalline solid solutions occurs via site exchange between atoms and vacancies [13]. The most general approach describing diffusion in an isotropic crystal in a reference frame fixed to the lattice is given by the Onsager relations between the diffusive fluxes $\mathbf{j}_i$ and the gradients of the chemical potentials μ_k [14, 15]

$$\mathbf{j}_i = -\sum_{k=0}^{n} L_{ik} \nabla \mu_k, \quad i = 0, \ldots, n, \tag{1}$$

where n is the number of atomic components ($i = 1, \ldots, n$) in the system and the index 0 is reserved for vacancies. The L_{ik} coefficients represent a symmetric, positive definite matrix. The gradients of the chemical potentials are related by the Gibbs–Duhem relation [16]

$$\sum_{i=0}^{n} y_i \nabla \mu_i = 0, \tag{2}$$

where y_i denotes the site fraction of species i (i.e. the number of lattice sites occupied by species i divided by the overall number of lattice sites).

Due to the vacancy mechanism the fluxes are constrained by

$$\sum_{i=0}^{n} \mathbf{j}_i = 0. \tag{3}$$

Since (3) holds for arbitrary gradients of chemical potentials $\nabla\mu_k$ ($k = 0, \ldots, n$), inserting (1) into (3) yields constraints amongst the kinetic coefficients L_{ik},

$$\sum_{i=0}^{n} L_{ik} = 0, \quad k = 0, \ldots, n, \tag{4}$$

and the diffusional law (1) can be written as

$$\mathbf{j}_i = -\sum_{k=1}^{n} L_{ik}\nabla(\mu_k - \mu_0), \quad i = 1, \ldots, n, \tag{5}$$

where the sum runs only over the atomic components. The vacancy flux $\mathbf{j}_0$ can be calculated from the constraint (3).

The gradient of the chemical potential of vacancies $\nabla\mu_0$ can be eliminated from (5) using (2), which leads to

$$\mathbf{j}_i = -\sum_{k=1}^{n}\left(\frac{L_{ik}}{y_k} - \frac{L_{i0}}{y_0}\right) y_k \nabla\mu_k, \quad i = 0, \ldots, n. \tag{6}$$

In the framework of the Random Alloy model [2] the diffusion kinetics is determined by the exchange rates ω_i of the vacancies with species i. The n kinetic parameters ω_i therefore determine the free parameters in this model. In strict mathematical reasoning the number of independent coefficients is equal to the number of free parameters n. However, since the relations between the kinetic coefficients are not trivial to determine, in practice the number of independent coefficients L_{ik} in the Random Alloy model is equal to $n(n-1)/2$ (symmetry of the Onsager matrix, flux constraint and n sum rules [17]). In the theoretical approaches of [2, 3] the coefficients L_{ik} are expressed as functions of the exchange rates ω_i or of the tracer diffusion coefficients D_i. In the concepts of [1, 4], the coefficients L_{ik} are only related to the experimentally accessible tracer diffusion coefficients D_i of atomic species i, without consideration of the microscopic details of the diffusion process. Since the Random Alloy model has frequently been employed for diffusion investigations using different assumptions, we have again chosen this model for our simulations to compare the predictions of the different approaches. We restrict our investigations to binary alloys with vacancies.

2.1. *Binary ideal solution*

In the binary system, A and B denote the two atomic species and V the vacancies. For ideal solutions the chemical potentials are given by [16]

$$\mu_i = \mu_{0i} + RT \ln y_i, \quad i = \mathrm{A, B, V}, \tag{7}$$

where μ_{0i} is a constant, R is the gas constant and T the absolute temperature. The Gibbs–Duhem relation (2) is then a direct consequence of the trivial condition

$$y_\mathrm{A} + y_\mathrm{B} + y_\mathrm{V} = 1. \tag{8}$$

Hence, for ideal solutions (1) can be rewritten in the form

$$\begin{aligned} \mathbf{j}_{\mathrm{A}} &= -RT\left(\frac{L_{\mathrm{AA}}}{y_{\mathrm{A}}}\nabla y_{\mathrm{A}} + \frac{L_{\mathrm{AB}}}{y_{\mathrm{B}}}\nabla y_{\mathrm{B}} + \frac{L_{\mathrm{AV}}}{y_{\mathrm{V}}}\nabla y_{\mathrm{V}}\right), \\ \mathbf{j}_{\mathrm{B}} &= -RT\left(\frac{L_{\mathrm{BA}}}{y_{\mathrm{A}}}\nabla y_{\mathrm{A}} + \frac{L_{\mathrm{BB}}}{y_{\mathrm{B}}}\nabla y_{\mathrm{B}} + \frac{L_{\mathrm{BV}}}{y_{\mathrm{V}}}\nabla y_{\mathrm{V}}\right), \\ \mathbf{j}_{\mathrm{V}} &= -RT\left(\frac{L_{\mathrm{VA}}}{y_{\mathrm{A}}}\nabla y_{\mathrm{A}} + \frac{L_{\mathrm{VB}}}{y_{\mathrm{B}}}\nabla y_{\mathrm{B}} + \frac{L_{\mathrm{VV}}}{y_{\mathrm{V}}}\nabla y_{\mathrm{V}}\right). \end{aligned} \tag{9}$$

The diffusional process can now alternatively be described by equation (5) or (6). While in the first description one has to deal with differences among the gradients of site fractions, in the latter differences among the kinetic coefficients occur. In the binary case the two characterizations read

$$\begin{aligned} \mathbf{j}_{\mathrm{A}} &= -RTL_{\mathrm{AA}}\left[\frac{\nabla y_{\mathrm{A}}}{y_{\mathrm{A}}} - \frac{\nabla y_{\mathrm{V}}}{y_{\mathrm{V}}}\right] - RTL_{\mathrm{AB}}\left[\frac{\nabla y_{\mathrm{B}}}{y_{\mathrm{B}}} - \frac{\nabla y_{\mathrm{V}}}{y_{\mathrm{V}}}\right], \\ \mathbf{j}_{\mathrm{B}} &= -RTL_{\mathrm{BA}}\left[\frac{\nabla y_{\mathrm{A}}}{y_{\mathrm{A}}} - \frac{\nabla y_{\mathrm{V}}}{y_{\mathrm{V}}}\right] - RTL_{\mathrm{BB}}\left[\frac{\nabla y_{\mathrm{B}}}{y_{\mathrm{B}}} - \frac{\nabla y_{\mathrm{V}}}{y_{\mathrm{V}}}\right], \end{aligned} \tag{10}$$

or

$$\begin{aligned} \mathbf{j}_{\mathrm{A}} &= -RT\left[\frac{L_{\mathrm{AA}}}{y_{\mathrm{A}}} - \frac{L_{\mathrm{AV}}}{y_{\mathrm{V}}}\right]\nabla y_{\mathrm{A}} - RT\left[\frac{L_{\mathrm{AB}}}{y_{\mathrm{B}}} - \frac{L_{\mathrm{AV}}}{y_{\mathrm{V}}}\right]\nabla y_{\mathrm{B}}, \\ \mathbf{j}_{\mathrm{B}} &= -RT\left[\frac{L_{\mathrm{BA}}}{y_{\mathrm{A}}} - \frac{L_{\mathrm{BV}}}{y_{\mathrm{V}}}\right]\nabla y_{\mathrm{A}} - RT\left[\frac{L_{\mathrm{BB}}}{y_{\mathrm{B}}} - \frac{L_{\mathrm{BV}}}{y_{\mathrm{V}}}\right]\nabla y_{\mathrm{B}}, \end{aligned} \tag{11}$$

where $L_{\mathrm{AB}} = L_{\mathrm{BA}}$. Both equations allow experimental access to the kinetic coefficients by measuring site fraction gradients and fluxes. The coefficients L_{ik} depend in a non-trivial way on the site fractions y_{A} and y_{B}. Usually, this dependence is separated by introducing a collective correlation factor f_{ik} defined by [18, 19]

$$L_{ik} = L_{ik}^{(0)} f_{ik}, \tag{12}$$

with

$$L_{ik}^{(0)} = \frac{r^2 y_0 \omega_i y_i}{6RT\Omega}.$$

This is similar to the definition of the tracer correlation factor f_i via

$$D_i = \frac{r^2 y_0 \omega_i f_i}{6}, \tag{13}$$

where D_i is the tracer diffusion coefficient and r the distance of an elementary diffusion jump; the product of the vacancy concentration and the exchange frequency $y_0\omega_i$ is called the jump frequency. In both cases, the only parameters depending on concentration in a non-trivial way are the collective and tracer correlation factors f_{ik} and f_i, respectively. However, it should be emphasized that f_i and f_{ik} are different parameters, and exact relations between them hold only in some special cases. The diagonal collective tracer correlation factor can be expanded as a sum of the tracer correlation factor and a two-particle correlation factor. If the concentration of one species tends to zero, the corresponding diagonal collective correlation factor tends to the tracer correlation factor [20]. The challenge addressed in this paper is to determine L_{ik} as a function of measurable parameters, such as D_i.

2.2. *Darken's concept*

Originally, Darken's theory was designed for systems where no gradient of μ_V and, hence, of y_V exists in the system [1, 15]. It is assumed that Fick's first law holds for components A and B separately

$$\mathbf{j}_i = -\frac{D_i}{\Omega}\nabla y_i, \quad i = \mathrm{A}, \mathrm{B}, \tag{14}$$

where Ω is the mean atomic volume. A comparison of equations (9) and (14) results in

$$L_{\mathrm{AA}} = \frac{D_{\mathrm{A}} y_{\mathrm{A}}}{RT\Omega}, \qquad L_{\mathrm{BB}} = \frac{D_{\mathrm{B}} y_{\mathrm{B}}}{RT\Omega}, \qquad L_{\mathrm{AB}} = 0. \tag{15}$$

The full L_{ik} matrix can be determined by making use of the constraints (4).

2.3. *Manning's concept*

Manning calculated the kinetic coefficients L_{ik} for the Random Alloy by means of the exchange frequencies ω_i or the tracer diffusion coefficients D_i of all atomic components [2]. The latter equations read

$$L_{ik} = \frac{y_i D_i}{RT\Omega}\left(\delta_{ik} + \frac{1-f_0}{f_0}\frac{y_k D_k}{y_{\mathrm{A}} D_{\mathrm{A}} + y_{\mathrm{B}} D_{\mathrm{B}}}\right), \quad i,k = \mathrm{A}, \mathrm{B}, \tag{16}$$

and

$$L_{i\mathrm{V}} = -\frac{y_i D_i}{RT\Omega f_0}, \quad i = \mathrm{A}, \mathrm{B}; \qquad L_{\mathrm{VV}} = \frac{y_{\mathrm{A}} D_{\mathrm{A}} + y_{\mathrm{B}} D_{\mathrm{B}}}{RT\Omega f_0},$$

where f_0, the geometric correlation factor, depends only on the lattice type of the crystal and the diffusion mechanism (e.g. $f_0 \approx 0.7815$ for the vacancy mechanism in a fcc alloy). Manning's theory is based on the definition of a single escape frequency for the vacancy, that is a single time constant for the loss of correlations between vacancy/atom exchanges. The resulting equations differ significantly from Darken's result due to $L_{\mathrm{AB}} \neq 0$. The L_{ik} coefficients given by relations (16) fulfil the constraints (4) trivially. Lidiard showed [21] that Manning's equations (16) could be derived without considering the Random Alloy model. His reasoning is based on two macroscopic assumptions, the relation between self- and chemical diffusion and that between the mobility of the atoms in the pure material and the alloy.

2.4. *Moleko* et al.*'s concept*

Using linear response theory, Moleko *et al.* calculated the kinetic coefficients for the Random Alloy model [3]. The crucial difference to Manning's approach is that, in this calculation, different escape frequencies for each atomic component are assumed. Using a self-consistent approach to decouple the resulting equations yields, for the collective correlation factors,

$$\begin{aligned} f_{\mathrm{AA}} &= 1 - \frac{2\omega_{\mathrm{A}} y_{\mathrm{B}}}{\Gamma}, \quad & f_{\mathrm{AB}} &= \frac{2\omega_{\mathrm{B}} y_{\mathrm{B}}}{\Gamma}, \\ f_{\mathrm{BA}} &= \frac{2\omega_{\mathrm{A}} y_{\mathrm{A}}}{\Gamma}, \quad & f_{\mathrm{BB}} &= 1 - \frac{2\omega_{\mathrm{B}} y_{\mathrm{A}}}{\Gamma}, \end{aligned} \tag{17}$$

with

$$\begin{aligned} \Gamma = {} & \frac{1}{2}(M_0 + 2)(y_{\mathrm{A}}\omega_{\mathrm{A}} + y_{\mathrm{B}}\omega_{\mathrm{B}}) - \omega_{\mathrm{A}} - \omega_{\mathrm{B}} + 2(y_{\mathrm{A}}\omega_{\mathrm{B}} + y_{\mathrm{B}}\omega_{\mathrm{A}}) \\ & + \left\{ \left[\frac{1}{2}(M_0 + 2)(y_{\mathrm{A}}\omega_{\mathrm{A}} + y_{\mathrm{B}}\omega_{\mathrm{B}}) - \omega_{\mathrm{A}} - \omega_{\mathrm{B}} \right]^2 + 2M_0\omega_{\mathrm{A}}\omega_{\mathrm{B}} \right\}^{1/2}, \end{aligned}$$

where

$$M_0 = \frac{2f_0}{1 - f_0}.$$

L_{ik} can then be obtained using equation (12). Note that, in principle, Moleko *et al.*'s concept also allows us to relate the tracer diffusion coefficients to the L_{ik} coefficients. In [19] the diffusion coefficients are given as a function of the jump frequencies, $D_i = D_i(\omega_{\mathrm{A}}, \omega_{\mathrm{B}})$. Therefore, inverting these equations, yielding $\omega_i = \omega_i(D_{\mathrm{A}}, D_{\mathrm{B}})$, and inserting the result into (17) results in $L_{ik} = L_{ik}(D_{\mathrm{A}}, D_{\mathrm{B}})$. Since the equations are quite complex, no simple analytic results can be given for the inversion.

2.5. *Allnatt* et al.*'s concept*

Allnatt *et al.* derived an expression for the kinetic coefficients L_{ik} similar to the Einstein formula for the tracer diffusion coefficients. The tracer diffusion coefficient can be expressed as [15, 22]

$$D_i = \frac{\langle \Delta \mathbf{r}^2 \rangle_i}{6t} = \frac{(1/N_i)\sum_{m=1}^{N_i} \Delta \mathbf{r}_i^2(m,t)}{6t}, \quad i = \mathrm{A}, \mathrm{B}, \tag{18}$$

where $\Delta \mathbf{r}_i(m,t)$ is the displacement of atom m of species i during time t and N_i is the number of atoms of species i. Allnatt *et al.*'s concept enables us to evaluate all L_{ik} coefficients by means of generalized Einstein formulae [12, 23]

$$L_{ik} = \frac{\langle \Delta \mathbf{R}_i(t) \cdot \Delta \mathbf{R}_k(t) \rangle}{6n\Omega RTt}, \quad i,j = \mathrm{A}, \mathrm{B}. \tag{19}$$

Here, $\Delta \mathbf{R}_i(t)$ denotes the sum over all displacements of atoms of kind i at time t, i.e.

$$\Delta \mathbf{R}_i(t) = \sum_{m=1}^{N_i} \Delta r_i(m,t). \tag{20}$$

The brackets in (19) denote a thermodynamic average, n denotes the number of moles of all species and T the temperature. Again, the full L_{ik} matrix can be determined using (4). Allnatt *et al.*'s concept gives no analytical results, but is a perfect tool for measuring the kinetic coefficients in a Monte Carlo computer experiment.

2.6. ***Generalized Svoboda* et al. *concept***

Svoboda *et al.* [4] used the thermodynamic extremal principle of maximal dissipation [24] for the derivation of the diffusional law for constrained fluxes. As a starting point it was assumed that the total Gibbs energy dissipation rate Q is given as a quadratic form of the fluxes

$$Q = \int_V \left(\sum_{i,k=0}^{n} B_{ik} j_i j_k \right) \mathrm{d}V, \tag{21}$$

with the matrix B_{ik} being symmetric and positive definite. According to the derivation in [4] the thermodynamic extremal principle asserts that

$$\delta\left(U + \frac{Q}{2} \right) = 0, \tag{22}$$

where U is the rate of change of the Gibbs energy and Q is the rate of Gibbs energy dissipation within the system due to the diffusion process. Insertion of the respective quantities into (22) leads to

$$\delta\left(\int_V \sum_{i=0}^{n} j_i \nabla \mu_i + \frac{1}{2} \int_V \sum_{i,k=0}^{n} j_i j_k B_{ik} \right) = 0. \tag{23}$$

Eliminating the vacancy flux by using the flux constraint (3) in (23) leads to

$$\delta\left(\int_V \sum_{i=1}^{n} j_i \nabla(\mu_i - \mu_0) + \frac{1}{2} \int_V \sum_{i,k=1}^{n} C_{ik} j_i j_k \right) = 0, \tag{24}$$

where the summation now runs only from 1 to n. The matrix C_{ik} is defined by

$$C_{ik} \equiv B_{ik} - B_{0k} - B_{i0} + B_{00}. \tag{25}$$

Note, firstly, that the matrix C_{ik} is also symmetric as is B_{ik}, and, secondly, that the entries C_{i0} are zero. The latter property is due to the elimination of the vacancy flux; since it is completely determined by the atomic fluxes, it cannot contribute to the dissipation. Differentiation of (24) with respect to j_i leads to

$$\sum_{k=1}^{n} C_{ik} j_k = -\nabla(\mu_i - \mu_0). \tag{26}$$

Inversion of this equation and comparison with the diffusion law in the Onsager form given by (10) results in

$$j_i = -\sum_{k=1}^{n} C_{ik}^{-1} \nabla(\mu_k - \mu_0) = -\sum_{k=1}^{n} L_{ik} \nabla(\mu_k - \mu_0). \tag{27}$$

Consequently, the identity

$$L_{ik} = C_{ik}^{-1}, \quad i,k = 1,\ldots,n \tag{28}$$

applies. The remaining coefficients L_{i0} can be determined by making use of (4). Conversely, given the Onsager matrix L_{ik} results in the dissipation rate Q

$$Q = \int_V \sum_{i,k=1}^{n} L_{ik}^{-1} j_i j_k. \tag{29}$$

An alternative approach to relate the dissipation matrix B_{ik} to the Onsager coefficients can be obtained by working in the special coordinate system that renders a diagonal form for B_{ik}. The special case of a diagonal dissipation matrix was discussed in [4]. With $B_{ik} = \delta_{ik}/A_i$, δ_{ik} the Kronecker delta, the resulting matrix $C_{ik} = \delta_{ik}/A_i + 1/A_0$ can be inverted analytically and leads directly to the form of the kinetic coefficients given in [4]

$$L_{ik} = A_i\left(\delta_{ik} - \frac{A_k}{\sum_{l=0}^{n} A_l}\right), \quad i, k = 0, \dots, n. \tag{30}$$

Based on a treatment by Lidiard, the coefficients A_i can be determined in the following way. In the multicomponent system the fluxes are given by the formulae

$$\mathbf{j}_i = -A_i \nabla\mu_i + \frac{A_i}{\sum_{k=0}^{n} A_k} \sum_{k=0}^{n} A_k \nabla\mu_k, \quad i = 0, \dots, n, \tag{31}$$

which can be rewritten in the form

$$\mathbf{j}_i = -A_i(\nabla\mu_i - \nabla\mu_0) + \frac{A_i}{A_0}\mathbf{j}_0, \quad i = 1, \dots, n. \tag{32}$$

We consider the special case of the tracer diffusion of a radioisotope in a system that is chemically in equilibrium. The only driving forces in the system are the opposite concentration gradients of the radioisotope of component i, denoted by i', and of the usual atoms of component i. No gradients of the chemical potentials of vacancies and no vacancy fluxes exist. For an ideal solution of the tracer equation, (32) can be rewritten as

$$\mathbf{j}_{i'} = -A_{i'} \nabla\mu_{i'} = -A_{i'} \frac{RT}{y_{i'}} \nabla y_{i'}. \tag{33}$$

In the tracer experiment, Fick's first law (14) applies. A comparison of equations (14) for the tracer i' and (33) results in

$$A_{i'} = \frac{y_{i'} D_{i'}}{\Omega RT}. \tag{34}$$

The remaining task is to evaluate A_0. Using (31) the vacancy flux in a tracer experiment can be formally expressed as

$$\mathbf{j}_0 = \frac{A_0}{\sum_{k=0}^{n} A_k}(A_i \nabla\mu_i + A_{i'} \nabla\mu_{i'}) = 0. \tag{35}$$

The vacancy flux consists of two fluxes due to $\nabla\mu_i$ and $\nabla\mu_{i'}$, which compensate each other. The different correlation factors means that, for the same driving force, the diffusive flux of vacancies is approximately $1/f_0$ times larger and opposite to that of the atoms—this approximation corresponds to Lidiard's second assumption [21] mentioned earlier. A comparison of (33) and of the first term on the right-hand side of (35) multiplied by f_0 leads to

$$A_{i'} \nabla\mu_{i'} = f_0 \frac{A_0}{\sum_{k=0}^{n} A_k} A_{i'} \nabla\mu_{i'}, \tag{36}$$

and, therefore,

$$A_0 = -\frac{1}{1 - f_0} \sum_{i=1}^{n} A_i. \tag{37}$$

In the special case of a binary alloy

$$A_{\mathrm{V}} = -\frac{1}{1-f_0}(A_{\mathrm{A}} + A_{\mathrm{B}}). \tag{38}$$

Note that this is different from the expression in the appendix of [4], where vacancy correlation effects were neglected.

Insertion of A_{V} from (38) into (30) using (34) leads directly to Manning's expressions (16). Since [21] showed that Manning's findings are independent of the microscopic details of the model, the similarity of the results might not be surprising.

A number of models for the evolution of the material microstructure or properties at elevated temperatures can be derived from the Onsager extremal principle formulated for discrete state parameters [25]. Such models may be further improved by expressing the dissipation rate Q by means of Onsager coefficients as shown in this paper. The advantage of this approach is that it can be utilized in the future for the development of finite-element codes.

2.7. *Summary*

We have presented four different concepts of diffusion laws, each expressing the kinetic coefficients as a function of the tracer diffusion factors $L_{ik} = L_{ik}(D_{\mathrm{A}}, D_{\mathrm{B}})$ (I) or as a function of the exchange frequencies $L_{ik} = L_{ik}(\omega_{\mathrm{A}}, \omega_{\mathrm{B}})$ (II). Firstly, the concept of Darken giving a result of form (I) proves to be a poor description of the diffusional process. Secondly and thirdly, Manning's and Moleko *et al.*'s concepts give the kinetic coefficients in both forms (I) and (II). Both results of Moleko *et al.* provide an accurate description of the diffusion process, whereas only result (II) of Manning's concept proves to be accurate (in fact, for a binary random alloy, the results (II) of Moleko *et al.* and Manning are equivalent) [18, 26, 27]. Fourthly, Svoboda *et al.*'s concept, an entirely macroscopic description, gives the Onsager coefficients in form (I). With additional assumptions concerning the role of the vacancies, the results (I) of Svoboda *et al.* and Manning are equivalent.

3. Microscopic model

The simulations were performed on a fcc lattice (lattice constant a) consisting of 16 cubic unit cells including four atoms in the x direction and 64 unit cells in the y and z direction, respectively, corresponding to $N = 4 \times 16 \times 64^2 = 262\,144$ lattice sites. While on the x axis (the direction of the imposed flux) fixed boundaries were chosen, periodic boundary conditions were implemented for the other directions. The lattice was occupied randomly with atoms A and B and vacancies with fixed site fractions y_{A}, y_{B}, and y_{V}, respectively. The system evolved in time by the exchange of a randomly chosen vacancy with one of its 12 nearest neighbours (NN). According to the Random Alloy model [2] the exchange of an A (B) atom and a vacancy is accepted with a fixed probability of $p_{\mathrm{A}} = 1$ ($p_{\mathrm{B}} \leq 1$—the results shown here were obtained with $p_{\mathrm{B}} = 0.1$). The time unit of our simulation was one Monte Carlo step (MCS), i.e. one jump trial per lattice site. To improve the statistics, up to five independent runs were performed to obtain a single data point. Since no interaction between the atoms is considered, the model alloy represents an ideal solution, and, consequently, the chemical potentials are given by (7).

3.1. *Determination of tracer diffusion constants D_i and collective correlation factors f_{ik}*

The diffusion coefficients D_A and D_B were determined as a function of composition by measuring the mean square displacement (MSD) of the different atomic species. The displacement vector $\Delta\mathbf{r}$ of each single atom was monitored and after each MCS the MSD was calculated separately for the two atomic species. Using the well-known Einstein relation [15, 22] (18) the tracer diffusion constant D_i is determined by a linear regression of the MSD with respect to time. The resulting diffusion coefficient showed a significant concentration dependence (see figure 2), as predicted in [3] and confirmed in [19]. Our results are in full agreement with these former results.

The collective correlation factors f_{ik} are determined in a similar way. According to Allnatt *et al.*'s concept, the displacement of all atoms of one species now has to be considered, not only the displacement of one single atom (see equation (19)). Results are shown in figure 3.

3.2. *Determination of kinetic coefficients L_{ik}*

To obtain the kinetic coefficients L_{ik}, constant fluxes j_A, j_B and j_V are imposed on the system. From the resulting measured concentration gradients ∇y_A, ∇y_B (and $\nabla y_V = -\nabla y_A - \nabla y_B$) the coefficients L_{AA}, L_{AB}, L_{BA} and L_{BB} are then calculated according to equation (10). Imposing the fluxes on the system was done in the following way. A suitable time interval Δt was chosen (see below). After each interval Δt an atom of species i on the outermost right boundary lattice plane was selected at random and exchanged with an atom of species k on the outermost left boundary lattice plane. This causes a constant flux of i atoms along the x axis with

$$j_i = (\Delta t \cdot d^2)^{-1}, \tag{39}$$

and, additionally, a negative flux of k atoms balancing the i flux ($d = 64$ in our simulations). The most general situation is imposed when the balance is established by the flux of both of the other species. As an example, the flux of A atoms is balanced by fluxes of B atoms and vacancies by exchanging every nth time an A atom with a vacancy, otherwise an A atom is exchanged with a B atom. The resulting fluxes are then

$$j_A = (\Delta t \cdot d^2)^{-1}, \tag{40}$$

$$j_B = -\left(\frac{n}{n-1}\Delta t \cdot d^2\right)^{-1}, \tag{41}$$

$$j_V = -(n\Delta t \cdot d^2)^{-1}. \tag{42}$$

Evidently, the conservation of fluxes (3) is fulfilled. Starting the simulation from a random configuration of atoms, such an additional exchange rule gave rise to a concentration gradient that reached a steady state after approximately 10 000 MCS (figure 1). Our choice that the lattice dimension in the x direction was much smaller than in the y and z direction (16 versus 64) assured linear concentration profiles, i.e. constant concentration gradients, with satisfying accuracy. The fluxes had to be chosen sufficiently large to ensure measurable gradients, but small enough to account for the mobility of the atoms and therefore to avoid accumulation of one sort of atom on one side. These conditions impose an upper and lower limit on the

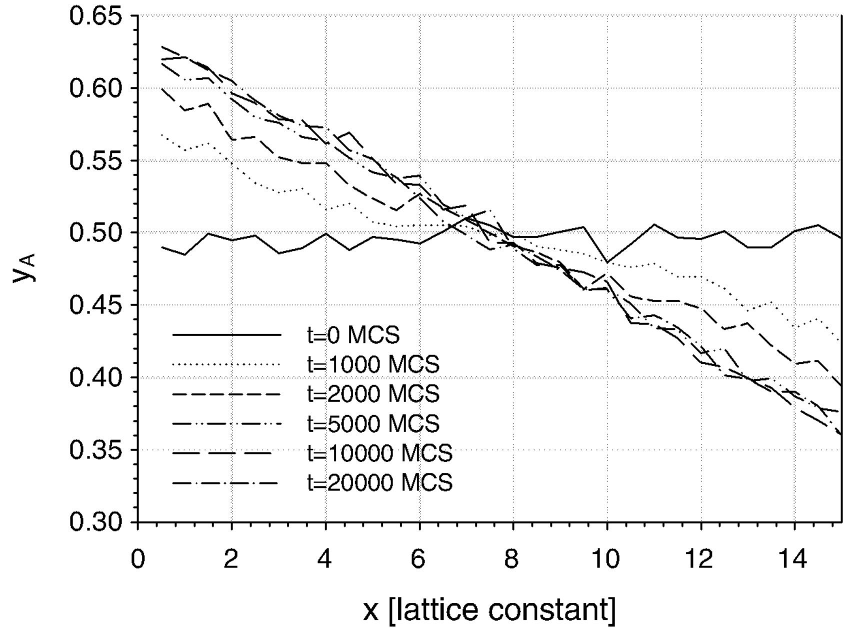

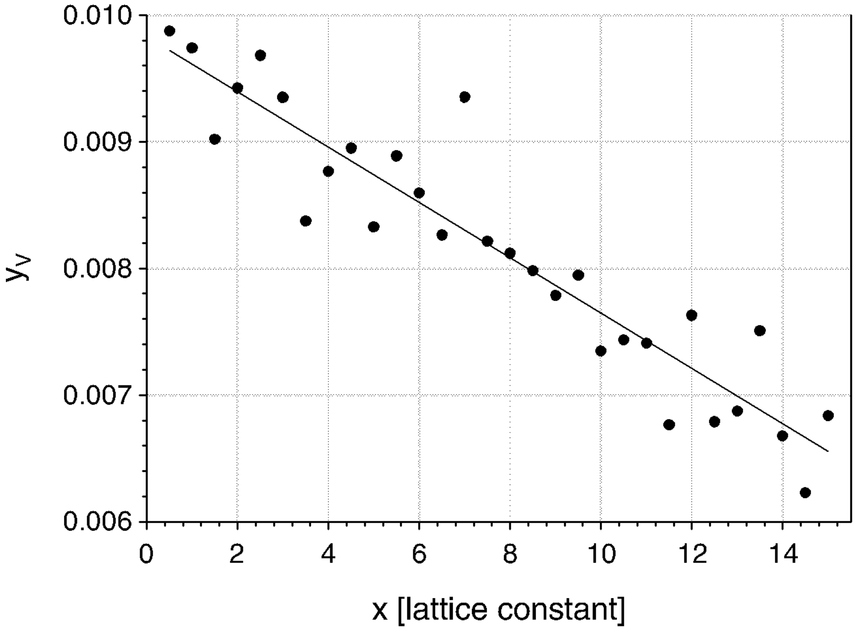

Figure 1. Top: A typical time evolution of the concentration profile for the A atoms. The initial horizontal condition of the simulation ($t = 0$ MCS, solid line) is a random distribution of the atoms, resulting in a horizontal concentration curve without any gradient. At later times ($t = 1000$, 2000, 5000, 10 000 and 20 000 MCS, respectively) the imposed flux ($j_A = 0.001$ $(a^2 * \text{MCS})^{-1}$, $j_B = -0.001$ $(a^2 * \text{MCS})^{-1}$, $j_V = 0$) leads to the formation of a concentration gradient, which reaches a steady state at approximately 10 000 MCS. Bottom: The resulting gradient for the vacancy-site fraction (averaged over ten runs from 10 000 to 20 000 MCS). Since the vacancy flux is zero, the emerging gradient shows that the Onsager matrix is not diagonal.

Table 1. Combinations of fluxes used. The fluxes are measured in $10^{-4}(a^2 * \mathrm{MCS})^{-1}$.

Run	j_A	j_B	j_V
1	4.8	−4.8	0.0
2	8.0	0.0	−8.0
3	0.0	4.8	−4.8
4	8.0	−4.0	−4.0
5	−1.2	2.4	−1.2
6	−2.4	−2.4	4.8

choice of Δt. A suitable time interval was found (see table 1) for the concentration ranges investigated in this work.

Each equation of (10) comprises two unknowns, L_AA, L_AB or L_BA, L_BB. Hence, at least two independent computer experiments corresponding to two different imposed fluxes are necessary to determine the kinetic coefficients L_{ik}. The accuracy of the results can be improved significantly by imposing a greater variety of fluxes and studying their effect. For this investigation, six flux situations, as different as possible, were used (see table 1 for the fluxes).

The overdetermined set of equations (two unknowns and six equations) can be solved by transforming the problem into a least-square problem [28].

The missing data for the tracer simulation for site fractions less than 0.1 and for the kinetic coefficients also for site fractions larger than 0.9 is due to the impracticability of obtaining continuous and measurable site fraction profiles for a small number of atoms.

4. Results of the simulations

As a first test of this new method of flux-gradient measurement, a simulation according to a classical tracer experiment was performed. In such a tracer experiment the only non-vanishing site fraction gradient emerges from chemically identical isotopes A and A′. The relation between the atomic flux and the concentration gradient is then given by Fick's first law (14). The tracer experiment is simulated by subdividing the A atoms into two classes, A and A′. A flux is now imposed on the system by exchanging A and A′ atoms only, producing neither a flux nor a gradient in B atoms or vacancies. The gradient in A (and therefore in A′, since $\nabla y_{\mathrm{A}'} = -\nabla y_\mathrm{A}$) is measured and the diffusion coefficient is obtained from

$$D_\mathrm{A} = -\Omega \frac{j_\mathrm{A}}{\nabla y_\mathrm{A}}, \tag{43}$$

where $\Omega = 1/4a^3$, a being the lattice constant. Figure 2 shows the diffusion coefficient D_A as a function of composition obtained from the tracer experiment. For comparison, the results for D_A are plotted evaluating the mean square displacement (MSD) of the atoms. The two sets of data coincide within the error bars.

The large open symbols in the three plots of figure 3 summarize the simulation results for the kinetic coefficients L_{ik} as a function of composition. Not included in the figure are the coefficients L_AV, L_BV and L_VV, since they are deduced using (4) without new information. In the evaluation, symmetry of the matrix was not

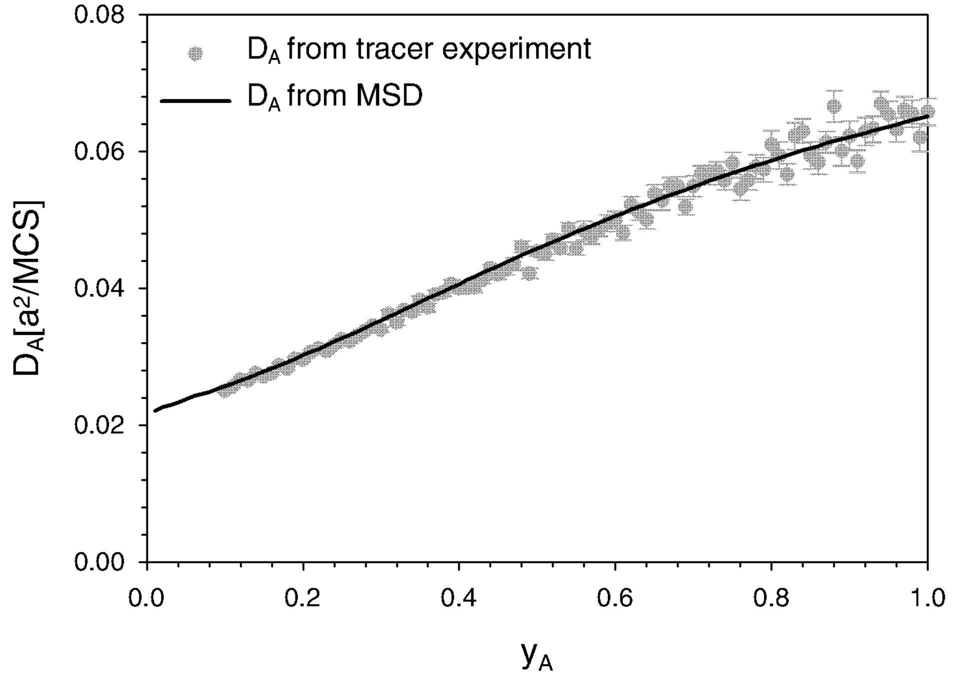

Figure 2. The tracer diffusion coefficient D_A determined by a tracer computer experiment and by the MSD calculation. The error bars were calculated according to the fitting error of the resulting concentration gradients.

assumed, therefore L_{AB} and L_{BA} are independent results plotted in the same graph. The small black symbols are the result for the kinetic coefficients obtained by means of the generalized Einstein formulae (see equation (19)). The error bars indicate that, with the latter simulation, less noisy results can be obtained even with smaller computational effort. For comparison with the simulation results the different lines present the analytical predictions of the concepts of Moleko *et al.*, Svoboda *et al.* and Darken. The general tendency of the computational and theoretical results is identical, e.g. L_{AA} increases with a larger site fraction of the faster A atoms. A closer look, however, reveals clear distinctions, which are most obvious for the different kinetic coefficients at varying compositions. For instance, in the case of L_{AA} the differences are greatest for a large site fraction of A atoms. Also, the error bars for the direct L_{ik} measurements become very large. All plots show good agreement between Moleko *et al.*'s result and the simulation results using the generalized Einstein formulae. The assumption of Darken of vanishing off-diagonal terms in the Onsager matrix causes the predictions to deviate significantly.

5. Discussion

Due to correlation effects, diffusion in crystalline solids proves to be a non-trivial problem. Figure 2 shows the tracer diffusion coefficient as a function of composition for the faster diffusing species. Although the model is as simple as possible a marked concentration dependence can be observed, which can be easily

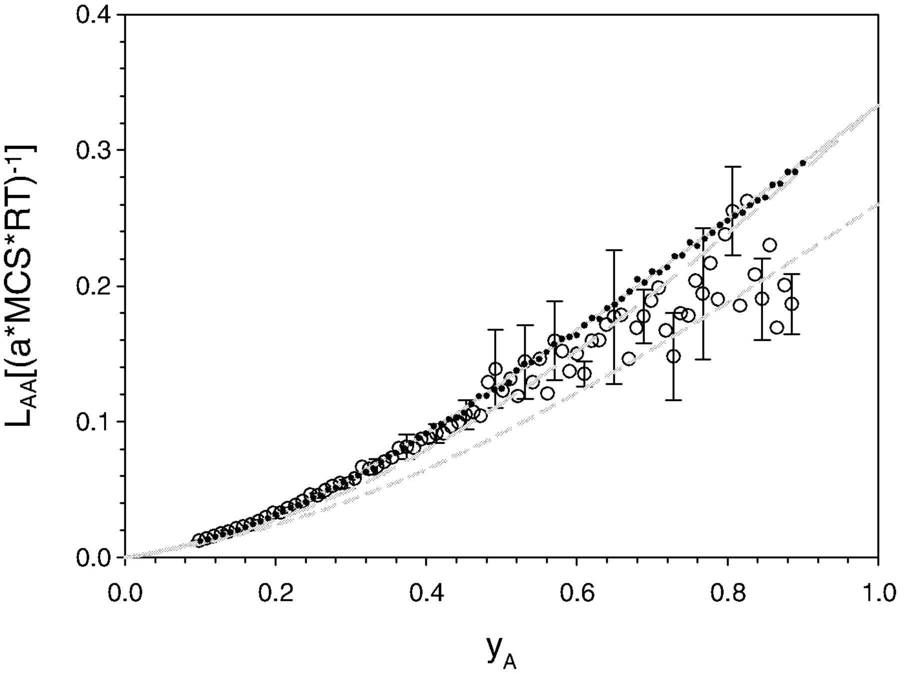

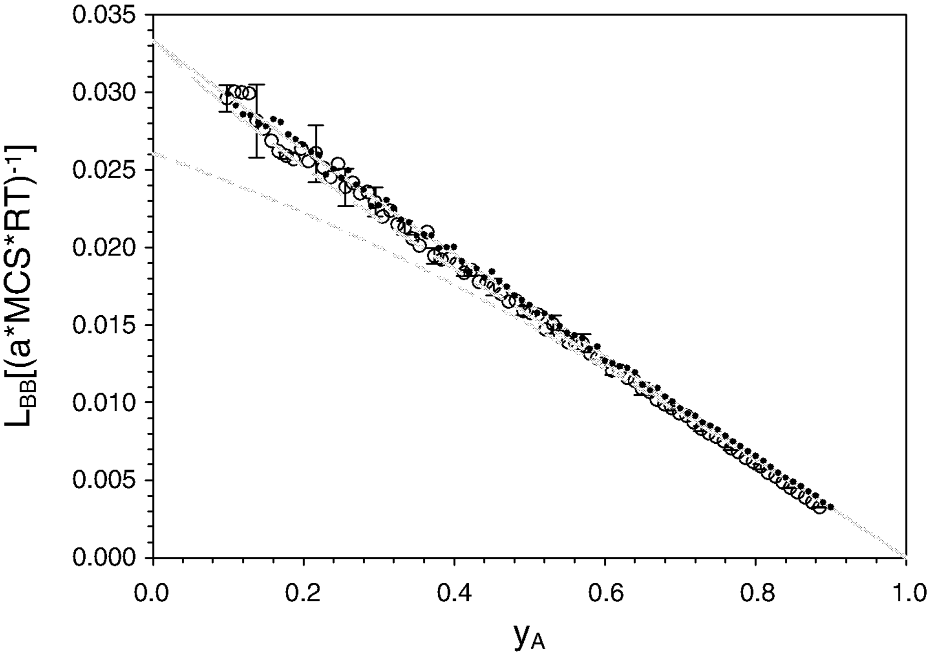

Figure 3. The kinetic coefficients L_{AA}, L_{AB}, L_{BA} and L_{BB} (circles) as a function of composition according to the measurement described in the text averaged over five independent runs. Short dashed lines show the prediction of Darken (equation (15)), the long dashed lines show the prediction of Svoboda *et al.* according to equation (30) and the measured diffusion coefficients and the full lines show the prediction of Moleko *et al.* (equation (17)) for a ratio of jump frequencies of 0.1. Small black symbols represent the results of measurements according to the generalized Einstein formulae.

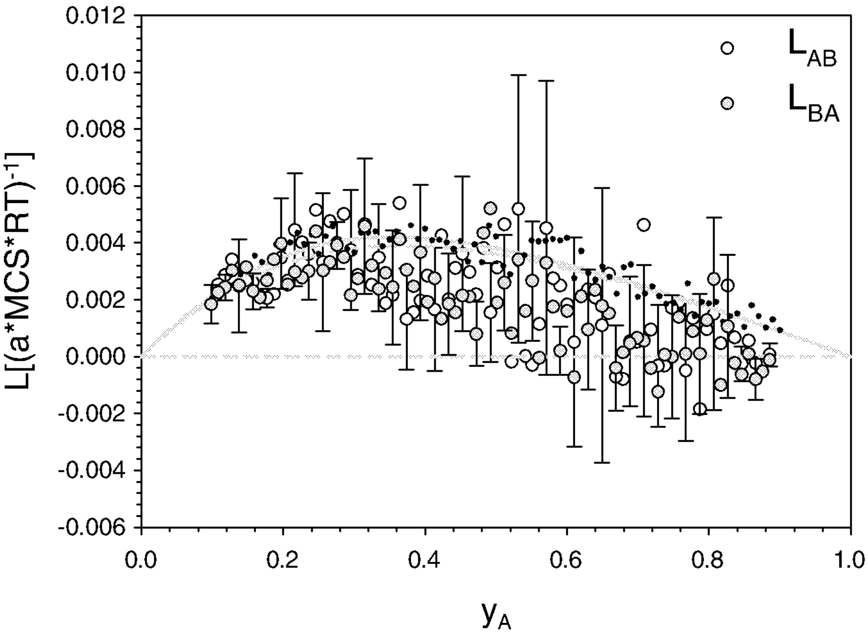

Figure 3. Continued.

understood qualitatively. At low A concentrations the fast A atoms are fully isolated and not able to perform any 'effective' jumps, since either there is no nearby vacancy, because of the slow B atoms, or the vacancy and the neighbouring A atom keep changing place without winning any ground, i.e. the jumps are highly correlated. Considering the extreme case of immobile B atoms, the diffusion coefficient of the fast component can even drop to zero, when the A concentration falls below the percolation threshold. A quantitative investigation to obtain explicit formulae for $D_i(y_A)$ can only be performed using considerable approximations.

Due to the existing chemical gradients the derivation of the Onsager coefficients is even more complicated. Our simulations show that the L_{ik} matrix is not diagonal—the assumption Darken's concept is based on—e.g., since a vacancy gradient emerges, although the vacancy flux is exactly zero (see figure 1, bottom).

Performing a classical tracer experiment and measuring the kinetic coefficients, our method of imposing fluxes on a diffusing system and measuring the resulting site fraction gradients is capable of yielding the correct values for the tracer diffusion coefficients and the Onsager coefficients L_{ik}. The driving force for vacancies is explicitly taken into account. The symmetry of the Onsager matrix was verified by measuring L_{AB} and L_{BA} separately. These simulations are performed far from chemical equilibrium, so that nonlinear effects might not be negligible. In contrast, this problem does not arise in the generalized Einstein simulations, since these are done in a chemically homogenous system without any gradients. We assume that nonlinear effects are the reason for the divergence of the simulation results for L_{ik} for high concentrations from the predictions of Moleko *et al.* and the results obtained from the generalized Einstein equations.

Using a diagonal dissipation rate in the theory of Svoboda *et al.* gives results that diverge significantly for the entire site fraction range. But since in Svoboda *et al.*'s argumentation there are special assumptions on the form of A_V, it is legitimate to ask whether it is possible to describe the diffusion process in the framework of Svoboda *et al.*'s theory using a more suitable choice of A_V.

In this context it is useful to refer to the sum rules that exactly apply to the Random Alloy [17]. In terms of collective correlation factors f_{ij} (defined in (16)), the sum rules read

$$\frac{1-f_{AA}}{\omega_A y_B} = \frac{1-f_{BB}}{\omega_B y_A} = \frac{f_{AB}}{\omega_B y_B} = \frac{f_{BA}}{\omega_A y_A}. \tag{44}$$

Moleko *et al.*'s equation for the kinetic coefficients fulfills these equations trivially. In the case where Svoboda *et al.*'s equations apply to the Random Alloy, one necessary condition is that they fulfil the sum rules. Equations (30) can be rewritten in terms of collective and tracer correlation factors

$$f_{ik} = f_i \delta_{ik} - \frac{f_i f_k y_k \omega_k}{y_A \omega_A f_A + y_B \omega_B f_B + a_V}, \tag{45}$$

where $a_V = (6\Omega RT/r^2)A_V$ is left as an adjustable parameter. Insertion of these expressions into the sum rules leads to the following two equations with the only unknown a_V:

$$\begin{aligned} (1-f_A)(y_A\omega_A f_A + y_B\omega_B f_B + a_V) + f_A^2\omega_A y_A &= -f_A f_B \omega_A y_B, \\ (1-f_B)(y_A\omega_A f_A + y_B\omega_B f_B + a_V) + f_B^2\omega_B y_B &= -f_A f_B \omega_B y_A. \end{aligned} \tag{46}$$

These equations are therefore only solvable if

$$\frac{f_A\omega_A}{1-f_A} = \frac{f_B\omega_B}{1-f_B} \tag{47}$$

holds. In figure 4 the left- and right-hand sides of this equation are plotted against each other. From the deviation from the straight line, it is obvious that the condition is not fulfilled.

To make our point clear: starting from a diagonal dissipation rate, Svoboda *et al.*'s equations (30) are derived with a strictly physical reasoning based on non-equilibrium thermodynamics. No other approximation was made, the only parameter left was A_V. But even for the simple Random Alloy model, no value for A_V fulfilling the sum rules (44) can be found. Consequently, a diagonal dissipation rate is not sufficient to describe the diffusional process in a multicomponent alloy.

In conclusion, we have introduced a method that is capable of calculating Onsager's coefficients in a model system by measuring the atomic fluxes and the site fraction gradients, including the specific role of vacancies. Despite the special boundary conditions in the simulation, our method is based on experimentally accessible parameters and is more closely related to a physical experiment in a real system than the method using the generalized Einstein equations. This new method can be further exploited to study systems more sophisticated than the Random Alloy model. One straightforward extension is to incorporate an interaction Hamiltonian into the system by introducing pair interactions (see e.g. [29, 30]) between atoms and vacancies. This opens up the possibility of studying the diffusion process in a much more general system beyond the ideal solution, where chemical interactions among the constituents lead, for instance, to the emergence of order [31]. An important

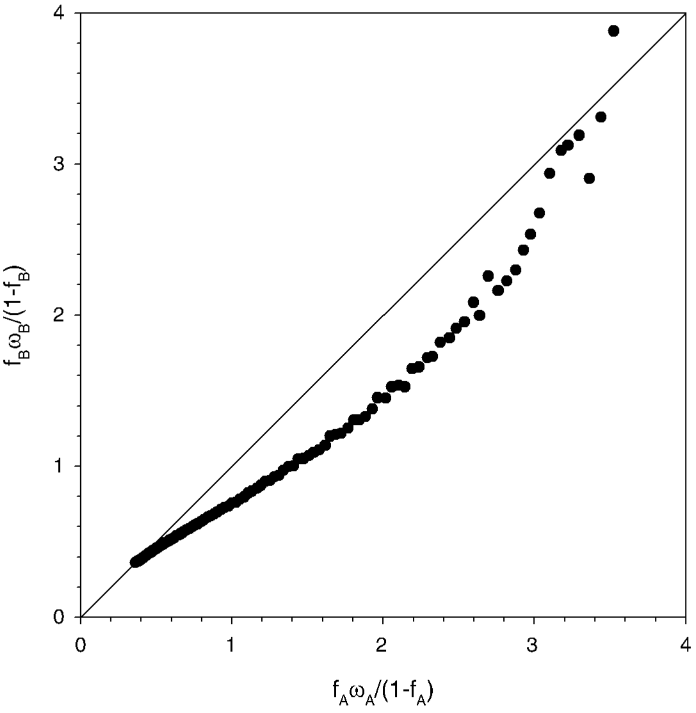

Figure 4. The left-hand side of equation (47) is plotted as a function of the right-hand side. The data points do not lie on the straight line $y = x$, consequently a diagonal form of the dissipation matrix is not sufficient to describe diffusion in Svoboda *et al.*'s concept.

condition, however, is to either treat the vacancies as an independent chemical species for the interactions [32] or to keep the vacancy concentration constant. The method is also not restricted to binary systems, but can be used to determine the Onsager coefficients L_{ik} in multicomponent systems.

Acknowledgement

The numerical results presented in this work were obtained using the computational resources of the Schroedinger cluster of the University of Vienna.

References

[1] L. Darken, Trans. Am. Inst. Min. Engrs **175** 184 (1948).
[2] J.R. Manning, Phys. Rev. B **4** 1111 (1971).
[3] L.K. Moleko, A.R. Allnatt and E.L. Allnatt, Phil. Mag. A **59** 141 (1989).
[4] J. Svoboda, F.D. Fischer, P. Fratzl, *et al.*, Acta mater. **50** 1369 (2002).
[5] G.E. Murch and R.J. Thorn, Phil. Mag. A **39** 673 (1979).
[6] G.E. Murch, Phil. Mag. A **41** 157 (1980).
[7] K.W. Kehr, K. Binder and S.M. Reulin, Phys. Rev. B **39** 4891 (1989).
[8] G.E. Murch and R.J. Thorn, Phil. Mag. A **36** 529 (1977).
[9] G.E. Murch and R.J. Thorn, Phil. Mag. A **39** 259 (1979).
[10] G.E. Murch, Phil. Mag. A **46** 151 (1982).

[11] G.E. Murch, in *Diffusion in Crystalline Solids*, edited by G.E. Murch and A.S. Nowick (Academic Press, New York, 1984).

[12] A.R. Allnatt and E.L. Allnatt, Phil. Mag. A **49** 625 (1984).

[13] J. Philibert, *Atom Movements: Diffusion and Mass Transport in Solids* (de Physique, Les Ulis, 1991).

[14] I. Prigogine, *Introduction to Thermodyamics of Irreversible Processes*, 4th edition (Interscience, New York, 1967).

[15] M.E. Glicksmann, *Diffusion in Solids—Field Theory, Solid State Principles and Applications* (Wiley, New York, 2000).

[16] A.D. Pelton, in *Phase Transformations in Materials*, edited by G. Kostorz (Wiley–VCH, New York, 2001).

[17] L.K. Moleko and A.R. Allnatt, Phil. Mag. A **58** 677 (1988).

[18] I.V. Belova and G.E. Murch, Phil. Mag. A **80** 599 (2000).

[19] I.V. Belova and G.E. Murch, Phil. Mag. A **80** 1469 (2000).

[20] A.R. Allnatt and A.B. Lidiard, *Atomic Transport in Solids* (Cambridge University Press, New York, 1993).

[21] A.B. Lidiard, Acta metall. **34** 1487 (1986).

[22] G.E. Murch, in *Phase Transformations in Materials*, edited by G. Kostorz (Wiley–VCH, New York, 2001).

[23] A.R. Allnatt, J. Phys. C **15** 5605 (1982).

[24] L. Onsager, Phys. Rev. **37** 405 (1931).

[25] J. Svoboda and I. Turek, Phil. Mag. B **64** 746 (1991).

[26] G.E. Murch and I.V. Belova, Phil. Mag. A **80** 2365 (2000).

[27] I.V. Belova and G.E. Murch, Phil. Mag. A **81** 1749 (2001).

[28] W.H. Press, S.A. Teukolsky, W.T. Vetterling, *et al.*, *Numerical Recipes in C*, 2nd edition (Cambridge University Press, Cambridge, 1992).

[29] K. Yaldram and K. Binder, J. statist. Phys. **62** 161 (1991).

[30] R. Weinkamer, P. Fratzl, B. Sepiol, *et al.*, Phys. Rev. B **58** 3082 (1998).

[31] I.V. Belova and G.E. Murch, Phil. Mag. A **78** 1085 (1998).

[32] R. Weinkamer and P. Fratzl, Europhys. Lett. **61** 261 (2003).

R. Weinkamer, M. A. Hartmann, Y. Brechet and P. Fratzl
Architectural changes of trabecular bone caused by the remodeling process
Mater. Res. Soc. Symp. Proc. **874**, L.1.9.1 (2005)

Mater. Res. Soc. Symp. Proc. Vol. 874 © 2005 Materials Research Society L1.9.1

Architectural changes of trabecular bone caused by the remodeling process

Richard Weinkamer[1], Markus A. Hartmann[1], Yves Brechet[2], and Peter Fratzl[1,3]
[1] Max Planck Institute of Colloids and Interfaces, Dept. of Biomaterials, Potsdam, Germany
[2] ENSEEG, LTPCM, Domaine Universitaire de St. Martin d'Hères, Cedex, France
[3] Ludwig Boltzmann Institute of Osteology at the Hanusch Hospital of WGKK and AUVA Trauma Centre Meidling, 4th Medical Department, Hanusch Hospital, Vienna, Austria

ABSTRACT

Using a stochastic lattice model we have studied the architectural changes of trabecular bone occurring while the structure is remodeled. Our model considers the mechanical feedback loop, which control the remodeling process. A fast algorithm was employed to solve approximately the mechanical problem. A general feature of the model is that a networklike structure emerges, which further coarsens while the bone volume fraction remains unchanged. Decreasing the mechanical response of the system by either lowering the external load or the internal mechano-sensitivity leads not only to a reduction of the bone volume fraction, but results in topological changes of the trabecular bone architecture, where the loss of horizontal trabeculae is the most obvious effect.

INTRODUCTION

Living bone gains the ability for adaptation by a mechanobiological remodeling process. Mechanobiology in general deals with the question of how load-bearing tissues are produced, maintained and adaptated by specialized cells actively responding to mechanical stimuli in their environment [1]. Another important example of a mechanobiological process in the human skeletal system beside remodeling is tissue differentiation occurring in bone development and fracture healing. Compact and trabecular bone is continuously remodeled in an interplay of bone resorbing osteoclasts and bone depositing osteoblasts. Being mechanically controlled - an idea dating back to the end of the 19th century – bone remodeling follows the principle that bone is removed where it is mechanically not needed and deposited in highly stressed regions in order to avoid overloading (Wolff-Roux law). Different time scales are active during remodeling: while the response of the cells sensing a mechanical stimulus is thought to be rather instantaneous, the complete resorption of a bone packet takes already a few weeks, the deposition of bone even a few months. The turnover time for the whole trabecular structure is about 4-5 years [2].

In a computational approach of bone remodeling two different problems have to be solved (Fig. 1): given a networklike, trabecular architecture, the structure first has to be mechanically assessed calculating the stresses and strains within the structure. In a second step the result is then fed back to the biological part of the model, where a remodeling rule specifies the local probabilities for bone resorption and bone deposition as a function of the mechanical stimulus. Implementing the Wolff-Roux law in a computer model and using finite element methods (FEM), it was successfully demonstrated that an optimized trabecular architecture emerges, is maintained and adapts to varying loads [3]. Our approach is to use a lattice model and to remodel the structure only via removing or adding small bone packets from the marrow/bone interface. The computation time saved by an approximate treatment of the mechanics allows us to study the effect of different realizations of the control system on the architectural evolution of trabecular bone inside a human vertebra during a human life time.

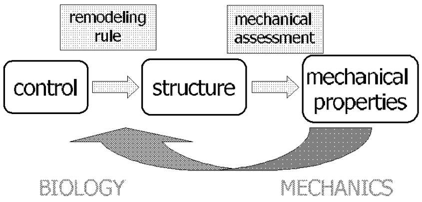

Figure1. The feedback of mechanical information to the biological system at the core of the control system of (computational) bone remodeling.

THE MODEL

In our two-dimensional model (an extension to three dimensions is straightforward) the spongious structure of trabecular bone inside a human vertebra is mapped on a simple cubic lattice. Occupied sites on the lattice correspond to sites filled with bone matrix, unoccupied sites are filled with marrow (Fig. 2). The outer thin shell of the vertebra is modeled by a fixed layer of occupied sites at the boundary of the system. We assume that the system is uniaxially loaded with a force F_z. The inwaisting form of the vertebra translates a vertical deformation ΔL_z also in a horizontal one, $\Delta L_x = k\,\Delta L_z$, resulting in a biaxial loading situation with effective forces $F_z^* < F_z$ and F_x^*, which can be calculated using an energy minimizing argument [4]. According to Figure 1 the two steps of the computation are:

(1) mechanical assessment:

The most accurate method nowadays available to obtain the local stresses and strains in complex structures is the finite element method (FEM). The drawback of this method is that computation time even for a single calculation of a human vertebra is excessive despite of adapted FEM codes and making use of parallel processing in supercomputers [5]. But several million remodeling events – each connected with a resorption/deposition of a small bone packet with a volume of about 0.05 mm^3 - take place in a human vertebra during life time. Having our main interest in the control of the remodeling process (left part of Fig. 1) rather than on mechanical problems, we employed an approximate but fast algorithm to mechanically assess the structure. In a first step, using a two-way painting algorithm [6], the occupied sites which are loaded are determined following the idea that the force is transmitted through the network via nearest neighbor contacts. Assuming equal forces in the different branches of the loaded structure, the local strain along the loading direction is then highest where the cross section of the trabecula is lowest (Fig. 2, left). Details and formulas can be found in [4]. We consider here this local strain as the mechanical stimulus sensed by the cells and influencing bone remodeling. Under the assumption of a homogeneous and isotropic bone material this is equivalent to the local pressure on each bone element as introduced in [4].

(2) remodeling rule:

The remodeling rule specifies the probability that (i) a occupied site at the bone-marrow interface is resorbed (osteoclast action) and that (ii) bone is newly deposited at the interface changing an unoccupied to an occupied site (osteoblast action) as a function of the local stimulus. For these effective probabilities, which include all the intricate details of the mechanotransduction process in bone, no reliable experimental data is available and therefore the form of the remodeling rule has only been conjectured [7]. For bone resorption we assume a constant probability P^-. In our model the Wolff-Roux law is reflected only in the bone forming probability P^+ of the osteoblasts. The functional dependence of P^+ on the mechanical stimulus ε is characterized by a threshold value ε_c, at which the "mechanostat" gets strongly activated (Fig. 2, right). Below the threshold the probability for bone deposition is low ($P^+ = \alpha$), above the threshold P^+ increases linearly with ε. A crucial dimensionless parameter characterizing the mechanical control in our model – denoted by $\hat{\varepsilon}_c$ - is the threshold value ε_c essentially normalized by the external force F_z. Hence, $\hat{\varepsilon}_c$ can be increased either by enhancing the mechano-sensitivity of the system, i.e., lowering ε_c, or by applying a larger external force F_z. The time within each site had on average one occasion to change from bone to marrow or vice versa defines the time unit 1 MCS. The conversion in real time based on a turnover time of the whole vertebra of 4 years yields 100 MCS ≡ 1 year.

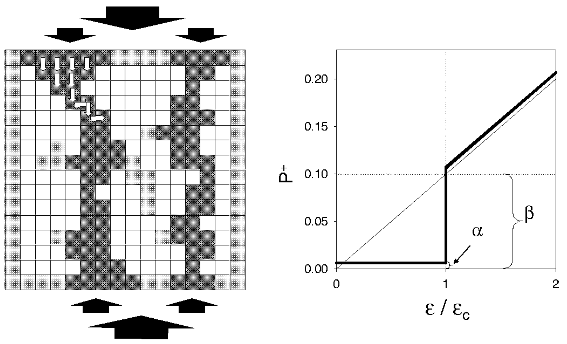

Figure 2. Schematic view of the lattice model of trabecular bone and its mechanical assessment (left). Light gray squares are sites occupied by bone including a layer at the boundary. Dark gray squares show the occupied sites, which are loaded. They are determined by a "painting algorithm" running from top to bottom and back to top, where the force is transmitted to occupied elements in the next layer and its nearest neighbors (as indicated by the small white arrows). The total force (represented by large arrows) is divided into equal parts for each loaded branch (smaller black arrows). The local strain along the loading direction is highest where the cross section of the branch is smallest. On the right: the assumed remodeling rule for the local deposition probability P^+ of new bone at the bone/marrow interface as a function of the mechanical stimulus.

RESULTS

Figure 3 shows snapshots of the time evolution of our model for three different values of the mechanical control parameter $\hat{\varepsilon}_c$, i.e., for instance from a higher to lower mechanical sensitivity of the system from left to right. All these simulations were started with a random configuration of a bone volume fraction close to one ($\rho_{init} = 0.95$). At an initial stage, while the bone volume fraction decreased, a networklike structure emerged with trabeculae preferentially in vertical and horizontal direction. At a second stage of the time evolution the bone volume fraction remained practically unchanged. The microstructure, however, evolved by a coarsening process, i.e., by reducing the number of trabeculae and thickening the remaining ones. These features are independent of the value chosen for the control parameter $\hat{\varepsilon}_c$. Comparing the resulting microstructure for different $\hat{\varepsilon}_c$ values, the difference in the bone volume fraction is most obvious ($\rho \approx 0.5$ (Fig. 3, right) to $\rho \approx 0.37$ (left). We obtained approximately a linear relationship between the steady-state value of ρ and $1/\hat{\varepsilon}_c$ [4]. In our two-dimensional model a 10% reduction of the external load, therefore, leads on the long run to a 10% reduction of the bone volume. The loss in bone volume is only partially compensated by a reduction in the trabecular thickness. The decrease in bone volume results in topological changes with the loss of horizontal trabeculae as an example. This anisotropy between vertical and horizontal trabeculae, which develops also in each simulation run with proceeding time, is the dominating feature for high $\hat{\varepsilon}_c$ values leading to a columnar structure with only vertical trabeculae at very high values.

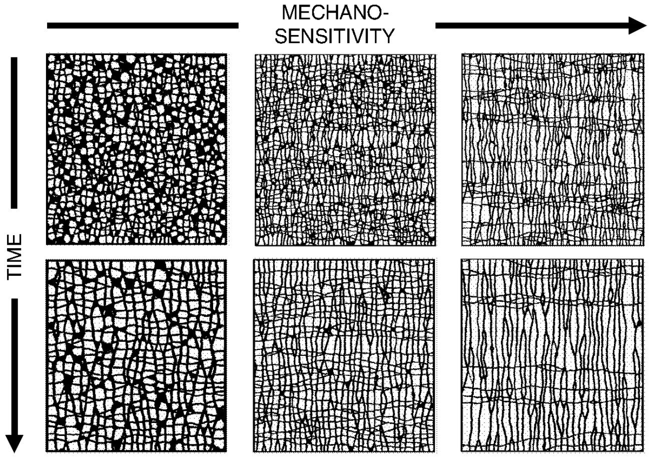

Figure 3. Simulation snapshots at two different times (upper row $t = 2.5$ kMCS and lower row $t = 5$ kMCS) and three different values for the mechano-sensitivity of the control system. Bone matrix is indicated black, marrow white. All simulations were started from a random arrangement of occupied sites of high volume fraction ($\rho_{init} = 0.95$).

We have further investigated the behavior of our model when started not with a random configuration but with completely regular quadratic grids as initial configuration. Also in this case the bone volume fraction reached a steady state value and the value proved to be independent of the starting configuration. The resulting architecture, however, clearly reflected the regularity of the starting point. In the case that the bone volume is distributed into few thick trabeculae, the topology of the starting configuration was almost completely preserved underlining the stability of such a configuration. Nevertheless, the structure displayed an anisotropy with thinner trabeculae in horizontal direction. When the simulation was started with a grid of a greater number of thinner trabeculae, this emerging anisotropy leads to a significant change in the topology by loosing the majority of horizontal trabeculae.

The elastic properties of our bone model are summarized in Figure 4. For cellular structures the relation between the effective Young's modulus, E_*, and the volume fraction, ρ, is typically described by a power-law:

$$E_* \propto \rho^{\kappa} .$$

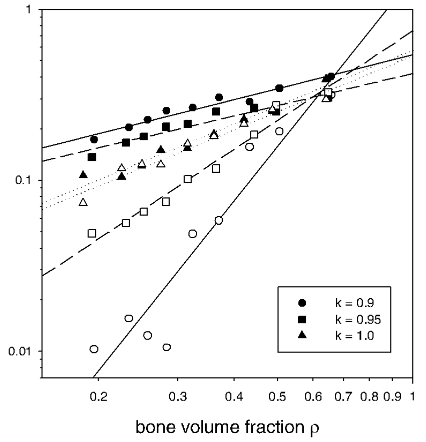

Figure 4. Double logarithmic plot of the effective Young's modulus, E^*, versus the bone volume fraction ρ for different values of *k*. Full symbols denote the modulus in *z*-direction, open symbols in *x*-direction. Data points correspond to simulation runs with different control parameter $\hat{\varepsilon}_c$. The straight lines are linear regressions for each data set performed separately.

For regular structures the exponent κ can be calculated [8] and was verified experimentally. An exponent κ close to 1 is found in structures which are predominantly deformed by compression and stretching, while $\kappa \approx 3$ is obtained when bending dominates [8]. In samples of trabecular bone values for κ between approximately 1.5 and 2.2 were found depending on the anatomical site [9]. Moreover, the influence of the microarchitecture cannot be neglected [10], in case of bone this influence is summarized under the term bone architectural quality. Due to the two-dimensionality of our model we cannot expect a reasonable reproduction of the elastic properties of real bone. Figure 4 shows the effective moduli in *z*- and *x*-direction, E_z and E_x, for different values of *k* (as defined in the model section). For $k = 1$, which corresponds to an equal loading in vertical and horizontal direction, the data both in *z*- and *x*-direction can be fitted by an exponent κ close to 1. With $k < 1$ the more realistic situation of a preferential loading in vertical direction is obtained, resulting in a stiffer architecture in *z*-direction compared to the *x*-direction. This redistribution of the force results in an increase of κ_z and a decrease of κ_x.

DISCUSSION AND CONCLUSIONS

An interesting property of our model of bone remodeling is the implicit time arrow present in our system which directs the evolution towards coarser architectures. The reason is that trabeculae which are separated by the resorption of bone packets from the surface are lost, exactly in the same way as perforation leads to the loss of the trabeculae in real bone. In contrast to modeling approaches where the remodeling is based on the minimization of a kind of energy functional and therefore stops once an optimized architecture is reached, the microarchitecture in our model continues to "age" whereas the bone volume fraction stays unchanged. A coarser structure is actually a feature observed in vertebrae of old patients. Another important feature, the reduced bone mass especially observed in osteoporotic patients, has to be interpreted in the framework of our model as either a change in the external loading or the internal control system. The reason for the latter could be connected with hormonal changes or demands for calcium homeostasis bringing to mind that load bearing is not the sole function bone has to fulfill.

REFERENCES

1. M. C. H. van der Meulen and R. Huiskes, *Journal of Biomechanics*, **35**, 401, (2002)
2. W. S. Jee, *Integrated Bone Tissue Physiology: Anatomy and Physiology*, in *Bone Mechanics Handbook*, Cowin, S. C., Editor. 2001, CRC Press.
3. R. Huiskes, R. Ruimerman, G. H. van Lenthe and J. D. Janssen, *Nature*, **405**, 704, (2000)
4. R. Weinkamer, M. A. Hartmann, Y. Brechet and P. Fratzl, *Physical Review Letters*, **93**, 228102, (2004)
5. J. Homminga, B. Van-Rietbergen, E. M. Lochmuller, H. Weinans, F. Eckstein and R. Huiskes, *Bone*, **34**, 510, (2004)
6. J. Parkinson, A. Brass, G. Canova and Y. Brechet, *Journal of Biomechanics*, **30**, 549, (1997)
7. H. M. Frost, *Anat Rec*, **219**, 1, (1987)
8. L. J. Gibson and M. F. Ashby, *Cellular solids : structure and properties*. 2nd ed. Cambridge solid state science series. 1997, Cambridge ; New York: Cambridge University Press.
9. E. F. Morgan, H. H. Bayraktar and T. M. Keaveny, *Journal of Biomechanics*, **36**, 897, (2003)
10. A. Woesz, J. Stampfl and P. Fratzl, *Advanced Engineering Materials*, **6**, 134, (2004)

M. A. Hartmann, R. Weinkamer, Th. Zemb, F.D. Fischer and P. Fratzl
Switching mechanics with chemistry – a model for the bending stiffness of
amphiphilic bilayers with oppositely charged head groups
submitted

Switching mechanics with chemistry – a model for the bending stiffness of amphiphilic bilayers with oppositely charged head groups

Markus A. Hartmann,[1] Richard Weinkamer,[1] Thomas
Zemb,[2] Franz Dieter Fischer,[3] and Peter Fratzl[1,*]

[1]*Max Planck Institute of Colloids and Interfaces,*
Am Mühlenberg 1, D-14476 Potsdam
[2]*LIONS at DRECAM/SCM, C.E. Saclay F-91191 Gif sur Yvette*
[3]*Institute of Mechanics, Montanuniversität Leoben,*
Franz-Josef Straße 18, A-8700 Leoben

(Dated: January 16, 2006)

Abstract

Bilayer structures in catanionic systems experimentally showed peculiar mechanical behavior. The observed increase in the bending stiffness is supposedly connected to additional hydrogen bonds forming between anionic head groups. With a simple model we can explain the extreme sensitivity of the bending stiffness of the membrane on the molar ratio of the charged molecules. This effect is further amplified by the sandwich-like structure of the membrane, where the apolar core seperating the head groups acts via a kind of lever-arm principle. As a consequence of these combined effects the model membrane changes from a soft behavior with bending rigidities in the order of 10 $k_B T$ to an extremely stiff membrane with a bending stiffness more than 2 orders of magnitude larger where most of this change occurs within a molar ratio interval smaller than 0.1.

Amphiphilic molecules are well known for their ability to self assemble into “films” with defined area, stiffness and curvature [1]. These films assemble into complex geometrical structures, such as micelles, vesicles, “sponge” or lamellar phases when dissolved in water [2]. The chemical potential of any surfactant assembly can be expressed as a function of the integrated average curvature, the so-called packing parameter, and the area per head group. When a configuration of zero average curvature is stablest, amphiphiles form bilayer structures stacked in smectic order - usually in multilayered vesicles [3, 4]. For a membrane composed of a mixture of two amphiphiles with oppositely charged head groups [5], the lateral cohesion energy of the bilayer is much stronger than of all other known types of bilayers. This so-called “catanionic” systems [6] off stoichiometry and in absence of excess salt, i.e., “true catanionics”, show very peculiar behavior, such as fragmentation of lamellae upon dilution into micron-sized rigid nanodiscs [7]. Measurements of the mechanical properties of these nanodiscs yielded bending rigidities of the order of hundreds to thousands k_BT or Young’s moduli of the order of hundreds of MPa, i.e., at least two orders of magnitude larger than electrically charged bilayers [8]. Another special feature of true catanionics is the extreme sensitivity of the phase diagram with respect to the molar ratio between anionic and cationic surfactants. While at equimolar ratio, only concentrated liquid crystals are formed, close to molar ratios 1/3 or 2/3 large domains of colloidal stability can be observed, e.g., cylindrical micelles, punctuated planes and polyhedra, respectively [9, 10]. These systems show the highest bending stiffness yet reported for a self-assembled system based upon surfactants, indicated by giant colloids which are molecularly flat over a length of 10 micrometers and more, and therefore are observable directly under the optical microscope. Since the in-plane persistence length is given by a molecular scale pre-factor multiplied by an exponential of the bending stiffness [11], the bending constant has to exceed 100 k_BT. These peculiar experimental observations motivate our modeling and exploration of the mechanical properties of bilayers made of amphiphilic molecules with oppositely charged head groups occupying a triangular lattice. The formation of additional bonds between anionic head groups is modeled by a spring network. Our model therefore displays some resemblance to models of the membrane-associated cytoskeleton of living cells, e.g., of erythrocytes [12]. Important differences are the development of a specific order in our networks and the high stiffness of the springs which allow the assumption of a flat membrane neglecting effects of undulation [11, 13].

On a mesoscopic scale our model membrane as sketched in FIG. 1 consists of an apolar core with a width h and an upper and lower polar layer formed by the head groups of the molecules. The mechanical behavior of the membrane is described by the bending stiffness of the apolar core κ_0, and the in-plane stiffness of the polar layers represented by their in-plane tension modulus Y, i.e. the two-dimensional analog of the modulus of elasticity E (Y is therefore measured in units force/length). Due to the sandwich structure, the bending stiffness κ of the whole membrane is given by [14]

$$\kappa = \kappa_0 + \frac{h^2}{2} Y. \tag{1}$$

Different from the reported h^2-dependence of κ_0 [15], the same dependence for the second term is simply the result of the sandwich structure. With our model we want to understand the effect of additional bonds between the head groups on Y and consequently on the mechanical behavior of the whole membrane. The experimental scenario we model is a fluid membrane where the oppositely charged head groups arrange themselves according to the thermodynamic equilibrium at temperature T. Due to a change in the solvent conditions, the configuration of molecular heads "freezes" and additional bonds between the head groups develop. In the microscopic part of the model the closely packed molecules with either positively or negatively charged headgroups occupy a triangular lattice with lattice spacing a. The electrostatic interactions between the polar heads are described by nearest neighbor interactions only using a standard Ising model [16]. The sign of the single interaction parameter, the so-called exchange energy J, is chosen to ensure an antiferroelectric ordering between the polar heads [17]. An equilibrium configuration of the positively and negatively charged heads is obtained using standard Monte Carlo techniques [18]: changes in the configuration are perfomed by Kawasaki dynamics, i.e., an exchange of two molecules, the decision if the exchange is executed follows a standard Glauber algorithm. Monitoring order parameters in the system the attainment of thermal equilibrium was verified [17]. This equilibrium configuration is then fixed, and nearest neighbors are assumed to be connected by linear elastic springs. Two nearest neighbor molecules with negative charge are assigned a spring constant k_1, all other headgroup pairs are connected by springs with $k_2 \ll k_1$.

The mechanical properties of the layers can be described by a stiffness matrix relating the in-plane normal tensions σ_1 and σ_2 and the in-plane shear tension τ (all measured in units force/length) to the in-plane strains ϵ_1 and ϵ_2 and the in-plane shear angle γ.

$$\begin{pmatrix} \sigma_1 \\ \sigma_2 \\ \tau \end{pmatrix} = \begin{pmatrix} Q_{11} & Q_{12} & Q_{13} \\ Q_{12} & Q_{22} & Q_{23} \\ Q_{13} & Q_{23} & Q_{33} \end{pmatrix} \begin{pmatrix} \epsilon_1 \\ \epsilon_2 \\ \gamma \end{pmatrix}, \tag{2}$$

The stiffness matrix has a priori six independent entries. All of them were determined by performing three independent computational mechanical tests by imposing different deformations on the system and taking care of appropriate boundary conditions. Using a Monte Carlo algorithm the position of the molecules in elastic equilibrium was determined. The resulting forces on the boundaries were finally transformed into the acting tensions to calculate the elastic coefficients using Eq. (2) with the result,

$$Q_{11} - Q_{22} \approx Q_{13} \approx Q_{23} \approx Q_{11} - Q_{12} - 2Q_{33} \approx 0, \tag{3}$$

for all molar ratios. Thus, the layers show isotropic elastic behavior and therefore the number of independent elastic parameters can be reduced to two only, the tension modulus, Y, and the two-dimensional Poisson ratio ν,

$$Y = Q_{11}(1 - \nu^2) \qquad \nu = \frac{Q_{12}}{Q_{11}}. \tag{4}$$

The connection to the widely used area compression modulus K_A [15] reads as

$$K_A = \frac{Q_{11}(1+\nu)}{2} = \frac{Y}{2(1-\nu)}. \tag{5}$$

For the numerical simulations we chose for the geometry of the membrane a thickness of the apolar core $h = 3$ nm [7]. For the bending stiffness of the apolar core values ranging from 3 to 50 k_BT have been reported [15], our choice was $\kappa_0 = 10\ k_BT$. To study the influence of the ordering due to the electrostatic interaction between the head groups, simulations were performed with two different values for the Ising exchange energy J, $J = 1\ k_BT$ and $J = 0$, latter corresponding to a random arrangement of the molecules. For the additional bonds we assume that hydrogen bonds form between anionic head groups, more specific between parallel carboxylates [19]. The binding energy for this configuration is about 2 k_BT [20]. To transform this energy into a value for the spring constant k_1, we consider a Lennard-Jones potential with an equal binding energy and an equilibrium spacing $a = 0.8$ nm. A Taylor expansion gives for the harmonic term

$$k_1 \approx \frac{72W}{a^2} = 180\ k_BT/\mathrm{nm}^2 \approx 4.5\ \mathrm{eV/nm}^2. \tag{6}$$

The spring constant between the other headgroup pairs should be orders of magnitude smaller so that the contribution of the apolar core κ_0 dominates in the case without additional bonds. We set $\gamma = k_1/k_2 = 10^4$.

Model membranes with a different composition of anionic and cationic molecules have been studied covering the whole molar ratio range from pure cationic ($c_A = 0$) to pure anionic layers ($c_A = 1$). The choice $J = 1\ k_BT$ resulted in the tendency that anionic molecules try to be surrounded by cationic ones and vice versa. For sufficiently large molar ratios, a continuous triangular network of additional bonds emerges with holes due to the presence of dispersed cationic molecules (FIG. 2a). For molar ratios c_A close to 2/3, a regular super-lattice is formed (FIG. 2b). The honeycomb structure is due to an individual cationic molecule surrounded by six anionic molecules. For small molar ratios, the percolated network of additional bond breaks into separated islands of additional bonds (FIG. 2c).

FIG. 3 summarizes our results concerning the mechanics of the model membrane as a function of its composition. Plotted are the tension modulus Y, the two-dimensional Poisson ratio ν and the bending stiffness κ together with the effective elastic modulus $\overline{E}$ defined as $\overline{E} = \frac{12(1-\nu^2)}{h^3}\kappa$, with $\nu = 1/3$. The two different curves allow a comparison between the case where the electrostatic interaction between the charged headgroups results in an ordering of the molecules and the case of a random arrangement of the molecules. For both, Y and κ, the general behavior is characterized by a transition over several orders of magnitude from low to high values, i.e., from soft to stiff behavior, when the molar ratio is increased. Significant differences between the ordered and the random case occur only in the range between $c_A = 0.6$ and $c_A = 0.8$ where the transition substantially takes place. The effect of the order consists in postponing the transition to higher molar ratios and therefore steepening the switching from soft to stiff. In this range $c_A = 0.6 - 0.8$ the two-dimensional Poisson ratio ν takes values close to 1 in the case of ordering, while it is roughly 1/3 for all molar ratios in the random case, which is the exact value for an isotropic two-dimensional solid, if the Cauchy relation is valid [21].

In some limiting cases analytical results can be obtained, which are in full agreement with the computational results. For a pure anionic configuration ($c_A = 1$) the only springs present are that of type k_1 and the triangular lattice is mechanically described by $Y = 2/\sqrt{3}k_1$ and $\nu = 1/3$. Hence the additional bonds increase the bending modulus by $\Delta\kappa = h^2 k_1/3$ resulting in a maximum stiffness of the membrane of $\approx 910\ k_BT$. For a completely ordered lattice, which can be formed for $c_A = 2/3$, the stiff bonds form a honeycomb lattice (see (FIG. 2b) and the two-dimensional Poisson ratio is given by $\nu = \frac{2(\gamma^2+\gamma+1)}{2\gamma^2+11\gamma+5}$, $\gamma = k_1/k_2$. In the limit $\gamma \rightarrow \infty$ then $\nu \rightarrow 1$ and therefore with Eq. (4) $Y \rightarrow 0$ reflecting that a honeycomb lattice is a kinematically undetermined structure that can be stretched or sheared without stretching any bond. To understand the transition between soft and stiff, the percolation properties of the network of additional bonds are crucial. For the random case on a triangular lattice a conductivity backbone is formed at the site percolation threshold $c_A = 0.5$ [22]. Since the conductivity backbone contains quasi-one dimensional structures which do not resist deformation through changes in the bond angles [23] (like noted above for the honeycomb structure), the formation of a rigid backbone is essential for the stiffening [24]. The rigidity percolation on the (random) triangular lattice was found to occur around a bond probability $p_{ce} = 0.65$ [25]. This would correspond to a rigidity percolation at a site concentration $c_A = 0.81$, but for our case this value is too high, since a random arrangement of atoms is not equivalent to a random arrangement of bonds. In the case of an electrostatic ordering between the molecules the onset of the rigidity percolation is postponed to high values of c_A. Firstly the ordering opposes the formation of additional bonds. For instance, compared to a random configuration in the ordered honeycomb structure the number of additional bonds is reduced by a factor of 3/4. And secondly, in the honeycomb framework of the additional bonds each honeycomb cell is kinematically undetermined. Beyond a concentration of $c_A = 2/3$ in the case of full order, each additional anionic atom placed in the center of a honeycomb cell causes the formation of six additional bonds and the cell becomes stiff. In our model the rigidity percolation transition is less pronounced due to the existence of soft springs and due to thermal disorder. The stiffening effect of the polar layer is reflected in the behavior of the bending stiffness κ only when the stiffening of the surface bonds markedly exceeds κ_0, which happens beyond $c_A = 0.65$ (FIG. 3). The energies of the additional microscopic bonds are rather low, however the stiffening effect due to the percolation stiffness is tremendously enhanced as a result of the sandwich-like structure of the membrane (Eq. (1)).

Although the specifities of the experiments are not captured in our model, two main experimental observations make us confident that the mechanism, which allows the model membrane to change the mechanical properties in a very narrow concentration range, is also acting in real catanionic systems. First are the high bending rigidities observed in nanodiscs and in polyeders. Second the high sensitivity of the system to small changes in the molar ratio between cations and anions in certain concentration ranges. This sensitivity could also be the reason for the intriguing coexistence of facetted and un-facetted bent spheres which can be observed in freeze fracture microscopy. This has been up to now considered as an artifact or due to the presence of impurities. In the case when the molar ratio is around the stiffening transition, local fluctuations in the composition, which can be as large as 10 % [26], can be responsible for finding colloids with mechanical stiffness varying one order of magnitude in the same sample, unfacetted soft and facetted stiff colloids.

We acknowledge support from the French-German network “Complex fluids in thin films”.

---

* Electronic address: Peter.Fratzl@mpikg.mpg.de

[1] S. Hyde, *The language of shape* (Elsevier, Amsterdam-Lausanne, 1997).

[2] T. N. Zemb, Colloid Surf. A-Physicochem. Eng. Asp. **130**, 435 (1997).

[3] J. N. Israelachvili, D. J. Mitchell, and B. W. Ninham, Journal of the Chemical Society-Faraday Transactions II **72**, 1525 (1976).

[4] M. Dubois and T. Zemb, Current Opinion in Colloid & Interface Science **5**, 27 (2000).

[5] H. Fukuda, K. Kawata, H. Okuda, and S. L. Regen, J. Am. Chem. Soc. **112**, 1635 (1990).

[6] P. Jokela, B. Jönsson, B. Eichmüller, and K. Fontell, Langmuir **4**, 187 (1988).

[7] T. Zemb, M. Dubois, B. Deme, and T. Gulik-Krzywicki, Science **283**, 816 (1999).

[8] M. Dubois, T. Gulik-Krzywicki, B. Deme, and T. Zemb, Comptes rendues de l'academie des sciences serie II fascicule C-Chemie **1**, 567 (1998).

[9] M. Dubois, B. Deme, T. Gulik-Krzywicki, J. C. Dedieu, C. Vautrin, S. Desert, E. Perez, and T. Zemb, Nature **411**, 672 (2001).

[10] T. Zemb and M. Dubois, Aust. J. Chem. **56**, 971 (2003).

[11] U. Seifert and R. Lipowsky, in *Structure and Dynamics of membranes*, edited by R. Lipowsky and E. Sackmann (Elsevier Science, Amsterdam-New York, 1995).

[12] S. K. Boey, D. H. Boal, and D. E. Discher, Biophys. J. **75**, 1573 (1998).

[13] G. Gompper and D. M. Kroll, J. Phys.-Condes. Matter **9**, 8795 (1997).

[14] L. D. Landau and E. M. Lifschitz, *Elastizitätstheorie* (Akademie Verlag, Berlin, 1991).

[15] D. Boal, *Mechanics of the Cell* (Cambridge University Press, Cambridge, 2002).

[16] R. Weinkamer, P. Fratzl, B. Sepiol, and G. Vogl, Phys. Rev. B **58**, 3082 (1998).

[17] M. K. Phani, J. L. Lebowitz, M. H. Kalos, and O. Penrose, Phys. Rev. Lett. **45**, 366 (1980).

[18] R. Weinkamer, P. Fratzl, H. S. Gupta, O. Penrose, and J. L. Lebowitz, Phase Transit. **77**, 433 (2004).

[19] M. L. Lynch, Y. Pan, and R. G. Laughlin, J. Phys. Chem. **100**, 357 (1996).

[20] S. Zhu, M. Heppenstall-Butler, M. F. Butler, P. D. A. Pudney, D. Ferdinando, and K. J. Mutch, J. Phys. Chem. B **109**, 11753 (2005).

[21] M. Born and K. Huang, *Dynamical theory of crystal lattices* (Clarendon Press, Oxford, 1988).

[22] S. C. van der Marck, Phys. Rev. E **55**, 1514 (1997).

[23] S. Feng, B. I. Halperin, and P. N. Sen, Phys. Rev. B **35**, 197 (1987).

[24] A. R. Day, R. R. Tremblay, and A. M. S. Tremblay, Phys. Rev. Lett. **56**, 2501 (1986).

[25] M. Sahimi and J. D. Goddard, Phys. Rev. B **32**, 1869 (1985).

[26] M. Dubois, L. Belloni, T. Zemb, B. Deme, and T. Gulik-Krzywicki, Prog. Colloid. Polym. Sci. **115**, 238 (2000).

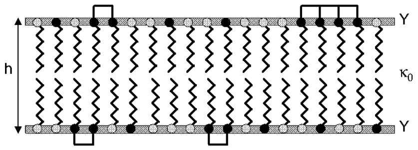

FIG. 1: (Color Online) A cut through a lipid bilayer membrane. The two differently charged head groups are shown as dark (anionic) and light circles (cationic), respectively. The black bars connecting two neighboring anionic molecules indicate the formation of additional bonds (e.g., hydrogen bonds).

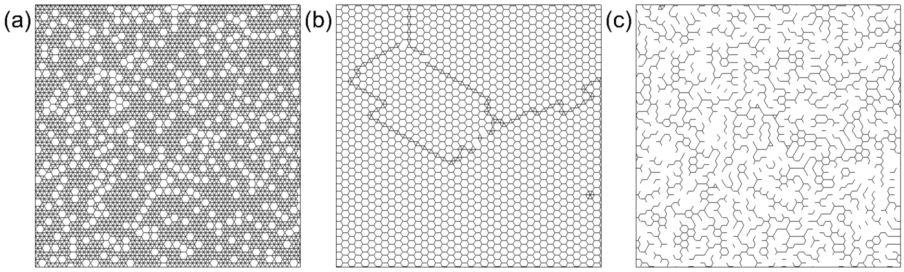

FIG. 2: Three typical configurations for different molar ratios and a temperature of $J/k_BT = 1$ are plotted for (a) $c_A = 0.9$, (b) $c_A = 0.67$ and (c) $c_A = 0.5$, respectively. The additional bonds between anionic molecules are marked by small bars.

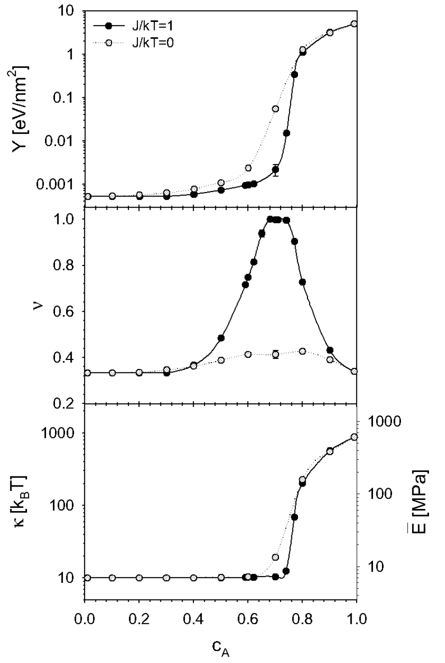

FIG. 3: (Color online) Tension modulus Y (top), two-dimensional Poisson ratio ν (middle) of the head group region and the bending stiffness κ as well as the (effective) elastic modulus $\overline{E}$ (bottom) of the complete sandwich structure plotted as a function of composition. The behavior for two different temperatures is shown ($J/k_BT = 1$ and $= 0$, respectively). The lines drawn are guides to the eyes. Note the semilogarithmic scale in the plots at the top and bottom.

Acknowledgements

Without the help and support of several people writing this thesis would not have been possible or would definitely not have been that much fun. Saying "Thank you" to all of you is the least I can do.

First, I want to thank Peter Fratzl for giving me the opportunity to join his research department – first in Leoben, then in Potsdam – and to write this thesis. Thank you for many fruitful discussions and for finding time whenever your help was needed. A better boss can hardly be found!

Second, many thanks go to my "little boss" and flat mate Richard Weinkamer. Not only that Ricci is an ingenious "Übungsleiter", the same holds for him as a group leader. Being there whenever any problem arose and willing to discuss in every detail Ricci provided invaluable help in preparing this thesis. Besides being my group leader Ricci also became a very good friend. On the one hand, sharing the flat with Ricci posed only minimal problems: daily discussions on the TV-program (I will never understand how one can watch the life of common soldiers in the north-Korean army after one day of work, while Ricci persistently refused to watch enjoyable TV-series like *Buffy* or *Charmed*), who is allowed to use the comfortable TV-chair (and after all, it was me who bought it) and the common discussions on cleaning up (but since neither of us was insisting on a perfectly clean flat, it worked out well). On the other hand, the living together of two individuals that different, brought lots of colour to our lives – even if the long lasting discussions on the Roman Catholic church mostly ended with Ricci calling me childish.

Third, I want to express my gratitude to my collaborators Jiri Svoboda and Franz-Dieter Fischer, who were always willing to discuss arising problems, perform additional calculations and that gave good advice in finishing my first publication.

Fourth, I want to thank all of my colleagues that made life purely wonderful. First of all my office mates first in Leoben, then in Potsdam. Barbara Aichmayer started her PhD thesis almost at the same time as I did, so we led an almost parallel "PhD life". And by the way, Barbara you were the only one that made me separate garbage in the office (and do not worry, next

time I will vote for the Green Party). Manjubala Inderchand, who taught me much about India and indian life style and who showed me the art of preparing puri. And finally Antje Reinecke our newcomer from the theory department, who brought much of (green) life and the noise of little kittens (thanks to Bill Gates for this) to our office. Thanks to all of you for bearing the sound of great opera in our office!

Burgi Gierlinger, Karin Jungnikl and Wolfgang Wagermaier were always there to spent a beautiful evening after one long day at work. Burgi's gnocchi and mojitos are legendary, as well as her speedy way of driving (both, the car and the bike) and her outstanding bad- and speedminton abilities (and some day I will reveal your psychological tricks that make you defeat me). I also want to thank you for many nice evenings in the cinema, sharing the "fresh" air with me and just being there whenever you were needed. Karin never failed the expectations to narrate one of her famous "Karin's stories" and for sure she always found some new and/or exotic ingredient for an otherwise normal dish. Since Wolfgang, the master of the barbecue, joined the department everybody else could take the train schedules from the wall, since he knew them all by heart. Always willing to help, Wolfgang rescued many of his colleagues from paying incredible sums to the church by providing help and information how to quit. Sharing the office with Ricci Wolfgang could really understand and share my "pains". Alexander Wöß, who in his own words is "reactionary, even for Leoben", was at least never silent and could definitely not be overseen by anyone – a quality that exponentiated with the amount of consumed alcohol. And Alex, being the great organiser of the biomaterials soccer team in the 2004 tournament and then missing it yourself, was really not your fault – could almost have happened to everybody else! Michaela Eder and Luna Goswami were always willing to circumvent the canteen. Michaela (her "Semmelknödel" are marvellous) was most of the time in a very good mood. Spending time with her was always relaxing and most of the time just fun. Although she can be very destructive at work (her wood fibres know why), she is very constructive everywhere else! Luna, sceptical and very talkative, always told everything, but also wanted everything to be told. Lunch sessions, coffee breaks or train journeys home never were boring with her. And after all I learned that India is a big country! Helfried Mollay, who spent much too little time at our institute, was one of the persons one could talk to about the really important things. It was a rememberable train journey back to Berlin (probably not only for us, but also for all other travellers), when we recited the dialogs from *Star Wars* by heart. And – to put it simple – Heli's recipe for the marinated salmon is still unmatched. Together with Burgi, Michaela and me Heli was a real fresh air lunatic! Davide Ruffoni, our italian import, is an invaluable help

in translation of italian opera libretti. Furthermore helping Davide quit the church was one of my greatest pleasures (rescuing others from the pope's hard grip is always satisfying, even if Ricci already sees me burn in hell! But can I leave Wolfgang alone there?). Another highlight on the train rides home after a long day's work were the geographical discussions with Aurelien Gourrier. No matter where our discussions started, after some time Aure had to put out his calendar with the world map at the end! And the french cheese he brought with him from one of his journeys home was a real experience (not only for us who ate it, but also for all others! Guess why!). And Aure, I will also never forget your last minute manoeuvre in the final corner during our go-kart race that ruined my victory (yes, Alex, I was second in the end as everybody knows!).

Also the group leaders shall not be forgotten: Oskar Paris, Ingo Burgert and Himadri Gupta. The invitations to Oskar's place were always culinary events of extra class. As his favourite betting partner Ingo had lots of fun with me, but I am sure that I only missed the year and that Bayer Leverkusen is going to win the german championship somewhen! Although a real expert in soccer, all other sports were quite unfamiliar to Ingo. Michael and Ralf Schumacher he only appreciated for their "Schumiletten" and the great idea of selling the emissions of their Formula 1 cars in tins he only made fun of! But Ingo, this idea is that ingenious that you can call it an act of art! As the first "intruder" in the institute Himadri gave life to the new department and paved the way for the next to come.

But it was not only the biomaterials department that made life at the institute purely wonderful. There was also a strong interaction with the other departments which manifested in a variety of social events. Here I want to mention the "Kaffeerunde" of the Interface Department as a fix point of social interaction. Especially Marc Nolte, who is an active organiser of game evenings. Anja Günther I have to say thank you for two remarkable city travels, one to Rome, the eternal city, and one to Vienna.

But not only the scientific staff was responsible for a good life. Kerstin Gabbe, the good soul of our department, was always helpful in each aspect, be it in booking a travel, in providing the office with the required equipment or – most important – in refilling the coffee-resources. Hans-Jürgen Schanze and Michael Born kept the computer, our most important working tool, running. Bodo Ryschka is a master in reorganising an office and an invaluable help in each office improvement try. For me as a computer scientist, not used to the strange world of hammers, nails and screws, his advice was often of tremendous importance.

So, after a wonderful time at the institute just let me tell you . . . but wait, let me say it with Mozart, I think there is no better way:

Nie werd' ich Eure Huld verkennen,
mein Dank bleibt ewig Euch geweiht …
Wer soviel Huld vergessen kann,
den seh' man mit Verachtung an!
Die Entführung aus dem Serail, 3. Aufzug

Curriculum Vitae

Personal Data

Name:	Hartmann
First Name:	Markus
Date of Birth:	15. February 1977
Place of Birth:	Vienna, Austria
Family Status:	Single

Academic Qualifications

1995 – 2000:	Master of Physics (Mag. rer. nat.), University of Vienna, Austria
Master Thesis:	*Messung von ionenstrahlinduzierten Spannungen in Glas mittels Röntgenbeugung* Hahn-Meitner-Insitute, Berlin and University of Vienna
2002 – March 2003:	PhD student, Erich-Schmid-Institute, Austrian Academy of Sciences, Leoben, Austria
April 2003 – present:	PhD student, Max-Planck-Institute of Colloids and Interfaces, Potsdam, Germany

Attended Conferences, Workshops and Schools

September 2002:	OEPG Annual Meeting, Leoben, Austria
March 2003:	DPG Annual Meeting, Dresden, Germany
July 2003:	CISM course on *Bone Cell and Tissue Mechanics*, Udine, Italy
March 2004:	DPG Annual Meeting, Regensburg, Germany
March 2004:	Spring school *Physics meets Biology*, Research Center Jülich, Germany

September 2004: *Micro-Mechanical Properties of Biomaterials*, Tomar, Portugal
March 2005: DPG Annual Meeting, Berlin, Germany
March 2005: APS Annual Meeting, Los Angeles, USA
May 2005: Annual Meeting of the French-German Network, Rouen, France

Other
February 2001 – October 2001: Military Service

Selbständigkeitserklärung

Hiermit erkläre ich eidesstattlich, dass ich die hier vorliegende Arbeit selbst verfasst und nur die angegebenen Hilfsmittel verwendet habe.

Potsdam, 5. September 2005